

ORIENTATION OF POLYMER FILMS FOR IMPROVEMENT OF DIELECTRIC
PROPERTIES IN HIGH-ENERGY DENSITY CAPACITOR APPLICATIONS

A Dissertation

Submitted to the Faculty

of

Purdue University

by

Megan E. Forshey

In Partial Fulfillment of the

Requirements for the Degree

of

Doctor of Philosophy

December 2019

Purdue University

West Lafayette, Indiana

THE PURDUE UNIVERSITY GRADUATE SCHOOL
STATEMENT OF DISSERTATION APPROVAL

Dr. Mukerrem Cakmak, Chair

Department of Materials and Mechanical Engineering

Dr. Chelsea Davis

Department of Materials Science and Engineering

Dr. John Howarter

Department of Materials Science and Engineering

Dr. Jeffrey Youngblood

Department of Materials Science and Engineering

Approved by:

Dr. David Bahr

Head of Department of Materials Science and Engineering

To my husband, Gustavo Guzman because, through all the health issues and hardship, you convinced me that I could do this.

ACKNOWLEDGMENTS

Thank you to Dr. Cakmak and group for your support during my time at Purdue University. Thank you to PolymerPlus, A. Schulman, and PolyK for kindly providing materials used in this work. Thank you to the Office of Naval Research for dielectric testing and University of Connecticut students for all your help.

PREFACE

“Don’t aim at success—the more you aim at it and make it a target, the more you are going to miss it. For success, like happiness, cannot be pursued; it must ensue, and it only does so as the unintended side-effect of one’s personal dedication to a cause greater than oneself or as the by-product of one’s surrender to a person other than oneself. Happiness must happen, and the same holds for success: you have to let it happen by not caring about it. I want you to listen to what your conscience commands you to do and go on to carry it out to the best of your knowledge. Then you will live to see that in the long run—in the long run, I say—success will follow you precisely because you had forgotten to think of it.”

Viktor E. Frankl, Holocaust Survivor

Man’s Search for Meaning

TABLE OF CONTENTS

	Page
LIST OF TABLES	xi
LIST OF FIGURES	xii
ABSTRACT	xxi
1 Introduction	1
2 Literature Survey	9
2.1 Capacitor technology and applications	9
2.1.1 Current state of the art	9
2.1.2 High energy density applications	10
2.2 Materials for improved polymer dielectrics	11
2.2.1 Polyethylene terephthalate (PET)	12
2.2.2 Fluoropolymers	19
2.2.3 Ethylene vinyl alcohol copolymer (EVOH)	32
2.3 Dielectric properties of polymers	37
2.4 Methods to improve dielectric properties of polymer materials	39
2.4.1 Copolymers, blends and nanocomposites	39
2.4.2 Microlayering	40
2.4.3 Multilayer film orientation	51

	Page
2.5 Real-time techniques for online polymer mechano-optical property measurement	53
2.5.1 Custom built uniaxial stretcher	53
2.5.2 Instrumented biaxial stretcher	55
2.5.3 Heat setting chamber	60
2.6 Offline characterization techniques	61
2.6.1 X-ray diffraction	61
2.6.2 Crystalline orientation factor	65
2.6.3 Thermal characterization	68
2.6.4 FTIR	70
2.6.5 Atomic force microscopy (AFM)	72
3 MICROLAYERED PET/PVDF FILMS: MECHANO-OPTICAL BEHAVIOR IN UNIAXIAL EXTENSION	75
3.1 Introduction	76
3.2 Materials and experimental procedures	81
3.3 Results and discussion	84
3.3.1 Selection of processing temperature	84
3.3.2 Uniaxial Stretching	88
3.3.3 Characterization	94
3.3.4 Dielectric properties	107
3.3.5 AFM and Structural Model	112
3.4 Conclusions	114

	Page
3.5 Acknowledgements	117
4 MICROLAYERED PET/PVDF FILMS: EFFECT OF ORIENTATION AND ANNEALING ON DIELECTRIC PROPERTIES	118
4.1 Introduction	119
4.2 Materials and experimental procedures	124
4.3 Results and discussion	127
4.3.1 Selection of processing temperature	128
4.3.2 Isothermal crystallization simulation at 150°C	130
4.3.3 Quantitative thickness uniformity evaluation	131
4.3.4 Annealing Experiments	133
4.3.5 Characterization	140
4.3.6 Dielectric properties	153
4.4 Conclusions	159
4.5 Acknowledgements	161
5 MECHANO-OPTICAL BEHAVIOR OF UNIAXIALLY ORIENTED FLUOROPOLYMER FILMS: ETHYLENE TETRAFLUOROETHYLENE COPOLYMER (ETFE) AND TETRAFLUOROETHYLENE- HEXAFLUORO- PROPYLENE-VINYLDENE FLUORIDE TERPOLYMER (THV)	162
5.1 Introduction	163
5.2 Materials and experimental procedures	167
5.3 Results and discussion	170
5.3.1 Uniaxial Stretching	170
5.3.2 Characterization	175

	Page
5.3.3 Structural Hierarchy Model	185
5.4 Conclusions	188
5.5 Acknowledgements	190
6 MECHANO-OPTICAL BEHAVIOR AND MORPHOLOGY OF UNIAX- IALLY ORIENTED POLYETHYLENE TEREPHTHALATE (PET) AND ETHYLENE VINYL ALCOHOL COPOLYMER (EVOH) COMPOUNDED BLEND FILMS AND THREE LAYER COEXTRUDED FILMS	191
6.1 Introduction	192
6.2 Materials and experimental procedures	196
6.2.1 Materials	196
6.2.2 Processing	197
6.3 Results and discussion	200
6.3.1 Differential scanning calorimetry (DSC)	200
6.3.2 Mechano-optical properties	202
6.3.3 X-ray scattering	210
6.3.4 Orientation factors	214
6.4 Conclusions	219
6.5 Acknowledgements	220
7 Summary and recommendations	221
7.0.1 Chapter 3 Summary	221
7.0.2 Chapter 4 Summary	222
7.0.3 Chapter 5 Summary	224

	Page
7.0.4 Chapter 6 Summary	225
7.0.5 Recommendations	226
REFERENCES	228
A Supporting figures for Chapter 3	249
B Supporting figures for Chapter 4	251
C Supporting figures for Chapter 5	253
D Supporting figures for Chapter 6	257
VITA	260

LIST OF TABLES

Table	Page
3.1 Relevant intrinsic properties of PET and PVDF [36], [144], [225], [70], [24]	94
4.1 Summary of γ -PVDF detected in samples stretched to 3.5X1 in UCW mode at 150°C and 20 mm/min, with or without annealing.	151
5.1 Mechano-optical properties for uniaxially stretched ETFE	174
5.2 Mechano-optical properties for uniaxially stretched THV	174
6.1 Technical properties for raw polymer materials as specified by supplier. .	196
6.2 Extruder barrel temperatures for polymer blends.	197
6.3 Overview of film structures tested in this study.	197
6.4 Film line processing conditions.	198

LIST OF FIGURES

Figure	Page
2.1 Chemical synthesis of ETFE [21].	29
2.2 Chemical synthesis of ETFE [21].	30
2.3 Chemical structure of EVOH [145].	32
2.4 Chemical saponification reaction to create EVOH polymer [147].	33
2.5 Microlayering coextrusion diagram, for a two polymer system (extruders A, B) with skin layer (extruder C).	41
2.6 Uniaxial stretcher illustration and experimental setup.	54
2.7 Simplified schematic of the components in instrumented uniaxial stretcher [210].	55
2.8 Illustration of biaxial stretcher, upgraded to measure real-time spectral birefringence [211].	56
2.9 Illustration of white light telescope setup in biaxial stretcher.	57
2.10 Intensity versus wavelength curve resulting from polarized light signals [211].	58
2.11 Use of Cauchy equation to determine retardation values [211].	58
2.12 24-dot matrix pattern to measure X, Y strains [211].	59
2.13 Annealing chamber illustration and experimental setup	61
2.14 Relevant orientation directions for crystal cell via Wilchinsky method [214].	67
3.1 DSC for individual PET and PVDF materials, with highlighted regions for ideal processing temperatures of each.	84

Figure	Page
3.2 32-layer film (a) roll as received and (b) optical microscope cross-section image.	85
3.3 Characterization of 32-layer film as received via WAXS.	85
3.4 Cartoon representation of different morphological states of each polymer in different regions of the DSC curve. In (a) PVDF is semi-crystalline, PET is amorphous and glassy, (b) PVDF is semi-crystalline, PET is amorphous and rubbery, (c) PVDF and PET are semi-crystalline, (d) PVDF partially molten, PET semi-crystalline and (e) PVDF fully molten, PET semi-crystalline.	87
3.5 True stress, true strain curve for 32 layer sample stretched uniaxially at several different temperatures. Dashed vertical lines represent onset of strain hardening. All curves are offset by 8 MPa, except for 200°C sample, which is offset by 13 MPa.	89
3.6 a) Stress strain, b) strain optical, c) stress optical and d) birefringence, time data for films stretched 5.5X uniaxially at 10 mm/min and 95, 150, and 185°C then quenched with cold air for 30 min.	91
3.7 DSC (1st heat) curves for uniaxial stretching temperature study at 10 mm/min. Figure a) shows final (5.5x extension) for each temperature as well as cast film, b) time slice at 95°C, c) time slice at 150°C, and d) time slice at 185°C.	95
3.8 Calculated percent crystallinity of each polymer material in films stretched at 10 mm/min and 95, 150, and 185°C.	97
3.9 Stress optical data for 32L film stretched 5.5X, uniaxially at 10 mm/min and 95, 150 and 185 and [Right] SAXS patterns for time-slice study at corresponding stretch ratios along stress optical curves.	98
3.10 FTIR spectra for PVDF layer delaminated from 32L film samples stretched to 1.3X at 95, 150, and 185°C in uniaxial extension at 10 mm/min.	99
3.11 FTIR spectra for PVDF layer delaminated from 32L film samples stretched to 5.5X at 95, 150, and 185°C in uniaxial extension at 10 mm/min.	100
3.12 Select 1D WAXS curves for 32L film stretched at 95°C in uniaxial extension at 10 mm/min.	103

Figure	Page
3.13 Select 1D WAXS curves for 32L film stretched at 150°C in uniaxial extension at 10 mm/min.	103
3.14 Select 1D WAXS curves for 32L film stretched at 185°C in uniaxial extension at 10 mm/min.	104
3.15 Summary of PVDF crystal forms as detected by DSC, FTIR, and WAXS characterization methods.	105
3.16 Dielectric constant (room temperature and f=1 kHz) for a series of 32L films stretched in uniaxial extension at 95 and 150°C overlaid with PVDF orientation factors.	109
3.17 Dielectric constant (room temperature and f=1 kHz) for a series of 32L films stretched in uniaxial extension at 95 and 150°C overlaid with birefringence and PET percent crystallinity.	109
3.18 Dielectric Loss (room temperature and f=1 kHz) for a series of 32L films stretched in uniaxial extension at 95 and 150°C overlaid with PVDF orientation factors.	111
3.19 Dielectric constant (room temperature and f=1 kHz) for a series of 32L films stretched in uniaxial extension at 95 and 150°C overlaid with birefringence and PET percent crystallinity.	111
3.20 AFM phase images, and 2D SAXS patterns for PVDF layer only (delaminated from 32L PET/PVDF system). Films portrayed are as cast, as well as uniaxially oriented at 150°C at 10 mm/min and varying draw ratios.	113
4.1 Annealing chamber illustration and experimental setup.	125
4.2 Cartoon representation of morphological states of each polymer in different regions of the DSC curve. In (a) PVDF is semi-crystalline, PET is amorphous and glassy, (b) PVDF is semi-crystalline, PET is amorphous and rubbery, (c) PVDF and PET are semi-crystalline, (d) PVDF partially molten, PET semi-crystalline, (e) PVDF partially molten, PET semi-crystalline, (f) PVDF fully molten, PET semi-crystalline, and (f) PVDF fully molten, PET partially molten.	128

Figure	Page
4.3 Isothermal heating experiment for PVDF layer delaminated from 32L film as cast, conducted in DSC to simulate morphology development during thermal equilibration step prior to stretching. Program: heat from 25°C to desired 150°C at 20 K/min, hold 15 min, cool to 25°C at 20 K/min, reheat to 300°C at 10 K/min.	130
4.4 Quantitative evaluation of thickness uniformity for 32L film stretched in UCW mode at 150°C at 20 mm/min.	132
4.5 Close-up of PVDF melting peak DSC curve to proved explanation of selection of annealing temperatures for microlayer sample stretched in UCW mode to 3.5X1, at 150°C and 20 mm/min.	133
4.6 Birefringence during 1 hour annealing at T1, 155°C for 32L film stretched in UCW mode to 3.5X1 at 20 mm/min and 150°C.	134
4.7 Birefringence during 1 hour annealing at T2, 170°C for 32L film stretched in UCW mode to 3.5X1 at 20 mm/min and 150°C.	135
4.8 Birefringence during 1 hour annealing at T1, 173°C for 32L film stretched in UCW mode to 3.5X1 at 20 mm/min and 150°C.	135
4.9 Birefringence during 1 hour annealing at T1, 177°C for 32L film stretched in UCW mode to 3.5X1 at 20 mm/min and 150°C.	136
4.10 Birefringence during 1 hour annealing at T1, 177°C for 32L film stretched in UCW mode to 3.5X1 at 20 mm/min and 150°C.	136
4.11 Evolution of birefringence during 1 hour annealing at specific temperatures for 32L film stretched in UCW mode to 3.5X1 at 20 mm/min and 150°C.	138
4.12 SAXS data for temporal evolution study for sample stretched at 3.5X1, 150°C, then annealed at 180°C, in which films were stretched to specific time intervals then quenched and studied offline for morphology development. (SAXS images for composite 32L film).	139
4.13 Calculated percent crystallinity for PVDF crystal forms α , β , γ and γ' , and PET, corresponding to DSC thermograms shown for UCW samples stretched to 1.5X1 at 150°C and 20 mm/min and annealed for one hour at T ₁ -T ₅	140

Figure	Page
4.14 Calculated percent crystallinity for PVDF crystal forms α , β , γ and γ' , and PET, corresponding to DSC thermograms shown for UCW samples stretched to 2.5X1 at 150°C and 20 mm/min and annealed for one hour at T ₁ -T ₅	141
4.15 Calculated percent crystallinity for PVDF crystal forms α , β , γ and γ' , and PET, corresponding to DSC thermograms shown for UCW samples stretched to 3.5X1 at 150°C and 20 mm/min and annealed for one hour at T ₁ -T ₅	142
4.16 SAXS and WAXS images for 32L films stretched in UCW to 3.5X1 at 150° and 20 mm/min then annealed to select temperatures for 1 hour. (Both SAXS and WAXS pictured here are for composite structure. SAXS patterns for delaminated films shown next to AFM images).	144
4.17 WAXS image with scattering peaks and corresponding crystal planes identified.	145
4.18 1D WAXS data for 32L film at select annealing temperatures for 1 hour, 32L film stretched in UCW to 3.5X1 at 20 mm/min (composite film structure).	146
4.19 AFM phase images for a) 3.5X1, 150°C stretched film, annealed at b) 155°C, c) 170°C, d) 173°C, e) 177°C, and f) 180°C. AFM images are presented alongside SAXS patterns for PVDF only (delaminated from layered structure) and structural cartoon model is postulated.	148
4.20 Select FTIR data for 32L film at select annealing temperatures for 1 hour, 32L film stretched in UCW to 3.5X1 at 20 mm/min (delaminated PVDF layer only).	150
4.21 Dielectric constant measured at room temperature (left y-axis) versus calculated orientation factors for PVDF (right y-axis) for films stretched in UCW mode to 3.5X1, at 150°C and annealed at temperatures displayed on x-axis.	153
4.22 Dielectric loss measured at room temperature (left y-axis) versus calculated orientation factors for PVDF (right y-axis) for films stretched in UCW mode to 3.5X1, at 150°C and annealed at temperatures displayed on x-axis.	154

Figure	Page
4.23 Dielectric constant measured at room temperature (left y-axis) versus birefringence and calculated percent crystallinity for PET (right y-axis) for films stretched in UCW mode to 3.5X1, at 150°C and annealed at temperatures displayed on x-axis.	155
4.24 Dielectric loss measured at room temperature (left y-axis) versus birefringence and calculated percent crystallinity for PET (right y-axis) for films stretched in UCW mode to 3.5X1, at 150°C and annealed at temperatures displayed on x-axis.	156
4.25 Dielectric property measurements (temperature ramp, increasing temperature at f=1kHz) for a series of 32L films stretched in UCW mode, 3.5X1, at 20 mm/min at 150°C annealed for 1 hour at select temperatures a) dielectric constant and b) dielectric loss.	157
5.1 Chemical structures for [top] ETFE and [bottom] THV.	167
5.2 DSC curves of as cast THV and ETFE films.	171
5.3 (a) True stress, true strain, (b) true stress-birefringence, and (c) true strain-birefringence curves for ETFE uniaxially oriented at varying stretch temperatures and a rate of 10 mm/min.	172
5.4 (a) True stress, true strain, (b) true stress-birefringence, and (c) true strain-birefringence curves for THV uniaxially oriented at varying stretch temperatures and a rate of 10 mm/min.	173
5.5 DSC curves for ETFE samples as cast and after uniaxial orientation.	176
5.6 DSC curves for THV samples as cast and after uniaxial orientation.	177
5.7 Strain-optical temporal evolution study and evolution of microstructure via wide and small-angle X-ray scattering images for uniaxially oriented THV and ETFE films at 145°C.	179
5.8 Stress-optical temporal evolution study and evolution of microstructure via wide and small-angle X-ray scattering images for uniaxially oriented THV and ETFE films at 145°C.	180

Figure	Page
5.9 Calculated d-spacing (left y-axis) and crystalline orientation factors (right y-axis) for ETFE temporal evolution samples stretched at 145°C and 10mm/min.	182
5.10 Calculated d-spacing (left y-axis) and crystalline orientation factors (right y-axis) for THV temporal evolution samples stretched at 145°C and 10mm/min.	183
5.11 ETFE structural model cartoon, with SAXS images and AFM for supporting detail. Stretching direction is vertical.	187
5.12 THV structural model cartoon, with SAXS images and AFM for supporting detail. Stretching direction is vertical.	188
6.1 Chemical structures for materials used in this study.	196
6.2 DSC curves for films a) as cast, with yellow indicating processing window and b) after stretching at 90°C and 30 mm/min to 3.5X initial length.	200
6.3 Calculated percent crystallinity of films both before and after stretching at 90°C and 30 mm/min to 3.5X initial length, normalized for amount of a) PET and b) EVOH in the film.	201
6.4 True stress, true strain curves for film samples stretched at 90°C and 30 mm/min to 3.5X initial length; a) 20% EVOH films, b) 40% EVOH films, and c) 60% EVOH films.	203
6.5 Mechano-optical properties calculated for PET/EVOH blend and layer films after stretching at 90°C and 30 mm/min to 3.5X initial length. a) Modulus, b) onset strain hardening, c) stress optic constant, and d) strain optic constant.	204
6.6 Stress optical curves for film samples stretched at 90°C and 30 mm/min to 3.5X initial length; a) 20% EVOH films, b) 40% EVOH films, and c) 60% EVOH films.	206
6.7 Strain optical curves for film samples stretched at 90°C and 30 mm/min to 3.5X initial length; a) 20% EVOH films, b) 40% EVOH films, and c) 60% EVOH films.	208

Figure	Page
6.8 SAXS and WAXS images at temporal evolution intervals, strain optical data for 40% EVOH blend and layered films stretched at 90°C and 30 mm/min to 3.5X initial length.	211
6.9 SAXS and WAXS images at temporal evolution intervals, stress optical data for 40% EVOH blend and layered films stretched at 90°C and 30 mm/min to 3.5X initial length.	213
6.10 Calculated orientation factors for blend films (peak deconvolution applied) and delaminated PET from 20, 40, and 60% layered films stretched at 90°C and 30 mm/min to 3.5X initial length.	216
6.11 Calculated c-axis crystalline orientation factors for blend and delaminated EVOH from 20, 40, and 60% layered films stretched at 90°C and 30 mm/min to 3.5X initial length.	217
6.12 Calculated c-axis crystalline orientation factors for 40% layered films stretched at 90°C and 30 mm/min to a sequence of true strain values, then delaminated into individual PET and EVOH layers, compared to blend films.	218
A.1 Verification of real time change in sample thickness during stretching calculated using (a) laser and (b) camera data versus actual measured thickness. Plot (c) compares corrected values to actual measured thickness.	249
A.2 FTIR spectra for select samples to verify delamination was successful in producing a single PVDF layer.	249
A.3 Wide angle X-ray scattering images for time slice temperature study films stretched at a) 95°C, b) 150°C, and c) 185°C at a rate of 10 mm/min.	250
B.1 FTIR spectra of PET control film, as cast, compared to PET layer delaminated from 32L microlayer film as cast. Both PET curves show strong absorption peak at 1710 cm ⁻¹ . PVDF samples shown were also delaminated from 32L microlayer film- 1) as cast, 2) after uniaxial orientation to 3.5X1 at 150°C and finally, stretching same conditions as 2, with 1 hour annealing at 3) 155°C and 4) 170°C.	251
B.2 SAXS and WAXS images for annealing chamber at select annealing temperatures for 1 hour annealing, 32L film stretched in UCW to 1.5X1 and 2.5X1 at 150°C and 20 mm/min.	252

Figure	Page
C.1 Laser system predicted thickness for ETFE films.	253
C.2 Camera system predicted thickness for ETFE films.	253
C.3 Camera system predicted thickness for THV films.	254
C.4 Camera system predicted thickness for THV films.	254
C.5 Small angle X-ray scattering patterns for uniaxially oriented THV films, showing structural evolution from as cast state.	255
C.6 Small angle X-ray scattering patterns for uniaxially oriented ETFE films, showing structural evolution from as cast state.	255
C.7 Wide angle X-ray scattering patterns for uniaxially oriented THV films, showing structural evolution from as cast state.	256
C.8 Wide angle X-ray scattering patterns for uniaxially oriented ETFE films, showing structural evolution from as cast state.	256
D.1 Verification of thickness calculations made by laser device during uniaxial stretching.	257
D.2 WAXS images for blend and layer films in as cast state.	257
D.3 WAXS images for blend and layer films after stretching at 90°C and 30 mm/min to 3.5X initial length.	258
D.4 SAXS images for blend and layer films in as cast state.	258
D.5 SAXS images for blend and layer films after stretching at 90°C and 30 mm/min to 3.5X initial length.	258
D.6 1D WAXS curves for 20% EVOH layered film after stretching 90°C and 30 mm/min to 3.5X initial length, versus individual separated layers. . .	259
D.7 Example deconvolution of $2\theta = 26.24^\circ$ PET peak from WAXS.	259

ABSTRACT

Forshey, Megan E. Ph.D., Purdue University, December 2019. Orientation of Polymer Films for Improvement of Dielectric Properties in High-Energy Density Capacitor Applications. Major Professor: Mukerrem Cakmak.

For over 20 years, biaxially oriented polypropylene (BOPP) has been used in capacitors as the dielectric material. BOPP has very high breakdown strength, low electric loss, and is relatively inexpensive however, it suffers from low dielectric constant and low usage temperature. The ever growing technology market requires more robust capacitors which can be used in high temperature and pulsed power applications, and the aim of this research is to meet or exceed dielectric properties of BOPP by combining specific polymer materials in layered structures, biaxially orienting the films, and heat setting the films to further improve thermal stability. Post-processing is done on custom built machines which track real-time true stress, true strain and birefringence values, allowing for a more complete picture of mechano-optical properties generated during the stretching process. These data, along with offline characterization techniques such as X-ray scattering and DSC, were coupled with dielectric property testing to help form relationships between polymer processing, morphology, and dielectric properties.

In Chapter 3, microlayer PET and PVDF (50:50 ratio) films with 32 total layers and thickness around 125 micron were provided by PolymerPlus. Films were first stretched uniaxially at varying temperatures in order to optimize processing conditions. Characterization confirmed PVDF crystal form transformation from α to β when films were stretched at 95°C, and presence of γ - PVDF when stretched in molten state at 185°C, sandwiched between solid PET layers. Dielectric properties

were tested for films stretched at 150°C, which exhibited low dielectric constant when PVDF spherulites or smaller, broken up fibrils were present, but improved dielectric constant when PVDF morphology consisted of long, highly ordered fibrils. Uniaxial drawing helped lower dielectric loss, and it further significantly decreased at very high strains. In this case, morphology of uniaxially drawn PET did not have a strong correlation with dielectric constant, but higher PET crystallinity and orientation likely helps to lower dielectric losses.

Polymer microlayer films consisting of 32 layers, 50:50 ratio PET to PVDF films were also studied extensively using thermal heat setting technique. Samples with good thickness uniformity after stretching were selected for these experiments, and offline characterization techniques were applied to study morphology. Films were annealed at temperatures around PVDF melting peak, which caused transformation of PVDF polymorphs from primarily α to combined α and γ and/or γ' forms. When oriented at 150°C to 1.5X1, γ and γ' -PVDF were detected in small amounts (via DSC) after annealing at 172°C, and only γ' after higher temperature annealing. Stretching at 150°C to higher strains produced high amounts of γ' -PVDF only when annealed at 155°C for films stretched to 3.5X1, and annealed at 150°C for films stretched to 2.5X1. Offline characterization led to development of a structural model for PVDF layers alone, by de-laminating film layers. Then, morphology was correlated with dielectric properties by testing films at room temperature, and at constant frequency, in temperature ramping experiments. Temperature ramping dielectric experiments showed that high percent crystallinity of PET may also help improve loss behavior at high temperatures. Furthermore, samples containing γ and/or γ' -PVDF had increasing dielectric constant with increasing temperature, however dielectric loss also greatly increased with increasing temperature. A significant conclusion was that the annealed sample without γ or γ' -PVDF present had only a slightly lower dielectric constant at high temperature testing, but also had much lower loss, making it a potential candidate for high temperature capacitor applications.

Other materials for potential dielectric film applications were studied as well. Two fluoropolymer films consisting of monolayers of ETFE and THV were uniaxially oriented and their morphology was characterized offline to elucidate structure-process-property relationships. Film samples produced were not large enough to be tested for dielectric properties, however morphology development during uniaxial orientation was evaluated. Both films showed nearly affine stretching behavior, and mechano-optical properties were studied during stretching at several temperatures. Combinations of X-ray scattering experiments and AFM led to proposed morphological structure models for each material at varying levels of deformation.

Finally, in collaboration with A. Schulman, Inc., PET and EVOH compounded blend and three layer PET-EVOH-PET films were oriented uniaxially and the morphology of the two was compared to each other. Potential applications include high barrier food packaging applications, due to the very high oxygen barrier but poor water vapor barrier of EVOH, which can be complimented by PET's high water vapor barrier. Uniaxial orientation of these two film systems showed that mechano-optical behavior was significantly different for blend versus layered films. Crystalline orientation factors were calculated from 1D WAXS data, which showed PET orientation was largely unaffected by increasing EVOH content in blend films, but blending decreased orientation of EVOH. PET's orientation in layered films was also largely unaffected by amount of EVOH in inner layer. EVOH's orientation factor was higher in all layered film compositions compared to neat EVOH film after stretching, suggesting that the coextrusion process is beneficial to increasing orientation of EVOH.

Combination of polymer materials using different processes such as blending, nanocomposites, or multilayering allows for properties unique to individual polymer components to be combined into a single structure. The bulk of this work discusses use of microlayer polymer films for improved dielectric properties. Other techniques explored to create synergistic property effects of polymers are co-polymerization of

fluorine containing monomers (ETFE copolymer and THV terpolymer, Chapter 5) and blending (PET and EVOH, Chapter 6).

The overall goal of this work is to gain knowledge of how polymer structure is affected by uniaxial orientation and heat setting processing methods, while attempting to link this morphology to development of dielectric properties. Custom built machines which map true stress, true strain, and birefringence in real-time during these processes provide a unique way to study these phenomena. Dielectric polymers with higher energy density at high temperatures will hopefully be able to surpass dielectric properties of BOPP, allowing for development of high-tech applications such as the railgun, hyperloop, hybrid car batteries, and photovoltaics to become a reality. This work is funded by and in collaboration with the U.S. Navy's Office of Naval Research (ONR).

1. INTRODUCTION

There is an undisputed need to create higher energy density capacitors which can be used at high operating temperatures in order to meet growing needs of technological advancement. Polymers are an excellent material choice for the dielectric component in capacitors. Most polymers are naturally insulating materials, are lightweight, relatively inexpensive, and easy to process (compared to ceramics, for example) and, perhaps most importantly, have unique properties which can be tailored based on their structure and morphology and therefore the processing conditions which inherently determine these parameters. Since the 1950s, polymers such as polypropylene (PP), polyethylene terephthalate (PET), and polycarbonate (PC) have been used as dielectric component for capacitors, with metalized, biaxially oriented polypropylene (BOPP) having the highest energy density, or amount of energy a capacitor can store in an electric field, of commercial capacitors [1]. BOPP has very high energy density due to its high breakdown strength, but the specific link between structure and electrical property values for this result is not well understood [2]. Furthermore, BOPP has low dielectric constant and low usage temperature, the first of which shows great potential for improvement and the latter meaning it cannot be used in high temperature devices. For these reasons, we aim to find polymer materials which can replace BOPP as the dielectric film for high-tech capacitor applications. In order to be successful, replacement materials should have, in comparison to BOPP, improved dielectric constant, comparable or improved dielectric breakdown strength and loss, and ability to be used at very high temperatures.

The purpose of this dissertation is to obtain a better understanding as to how polymer structure can be tailored by processing operations to improve dielectric properties, including dielectric constant and breakdown strength, while maintaining reasonable

electrical loss values. Strategies for improving energy density in polymer capacitor films include selection of appropriate materials, processing to tailor structure and morphology, and the ability to understand how and why this structure develops (i.e. via offline characterization techniques) and be able to link it to final, measured dielectric properties. Materials used in this study are: PET and PVDF (homopolymer) multi-layer films, and ETFE and THV monolayer films. Additionally, oriented PET/EVOH films were investigated for barrier improvement.

PET is the second most common polymer dielectric material for capacitors, and has higher dielectric constant than BOPP (around 3.3) with higher usage temperature up to 125°C. However, biaxially oriented PET (BOPET) cannot be used alone for pulsed power applications due to relatively high electrical loss that compounds as temperature and frequency increase [3]. As with all polymers, the structure of PET is very important in determining its final properties. PET is a slow crystallizing polymer, meaning it can be quenched into nearly fully amorphous state after processing. The short range amorphous order of PET has been investigated by electron microscopy and XRD [4], [5]. The crystal structure of PET has been well characterized, beginning around 1954 by Daubeny [6]. Although it only accounts for a small amount of structure in unoriented PET, the crystalline morphology of this material has been proven to have a significant effect on its final properties. Crystallization can occur as spherulitic growth during slow cooling from the melt or during annealing, or via strain induced crystallization when stretched in rubbery state. Structure development during strain induced crystallization of PET depends on both stretching temperature and rate due to competing mechanisms of chain relaxation and nucleation events [4], [7]. PET has four morphological deformation regimes when subjected to orientation, and crystalline content typically obtained is around 5-20% depending on temperature, rate and mode of deformation [8]. Orientation of PET also causes phenyl rings to reorient nearly perpendicular to PET chain axis, which can be observed via WAXS experiments [8]. It is well known that orientation of PET has a significant impact on its properties - for example, yield stress [9], [10], gas perme-

ability [11], optical properties [12], [13], and film quality such as thickness uniformity and surface roughness [14]. Finally, thermal annealing or heat setting of PET is a crucial step in creating a thermally stable film after orientation of the material [15]. It has been shown that orientation of semi-crystalline polymers is crucial for obtaining usable dielectric films for high temperature capacitor applications [16], [17], [18]. The improvement of mechanical properties obtained from biaxial orientation is a necessary baseline for producing film capable of being used in capacitors, and these properties are further tailored and improved by use of heat setting. Specifically, high Young's modulus, improved thermal stability, reduction of mechanical property unbalance, and tailored morphological structure prevent further stretching, necking, and shrinkage during winding, while producing high quality films with uniform thickness distribution and acceptable surface roughness [16],[17]. Without these attributes, polymers cannot practically be used for high energy density capacitors. Mechanical properties and polymer morphology are also directly linked to dielectric properties such as breakdown strength, where biaxial orientation of PP, and PET improves dielectric strength by at least two times compared to unoriented and uniaxially oriented materials [17], [18]. The justification for using oriented and heat set polymers such as PET for improvement of high energy density capacitors is obvious as outlined above, and therefore, understanding links between processing, morphology, and dielectric properties is crucial to this work.

Polyvinylidene fluoride, or PVDF, has the highest known dielectric constant of any polymer and is therefore an attractive solution for dielectrics. However, used on its own, PVDF suffers from very high losses and low breakdown strength. Biaxial orientation of PVDF (BOPVDF) can help improve dielectric properties, but losses, due to in-plane switching of dipoles when exposed to an electric field are still too high to allow for its use as a capacitor film on a large scale [19], [20]. Compared to other fluoropolymers, PVDF has a relatively low melting point (around 170-175°C) due to its flexible backbone, and therefore its maximum usage temperature is also relatively low at around 150°C [21]. The amorphous state of PVDF was found by Tonelli, et al.

to have a dielectric constant around 4-6 which is significantly lower than that of the crystalline phase (nearly 10) [22]. Therefore, maximizing crystallinity should be beneficial to improving dielectric constant of the material. PVDF is a highly crystalline material (about 50-70% in general) consisting of at least four or five crystalline forms. The α (Form II), β (Form I), and γ (Form III) forms are most common and therefore the most well studied. α PVDF is non-polar and occurs from quiescent crystallization from the melt state, β form is the most polar and electrically active form of PVDF with both piezoelectric and pyroelectric properties, and γ PVDF is very similar to α but with a shift in the crystal plane c-axis [23], [24]. The different crystal forms of PVDF can be quantified using a combination of characterization techniques. Since there is some overlap in peaks and signals among these forms, several techniques must be used in combination with one another to get a clear picture of the amount of each form, specifically wide angle x-ray scattering (WAXS), FTIR absorption spectra, and differential scanning calorimetry (DSC). An overview of the use of these techniques to quantify PVDF crystal forms will be discussed later in this work, and an excellent review of the characterization of PVDF is presented by Martins, et al. [25]. Since PVDF has a high percent crystallinity, it is crucial to understand how and why each crystal form is created and how it affects the final material properties. There are very few studies in the literature which quantify the effect of crystal form of PVDF on dielectric properties of the material [26], [27], [28]. There is some evidence, presented by Zhao and co-workers in 2016, that γ PVDF has relatively higher dielectric constant, less loss, and lower hysteresis than the α and γ forms but his claim has not been well substantiated by other researchers [28]. In an attempt to take advantage of the inherently high breakdown strength of PET and high dielectric constant of PVDF, these two materials were coextruded into microlayer structures containing 32 total layers, with film thickness around 125 micron and were provided by Polymer-Plus. These films were subjected to many different processing conditions in uniaxial extension as true stress, true strain, and birefringence were measured online. Further offline characterization was done to link processing-structure-property relationships.

Uniaxial orientation of these films is described in Chapter 3. These films were also studied extensively via thermal annealing, by selecting films with good thickness uniformity, and heat setting them to improve thermal stability. Annealed films were also studied offline using several characterization methods. The results of annealing experiments is described in Chapter 4.

Two other fluoropolymer materials were investigated in this work for use in high temperature capacitor applications: ethylene tetrafluoroethylene copolymer (ETFE) and tetrafluoroethylene- hexafluoropropylene- vinylidene fluoride terpolymer (THV). PVDF's low usage temperature and high losses does not allow for use as a single component for polymer dielectric film. To combat these negatives, other fluorine-containing monomers - such as tetrafluoroethylene (TFE) and hexafluoropropylene (HFP) - can be co-polymerized into materials with higher melting point, easier processability, and without phase separation that may occur when blending. By taking advantage of properties of each individual monomer, improved thermal and electrical properties can be achieved. For example, copolymerization of -VDF and -TFE monomers creates ETFE, which has high thermal stability due to the -TFE component, as well as high dielectric constant and the ability to be melt processed due to the -VDF unit [29]. THV terpolymer combines properties mentioned above for -TFE and -VDF, with -HFP component added to reduce melting temperature (i.e. lowering cost of production) while maintaining high thermal stability [29]. ETFE and THV are both melt processable, semi-crystalline polymers with ETFE being about 40-60% crystalline and THV around 10%. Crystal structure and deformation behavior of ETFE has been relatively well characterized in the literature, mainly by Tanigami, et al. [30], [31], [32]. Main findings in these reports are that, under uniaxial deformation, ETFE forms a mesophase transition below 100°C but acts like a rubber when stretched above this transition temperature [31]. Thorough characterization of ETFE's structure was published by Funaki, et al. [33], [34], [35]. ETFE's dielectric properties include: a dielectric constant of 2.6 (106 Hz) and breakdown strength of approximately 14.6 kV/mm, with very low electric loss of 0.010 (at 1 kHz) [21], [36].

THV, on the other hand, is a much newer material, having first been synthesized in the 1990s and is therefore considered to be the newest fluoropolymer material. Hence, it has not been as well characterized in literature as ETFE or PVDF, for example. THV has a dielectric constant of 4-5 (106 Hz), breakdown strength 48-62 kV/mm, and electrical loss around 0.09-0.14 (at 1 kHz) [36], [21]. The crystal structure of THV before and after uniaxial orientation was studied by Freimuth and co-workers, who determined that the crystal structure could not be completely quantified using WAXS (due to only a small number of peaks present), but that it likely has a similar crystal structure to PTFE and PVDF, which are hexagonal (and can be approximated as such) [37]. Rheological [38], [39], dielectric [29], [40], and characterization via NMR [41], optical properties [42], spectroscopic properties [43], [44] and thermodynamical [45] properties of THV have all been studied in the literature, but very few describe morphology related to orientation.

Two monolayer films of ETFE and THV were provided by PolyK Technologies, Inc., with starting thickness around 50 micron. Materials were oriented in uniaxial extension and properties characterized offline to study processing-structure-property relationships. Since these films were already so thin and contained initial machine direction orientation from the casting process, they were not currently able to be biaxially oriented. Therefore, sample sizes were not large enough for dielectric property testing. Results for morphological structure development during uniaxial orientation of THV and ETFE fluoropolymer films is discussed in Chapter 5.

Finally, ethylene vinyl alcohol copolymer (EVOH) is a high oxygen barrier material that has a high percent crystallinity and is optically transparent and highly polar. Because of these features, the main application for EVOH is in high oxygen barrier packaging for food and medical industries. There are, however, several downfalls to EVOH which make it impossible to use on its own in these applications. For example, EVOH is prone to cracking, hard to orient (due to high crystallinity and fast crystallizing nature), and has a very high water affinity (i.e. highly sensitive to water

in the air). For these reasons, EVOH must be used as part of a laminate, blend, layered, or microlayered structure in order to be a useful barrier material. Furthermore, EVOH is a random copolymer and its properties and processability depend on the amount of each monomer present in its chemical structure. Specifically, higher ethylene content in the backbone makes the material easier to process but lowers oxygen barrier performance. EVOH's crystal structure and processing-structure-property relationships are also affected by the amount of each co-monomer. For example, EVOH with high vinyl alcohol (VA) content, above 27 mol% has monoclinic crystal structure and behaves more closely to polyvinyl alcohol (PVOH), whereas from 6-14 mol% VA content crystallizes into hexagonal structure like polyethylene [46]. In the range of 14-27 mol% VA, EVOH copolymer is said to be in a transition region, with pseudo-hexagonal crystal structure [46]. Orientation of EVOH is possible, and has been studied in layered or microlayered [47], [48], [49], composite [50], [51] and blend structures [52], [53] as some examples. The uniaxial and simultaneous biaxial orientation of EVOH blends and composites has been shown to determine final structure and properties of the material, depending on the stretching conditions as well as chemical composition of the copolymer [54], [47], [51]. Sequential biaxial orientation, on the other hand, is more difficult as shown by Breil, due to the creation of microfibrils in EVOH in the first stretching step that leads to films with overall poor quality and decreased properties [47].

In collaboration with A. Schulman, Inc., films of blended PET and EVOH, as well as a three layer system of PET-EVOH-PET were uniaxially oriented, and the final morphology of the two compared to each other. The potential use of these blend or multilayer films is for high barrier food packaging applications. This work is presented in Chapter 6.

The combination of polymer materials using processes such as co-polymerization, blending, nanocomposites, or multilayering allows for properties unique to individual polymer components to be combined into a single structure or film. The bulk of

this work discusses use of microlayer polymer films for improved dielectric properties. Microlayering coextrusion is a technique first patented by Dow Chemical Co. in the early 1960s [55], and has since been adapted and improved to create a continuous process which allows for two or three polymer materials to be combined in thin films with very thin (down to several nanometers) individual layers up to 8000 [56]. Other benefits of microlayering coextrusion include modular feedback design, allowing for number of layers and ratio of materials to be exchanged relatively easily, ability to scale up to an industrial level, and unique morphologies obtained from confined or “Z-plane” crystallization [56]. Microlayering coextrusion process has been widely studied in the literature, mainly by Baer and associates at Case Western Reserve University (some examples include [57], [58], [59]). Other techniques explored in this work to create synergistic property effect of polymers are co-polymerization of fluorine containing monomers (ETFE copolymer and THV terpolymer, Chapter 5) and blending (PET and EVOH, Chapter 6).

The overall goal of this dissertation is to provide a better understanding of how polymer structure is affected by uniaxial, biaxial and heat setting processing methods and ultimately create a link between this morphology and resulting dielectric (and other) properties. We aim to do so by using custom built machines which map true stress, true strain, and birefringence in real-time during these processes - a unique capability in our lab. Success in finding dielectric polymers with high energy density to replace BOPP and create capacitors which can be used in extreme, pulsed power applications, will allow for development and practical, cost-efficient use of high-tech applications such as the railgun, hyperloop, hybrid car batteries, and photovoltaics. This work is funded by and in collaboration with the U.S. Navy’s Office of Naval Research (ONR).

2. LITERATURE SURVEY

2.1 Capacitor technology and applications

This section gives a detailed analysis of current state of capacitor materials, as well as how they can be improved. Then, several innovative technologies which cannot exist without high energy density capacitors are described, as an indication of potential applications for the research described herein.

2.1.1 Current state of the art

Emerging technology continuously requires more compact electrical components which are longer lasting, have higher efficiency, perform faster at higher temperatures, and are thinner and lighter than ever before. Capacitors are key to accomplishing these goals, as their ability to store more charge in a smaller volume is often the limiting factor for many of these parameters [60]. A capacitor consists of two conductive plates surrounding an insulating (or dielectric) material which stores large amounts of energy in an electric field. Because the dielectric component limits energy density and therefore performance and efficiency of the device, it has gained the attention of materials engineers as new challenges arise in this field. In the past, substances such as glass, ceramics, and paper, which are low cost and naturally good insulators, were used as the dielectric component in capacitors [1]. However, in the 1950s polymers such as polyethylene, polystyrene, and polytetrafluoroethylene were first used as the dielectric material in capacitor films due to their versatility and intrinsic insulating nature, making them an excellent choice for replacement of traditional dielectric materials [61]. Compared to the previously mentioned materials, poly-

mers offer the advantages of easier processability, flexibility, chemical resistance, and customizability [1]. Current capacitor films are typically made of polymer materials, mainly polypropylene (PP), polycarbonate (PC), and polyethylene terephthalate (PET). The semi-crystalline nature of polypropylene allows for further enhancement of electrical properties via tailored morphology by biaxial orientation and metallized, biaxially oriented polypropylene (BOPP) has dominated the polymer dielectrics market for over 20 years due to its low loss, cost and stable capacitance at room temperature [60]. With the highest known energy density at breakdown (5 J/cm^3) of any commercial capacitor film, as well as very high breakdown strength (around 800 V/micron) and extremely low electrical losses (0.02 percent at 1 kHz) up to 85°C , BOPP is an excellent choice in many capacitor applications [61], [60]. However, it is not well understood why BOPP's specific structure leads to high dielectric properties, especially high breakdown strength, and one of the goals of this work is to try to understand this phenomenon [2]. Limiting factors for BOPP in dielectric applications include low dielectric constant, intrinsically low thermal conductivity, and low usage temperature; thus BOPP needs to be replaced in order to meet the needs of emerging capacitor applications which require high temperature environments, pulsed power, and higher energy density. In many cases, improving these factors simultaneously is contradictory; thus it has been accepted that any improvement in current dielectric material properties would be considered a success [61], [60].

2.1.2 High energy density applications

Pulsed-power applications such as the hyper loop and railgun, photovoltaic cells, hybrid automobile batteries, and healthcare devices such as pacemakers and microsensors, along with nearly every electronic consumer device will benefit from improved capacitor technology. All of these applications require longer lasting, more reliable capacitors which can safely withstand harsh environments; a feat which current capacitor technology is unable to accomplish. To improve these flaws, polymers with

higher thermal stability and better electrical properties have been investigated to replace BOPP, and techniques such as microlayering were later used to simultaneously combine and improve their properties such as the high breakdown strength of polycarbonate with the high dielectric constant of polyvinylidene fluoride [60]. To improve supercapacitor technology, the performance-limiting dielectric material must be enhanced by increasing energy density and breakdown strength, while minimizing electrical loss [60]. However, methods to improve one of the above properties often negatively impacts another; this conflicting parameter interaction is what makes optimization of capacitor dielectric materials so challenging [56].

2.2 Materials for improved polymer dielectrics

Polymers are a versatile material which can be used in a wide range of applications and are often more affordable, more lightweight and consume less energy to process than other materials such as metals and ceramics. Many strategies have been attempted to overcome the challenges associated with improving polymer dielectric properties. Selection of polymer materials is key to potentially creating improved dielectrics for capacitors, and the following section describes which materials were selected for the purpose of this study.

Common polymer dielectric film materials include polypropylene (PP), polyesters (polyethylene terephthalate, PET), polycarbonate (PC), polyphenylene sulfide (PPS), and polyvinylidene fluoride (PVDF) [3]. BOPP is the most commonly used polymer film for dielectric applications [3], [62] and further improvement of dielectric properties of PP have been observed using various techniques such as co-polymerization, crosslinking, blending of PP with high permittivity materials such as poly(vinylidene fluoride) [63] and acrylonitrile-butadiene-styrene [64], [3]. However, it is hypothesized that, by selecting appropriate materials and tailoring properties via processing, orientation, and annealing, BOPP capacitor properties can be met or exceeded by a

new, microlayer film system that has the added benefits of high usage temperature. Materials studied herein for this purpose include: PET, PVDF (homopolymer and co-HFP), ETFE, and THV. Additionally, PET and EVOH films were investigated for barrier improvement and will be discussed as well.

2.2.1 Polyethylene terephthalate (PET)

Having a 50% higher energy density than polypropylene, biaxially oriented PET is the second most common polymer dielectric film for capacitor applications, making it a promising candidate for replacement of BOPP in future applications due to its dielectric constant of around 3.3 (about 1.1 higher than BOPP) and higher temperature usage up to 125°C [3]. However, PET suffers from high electrical loss which are compounded as temperature and frequency increase and thus cannot be used alone in pulsed power applications [3].

To understand the mechanical and electrical properties of this polymer, it is first necessary to give a description of the molecular structure itself, along with its crystalline and amorphous states. PET's crystal structure has been proven by X-ray diffraction methods to be triclinic with a unit cell $a = 4.56 \text{ \AA}$, $b = 5.94 \text{ \AA}$, $c = 10.75 \text{ \AA}$, angles $\alpha = 98.5^\circ$, $\beta = 118^\circ$, and $\gamma = 112^\circ$, and crystalline density of 1.455 g/cm^3 [6]. Furthermore, the density of amorphous regions is assumed to be 1.335 g/cm^3 and fibers have a typical crystallinity ranging from around 48 to 64.5% [6]. PET is considered to have a nearly planar configuration, with carbon and oxygen atoms lying nearly in plane with one another, ester groups approximately 12° out of plane with the aromatic group, and the glycol group about 20° out of plane from the O-CH₂ bond [6]. These constraints are dictated mainly by size, and the forces between molecules are known to be purely Van der Waals [6].

Due to its slow crystallizing behavior, PET can be quenched to almost fully amorphous state, allowing for the study of short range amorphous order of this material.

Electron microscopy in diffraction mode using both dark and bright field contrast has shown that the morphology of amorphous PET is arranged in ordered domains of around 75 Å in diameter in a nematic arrangement, similar to liquid crystals; this structure is independent of temperature (i.e. below or above the materials glass transition temperature) [4], [5]. To confirm that order in the amorphous state was actually a bulk phenomenon and not artificially observed due to electron shadows in electron microscopy experiments, researchers conducted experiments by solution casting very thin PET films (order of 1000 Å thick), annealing at 290°C, quenching into 0°C bath and then observing morphology via XRD and electron microscopy [5]. These experiments confirmed previous descriptions of the 75 Å diameter ordered domains in amorphous PET which were shown to be amorphous via their XRD patterns and proven via dark-field electron microscopy to be a continuous structure throughout the bulk of the material (i.e. not just a surface phenomenon) [5]. This effect is a function of melt temperature of PET before quenching which affects the overall order of the structure and degree to which it can act as a nucleating agent to cold crystallization of PET - as temperature increases, both of these effects are diminished [5]. Therefore, the structure in polymer amorphous regions is not to be discounted; it is influenced greatly by temperature effects, can lead to and promote phenomenon such as nucleation of cold crystallization, and thus affects the overall micro- and macromolecular structure and subsequent mechanical properties of the polymer material as a whole.

Furthermore, crystalline structure of PET, though it typically accounts for only a small percentage of the total structure in the unoriented state, significantly affects the final properties of this material. Quiescent crystallization of PET occurs via spherulitic growth when cooling from the melt state or annealing at temperatures above T_g and can be observed readily under polarized light microscopy. During polymer processing, development of morphology largely depends on processing type, temperature, rate and other related variables. Strain-induced crystallization commonly occurs during orientation of PET below the point of strain hardening, and is dependent upon both stretching temperature and rate. For example, slow cold

drawing (below T_g) of PET fibers between 40°C and 100°C leads to stress induced crystallization via oriented amorphous regions forming paracrystalline structure from intermediate monoclinic crystals, which upon further deformation transform to their final triclinic geometry [4], [7]. It has been observed that the final triclinic structure's c-axis will be tilted at an azimuthal degree from the draw axis which depends on both annealing temperature and drawing speed [4]. At higher drawing rates the intermediate monoclinic structure is bypassed leading to a smaller degree of c-axis tilt compared to slowly drawn fibers [4]. The mechanism for tilting differs for low and high annealing temperature; at low temperatures c-axis tilt arises from the paracrystalline transition from monoclinic to triclinic crystal structure and at high temperatures a layer structure consisting of alternating crystalline and amorphous regions forms due to higher molecular mobility, leading to high stresses at the interface of crystalline and amorphous transition regions [4]. Therefore, the c-axis degree of tilt is determined by the material's ability to lower its free energy by either c-axis tilt or changing surface layer inclination degree when deformed in cold drawing conditions [4], [65].

More relevant to the current work, the processing of PET films are typically done while heated to the rubbery state and different methods of orientation (uniaxial, sequential biaxial, simultaneous biaxial, etc.) can lead to development of anisotropic mechanical, thermal, and optical film properties to varying degrees. Solid state deformation of polymers such as PET is well known to produce molecular orientation in stretching direction and have a large impact on polymer properties. Due to the strong covalent bonding in polymer backbone structures, which primarily consist of C-C bonds, alignment of macromolecules provides a strong resistance to strain in the stretching direction and decreased resistance to strain in transverse direction (where weaker van der Waals forces prevail) [66], [67], [68], [10], [69]. The mechanism of morphological development in oriented PET films and fibers has been widely studied mainly by the use of X-ray diffraction experiments, which conclude that, in general, morphology is determined by the competing processes of chain relaxation and nucleation events which are known to depend on drawing conditions (mainly temperature

and rate). Studies show that if drawing rate is relatively fast compared to relaxation time at a certain temperature, strain induced crystallization is delayed because polymer chains do not have the ability to align and form organized crystalline regions whereas when drawing rate is slower the relaxation of polymer chains occurs on a time scale relevant to stretching time and therefore chains can now align and initiate crystallization during the drawing process [70], [71], [7], [72], [65].

Due to the competition of these mechanisms, PET has four morphological deformation regimes during drawing, [65], [8], [13]. During elastic deformation, Regime I, amorphous chains orient in drawing direction and PET chains undergo change from gauche to trans conformation to lower their energy. In the second deformation regime, Regime II, a high increase in birefringence during stretching indicates increase in orientation and development of strain induced crystallization. Crystalline content developed in this region is around 5-20%, and trans content increases too as the gauche to trans conformational change continues. In Regime III, even higher crystallinity is developed, and as polymer chains approach their limit of finite extensibility, stress increases rapidly as the chains begin to resist additional orientation. Total percent crystallinity developed in this step depends on stretching rate and ratio and therefore, since crystallinity is driven by entropy of extension, increasing stretch rate and ratio lowers free energy associated with nucleation and crystal growth. As stretch ratio increases, it has also been demonstrated that phenyl rings orient in the plane of the PET film, observed by appearance of ($\bar{1}05$) peak, which is nearly perpendicular to PET chain axis, in WAXS experiments. Furthermore, (110) WAXS peak intensifies during stretching, indicating that phenyl groups become more parallel to film plane, with randomly distributed chain axes. Regime IV results in saturation of birefringence value but small increase in stress as the polymer chains reach finite extensibility and cannot physically stretch any further. In this region, crystallinity does not increase further and material is “muscle bound” meaning that its relaxation and orientation mechanisms are greatly suppressed.

As mentioned previously, it is well known that the orientation of PET has significant impact on its properties; the extent of which is largely dependent on processing conditions. A patent released by DuPont as early as 1959 recognized and reported on the methods for improving mechanical properties of PET by orientation [73]. Specifically, yield stress, thickness uniformity, surface roughness, permeability, shrinkage and tear strength, optical and dielectric properties, among others, are largely affected by the stretching process.

Although the yielding mechanism is not as well defined for polymers as for other materials like metals, the yielding phenomenon is observed as a mechanical response in the stress-strain curve to the transition from elastic to plastic deformation at constant strain (drawing) rate [10]. The Hencky-von Mises criterion for yielding of polymers incorporates the effect of hydrostatic pressure on polymers (since they are fairly compressible compared to metals), meaning there is also a difference between compressive and tensile yield stress for polymers and, to first approximation, force to yield increases linearly with increasing hydrostatic pressure [10]. Many studies support this conclusion, and specifically for PET, Rabinowitz and Ward have studied the effect of hydrostatic pressure on its yield and fracture stress and found that specimens tested in torsion at atmospheric pressure deformed in a ductile manner with yield stress increasing as hydrostatic pressure increases; however after annealing, the specimens showed brittle deformation behavior in which yield stress followed the same hydrostatic pressure dependence, suggesting that yield stress increases with orientation of PET [9]. Another study on PET sheet supports the claim that yield stress increases with pressure, and is affected by temperature and strain rate [74]. Therefore, yield strength is a function of orientation of polymers and depends on processing conditions such as pressure, temperature and strain rate.

Gas permeability, and especially oxygen permeability has been studied for PET film both before and after orientation. In a 2010 study on barrier properties in PET, Ozen, et al. found that simultaneous biaxial orientation of PET films to 2X2 and 3X3 re-

duced oxygen permeability by about 19% and 58%, respectively [11]. Explanation as to why barrier properties change during stretching is explained by stress-induced crystallization, which caused an increase in percent crystallinity of the PET film by about 6% and 17% when the film was stretched 2X2 and 3X3, respectively. Crystalline regions are more impermeable to gas and other particles and thus provide a tortuous path for propagation of such gases through the polymer film (as opposed to more permeable amorphous regions) therefore, orientation of polymers such as PET increases their barrier to gases such as oxygen [11].

Optical properties of PET change during orientation as well. Hassan and Cakmak found stress-optical behavior for PET follow four-stages while undergoing simultaneous biaxial orientation [13], [8]. Linear stress-optical behavior is observed in the first stage, with a stress-optical constant around 5.8 GPa^{-1} . Furthermore, this stress-optical behavior is valid except when PET is stretched at very low temperatures (near T_g) or very high rates, when glassy stresses are significant [75], [76].

Other properties of industrial and technical significance include thickness uniformity and surface roughness. To achieve homogeneous properties throughout a polymer film, thickness uniformity is crucial, and surface roughness can either enhance or debilitate the ability of the film to perform in certain applications including solar collector films, food packaging, and adhesion. Iwakura found that strain hardening, which occurs at relatively high stretch ratios and relatively low stretching temperature, decreases thickness deviation and surface roughness in PET films [14]. Up until the point of strain hardening, due to reorientation of the phenyl rings in PET chains, however, thickness uniformity first becomes worse and then improves [14]. Specifically, for this work, orientation of PET will help ensure thickness uniformity in the final product, which is critical for film quality and is a direct factor in determining dielectric strength of the material.

Polymer morphology can be further tailored by thermal heat setting, or annealing. Crystallization is facilitated by annealing the polymer film, and occurs via three

different mechanisms depending on the initial amount of orientation present in the sample [15], [71], [77]. Annealing of stretched PET at low degrees of orientation causes molecular relaxation [78]. At intermediate degrees of orientation, initial relaxation (decrease in birefringence) occurs, followed by a gradual increase then a leveling off of birefringence at long times. Finally, when starting with high degree of orientation, annealing causes rapid increase in PET's birefringence, which then levels off quickly [15].

Research overviewing the general properties and production techniques of polymer film capacitors was published by Habermel in 1970 [16]. This paper details the specific requirements for polymers to be used as dielectric film, such as resistance to moisture, good dielectric strength, and thickness uniformity. It also gives an overview of properties of main polymers used for dielectric film at the time - PET, PC, PP, PS and PTFE [16]. Along with general property requirements, improvement of mechanical properties via orientation of polymer films such as BOPET and BOPP is significant also to dielectric film applications. In 1988, Nash wrote a review detailing the use of polypropylene for capacitor, in which he states that the improvement of mechanical properties obtained by biaxial orientation is also crucial for producing capacitor grade films [17]. Specifically, high Young's modulus prevents stretching and necking during winding which can lead to relaxation and wrinkles in the roll. Along with high modulus, orientation prevents the film from deformation when the bubble collapses during film take up. Finally, unbalance in mechanical properties (defined as differing properties in various planes of the film due to unequal orientation) also can lower dielectric strength as well as causing shrinkage and necking [17]. Un-oriented films show catastrophic failures when used in capacitors in accelerated life tests, and uniaxially oriented materials showed similar failure to unoriented [17]. Furthermore, dielectric strength measurements on biaxially oriented films were at least two times higher than unoriented films, regardless of the material (specifically in this case polypropylene, polycarbonate, and polyethylene terephthalate) and this improvement in dielectric strength likely results directly from improvement of mechanical properties resulting

from orientation [17]. Blok and LeGrand published a report detailing the theory of electromechanical deformation in polymers and how it leads to dielectric breakdown initiation in these materials [18]. Specifically, the mechanism of electromechanical thinning, in which a localized force is experienced higher at thinner spots in the specimen causing mechanical deformation which further concentrates the electric field at this point, occurs and leads to dielectric breakdown [18], [17]. For this reason, film quality (thickness uniformity, lack of surface roughness, free from defects, isotropic mechanical properties) is crucial to obtaining polymer films with high dielectric properties. Polymer morphology is also tailored to a specific crystalline gradient structure which is referred to as “Hazy film” (for BOPP) that allows for ideal film impregnation so that polymers can successfully replace paper in dielectric films [17]. The downfall of PET, even in its oriented state, is high dissipation factor in operating temperatures above 100°C which leads to thermal runaway and subsequent failure [17]. However, the higher dielectric constant of PET compared to PP still makes it a good candidate for replacement, especially when strategic methods are used to combine it with other polymers such as blending and microlayering, which will be the focus of this work.

2.2.2 Fluoropolymers

Fluoropolymers are a relatively new class of materials with unique properties compared to other polymers because of their highly polar nature. Due to their generally low dielectric constants in comparison to metals and high chemical inertness, fluoropolymers are used mainly as insulators in energy and electronic industries [79]. Of particular interest to this study is the use of fluoropolymer films as a component in polymer dielectric films for capacitor applications due to recent push to develop new technologies requiring capacitors with very high energy density and low losses that can be used at high temperatures and/or in pulsed power applications [29], [60], [3], [2], [61].

Polyvinylidene fluoride [PVDF]

With the highest known dielectric constant ($k=10$) of any polymer material, polyvinylidene fluoride (PVDF) and its copolymers seem an obvious choice for high energy density capacitors. PVDF also has the strongest piezoelectric and pyroelectric response of any polymer by far [23]. Though PVDF was first discovered in 1961, its fascinating piezoelectric and pyroelectric properties were not discovered and reported on until 1969 by Kawai and 1971 by Bergman et al., and separately by Nakamura and Wada [24], [80], [81], [82]. These specific properties are caused when polymer chains are transformed to electrets as a result of macroscopic polarization [24]. PVDF is synthesized from vinylidene fluoride (VDF) monomer in free radical polymerization by either suspension or emulsion polymerization methods, with suspension polymerization leading to higher head-to-tail conformation ratio, and thus higher crystallinity, melting point, and better high-temperature mechanical properties [21]. This ratio is important because the other conformations, namely head-to-head and tail-to-tail, can be thought of as defects, leading to reduced crystallizability of the polymer and decreased mechanical properties [24]. Head-to-head, tail or tail-to-tail ratios can be quantified by using NMR (^{13}C or ^{19}F), IR, or FTIR spectra, described in more detail elsewhere [83], [84], [85], [86], [87], [88], [89], [24].

PVDF is unique compared to other fluoropolymers such as polytetrafluoroethylene (PTFE) due to its lower melting point (near 170°C , compared to typically 200°C or greater for other fluoropolymer materials) which results primarily from flexibility of chain backbone [21]. Though this means lower processing temperatures, it also implies lower usage temperature than other fluoropolymers; specifically, maximum usage temperature is around 150°C [21]. PVDF does, however, have excellent weatherability, relatively good chemical resistance, oxidative stability, strength and creep resistance [21]. These properties, along with the piezoelectric and pyroelectric properties of PVDF have shown valuable use in applications such as wire and

cable, chemical resistant valves, heat-shrinkable tubing, and, of course, piezoelectric materials [21].

The amorphous state of PVDF has been well studied using intrinsic-viscosity values and light-scattering of dilute solution, and its density was found to be 1.68 g/cm^{-3} at 20°C [24]. PVDF was found to have smaller molecular dimensions than the two parent components making up the polymer (i.e. polyethylene and polytetrafluoroethylene), which is likely due to the very strong interchain electrostatic interactions [24]. Unperturbed dimensions of PVDF were studied by Welch, and Ali and Raina and, together with modeling done by Tonelli, lead to assessment that the amorphous state of PVDF has a dielectric constant of between 4 to 6 [90], [91], [22], [92], [24]. This is significantly lower than the crystalline state (nearly 10), therefore it can be said that maximizing PVDF crystallinity improves dielectric constant. In contrast to the crystalline state, Tonelli also found that defects head-to-head and tail-to-tail do not adversely affect PVDFs amorphous state conformation [22].

PVDF is polymorphic and exhibits (at least) four different crystal structures, specifically α , β , γ , and δ -form. Most common is the α -form, which occurs quiescently from the melt and results in anti-parallel chains which cancels net dipole moment, making it non-polar [23]. α -form PVDF, also known as Form II, has $\text{TG}^+ \text{TG}^-$ conformation with dihedral angles $\text{T}=180^\circ$ and $\text{G}=45^\circ$, approximately, and c-axis repeat unit of 4.6 \AA [93], [24]. α -form PVDF is helical in conformation with unit cell dimensions (first discovered in 1966 by Lando et al.) of $a = 4.96 \text{ \AA}$, $b = 9.64 \text{ \AA}$, $c = 4.62 \text{ \AA}$, and angles $\alpha = \beta = \gamma = 90^\circ$ with density of 1.92 g cm^{-3} [94], [24]. Due to its specific antiparallel conformation, there are no steric strains of fluorine atoms and this is why α form is the lowest potential energy crystalline state [24]. It should also be noted that the other three most common crystalline forms, β , γ , and δ , can all be made from α -form PVDF with sufficient mechanical stress, heat or electric field; this property is unique to the α -form [24].

The β form, or Form I, consists of all-trans planar conformation, with dipoles pointing in the same direction, making it the most polar and electrically active crystal form of PVDF, and also the form with piezoelectric and pyroelectric properties [23]. The crystalline unit cell of β -PVDF was first described by Kondrashev and Galperin, et al. as two chains in orthorhombic crystal lattice with $a = 8.45\text{\AA}$, $b = 4.88\text{\AA}$, $c = 2.55\text{\AA}$ with density of 1.97 g cm^3 [94], [95], [24]. Controversy on agreement with this proposed crystal structure stemmed from the fact that all-trans molecules means fluorine atoms are closer together than their van der Waals radii allow; leading to the conclusion (using X-ray diffraction analysis, and confirmed by Raman and IR spectroscopy) that some chains are deflected at 7° to a statistically random degree [95], [87], [96], [94], [97], [24].

γ -PVDF easily transforms to β during orientation, and was not recognized as an independent crystalline form until 1972 when it was first characterized by Hasegawa [95]. However, controversy of exact unit cell dimensions was frequently proposed and refuted until more recently when Lovinger used XRD to study single crystals of γ -PVDF, leading to the conclusion that γ -PVDF is in fact monoclinic with unit cell dimensions of $a = 4.96\text{\AA}$, $b = 9.67\text{\AA}$, $c = 9.20\text{\AA}$, and angle $\beta = 93^\circ$ [98], [95], [88], [99], [100], [101], [102], [103], [104], [24]. γ form can be thought of as an intermediate between α and β -PVDF, with unit cell very similar to the later, differing only by shift of trans-planar chains in the c -axis [24].

δ -form PVDF has the same crystalline dimensions and conformation as the α form but dipole vectors point in same direction in δ form and in opposite directions for α , therefore the only difference is in interchain packing [93], [24]. Consequently, δ form PVDF is also called Form IIp (polarized), and can be made by high-electric field poling of the α form [24]. In 1980, Bachmann et al. found the crystal structure of δ -PVDF to be orthorhombic with dimensions $a = 4.96\text{\AA}$, $b = 9.64\text{\AA}$, $c = 4.62\text{\AA}$, with parallel dipole vectors [105].

Since PVDF is a highly crystalline polymer (about 50% or more on average), and in many cases properties directly result from its crystal structure, understanding how and why these crystalline forms occur and their effect on final dielectric and mechanical properties of the film is crucial.

Crystallizing PVDF from polar solutions leads to formation of primarily β -form when low evaporation rates are used, γ at intermediate evaporation rates, and α for higher rates [93]. Single crystal growth of α -PVDF [106], [107] and β -PVDF [108], [109], [106], [110] from solution is possible, however it is much more difficult to obtain γ form alone, but evidence shows that including positive ions (Ca^{2+} or Na^+) may help favor γ form crystallization over α [109], [24]. More recently, γ form PVDF crystals were produced via isothermal crystallization from solution at high temperature using KBr salt as a nucleating agent [111].

α -PVDF is easily crystallized from the melt and is in essence the only form crystallized from the melt up to 150°C [24]. Quiescent crystallization from the melt results in about 50% crystallinity, as evidenced by X-ray diffraction data and dilatometry (see [24] and many sources referenced within for verification). Crystallization kinetics for PVDF are well defined in the literature by, for example, Gianotti [112], Nakamura [113], and Mancarella and Martuscelli [114], [24]. Above 150°C, a second spherulitic form is observed, and has been demonstrated to be γ -PVDF [115], [116], [24]. Such spherulitic growth can be observed under polarized optical microscope, in which large, highly birefringent regions are classified as α form, and smaller and sometimes irregular spherulites belong to the γ form [24]. As crystallization temperature increases, γ form crystals become more regular and grow parallel to substrate, making birefringence of this form much smaller than α -PVDF [24]. In general, γ -PVDF nucleates sooner in higher temperature regions, but crystals grow much more slowly than the α form, so that α is initiated at tips of γ spherulites. Since α form grows more quickly, it engulfs γ crystals during growth, and only α -PVDF can be formed via directional solidification. Characterization of α and γ -PVDF via X-ray diffraction and electron

microscopy shows that, when crystalline forms are fully developed, both forms have the same interchain packing and unit cell orientation and only differ in intramolecular conformation; thus signifying the ease of phase transition between the two and also the inability to distinguish between the two forms via XRD data alone [101], [115], [24]. The two strongest crystalline reflections are (020) and (110) crystal planes for α and γ PVDF [24].

β form PVDF is more difficult to produce from the melt, but was first accomplished on freshly cleaved KBr substrate, producing lamellae which are oriented in [110] and $[1\bar{1}0]$ directions, with chains (and therefore dipoles) growing parallel to the substrate's surface [100], [24]. More recently, it has been shown that β -PVDF can also be formed from the melt at high pressures [117], [118], [119], under external electric field [120], [121], [122], [123], [124], or using ultra-fast cooling [125], [126], [25].

Solid state phase transitions from primarily α -PVDF can be induced thermally via annealing. At high temperatures, above about 160°C, α -PVDF is known to be converted to the γ form [115], [24]. The transformation has been shown to occur at boundaries between the two spherulites or at nuclei of α spherulites, and can be enhanced using nucleating agent such as KBr [115], [111], [24]. At high pressure of around 4 kbar, α to β transitions were first observed by Takemura [127], [128], [129] as a solid-state transition before melting of the α form, and additionally melting and recrystallization from α - β form at 278°C [24]. Under high electric fields, PVDF's non-polar α form transforms to the polar δ form and, at even higher electric fields (greater than 300 kVcm⁻¹), to β form PVDF; the mechanism of which will not be discussed here but can be found in more detail elsewhere [93], [24].

Of more importance to this work, solid-solid phase transformation of PVDF can also be accomplished by subjecting the material to high stresses during mechanical deformation. Under sufficient tensile stress, gauche-bonds transform to trans-bonds leading to α to β form transition, and this is the most common way in which β -PVDF is formed [93]. β crystals have been shown to preferentially orient with b-axis

primarily normal to film surface, with high degrees of cylindrical symmetry [130], [131]. This transformation was first observed by Lando [97], [94] to occur via uniaxial or biaxial deformation at temperatures between 50 and 100°C. Though it is possible to get α -PVDF to transform to β at higher temperatures (about 130°C as evidenced by Matsushige [129]), the amount of β form transformation significantly decreases with increasing stretch temperature, and instead the oriented α form is preferred [132], [24]. The necking mechanism was shown by Matsushige as the initiator for α to β transformation and optimum conversion occurs at stretching ratios between 3 and 4X [129], [133]. Orientation of α form is optimized when stretching from 140-150°C up to draw ratios around 4X, above which high stress development leads to conversion to β -PVDF [24]. When oriented, γ form PVDF undergoes near complete transition to β form [95], [134], [135] at all temperatures except when stretched near their melting point, where transformation from γ to β form is minimized and most molecules remain in oriented γ state [136], [99], [24].

Due to the unique properties associated with each crystalline form of PVDF, it is essential to have a way to characterize and quantify α , β and γ forms and, until recently, results have been contradictory due to the close or overlapping properties between the three forms. Martins et al. reported that it is possible to correctly identify each form using FTIR, XRD and DSC experiments but notes that all three are necessary to obtain a complete morphological evaluation due to overlapping peaks in some of these techniques [25]. Specifically, α form is quantified most easily by FTIR absorption spectra, producing characteristic bands at low wavenumbers which are unique to this form [25]. On the other hand, β and γ forms, though they each appear at different peaks than the α form, are difficult to distinguish from one another using FTIR as many of their bands occur at similar wavenumbers [25]. There are some bands which are characteristic to either the β or γ form in FTIR absorption spectra, but due to the closeness to one another, they are more useful as qualitative, rather than quantitative, evaluations [137], [138], [25]. Gregorio et al. shows how the Beer-

Lambert law can be used to quantify crystal forms in a sample containing only α and β -PVDF [139].

X-ray diffraction has also been used to quantify the amount of crystalline forms of PVDF. Again, it is noted that the γ form is difficult to quantify since it is hard to obtain a 100% γ -PVDF sample, and therefore difficult to obtain a characteristic diffractogram of the material. Using XRD (Cu $K\alpha_1$, $\lambda = 1.54 \text{ \AA}$), all three crystal forms show peaks around 20° but only α and γ at 18° ; thus they can be distinguished from β in this manner [25]. From the discussion above, it is clear that FTIR can cause confusion of β and γ forms, and XRD between γ and α but the combination of the two can be used to distinguish between all three [25].

Furthermore, DSC is a powerful technique in quantifying the three main crystal forms of PVDF. The thermodynamics of melting of PVDF is complicated due to the many crystalline structures and numerous ways in which they can be formed, as reviewed thoroughly by Bassett [24]. Consequently, each polymorph of PVDF has its own melting point. The highest melting form is γ -PVDF which results from solid-solid thermal transformation ($T_m = 190^\circ\text{C}$) from the α form and is sometimes referred to as γ' to make the distinction from melt grown γ form, which has a T_m near 180°C , [140], [137], [25], [24]. The melting point of α -PVDF is around $167\text{-}172^\circ\text{C}$ [141], [142], [139] which is similar to that of the β form [140], [137], [139]. However, β in unoriented state melts at 189°C , but the oriented value depends on stress and ranges from 166°C (when restrained) to 186°C (when sample is allowed to relax) [128]. For this reason, DSC cannot be used to quantitatively determine the difference between α and β form PVDF, but γ crystals are much easier to distinguish. Therefore, all three characterization techniques can be combined to get a clear picture of α , β , and γ form content of PVDF samples [25]. Review written by Martins et al. can be referenced for more information as to the mechanisms and methods mentioned above [25].

PVDF exhibits unique properties among polymers including its ferroelectric behavior. Ferroelectric materials such as PVDF exhibit both piezoelectric (mechanical

stress reversibly creates electricity) and pyroelectric (temperature reversibly creates electricity) properties making them invaluable as energy harvesting materials and as a replacement for ceramic transducers [24]. PVDF has excellent mechanical properties compared to common semi-crystalline polymers such as polyolefins, nylons etc., including very high impact strength, tensile and compressive strengths [24]. It is also very optically transparent but with great weathering and UV resistance, making it excellent for the use of solar energy harvesting applications [24]. PVDF has also found use in separation membranes due to its selective permeability and resistance to chemical and oxidative degradation [24].

As far as dielectric properties go, PVDF has a very high dielectric constant (9-10) but suffers from low breakdown strength and high losses. Biaxial orientation of PVDF (BOPVDF) can help improve these properties and has been studied by Jow, et al. [19] and more recently by Yang and co-workers [20]. Though BOPVDF retains its high dielectric constant and has breakdown strength near that of BOPP, it has high losses and leakage current which prevents it from being used on a large scale as a capacitor film [61].

The effect of PVDF crystal form on its dielectric properties was studied by Gregorio who found that, in samples of α and β -PVDF, increasing amounts of α form decreases both the real (ϵ') and imaginary (ϵ'') parts of the complex permittivity at high frequencies from 10^2 to 10^6 Hz [26]. According to Gregorio, orientation of dipoles occurs in the amorphous-crystalline interphase and the ability to respond to electric field thus depends strongly on the neighboring crystalline form [26]. This work also found that orientation of both α and γ -PVDF increases the dielectric constant and furthermore the dependence of complex permittivity on temperature in the range of 30-90°C at frequencies above 10^4 Hz [26]. Since it is easily produced by mechanical drawing and of interest to piezoelectric applications, dielectric properties of β form PVDF, compared to α -PVDF, have been relatively well characterized [27], however not much information of the γ form exists, due primarily to the difficulty in producing

it as the sole component of a film or fiber. Very recently, Zhao et al. prepared films of PVDF consisting mainly of one crystal form of PVDF, and found that γ -PVDF had relatively higher dielectric constant, less hysteresis, and loss compared to α and β films suggesting it would be desirable for pulse power applications [28]. However, these results have not been verified by other, independent researchers. One focus of this work was to investigate the validity of these findings in large scale extruded films, versus small samples produced in the lab, as were studied by Zhao and co-workers [28].

And finally, since PVDF has low thermal stability (with melting point around 174°C), it cannot be used as the sole dielectric component in capacitor pulsed power applications due to low charge-discharge efficiency, which is about 15% lower than BOPP [29]. One way to tailor fluoropolymer properties is by copolymerization which allows several monomers with unique and favorable properties, that may otherwise phase separate (i.e. thermodynamically immiscible), to be combined into a single material. Polytetrafluoroethylene (PTFE) has very high thermal stability (melting point greater than 400°C) and low dielectric loss (about 0.01%) but cannot be processed via melt extrusion and has a low dielectric constant [29]. Copolymerization of monomers VDF and TFE creates ethylene tetrafluoroethylene copolymer (ETFE), which takes advantage of the dielectric properties of both PTFE and PVDF and can be melt processed. Another fluoropolymer material, tetrafluoroethylene-hexafluoropropylene-vinylidene fluoride terpolymer (THV) combines TFE-HFP-VDF monomers. In addition to advantages mentioned above for TFE and VDF, the HFP (hexafluoropropylene) component helps to lower cost by reducing melting temperature without lowering thermal stability of the material [29]. Both THV and ETFE are melt processable and semi-crystalline fluoropolymers and details of each will be discussed in the following sections.

Ethylene tetrafluoroethylene copolymer (ETFE)

Developed in 1973, ETFE copolymer was one of the first polymers to combine fluorocarbon and hydrocarbon monomers and thus has properties somewhere in between these two extremes [79]. The hydrocarbon sub-unit gives better flexibility and mechanical properties compared to, for example, polyvinylidene fluoride (PVDF) homopolymer, and ETFE can be processed thermally by all processing methods for thermoplastics [21], [79]. Primary applications for ETFE are wire and cable insulation, followed by fuel tubing [21], [79].

Figure 9. The preparation of ETFE.

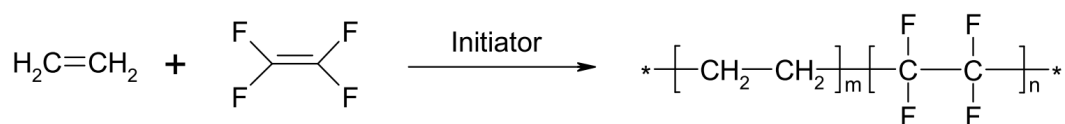


Fig. 2.1.: Chemical synthesis of ETFE [21].

ETFE is synthesized by suspension polymerization of ethylene and -TFE monomer units, as shown in Figure 2.1. Despite its bulky structure, ETFE has total percent crystallinity of about 40-60% and a close-packed, extended zigzag conformation, with melting temperature ranging from 225-300°C [21]. Usage temperatures for this material are between -100 and 150°C. ETFE has a dielectric constant of 2.6 (106 Hz) and breakdown strength of approximately 14.6 kV/mm, with very low electric loss of 0.010 (at 1 kHz) [21], [36].

Several previous studies have looked at morphology of ETFE and how it changes during orientation. In 1973, the crystal structure of an alternating copolymer ETFE was determined by Wilson and Starkweather to be either orthorhombic or monoclinic with a density of 1.9 g/cm³ and unit cell parameters $a = 9.6 \text{ \AA}$, $b = 9.25 \text{ \AA}$, and $c = 5.0 \text{ \AA}$ [143]. In a series of three papers published in 1986, Tanigami, et al. studied the crystal structure, crystal phase transition, and deformation mechanism of

ETFE [30], [31], [32]. These papers confirmed the orthorhombic crystal structure of ETFE, however they found lattice parameters of $a=8.57 \text{ \AA}$, $b=11.20 \text{ \AA}$, and $c=5.04 \text{ \AA}$, which vary slightly from previous studies due to newly discovered paracrystalline disorder [30]. In the second paper of this series, Tanigami discovered, by use of X-ray diffraction, the existence of a reversible, thermally induced first-order transition from ordered orthorhombic crystal phase to a disordered hexagonal mesophase of copolymer ETFE [32]. Tanigami also studied morphology of ETFE under uniaxial deformation and found that, below the temperature of mesophase transition ($T=100^\circ\text{C}$), ETFE films deform plastically by breaking up lamellar regions, leading to micro-void formation in amorphous regions. However, when ETFE films are stretched above the $T=100^\circ\text{C}$ transition temperature, they exhibit rubber-like deformation [31]. These results are important for choosing appropriate stretching parameters such as rate, temperature, etc. as well as what to look for in characterizing ETFE films; mainly if the existence of this disordered mesophase can be observed. Several papers by Funaki, et al. sought to re-examine the crystal structure of ETFE via fitting different crystal structure models using X-ray diffraction and found the structure to be monoclinic at very low temperatures (down to around -150°C) which transforms to psuedo-hexagonal form around 60°C (with the exact temperature being dependent on E/TFE ratio) [33], [34], [35].

Tetrafluoroethylene-hexafluoropropylene-vinylidene fluoride terpolymer (THV)

Figure 12. The preparation of THV.

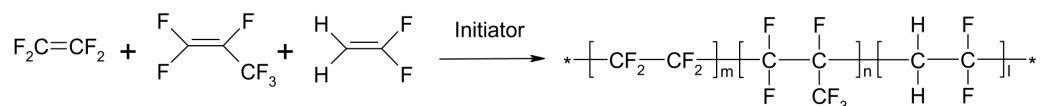


Fig. 2.2.: Chemical synthesis of ETFE [21].

Only developed in the mid-1990s, THV is the newest fluoropolymer but has already found wide use as a barrier film and again in wire and cable insulation applications

due to its excellent adhesion properties and low dielectric constant [21]. THV is prepared by free radical polymerization of the three monomers TFE, HFP and VDF, as shown in Figure 2.2.

Having three monomers allows for combination of the properties of each individual component, making THV a highly flexible and transparent material which can be processed at relatively low temperatures by extrusion or injection molding [21].

THV has a dielectric constant of 4-5 (106 Hz), breakdown strength 48-62 kV/mm, and electrical loss around 0.09-0.14 (at 1 kHz) [36], [21]. The THV material used in this study has a composition of TFE/HFP/VDF: 76/13/11 percent by mass.

Since it is such a new material, only a few sources exist which describe the structure and morphology of THV and the effect of orientation on this material. In 1996, Freimuth, et al. studied the structure of uniaxially oriented THV terpolymer with composition: 52 mol% VDF, 36 mol% TFE, 12 mol% HFP [37]. WAXS patterns showed two amorphous halos and one crystalline peak appearing around $q = 12 \text{ nm}^{-1}$, 27.5 nm^{-1} , and $q = 12.89 \text{ nm}^{-1}$, respectively. From this data, Freimuth also estimated a percent crystallinity in the as-molded sample of about 10% [37]. After stretching at 100°C to 4.5X draw ratio, WAXS patterns show reflections instead at around $q = 24.7 \text{ nm}^{-1}$ and $q = 49.3 \text{ nm}^{-1}$. Since there are few diffraction peaks, a crystalline unit cell could not be determined but evidence suggests the crystal structure is similar to hexagonal cells (of one crystalline permutation) of PTFE and PVDF [37]. SAXS patterns also showed lamellar long pattern $L = 12.0 \text{ nm}$ for the undeformed material [37]. After stretching to 4.5X draw ratio in temperature range $50\text{-}100^\circ\text{C}$, Freimuth and co-workers discovered a four-point SAXS pattern which transforms to a two-point one as stretching temperature increases [37]. In 2008, Emmons and co-workers studied changes in morphology of THV terpolymer under very high pressures and determined by X-ray diffraction that THV has a d-spacing of 4.9 \AA at the most intense diffraction peak [44]. This d-spacing is close to crystal structure phase IV of PTFE and, since the material had high -TFE monomer content,

it can be assumed that the TFE portion is that which is crystallizing and thus the PTFE phase IV crystalline unit cell can be reasonably approximated as the unit cell for THV of this composition [44]. Specifically, PTFE phase IV has a hexagonal unit cell structure with parameters $a = 0.566$ nm, $b = 0.566$ nm, and $c = 1.950$ nm [144]. Rheological [38], [39], dielectric [29], [40], and characterization via NMR [41], optical properties [42], spectroscopic properties [43], [44] and thermodynamical [45] properties of THV have all been studied in the literature, but very few describe morphology related to orientation.

2.2.3 Ethylene vinyl alcohol copolymer (EVOH)

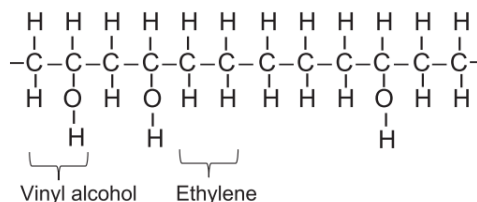


Figure 4.16 Chemical structure of EVOH.

Fig. 2.3.: Chemical structure of EVOH [145].

The last material to be discussed is ethylene vinyl alcohol copolymer (EVOH) which is not traditionally thought of as a dielectric material. However, EVOH has been well applied to and studied for high barrier applications, which have been shown to be an indicator of dielectric breakdown strength [146]. Since dielectric breakdown strength is theorized to be inhibited by increased tortuosity by, say, oriented crystals post film stretching, there is a similarity to the proposed mechanism of gas barrier propagation through thin films [61]. Therefore, this material could be interesting in studying the fundamentals of breakdown strength in polymer films.

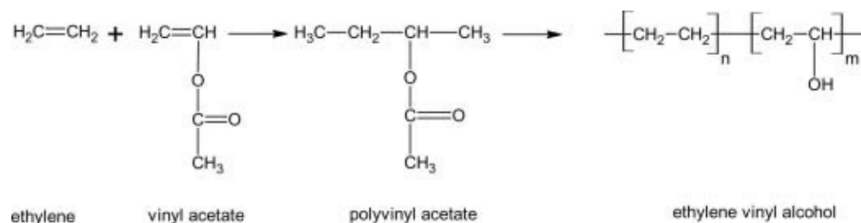


Fig. 2.4.: Chemical saponification reaction to create EVOH polymer [147].

EVOH is an optically transparent, highly crystalline, polar polymer which has an outstanding barrier to oxygen (very, very low permeability). EVOH is a random copolymer containing varying amounts of ethylene and vinyl alcohol monomers and it is typically described by the mol% of ethylene in its backbone, which can range from around 27 to 48 mol% commercially [145].

Side-chain vinyl alcohol groups provide the excellent oxygen barrier performance due to strong hydrogen bonds which reduce free volume [145]. Lower content of ethylene indicates higher gas barrier; however, higher ethylene content also makes the material easier to melt process so there is a trade-off in these two properties [145]. The barrier performance of EVOH is highly dependent on relative humidity of its surroundings, with lower ethylene content EVOH materials being more susceptible to these effects [145]. Furthermore, when used on its own, EVOH is prone to cracking and has high percent crystallinity, making it hard to process and orient. It is also very prone to intake of water in the air, and it swells when water is present creating voids that allow water to permeate through the structure easily [145]. To combat these difficulties, it can be sandwiched between layers of other polymers, such as Nylon-6, blended with an amorphous resin or ionomer, specially tailored during synthesis, layered between high water barrier materials, or quenched rapidly after processing to suppress crystallization [145]. Though oxygen barrier is often the most important for packaging applications, high barrier to oxygen does not necessarily imply high barrier to other small molecules, such as aromas and flavors. EVOH and PET, however, are

both decent barriers to aromas and flavor molecules, making them good candidates for the food packaging market [145].

Blends of EVOH with other polymers have also been evaluated for improved barrier and mechanical properties. For example, microlayer EVOH, low density polyethylene (LDPE), foam film structures were studied for barrier property improvement very recently by Feng [48]. Feng and co-workers were successfully able to make the EVOH/LDPE/foam structures with 50% lower density which maintained good barrier and mechanical properties [48]. Furthermore, the researchers pointed out that these properties could be further tailored fairly easily by adjusting material ratios in the film structure [48]. Due to the inherent immiscibility of PET and EVOH, a compatibilizer was used to help promote better interfacial adhesion. Maleic anhydride-grafted polyolefins are often used a tie layer in multilayer structures or compatibilizer in polymer blends, where the anhydride group bonds to the non-polar polymer and the -OH group bonds to EVOH [145].

EVOH's structure-processing relationships are complicated due to difficulties in orienting the material on its own. EVOH is polymorphic depending on copolymer composition and processing temperatures, but, with relatively high vinyl alcohol content, it has a singular, monoclinic crystal structure [46]. Since EVOH is a fast crystallizing polymer, it cannot be quenched into amorphous starting state, and can therefore be difficult to orient on its own. The crystalline structure of EVOH copolymers was studied by Takahashi, et al., who used NMR to show that all copolymers studied (with a range of EVA content from 0 to 100) were atactic, with monomers randomly linked in the backbone [46]. Furthermore, all EVOH copolymers used in this study were able to crystallize and had either monoclinic or orthorhombic crystal structure via WAXD observations [46]. EVOH with low vinyl alcohol content (6-14 mol%) has the hexagonal crystal structure of polyethylene, and when higher vinyl alcohol content is added to the copolymer, between 27 to 100%, the monoclinic crystal structure matching that of poly(vinyl alcohol) (PVOH) was observed [46]. There is a transition

range between 14 to 27 mol% vinyl alcohol, in which the material matches neither PVOH or PE's crystalline structure, rather it is said to be pseudo-hexagonal [46].

Uniaxial orientation of EVOH is not difficult to accomplish, however biaxial orientation has presented more of a challenge. Uniaxial orientation of EVOH and clay EVOH composites were studied in 2013 by Franco-Urquiza and co workers [51]. Stretching EVOH at moderate rate (100 mm/min) and temperatures above glass transition led to strain-induced crystallization and relaxation, as well as recrystallization of imperfect crystals [51]. At high drawing rates, diffusion and relaxation were suppressed leading to less structural variation in the film after stretching [51]. As drawing temperature increased, less pronounced strain hardening was observed, along with decrease in yield, modulus, and ultimate strength, as expected [51].

In general, biaxial orientation of EVOH is difficult because, when stretched biaxially near its melting point, EVOH displays sheet-like morphological structure caused by strong hydrogen bonding [147]. Sequential biaxial orientation of EVOH leads to microfibrillation of EVOH, leaving a very poor film quality, but simultaneous orientation at high stretch rate and low temperature, however, helped to suppress crystallization of EVOH and led to a high quality, biaxially oriented film with high oxygen barrier values [47]. The amount of ethylene monomer in the copolymer had a large effect on the stretching capability of EVOH films. Breil and co-workers found that sequential stretching could only be accomplished if EVOH had ethylene content greater than 44%, but simultaneous was possible for all compositions, down to 24% ethylene content [47].

EVOH/PP blends were prepared and studied by J. Ho Yeo and co-workers to study effects on oxygen permeability of biaxially oriented films [54]. This study found that viscosity ratio and resulting geometry and morphology of dispersed phase within the blend film after orientation played an important role on the oxygen barrier and properties of oriented blend films. Specifically, laminar morphology of EVOH within PP matrix was shown to improve barrier properties of the film by a factor of 10

compared to neat oriented PP film [54]. Effects of amount of compatibilizer present in the system, along with stretching rate, ratio and temperature were also investigated and found to have a large impact on final properties of the film. Barrier properties of EVOH/PP films increased as draw ratio and temperature increased and there was an optimum compatibilizer content in the blend, above which barrier properties were negatively impacted [54].

Also, oriented EVOH/PET blends were studied by Gopalakrishnan, et al. as early as 1971 [52] and EVOH/PET and EVOH/PEN blends by Kit and Schultz in 1995 [53]. Gopalakrishnan, et al. found that matching rheology of the individual components in the blend was important to obtaining films which can be oriented and have good properties afterwards [52]. A compatibilizer was also used in this study and found to be essential to obtaining improved barrier properties; all of the films with compatibilizer showed improved barrier properties to that of neat, oriented PET [52]. Oriented blend films containing EVOH and PET or PEN were also studied more recently by Kit and Schultz [53]. By varying stretching parameters, it was found that morphology of EVOH largely determines the extent to which barrier properties are improved or worsened in oriented blend films [53]. In agreement with Yeo [54], laminar morphology of EVOH with higher aspect ratio were shown to improve barrier properties of the blend films [53]. Kit found that oxygen barrier and mechanical properties were improved with addition of EVOH and orientation of the blend films as draw ratio increased and drawing temperature decreased [53]. Furthermore, water vapor permeability, which is decent in neat PET and PEN materials and very poor for EVOH, was not largely impacted with addition of up to 15% EVOH [53].

For the purpose of this research, PET and EVOH were chosen as common polymers in food packaging which, when combined together, may create synergistic effects on barrier and other film properties. However, the uniaxial orientation discussed in this work does not allow for a sample size large enough for barrier testing. Future testing on biaxial orientation of this film structures will provide a comparison of oxygen and

water vapor transmission permeability data, in addition to the structure-property relationships ordained by testing the films in uniaxial extension.

2.3 Dielectric properties of polymers

Dielectric permittivity, or the ability of a material to store electrical energy, is measured using dielectric (or impedance) spectroscopy over wide range of AC radial frequencies [148]. Dielectric spectroscopy measures permittivity and conductivity (materials ability to transfer electric charge) of a material as functions of temperature, frequency, and time, and combines the two values in a complex permittivity parameter, ϵ^* [148],

$$\epsilon^* = \epsilon' - j\epsilon'' \quad (2.1)$$

where ϵ' is “real” permittivity and ϵ'' is complex or loss factor.

A material’s relative permittivity is a measure of alignment of dipoles and the imaginary part of dielectric permittivity represents ionic conduction. Both of these values can also be calculated by [148],

$$\epsilon' = \frac{Cd}{\epsilon_o A} \quad (2.2)$$

and

$$\epsilon'' = \frac{d}{RA\omega\epsilon_o} = \frac{\sigma}{\omega\epsilon_o} = \frac{1}{\rho\omega\epsilon_o} \quad (2.3)$$

Where σ is conductivity, ρ is resistivity, C is capacitance, and R is resistance of the sample.

This set of equations can be used to directly measure permittivity value using an experimental setup consisting of a dielectric material sandwiched between two conductive plates that are connected to an applied voltage source [148]. Since permittivity depends on temperature, frequency and amount of applied voltage, these variables must all be specified when reporting dielectric parameters. After a certain “relaxation time”, the charges stored in a dielectric material will be released, as dipolar molecules rearrange in the system. The dielectric relaxation time, τ , is measured in dielectric spectroscopy as frequency as a function of complex permittivity, ϵ^* [148].

There are four standards for measuring breakdown strength of solid insulators which specify the procedure, number of samples to test, experimental setup and test voltage (more information can be found in [149]). However, there are a variety of methods capable of measuring the above mentioned parameters, and they can be further customized to allow for different sample geometries as well [149]. The procedure to measure electrical breakdown which is widely reported in literature typically includes depositing a metalized surface on the polymer film to act as an electrode, then clamping the metal electrode in parallel with the voltage source [150]. Discharge current and voltage across the capacitor are measured, allowing for breakdown voltage, peak current, pulse time parameters, voltage drop, and discharge energy to be calculated for each breakdown event, and more detail on this procedure can be found elsewhere [150]. Description of an automated system for measuring polymer film breakdown strength was reported by Xu, et al. in 2008 [151]. Breakdown for solid polymers typically follows a Weibull distribution,

$$\eta_1 = \eta_o \left(\frac{A_o}{A_1} \right)^{\frac{1}{\beta}} \quad (2.4)$$

Where η_1 is the Weibull characteristic breakdown field, η_o is breakdown field of initial area A_o , and area is A_1 and the Weibull slope parameter is β [61]. Since accurate prediction of dielectric aging and breakdown phenomenon in polymers does not cur-

rently exist, there is a need to develop such predictions using simulations such as molecular dynamics, for example [61].

2.4 Methods to improve dielectric properties of polymer materials

Polymer materials possess a vast range of properties, due inherently to their chemical structure, tacticity, or even processing history making them excellent solutions to many complex material engineering problems. Additionally, when properties of a single polymer are not quite suitable for an application, there are a range of engineering solutions to combine two or more polymers into a single solution and take advantage of each unique set of properties. These solutions include (among others) copolymerization, blending, nanocomposites, and microlayering. The following section discusses several techniques used in this work for improvement of polymer dielectric properties for high temperature capacitor applications.

2.4.1 Copolymers, blends and nanocomposites

Currently, biaxially oriented polypropylene (BOPP) is the state-of-the-art polymer material, with the highest known breakdown strength, low electrical losses and the ability to be used in high electric field due to self-healing properties. However, since the dielectric constant of polypropylene is very low, total energy density is only about 1.2 J/cm^3 at room temperature [3]. Since BOPP is an excellent capacitor material on its own, many researchers have tried to further improve this material using methods such as copolymerization, blending and nanocomposite technology.

Addition of flexible polar -OH group to side chain of polypropylene to form poly(propylene-co-undecen-11-ol) copolymer greatly increases dielectric constant from 2.2 in neat polypropylene to about 4.6, with energy density around 7 J/cm^3 [3], [152]. Another co-polymer solution includes cross-linkable materials, such as the isotactic

poly(propylene-co-p-(3(butenyl)styrene) family, which have dielectric constant around 3 that, due to the crosslinking, does not depend on temperature or frequency. Other advantages of this material include high breakdown strength with little hysteresis and energy density of 5 J/cm^3 [3], [152], [153].

Blending other polymers, such as low density polyethylene (LDPE), poly-vinyl chloride (PVC), and rubbers, with polypropylene can also help improve dielectric properties [3], [154]. An excellent combination is addition of polyvinylidene fluoride (PVDF) to polypropylene, due to PVDF's inherently high dielectric constant. Dang and co-workers found blends of PVDF and PP to have high permittivity value of 5.4 for 50:50 blend of PVDF/PP; a value which increased with temperature and was stable at both high and low frequency values [3], [63].

Use of fillers or nanofillers in polypropylene have also been widely studied. For example, glass beads, carbon black, silicate, and metal oxide particles (see Qi's review article for more detail [3]). In general, nanofillers added to polypropylene have been shown to help improve thermal stability of the system, increase percent crystallinity, increase permittivity, and lower loss compared to neat polypropylene [3].

2.4.2 Microlayering

Coextruded polymer films can be produced by both blown and cast film processes. Blown film is common for food packaging and medical applications. Producing coextruded (layered) structures often requires the use of several extruders and complicated die/manifold combinations. Cast film coextrusion with multi-manifold die can be used to produce up to 7 or 9 film layers, but typically requires one extruder for each polymer layer [56]. One such approach was developed and patented by Schrenk in 1975 and another, for blown film, by Dooley in 2004 [56], [155], [156], [157], [158]. With the development of Cloeren's NanoLayerTM feedblock in 2002, 1000 polymer layers

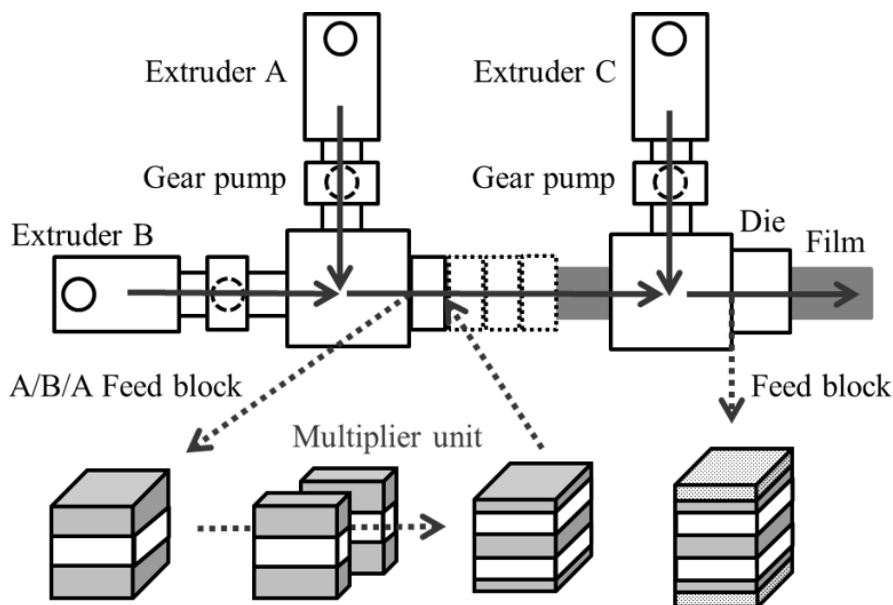


Fig. 2.5.: Microlayering coextrusion diagram, for a two polymer system (extruders A, B) with skin layer (extruder C).

could be produced for the first time in a single shot feedblock unit using variable layer selector plugs [56].

Unlike blend systems containing multiple polymers and/or nanofillers (which can be expensive and have many processing parameters to tune), or complicated multi-step lamination techniques, microlayer coextrusion feedblock technique consists of only a single, continuous process used to create layered polymer systems, and is the main technique used in this work [56]. The so-called layering feedblock technique builds off multi-manifold cast film coextrusion technique to combine hundreds to thousands of layers of two or more polymer materials. In the 1960s, Harder and Dow Chemical Co. first created a way to force hundreds to thousands of polymer layers into a single polymer film, using what they called interfacial surface generator method by using layered feedblocks [55]. Sequential layer multiplication works by passing a polymer melt stream with two- to five- layers first through a conventional feedblock, followed by one or more layer multiplication dies in series, which act to cut, spread, and stack the melt stream while doubling the number of layers [56]. Feedblock design is modular

for ease of process modification and the addition of layer-multiplying elements (also called interfacial surface generating devices) can be combined to produce nanolayer thick polymer layers, leading to unique properties for food packaging, optical, and dielectric applications [56]. As shown in Figure 2.5, by combining two or three layered melt streams, this process can create over eight thousand layers in one film, where for example, the number of layers for a two polymer system multiplies as $2^{[n+1]}$, and n is the number of multiplier units [159], [56].

Advantages of forced microlayer coextrusion include the ability to add a third polymer to the system in a three- to five-layer feedblock. By adding multipliers in series after the feedblock, an ABC or ATBTA (T referring to “tie” layer) repeating layer structure can be achieved [56]. Tie layers are commonly added to improve interfacial adhesion between polymers. Additionally, a sacrificial skin layer can be added after layer multiplication dies to help prevent instabilities during extrusion [42], [56]. Microlayer coextrusion also has the versatility to control relative composition and thickness of individual polymer layers. By varying screw speed or adjusting melt pump settings, polymer materials A and B can be extruded in different layer thicknesses [42], allowing for optimization of product formulation and cost, as well as forced confinement of one component [56]. The layer multiplier die process is more flexible and economical than single shot feedblock to create micro and nanolayer films, but suffers from higher pressure drop, and several types of viscosity spreading errors (which will be discussed later), and therefore, though it can successfully be used to create micro- and nanolayer film systems [160], [57], [58], [161] it has higher layer thickness deviation than the single shot method [56]. For this reason, single shot feedblock method is more commonly used in production commercially and sequential layer multiplying technique is used more widely in research and development to optimize film structures and properties before commercialization [56].

Several challenges in creating highly ordered polymer layer systems via microlayer coextrusion have also been evaluated in the literature. In 2010, Ponting et al. stud-

ied die path length modification to improve layer thickness uniformity and found that longer landing die length improved thickness uniformity by creating more equal velocity profile for polymers while contracting and spreading [42]. However, this subsequently increases residence time which can lead to polymer degradation and formation of contaminants such as gels in the system; so these two parameters must be balanced for system optimization. Rheology is perhaps the most important thing to consider when designing and optimizing precisely engineered micro- or nanolayered films. Polymers are non-Newtonian in the melt state, and have varying melt flow properties depending on molecular weight, extrusion temperature, etc. Melt flow instabilities can occur in all extruded polymer film processes, but the inherent nature of forcing two polymer materials together in very thin layers can lead to substantial rheological challenges [56]. These instabilities lead to poor film quality due to film and layer thickness variations, polymer intermixing, and irregular interfaces [56]. Several studies have tried to optimize interfacial stability of polymers in microlayer film structures, showing that increasing die gap, decreasing processing rate, increasing skin layer thickness or decreasing its viscosity and ratio of layer thicknesses are crucial to preventing instabilities [56], [162], [163]. Viscosity and elasticity mismatch of polymer components in one of the main causes of interfacial instabilities, causing encapsulation of one polymer by the other. The lower viscosity polymer moves more easily to the wall, encapsulating the other material; the degree to which this instability occurs depends on shear rate, residence time in extruder, and the degree of viscosity mismatch [56], [164]. Polymers with relatively high elastic storage modulus can also cause interface distortion from secondary flows competing with normal primary flow [56]. Both viscous and elastic flows are present in microlayer systems during extrusion, making optimization difficult. Studies show that small dies primarily suffer from viscous encapsulation, which moves along the die channel wall, while elastic encapsulation dominates for larger dies and creates flow patterns in different direction from the primary flow; therefore both are important factors to consider during process design [162]. Besides viscosity matching, layer interfaces are also af-

ected by the chemical and physical properties of polymers in layered systems. Layer interphase regions, where chemical solubility of the two touching materials creates an interphase layer of interwoven chains, can lead to interfacial slip due to decreased density depending on chemical compatibility of the materials, as measured by Flory-Huggins interaction parameter [56], [165]. Interfacial slip has been studied in detail by Macosko, et al., noting that multilayer cast or blown film processes create ideal shear conditions for interfacial slip phenomenon to occur [166], [167]. These studies found the importance of layer adhesion and material interactions on layer integrity in micro- or nanolayered films. For semi-crystalline polymers, crystallization can cause interfacial instability as layer thicknesses reach the size of crystallites. Dias and co-workers studied this in 2008, noting that crystals can influx between incompatible interfaces, and that thermal history is crucial for controlling size of crystallites so they cannot cause layer instabilities; one way to do so is to quench films quickly after casting to reduce spherulite size thus reducing this influx [168].

Microlayering coextrusion has been extensively studied at Case Western Reserve University, primarily by Baer and Hiltner [57], [58], [42] and also at the University of Minnesota [169] along with several universities in Europe [170] and China [171], [20], [56]. Layer definition and thickness uniformity have been studied at Case Western Reserve via cross-section AFM and polarized light microscopy, and show maintained layer integrity, with about 10-15% standard deviation in layer thickness for films greater than 32 layers [42], [172]. Nanolayer films with thickness on the order of wavelengths of UV, visible, or IR light appear to be colored or reflective due to internal scattering of light waves. This was first discovered by Alfrey and coworkers in 1969, in a film of 201 layers comprised of materials having index of refraction differences greater than 0.1 [173]. Alfrey also proposed a model for predicting such optical behavior, which can be studied in detail elsewhere [173], and this model was verified more recently by Baer, Hiltner, and associates in 2007 [172], [56]. This process can also be used to create gradient structures in which unequal amounts (thicknesses) of each polymer alternate in the film structure. Use of gradient structure in microlayering for

optical applications was first discovered in the early 1960s by Vasicek [174] and Francon [175]. Recently, optimization of gradient structures was studied by Ponting, et al., for use in various applications requiring films with unique optical and mechanical properties [42]. Micro- and nanolayer films have been used for unique optical applications including reflector films, optically active films, photopatternable films, and nanolayer-enabled polymer refractive optical devices, which will not be discussed in detail here; the reader is directed to source [56] for a summary of these applications.

Another important property of microlayer films is high barrier for food packaging and healthcare applications. Microlayer films can replace traditional barrier solutions such as coatings, laminates, inorganic fillers and blends, which often include several processing steps and can be expensive and difficult to scale up [176]. In the two-phase, gas permeation model for polymers, small molecules, such as O₂ and other gases, can permeate through amorphous regions of semi-crystalline polymers, and higher free volume facilitates easier transport therein. However, crystalline regions are considered to be impermeable and, therefore, crystalline structure helps facilitate higher barrier to small molecule transportation through polymer films by providing a more tortuous path for molecule permeation. Therefore, controlling polymer morphology and orientation is a main factor in predicting barrier properties [145]. In microlayer films, confinement of polymers in layers as low as 20 nm thick has led to unique morphology, essentially 1D confined structures consisting of highly oriented lamellar regions [56]. Many studies show the improvement of barrier properties in microlayer films including: syndiotactic polypropylene (sPP), [177], [178], polyethylene oxide (PEO) [179], [180], [181], [182], [183], [184], high density polyethylene (HDPE) [185], [186], poly(4-methylpentene) (P4MP1) [187], polycaprolactone (PCL) [188], [177], [189] [179], and polyvinylidene fluoride and its co-polymers [190]. Since PVDF is one of the main materials used in this study, its applications will be detailed further in the following paragraph.

PVDF and its copolymers are known to have high barrier to water and gases, due in part to its highly crystalline structure. Use of microlayering to further enhance these barrier properties has also been investigated. In one study, PVDF and PVDF-TFE (polyvinylidene fluoride co-tetrafluoroethylene copolymer) were microlayered with both polycarbonate (PC) and polysulfone (PSU) by Case Western Reserve researchers [190]. In their as-extruded state, films did not show improved barrier properties compared to neat components of the films. However, re-crystallizing films above the melting point of PVDF or PVDF-TFE (as applicable) produced an overall increase in O_2 barrier by 25-30X [190]. Increase in barrier properties for this system is due to specific structural dynamics of the PVDF or PVDF-TFE layers that occur due to confined crystallization of the material or during melt recrystallization. Specifically, Mackey and co-workers found that decreasing layer thickness and increasing melt recrystallization temperature increases the aspect ratio of oriented PVDF lamellae regions, while forming in-plane crystals that act as a barrier to propagation of small molecules through the film structure by creating a tortuous path for diffusion of the gas [190]. This finding shows the importance of morphology and texture in determining the properties of unorientated microlayer films.

Further orientation of microlayer films has also been shown to improve barrier, mechanical, and dielectric properties. Processing-dielectric-property relationships for microlayer films will be discussed in more detail in upcoming paragraphs. Since biaxially oriented polypropylene is used widely in food packaging and dielectrics (for capacitor films), [191] microlayer assemblies containing PP and other polymers have been oriented together to see if properties can be further enhanced without sacrificing optical properties (such as occurs by the addition of inorganic fillers) [192], [193]. Lin, et al. extruded PP/PEO microlayer films, consisting of 33 layers, which they biaxially oriented to reduce thickness of the layers to nanoscale, then melt-recrystallized PEO layers to achieve in-plane lamellar orientation [194]. AFM imaging of cross section of films before and after stretching showed PEO lamellae rotated from random to in-plane orientation when PEO layers were in nanometer range, which acts to improve

oxygen barrier by about 25 times compared to control BOPP films [194]. Furthermore, optical and mechanical properties did not suffer from the stretching or recrystallization process; transparency of microlayer films was similar to, and tear strength was improved by 10% compared to the control film [194]. Lin and co-workers also combined polycaprolactone (PCL) as a barrier layer in microlayer structures with PP in an attempt to improve properties of BOPP [195]. However, unlike for the case of PP/PEO films, PCL formed on-edge crystals due to transcrystallization at the layer interfaces which actually decreased barrier properties [195]. Adding a tie layer of polystyrene (PS) to separate the PCL and PP, however, causes confined crystallization of PCL which helps improve barrier properties of the film by 10X compared to BOPP with the addition of 15% PCL, and mechanical and optical properties did not change significantly compared to control BOPP film [195]. Another commonly used polymer for food packaging and dielectric capacitor films is biaxially oriented polyethylene terephthalate, or BOPET [196], [56]. Liu and co-workers combined PET with PVDF-TFE co-polymer in micro-to nanolayer structures to study barrier properties compared to neat BOPET [197]. When biaxially oriented, AFM showed edge-on lamellae in PVDF-TFE layers and stacked fibrils in PET, leading to a 2-3 times improvement in barrier when compared to BOPET due to the PET layers' structure [197]. However, melt recrystallization of the PVDF-TFE layer showed further barrier improvement by 10X compared to BOPET, as PVDF-TFE lamellar regions were confined in-plane with high aspect ratio [197]. Microlayer studies of oriented PP and PEO or PCL and PP with PVDF-TFE shows the high magnitude of barrier improvement that can be achieved in comparison to monolayer BOPP or BOPET films. Though improving barrier properties is not the primary objective of this work, these results are useful as they relate to the processing-structure relationships polymers commonly used in industry, especially BOPP and BOPET for capacitor applications. Furthermore, it has been postulated that, like small molecule permeants such as gases, electrons cannot penetrate through crystalline regions but rather travel through amorphous regions of semi-crystalline polymer systems to cause

dielectric phenomenon such as dielectric breakdown and aging [56]. Therefore, some of the same mechanisms to improve tortuous path of molecule propagation through polymer films may help to improve dielectric properties as well, and high gas and water barrier properties are often a strong indication of good dielectric properties in a given polymer film system [56].

The need for higher energy density capacitors which can be used at high temperatures while maintaining low losses has become increasingly dire as technology advances. For a linear, ideal capacitor energy density is represented as,

$$U_d = \frac{1}{2}\epsilon_o\epsilon_r E_B^2 \quad (2.5)$$

Where U_d represents the energy density, ϵ_o is permittivity of a vacuum (8.85×10^{-12} C²/Jm), ϵ_r is the real part of dielectric permittivity of the material (dielectric constant), and E_b is applied electric field.

The higher the energy density of material, the less material volume needed to obtain the same dielectric results; therefore, for obtaining compact, efficient capacitor devices, it is crucial to have a high energy density. Furthermore, dielectric constant is directly proportional to energy density, so the higher the dielectric constant, the higher the energy density. Also, breakdown or dielectric strength of the material is measured by the magnitude of applied electric field the material can withstand, represented by E_B in the above equation. Clearly, high breakdown strength is crucial to obtaining high energy density materials as the square of E_B is directly proportional to U_d . The phenomenon of breakdown in solid polymers depends on many factors, both intrinsic to the material itself and extrinsic; therefore, it is complex and cannot reliably be predicted for a given polymer, currently [61]. Breakdown can occur due to thermal runaway or electron avalanche, for example, and the electric field at which it occurs is higher for thicker films with less impurities and higher dielectric constant [61]. Intrinsic breakdown is a material property depending on chemical

structure, and therefore can be directly computed - whereas extrinsic (or engineering) breakdown can occur, for example, due to the type of electric field the solid is subjected to (i.e. AC versus DC), impurities such as carbonyl group common to polyolefins, and the environment in which voltage is applied (air versus liquid versus vacuum, etc.) [61]. Finally, though not directly represented in the definition of energy density, dielectric loss plays an important role in determining dielectric properties of a capacitor. There are several sources of dielectric loss, including the imaginary part of the macroscopic dielectric tensor (typically measured as loss tangent, or $\text{Tan}\delta$) which comes from delay in polarization response of a material to applied external field. The dielectric absorption phenomenon is another source of loss, and it is minimized for amorphous, non-polar dielectrics at high voltage. Finally, there is electrical conduction loss, which increases following an Arrhenius equation as temperature increases, and dominates losses at low frequency [61]. It should also be noted that peak in dielectric loss for polar polymers usually occurs at glass transition temperature or T_g ; therefore operating temperature range of the dielectric material should not include T_g to prevent premature breakdown due to high dielectric losses [61].

As mentioned previously, there are various methods of combining polymer materials in an attempt to obtain synergistic property improvement. Specifically, for dielectric property improvement, blends of polymer having high breakdown strength with high dielectric constant inorganic fillers can help to improve dielectric constant of the neat polymer. Two interesting examples include barium titanate in PVDF co-polymer matrix [198] and a core-shell titanium dioxide-polystyrene filler in polystyrene matrix [199], but generally it is seen that fillers negatively impact breakdown strength compared to the neat polymer material.

Given the versatility of microlayering coextrusion process, it has also been well studied as a means to further improve dielectric properties of polymers by combining different materials with, for example, high dielectric constant in one layer and high breakdown strength in the other. Literature contains extensive studies on the effects

of microlayering two or more polymer materials on dielectric properties; some important examples will be discussed here. Since PVDF has commonly been used as the high K layer in these studies. PVDF is highly polar, and therefore experiences dipole switching when exposed to electric field, causing high hysteresis and very high losses; therefore it is not an ideal capacitor material on its own. To combat this, polycarbonate (PC), which has relatively high breakdown strength, low losses and a linear dielectric hysteresis response, was combined in a microlayer film structure with PVDF (homopolymer) by Mackey, et al. [200]. By varying number of layers (i.e. layer thicknesses) and amount of each polymer, researchers found that electrical hysteresis decreased with increasing number of layers by the mechanism of PC layer preventing or blocking charge migration through the film [200]. Furthermore, thinner PVDF layers minimize charge migration and buildup at the interface between PVDF and PC, resulting in lower dielectric loss and hysteresis [200]. The combination of these two results means that microlayering PC and PVDF can both increase energy density and decrease loss in microlayer film systems. Researchers also combined P(VDF-HFP) copolymer (which has better processability than PVDF homopolymer) into microlayer films with PC [201], [202], [203], [56]. This study found improved energy density when film layers were in the nanometer range, with overall film thickness around 12 micrometers [203]. Also, the dielectric strength of the overall layered structure fit a series model, resulting in a relatively large value [203]. The reason for dielectric property improvement was postulated to be the “barrier effect”, in which one component in the structure (in this case PC) proved a barrier for breakdown charge [203]. One way to further improve dielectric properties of microlayer films is by interface modification. In the above film structure PC and co-PVDF, PMMA, SAN30, and poly(ethylene terephthalate-co-1,4-cyclohexanedimethylene terephthalate) (PETG) materials were used as tie layer due to specific interactions with PC and P(VDF-HFP) [204]. When PETG and SAN30 were used as tie layers in PC/P(VDF-HFP) microlayer structure, only small improvement in dielectric properties were observed; this was attributed to the fact that PETG and SAN30 do not strongly interact with P(VDF-HFP) [204].

On the other hand, PMMA tie layer, which interacts with both P(VDF-HFP) and PC layers, led to 25% increase in breakdown strength and lowered losses in the system, due to interdiffusion of PMMA into the other material layers which, helps to smooth dielectric constant distribution and reduce ion mobility [204]. Another example of microlayer systems studied recently for improved dielectric properties is polysulfone (PSF) and PVDF. Tseng and co-workers produced 32 and 256 layer films with 30/70 ratio by volume PSF/PVDF [205]. These materials were chosen for high dielectric constant of PVDF and the hypothesized ability of PSF to act as a barrier layer to trap electronic charges at the interface; also the two chemically have reasonable co-adhesion so use of a tie layer is not necessary [205]. This study found that when PVDF layers are thick, more charges are available leading to higher likelihood of breakdown, when PSF layers are thick, no conduction occurs and charges become trapped in interfaces between the layers [205]. When both PSF and PVDF layers are too thin (i.e. in the 256 layer film), few space charges exist and electrical conduction is allowed through PSF layers, lowering the breakdown strength and decreasing the electrical lifetime of the film; therefore layer size for both materials plays an important role in electrical properties of the film and this study states further optimization may be possible [205].

2.4.3 Multilayer film orientation

And finally, orientation of multilayer films is another strategy to tailor morphology and further improve dielectric properties of individual polymer components. Specifically, biaxial orientation of polymer films has been shown to reduce charge carrier mobility and increase dielectric breakdown strength in multilayer films [2]. In recent literature, Lin and co-workers found increased dielectric constant without impacting loss in microlayered, uniaxially oriented PVDF and low density polyethylene (LDPE) films, due primarily to orientation of PVDF and transformation from α form to β or γ form PVDF crystals [206]. Another study shows multilayer PET and P(VDF-TFE)

films which were biaxially oriented and dielectric properties studied in comparison to films of the individual components [146]. Carr, et al. coextruded multilayer PET and P(VDF-TFE) films with varying material ratio and layer thicknesses, with overall starting thicknesses of 200 micron [146]. Film thickness reduction and orientation was accomplished by simultaneous biaxial orientation, which results in PET undergoing strain induced crystallization from mostly amorphous regions, and the P(VDF-TFE) forms on-edge crystals due to confinement effect as layers become thinner [146], [207]. This study showed the importance of structure in both polymer layers in determining dielectric properties; specifically, maximum energy density was obtained after biaxially stretching the multilayer films, due to increased dielectric constant from on-edge P(VDF-TFE) crystals and oriented PET fibrils, and that heat setting the films resulted in lower energy density but also lower electrical hysteresis and loss [146]. The use of a PMMA tie layer to increase interfacial adhesion between PET and P(VDF-HFP) was subsequently studied by Yin, et al. [208]. Films of varying PMMA tie layer amount were fabricated via multilayer coextrusion. This study found an optimum PMMA content to be 8 vol%, and that interdiffusion between P(VDF-HFP) and PMMA layers along with biaxial stretching, led to increased β form PVDF crystal formation, resulting in a decrease in dielectric loss [208]. Furthermore, breakdown strength was improved by around 33%, and energy density at breakdown was increased by 150% compared to PET/P(VDF-HFP) films as extruded, without PMMA tie layer [208].

Although properties of biaxially oriented micro- or nanolayer films mentioned above were significantly improved from their individual components, we believe that dielectric properties of microlayered films can be further optimized by combining two carefully selected, thermally stable polymers with one containing high dielectric constant and the other high breakdown strength and low loss in a microlayer structure. By further biaxially orienting and/or heat setting the film, we hypothesize that a controlled morphology can be created and optimized to improve dielectric polymer properties. Furthermore, the use of custom-built, instrumented machinery to monitor

properties such as true stress, true strain, and birefringence in real time, is unique to this work and can help gain more knowledge as to the links between polymer processing-structure-property relationships.

2.5 Real-time techniques for online polymer mechano-optical property measurement

2.5.1 Custom built uniaxial stretcher

An instrumented uniaxial stretcher was custom built in our lab with a laser micrometer to detect sample width, a load cell for force measurements, CCD camera which detects a fluorescent yellow dot pattern and spectral setup to measure mechano-optical properties of polymer samples in real time during stretching experiments. Sample width and dot detection allow for calculation of film thickness in real time. The experimental setup is shown in Figure 2.6 and components of the machine are outlined in Figure 2.7. Use of real time width measurement allows for calculation of true stress

and true strain in real time. Measurements of optical retardation at the exact center of the film allows for calculation of birefringence values (at 546 nm wavelength) in real time during stretching. These calculations assume the following:

1) simple extension

$$D_t/D_o = W_t/W_o \quad (2.6)$$

2) incompressibility

$$L_o W_o D_o = L_t W_t D_t \quad (2.7)$$

Using these assumptions, the following parameters are calculated as follows:

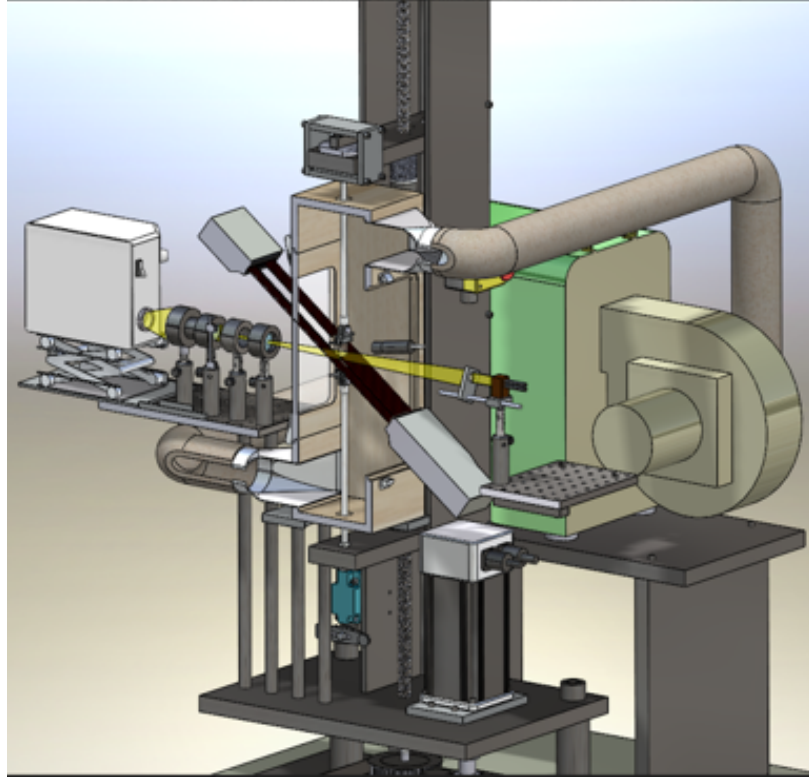


Fig. 2.6.: Uniaxial stretcher illustration and experimental setup.

Thickness:

$$D_t = (W_t/W_o)D_o \quad (2.8)$$

Birefringence:

$$\Delta n = R/D_t \quad (2.9)$$

True strain:

$$L_t/L_o - 1 = (W_o/W_t)^2 - 1 \quad (2.10)$$

True stress:

$$F_t/(W_t D_t) = F_t/[(W_t^2/W_o)D_o] \quad (2.11)$$

Where R is retardation, Δn is birefringence, D_o , W_o , L_o are initial thickness, width, and length respectively, and D_t , W_t , L_t , F_t , are time variations of thickness, width, length, and force.

Further details of this machine are listed elsewhere [77], [209], [210].

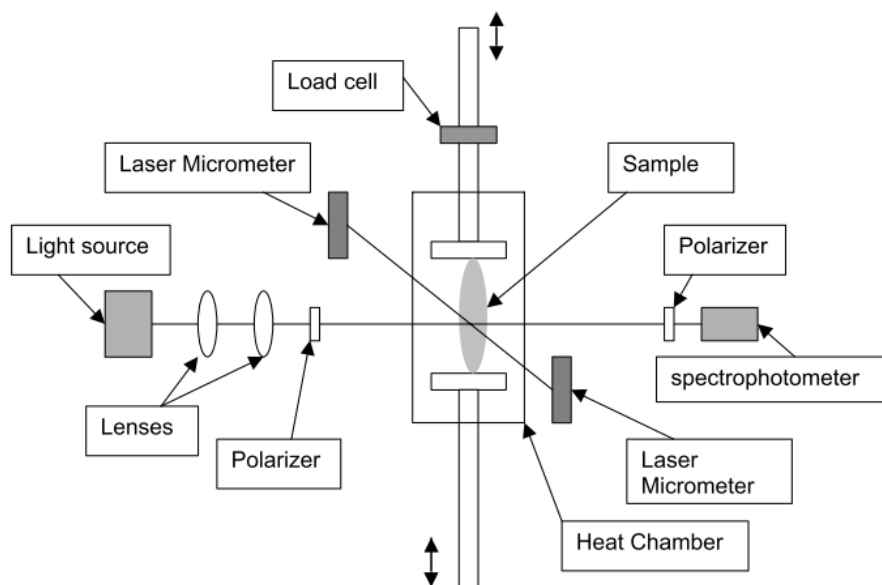


Fig. 2.7.: Simplified schematic of the components in instrumented uniaxial stretcher [210].

2.5.2 Instrumented biaxial stretcher

In a typical tenter frame biaxial orientation process, such as that used to produce BOPP, polymer film is cast, heated to an appropriate temperature, then stretched in the direction of machine extrusion (MD) first, followed by perpendicular stretching (TD), and finally, subjected to thermal heat setting, which acts to thermally stabilize the film (prevent shrinkage when re-heated, etc.). Each heating and processing step has a significant impact on polymer morphology, which is well known to affect the final properties of the material. For this reason, it is helpful to have a

way to track properties of polymer films in real time during each deformation step. Doctoral dissertation work by Mohamed Hassan in 2004 describes in detail the creation of new machines used in our lab to measure real time true stress, true strain, and birefringence of polymer films during both multiaxial deformation and thermal heat setting (discussed in the next section) [12]. The real-time spectral birefringence technique allows for quantitative determination of mechano-optical properties during simulated complex manufacturing processes and is the first of its kind. Specifically, it was designed to develop constitutive relationships to predict molecular behavior while processing polymers in regimes where current models do not apply [211].

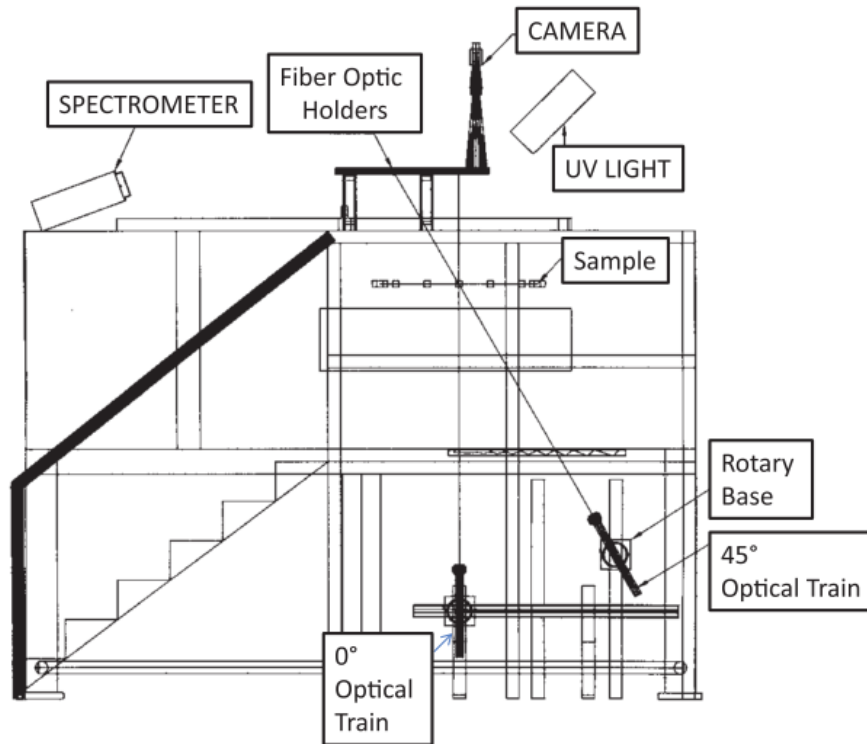


FIG. 6. Biaxial stretching machine and spectral birefringence system-side view.

Fig. 2.8.: Illustration of biaxial stretcher, upgraded to measure real-time spectral birefringence [211].

The instrument itself is made up of 3 main parts: spectral birefringence sensor assembly, high speed CCD camera detector, and the physical biaxial stretcher machine,

which will not be discussed in much detail here, but was outfitted as a vessel to contain these complex measurement devices - Figure 2.8 shows a side view of these elements. [211] The spectral birefringence sensor assembly consists of an optical train, including a white light source and polarizer, followed by the sample and analyzer.

One light source is placed on the same axis location as the sample, and the other at a 45° crossed position, allowing for the detection of both parallel and perpendicular light intensity signals (see Figure 2.9) [211]. Intensity versus wavelength curves are produced, and retardation due to sample interference is calculated by mathematically determining peak points of these spectral curves [211]. Resulting retardation versus wavelength data (Figure 2.10) are fit to a linear curve using Cauchy equation, as illustrated in Figure 2.11 [211].

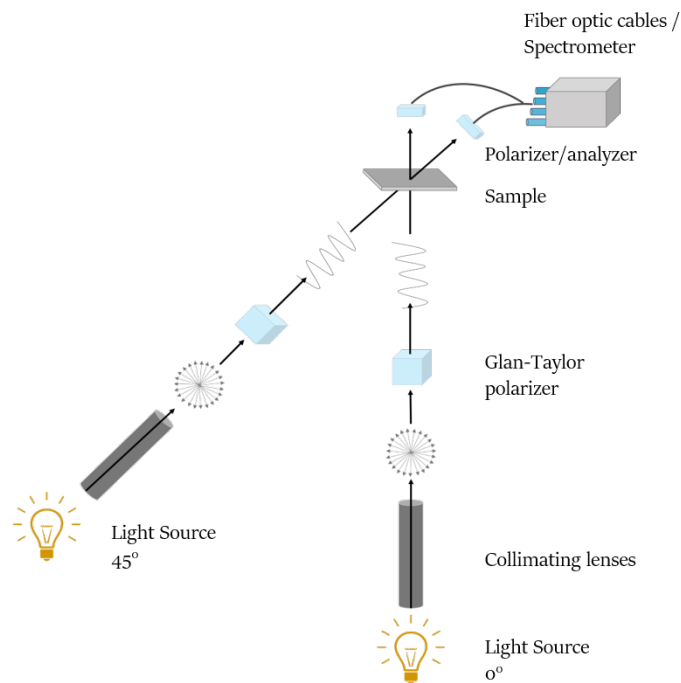


Fig. 2.9.: Illustration of white light telescope setup in biaxial stretcher.

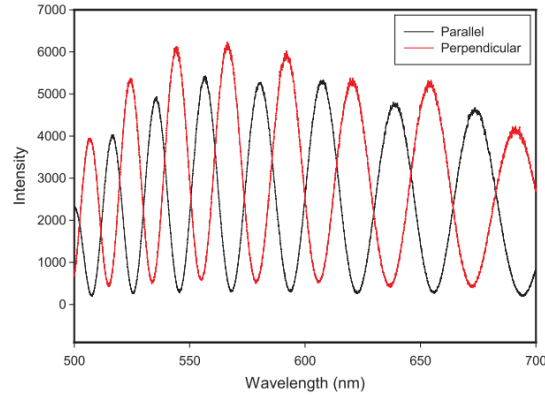


FIG. 2. Cross and parallel polarized light spectra.

Fig. 2.10.: Intensity versus wavelength curve resulting from polarized light signals [211].

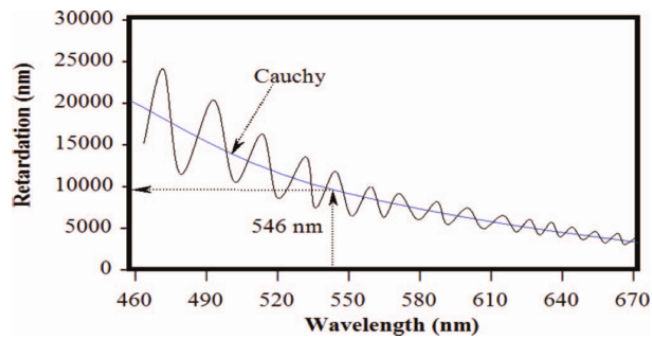


FIG. 4. Fitting a curve on the actual data and obtaining the retardation.

Fig. 2.11.: Use of Cauchy equation to determine retardation values [211].

From retardation values, in- and out - of plane birefringence can be calculated as follows:

$$\Delta n_{12} = \frac{R_o}{d} , \Delta n_{23} = -\frac{1}{d_o} \left[\frac{R_o - R_\phi \left(1 - \frac{\sin^2 \phi}{\bar{n}^2}\right)^{1/2}}{\frac{\sin^2 \phi}{\bar{n}^2}} \right] \quad (2.12)$$

Where d_o is film thickness, R_o retardation of film in normal direction, R_ϕ is retardation tilted to ϕ angle (0° or 45°) and \bar{n} is average refractive index of the film.

Both light sources are polarized using a Glan-Taylor prism and focused via collimating lenses to the geometric center of the sample [211]. The spot size of the light, position, and intensity can all be adjusted to ensure accurate acquisition of retardation data [211]. Light passing through the sample is then sent to fiber optics detectors connected to a six channel spectrometer which measures retardation of light intensity [211].

A high speed camera CCD detector looks directly down on the sample, and captures a 24 dot matrix pattern painted with fluorescent yellow dye, which is enhanced by use of a UV light (Figure 2.12). The camera follows these dots, and their positions in the X and Y directions are mapped as a function of time, such that real time true strain values of the sample can be deduced [211]. Assuming incompressibility of the material, and with the initial width, length, and thickness input into the system, real time thickness is calculated by a volume balance [211]. From all of these measurements, the computer system calculates values for true stress, true strain, and in- and out-of plane birefringence values as a function of time.

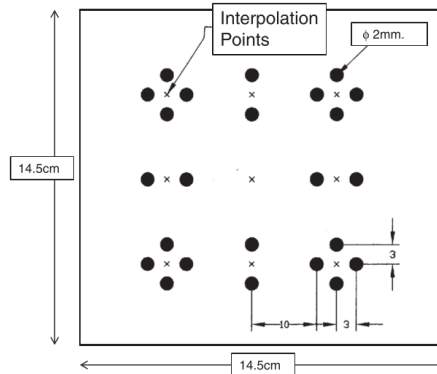


FIG. 8. Dot pattern for tracking the X and Y deformations.

Fig. 2.12.: 24-dot matrix pattern to measure X, Y strains [211].

The biaxial stretcher itself is set on a raised platform to accommodate the spectral systems beneath it, with the camera mounted directly above the machine [211]. It also has a heated chamber with glass door to ensure temperature equilibrium during stretching, and several thermocouples to measure the temperature at any given time

[211]. The mechanical stretching is accomplished via tenter frame clamps, with the capability to program application of loads in both the X and Y directions [211]. With its ability to measure in-plane and out-of plane retardation, true stress, and true strain values in real-time, this machine provides a novel way to relate complicated mechanical deformation of polymer films to their optical properties via birefringence.

A brief review of the principles behind and use of this technique were also published in *Review of Scientific Instruments* Journal in 2012 and can be referred to for more detail [211].

2.5.3 Heat setting chamber

Heat setting of slow-crystallizing polymers is an important processing step in which films, especially following orientation, are heated to just below their melting point, giving chains the thermal energy necessary for rearrangement via relaxation, crystal melting, and re-growth to help improve film properties and increase thermal stability. The spectral birefringence technique was instrumented into an annealing chamber which simulates the heat setting process of a constrained polymer film and can measure retardation of a white light source passing through the sample in real time (see Figure 2.13) [77], [212]. Optical train set-up is similar to the biaxial stretcher, however in this case a film is constrained inside a metal frame and rapidly inserted into a pre-heated chamber, allowing for nearly instantaneous readings of birefringence [77]. When the experiment is complete, the sample drops through a slit at the bottom of the chamber into a cold water bath to quench and freeze in morphology, which is further studied via off-line techniques such as DSC, X-ray scattering, electron microscopy, etc. [77].

Two white light sources pass through the heated, constrained sample at angles of 0° and 45° to measure in-plane and out-of-plane retardation (and therefore birefringence), respectively. In-plane birefringence, denoted by Δn_{12} , and out-of-plane

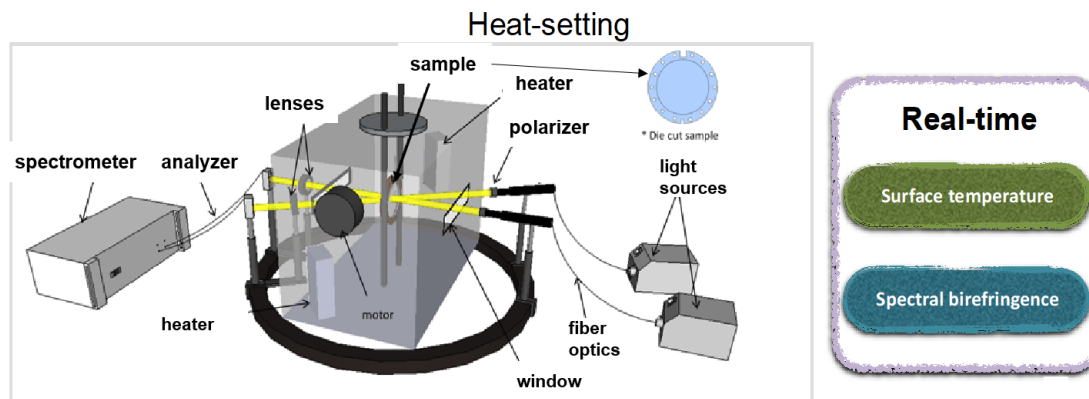


Fig. 2.13.: Annealing chamber illustration and experimental setup

birefringence, Δn_{23} , are calculated the same way as in biaxial stretcher apparatus, as illustrated in Equation 2.5.2.

2.6 Offline characterization techniques

2.6.1 X-ray diffraction

One technique that is particularly useful in determining structure and morphology of polymers is X-ray diffraction (XRD). Usually this method is used for crystallographic, however polymer lattice spacing, crystal perfection and percent, orientation, and conformation of amorphous chains can also be determined via XRD [213]. The setup of X-ray experiment, including sample, source, and detector placement, can be altered depending on which structural feature one wishes to measure. The source of electrons consists of a heated filament, which is kept at high negative potential (20-60 kV); X-rays are produced when these electrons are bombarded onto a metal target at high acceleration [213]. Source components are kept in a vacuum tube to prevent scattering with gas atoms or particles in the air. X-ray sources are typically made up of a single element (i.e. copper or chromium) so that only one wavelength is generated when

an accelerated atom ejects an electron from the inner shell of the target atom [213]. This creates a spectrum which contains discrete energies characteristic of the target element [213]. Most intense X-ray scattering events occur when electrons fall from second (L) shell to the first (K) shell, which is called K_α radiation.

The theory of X-ray diffraction is well known and will not be covered in depth here. In general, X-ray diffraction is a combination of the scattering effects of each atom in a crystal. Further effects come from crystal defects, scattering from non-crystalline moieties, relatively large microvoids, and stacked lamellae [213]. The basics of XRD are established by the Laue conditions, which describe a unit cell in reciprocal space which has plane hkl consisting of integer values. This relationship can be used to derive Bragg's law:

$$\frac{1}{d} = \frac{2\sin\theta}{\lambda} \quad (2.13)$$

Where λ is wavelength, d is distance, and θ is scattering angle.

Geometrical representation of the allowed values of hkl is known as the Ewald sphere. A sphere of radius $1/\lambda$ intersects the scattering vector only when Laue conditions for diffraction are met [213]. The summation of the contribution to scattering of the repeat unit is called a structure factor and gives an idea of relative scattering intensity of different planes in the same crystal [213]. Other contributions to structure factor include Lorentz factor (diffraction time), polarization factor (degree of polarization induced by scattering), multiplicity factor (number of planes contributing to diffraction), temperature factor (thermal atom vibrations reduce diffraction intensities), and absorption factor (size and shape of specimen) [214]. Complicated polymer crystals make structure factor determination more complicated, thus empirical determination via experiments is often more useful [213].

On a scale larger than individual crystals, several features can be detected which scatter X-rays at small angles, in a technique referred to as small angle X-ray scatter-

ing (SAXS). Small angle scattering does not bear any dependence on the structural characteristics at atomic scale; it is a completely independent technique [214]. Fluctuations in electron density on the order of 30 to 1000Å determine small angle X-ray scattering events, and the highest contrasting species are either amorphous-crystalline transitions, or microvoids [214]. For example, repeating lamellar structures in semi-crystalline polymers produces a scattering event due to the higher density in comparison to non-crystalline regions in the polymer, therefore resulting in a higher electron density [213]. In this case, the scattering pattern depends on size as well as spacing and shape of the scattering elements. SAXS is commonly used to determine what is called the lamellar long spacing, or d-spacing, which is the equal to the distance between lamellar stacks, including thickness of the lamellae and thickness of the amorphous region separating them. Oriented polymers give more sharp peaks (i.e. less arcing) but SAXS peaks are broadened due both to disorder in crystalline regions and wide ranges of d-spacings; these two effects cannot be separated [213]. Voids can also be detected via this method, as they represent the highest contrast between the material, with density of nearly zero [213]. Small angle scattering events are defined to take place at angles between 2 and 3° [214]. SAXS experimental setup requires well-collimated incident X-rays so that scattered intensities of such small angles can be detected, and the experiment must take place under vacuum to eliminate scattering from gas atoms and particulates in the air, such as dust [213]. Furthermore, all wavelengths other than the desired characteristic radiation must be removed via monochromator to help improve accuracy of diffraction measurements [214].

on the other hand, wide angle X-ray scattering occurs at 2θ angles from around 3° to theoretically up to 180°, though it should be noted most polymer scattering events occur below 90° [214]. Methods for detecting small features via XRD (wide angle X-ray scattering or WAXS) include: rotation and oscillation methods for powder samples, moving film method for single crystals or powder photographs, and the diffractome-

ter method, in which a photographic film captures X-rays and their intensities and a counter records the number of such events [213]. For polymer structure characterization, several complicating factors exist compared to other materials. For example, weak secondary bonding means intensities decrease rapidly with increasing angle, meaning less reflections must be used for identification [213]. Also, oftentimes large, perfect crystals of polymers cannot be grown. Finally, the exact location of pendant atoms cannot be ascertained thereby causing decreased sensitivity of this technique to polymer structure characterization [213]. Despite these challenges, WAXD can be successfully used to determine preferred crystal orientation, if phase separation occurs in polymer blends, and which crystal form is present in polymorphic samples [213]. Though it is difficult to fully characterize the crystalline structure of polymers via XRD, it is often not necessary and in many cases tables exist which give reflections and relative intensities for many common polymers, for example though published by ASTM [213].

As mentioned previously, determination of preferred orientation of a semi-crystalline sample can be accomplished using XRD. Many polymer forming operations induce preferred orientation of polymer chains and crystallites, and it is well known that this causes enhanced mechanical properties. Therefore, it is useful to quantify how well oriented a polymer sample is. To do so, it must first be acknowledged that, within reciprocal space, perfect crystal lattice positions are represented by a diffraction spot. In contrast, fully random orientation is accompanied by a ring around the full range of 2θ values, as there is equal probability of finding diffracting species anywhere in the sample [214]. When moieties are mis-oriented to some degree, an arc forms instead. A plot of intensity versus azimuthal angle at specific 2θ values is created, and the shape of the curve correlates to the degree of orientation [213]. For crystalline texture determination in two dimensions (with respect to two different axes), pole figure analysis can be used. Pole figure analysis is based on the method of stereographic projection, meaning if a single crystal were placed at the center of a sphere, normal lines to each lattice plane family would intersect the sphere posi-

tions [213]. A stereographic projection to the south pole of the sphere is first made, and then the intensity of each projection is represented via a contour plot, in which a corresponding concentration of poles indicates high orientation [213]. Pole figures represent stereographic projections of only one crystal plane.

WAXS can also be used to determine crystalline fraction of polymer samples. Since polymers are generally neither fully amorphous or fully crystalline, scattering comes from both crystalline and amorphous regions. Assuming scattering amplitude is the same regardless of whether the atom lies in a crystalline or amorphous phase, the only difference in scattering from amorphous regions occurs due to weak constructive scattering in many directions, rather than the discrete constructive scattering which occurs due to crystalline regions [213]. Consequently, if the exact shape of the amorphous curve can be determined and thus separated from the crystalline peak, the ratio of intensity of crystalline diffraction intensity to that of the amorphous one gives the crystalline fraction in the sample [213]. Information can also be determined from amorphous region scattering. In general, amorphous regions result in scattering patterns consisting of a diffuse halo (or set of halos) which occur due to short range order inherent to distance between neighboring atoms in the amorphous phase [214].

2.6.2 Crystalline orientation factor

Calculation of quantitative crystalline orientation can be accomplished using WAXS data, by the following method. The Herman's orientation factor gives a quantitative representation of the degree of axial orientation between crystalline axis and a fiber reference direction:

$$f_{\phi} = \frac{1}{2}(3 \langle \cos^2 \phi \rangle - 1) = 1 - \frac{3}{2} \langle \sin^2 \phi \rangle \quad (2.14)$$

where $\langle \cos^2 \phi \rangle$ and $\langle \sin^2 \phi \rangle$ are the mean-square cosine and sine averages over all crystallites of the angle between crystal and reference axis [214].

This equation was extended by Stein to specify degree of orientation of all three crystal axes with respect to Z reference direction:

$$\begin{aligned} f_{a,Z} &= \frac{1}{2}(3 \langle \cos^2 \phi_{a,Z} \rangle - 1) \\ f_{b,Z} &= \frac{1}{2}(3 \langle \cos^2 \phi_{b,Z} \rangle - 1) \\ f_{c,Z} &= \frac{1}{2}(3 \langle \cos^2 \phi_{c,Z} \rangle - 1) \end{aligned} \quad (2.15)$$

If crystal axes are orthogonal,

$$\cos^2 \phi_{a,Z} + \cos^2 \phi_{b,Z} + \cos^2 \phi_{c,Z} = 1 \quad (2.16)$$

and therefore, from Equation 2.14,

$$f_{a,Z} + f_{b,Z} + f_{c,Z} = 0 \quad (2.17)$$

For any crystallographic axis, $\langle \cos^2 \phi \rangle = 1$ for perfect Z alignment, $\frac{1}{3}$ for random alignment, and 0 for perpendicularity. The value f therefore shows values of 1, 0, and $-\frac{1}{2}$, respectively.

To determine $\langle \cos \phi \rangle$ value experimentally, mean-square cosine values can be calculated from plane normals in a pole figure XRD experiment, or from corrected intensity distribution corresponding to this pole figure. The calculation proceeds as follows:

$$\langle \cos^2 \phi_{hkl,Z} \rangle = \frac{\int_0^{\frac{\pi}{2}} I(\phi) \sin \phi \cos^2 \phi \, d\phi}{\int_0^{\frac{\pi}{2}} I(\phi) \sin \phi \, d\phi} \quad (2.18)$$

The above equations were developed by Stein for polyethylene, which has an orthorhombic crystal structure and therefore requires integration of two crystal planes which are normal to two directions in the crystal cell. For other geometries, including when two orthogonal crystal planes are not obtained in XRD data, Wilchinsky has modified this expression as follows, so that $\langle \cos^2 \phi \rangle$ can still be calculated [214].

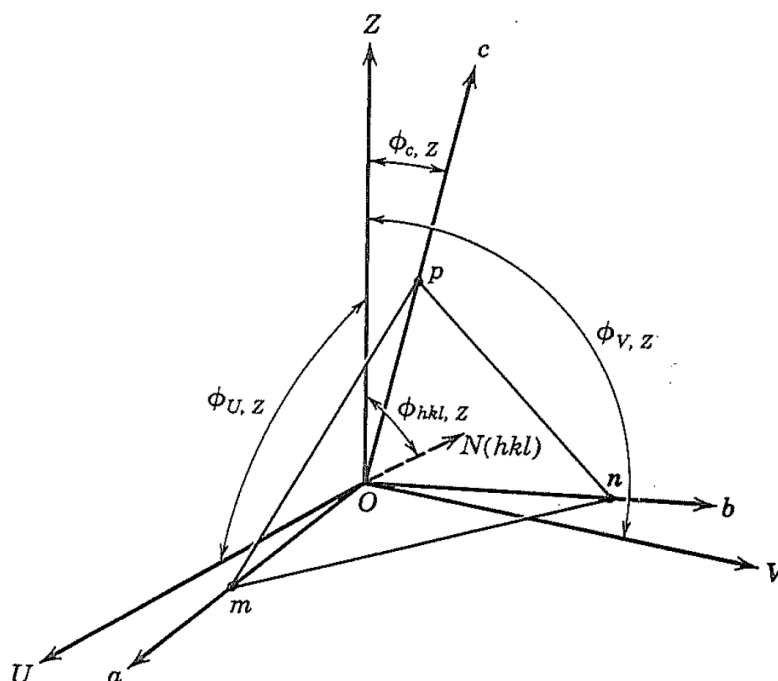


Fig. 2.14.: Relevant orientation directions for crystal cell via Wilchinsky method [214].

Where Z is reference direction in the sample specimen, a , b , and c are crystallographic axes, $N(hkl)$ is normal to reflecting planes with m , n , p intercepts, U , V , and c are the Cartesian coordinates where c is the crystallographic direction of interest. The crystal can be oriented in any direction with respect to U and V , with c co-incident with the Z direction (of interest). If Z and N are unit vectors in “ Z ” and “ N ” directions, e , f , and g are the direction cosines of N with respect to U , V , and c . Directions and relevant axes are shown in Figure 2.14.

From this description, the mean square cosine value of orientation of hkl plane with respect to the “Z” axis is calculated by:

$$\begin{aligned}
 \langle \cos^2 \phi_{hkl,Z} \rangle &= e^2 \langle \cos^2 \phi_{U,Z} \rangle + f^2 \langle \cos^2 \phi_{V,Z} \rangle + g^2 \langle \cos^2 \phi_{c,z} \rangle \\
 &+ 2ef \langle \cos \phi_{U,Z} \rangle \langle \cos \phi_{V,Z} \rangle + \\
 &+ 2fg \langle \cos \phi_{U,Z} \rangle \langle \cos \phi_{c,z} \rangle + \\
 &+ 2eg \langle \cos \phi_{c,z} \rangle \langle \cos \phi_{U,Z} \rangle
 \end{aligned}
 \tag{2.19}$$

This equation can be used in combination of data from six sets of planes to yield six equations with six unknowns, which are reduced to five unknowns by the orthogonality relationship:

$$\langle \cos^2 \phi_{U,Z} \rangle + \langle \cos^2 \phi_{V,Z} \rangle + \langle \cos^2 \phi_{c,z} \rangle = 1
 \tag{2.20}$$

The use of crystallographic symmetry and mirror planes for each respective crystal system are then used to reduce the equations further [214].

From experimental data obtained in this work, orientation factors were calculated using Wilchinsky method, with azimuthal scan of 2θ peak corresponding to the crystalline diffraction peak of interest corrected for background scattering by subtraction of azimuthal intensity of a peak significantly far away from any scattering.

2.6.3 Thermal characterization

Thermal polymer analysis can be accomplished via various techniques, including dynamic mechanical thermal analysis (DMTA), thermogravimetric analysis (TGA), thermal mechanical analysis (TMA), differential thermal analysis (DTA), and differential scanning calorimetry (DSC). DSC will be discussed in depth here, as it provides a useful, relatively simple way to measure thermal transitions of polymer

materials quantitatively. Usually, DSC employs a constant heating rate to measure material properties such as enthalpy or entropy changes. The experimental setup of DSC contains two sensors which are controlled by independent heaters that provide a flow of heat at constant heating rate [213]. A reference (empty) pan, usually made of aluminum, occupies one sensor, and the other contains the same pan geometry filled with a small (order of mg) amount of sample. The differential power input into each heater to maintain both the reference and sample pan at the program temperature is measured continuously and compared, and the output data is this differential power value plotted usually versus temperature [213]. Quantitatively, from an energy balance within the DSC system:

$$C_{p,s} = \frac{(Q_2 - Q - 1)m_s C_{p,c}}{(Q_3 - Q_1)m_s} \quad (2.21)$$

Where $C_{p,s}$ is specific heat capacity of the sample, m_s is the mass of the sample, $C_{p,c}$ is the specific heat capacity of a calibrant, $(Q_2 - Q_1)$ is the difference in heat between sample and reference, and $(Q_3 - Q_1)$ is the difference in heat between the calibrant and reference [213]. Integration of these curves plotted versus temperature gives enthalpy changes of the sample during the heating and/or cooling cycle(s). For polymer characterization, DSC is most useful for determining thermal transitions and percent crystallinity. Glass transition temperature (T_g) can be determined via several techniques, such as DTMA and DTA or DSC [213]. However, since T_g is a kinetic variable, its exact value depends on heating rate and method; thus it varies with the technique used to measure it [213]. Thermal history has an effect on thermal properties and also aging of polymer materials alters their thermal behavior due to the fact that the material densifies, causing specific volume and enthalpy to come closer to equilibrium values [213]. These effects must be taken into account before comparing absolute values of T_g between polymer samples. T_g is represented by a slope change in the heat capacity versus temperature curve obtained by DSC technique [213]. Crystalline

melting temperature is also not an absolute value, as it increases with increasing molecular weight and crystallinity. Further, larger crystals melt at a higher temperature, and vice versa, and some crystalline forms of polymorphic materials melt at different temperatures as well. Thus, breadth of melting peak is also important in determining the extent of size or perfection variation in crystalline regions [213]. Also, cooling speed affects crystal formation in polymers. When a polymer is quenched, upon reheating it will show a small pre-melting peak below the main melting transition, which represents crystals forming that did not have enough time or energy to do so in the initial cooling event [213]. By heating, cooling, and then reheating a polymer sample at a controlled, constant heating rate, the thermal history of the polymer can be erased to allow for properties inherent to the polymer material to be determined. The enthalpy of fusion is measured by integrating the endothermic melting peak in the heat capacity versus temperature curve. Percent crystallinity can also be determined from DSC experiments by comparing the measured enthalpy of fusion of melting to the theoretical enthalpy of fusion of a completely crystalline sample of the same polymer [213]. Since samples of this kind are nearly impossible to prepare, this value can be approximated using the Flory equation, and is typically available in the literature for many common polymers [215]. Quantitative percent crystallinity analysis of heat capacity data can be calculated using the following equation,

$$C_p = C_{p,c}f_c + C_{p,a}(1 - f_c) \quad (2.22)$$

Where C_p is heat capacity, f_c is crystalline fraction and subscripts c, a stand for crystalline and amorphous phases [213].

2.6.4 FTIR

Vibrational spectroscopy entails detection of energy level transition in molecules, resulting from interatomic bond vibration, and can provide detailed structural char-

acterization for many materials, including polymers. At room temperature, electrons are in their ground state and electromagnetic energy absorption may cause changes or transitions in these energy states [213]. Infrared spectroscopy involves molecular vibrations due to changes in electron distribution within a bond, resulting in a change in dipole moment [213]. When incident electromagnetic radiation with wavelength ranging from 2.5 to 25 μm (or wavenumber of 4000-400 cm^{-1}) in the infrared range (IR) is in phase with these vibrating dipoles, energy is transferred from radiation to the molecule [213]. IR spectrometers scan wavelength while continuously monitoring changing light intensity to determine when such electron elevations occur, resulting in a peak in the spectrum [213]. Characterization via IR spectroscopy relies on the principal that specific bond groups within a molecule absorb IR radiation in specific wavelengths, with little coupling. IR absorption frequencies are nearly constant, and absorption bands for a specific chemical bond will appear in the same general region of IR spectra regardless of sample [213]. Coupling can be useful in making distinctions between very similar molecules. For example, a blend of polypropylene and polyethylene spectra are superimposed from the homopolymer, whereas a copolymer of ethylene and propylene shows a different spectrum due to intrachain coupling [213]. Quantitative analysis of IR spectra can be accomplished using by application of the Beer-Lambert Law,

$$A = \text{Log} \frac{I_o}{I} = \epsilon cl \quad (2.23)$$

Where A is absorbance, I_o is incident light intensity, l is depth of absorbing medium at which I light intensity occurs, c is concentration of absorbing species, and ϵ is extinction coefficient.

If the extinction coefficient for material at a specific wavelength is known, concentration of the IR absorbing species can be determined, which works well for polymers in solution. However, quantitative analysis of solid polymer samples can be misleading, as absorption depends on other factors such as sample thickness, inhomogeneous distribution of additives, and extraneous light scattering [213]. Therefore, for polymers

it is more relevant to do quantitative comparison, unless a second detector is available containing a known reference standard which can be compared to the sample to be identified at the same time [213].

The hardware for IR spectrometry includes a double beam setup, in which a source (usually mercury bulb) emits radiation over the full IR electromagnetic range [213]. Two monochromators (i.e. double beam method) are used to maintain photon energy over the full range of wavelengths, and to reduce interference and absorption from materials other than the sample (i.e. lens, window, water vapor in air) [213]. Absorption of radiation is therefore the only difference in intensity of the two beams and is measured using optical null method [213]. Fourier transform infrared spectroscopy, or FTIR, is commonly used for rapid sampling and produces an interferogram which is converted to an absorption spectrum using Fourier transform mathematics, hence the name. In this technique, the light source passes through a Michelson interferometer which contains two mirrors, one fixed at 45° and the other moveable [213]. The light beam is then partially reflected and partially transmitted, and the two beams recombine at the beam splitter [213]. Then, the beam is passed through the sample and to the detector. The moveable mirror moves axially due to relative phase displacement of destructively scattered light, creating an oscillatory pattern known as an interferogram that represents the distribution of spectral absorption signal that reaches the detector [213]. As mentioned above, this interferogram is then converted to absorption spectrum mathematically by using a Fourier transform.

2.6.5 Atomic force microscopy (AFM)

Atomic force microscopy operates on the basic principle of repulsive forces generated by a very small, nano-sized probe interacting with a nonconducting surface, such as a polymer. The AFM probe follows the surface of the sample by either constantly (contact mode) or intermittently (tapping mode) contacting it. Besides mapping the

surface of materials down to very small, atomic scales, AFM is useful for measuring a range of properties of nonconducting materials, including adhesion, topography, and mechanical properties [216]. Because constant contact mode can damage soft materials, tapping mode is generally more useful for imaging polymer surfaces [216]. In AFM tapping mode, the probe oscillates at constant vibration amplitude at its resonance frequency, intermittently contacting the sample surface [217]. In the physical setup, a piezoelectric element causes the tip to vibrate at such frequency, and (in tapping mode) damping of this amplitude caused by the magnitude of energy dissipated due to attractive or repulsive forces from the sample to the tip causes feedback, which is measured from a laser focused on the tip [216]. This laser beam reflects on a photodetector, which measures torsion and bending, deflection, or oscillation of the cantilever [216]. The sample is moved back and forth horizontally under the tip, as vertical motion is controlled by a feedback loop in order to maintain constant amplitude of the tip's oscillation; this allows for a constant force on the sample surface [216].

Since relatively soft materials have varying degrees of sample hardness, tapping mode has also been adapted to adjust to these considerations, to prevent damage. Adjusting the driving and set point amplitude, which effectively changes the tip-to-sample force, allows force applied to the sample to vary, not only to protect delicate samples from damage, but it can also be used to distinguish between “soft” (low density or elastic modulus) and “hard” (high density or elastic modulus) features, such as amorphous and crystalline regions in polymers, respectively [216]. It is noted also that height contrast shows only minor, if any, changes in features in tapping mode; thus phase contrast is much more relevant to this discussion [216]. Specifically, phase images measure change in oscillating frequency of the probe due to attractive or repulsive interactions with the sample's surface [216]. Furthermore, the ratio of amplitude set point (A_{sp}) to driving amplitude (A_o) can be used to quantify the tapping force. According to Magonov and Reneker, when $\frac{A_{sp}}{A_o}$ ratio is high (0.8-0.9) phase shifts between regions of varying stiffness are relatively small, and this is referred to as light

or soft tapping [216]. Ratio of $\frac{A_{sp}}{A_o}$ from 0.8 - 0.3 is considered moderate tapping, and phase shifts become more pronounced such that materials with higher density (stiffness) appear to be brighter. At hard tapping conditions, $\frac{A_{sp}}{A_o}$ less than about 0.2, high density regions appear darker as phase contrast is reversed. This phenomenon is speculated to occur because the tip spends more time in contact with the soft surface in hard tapping mode compared to when tapping force is lighter [216]. Thus, tapping mode in AFM is a useful tool for imaging soft materials, such as polymers, and mapping adhesion and mechanical properties of materials with features in the range of 1 to 100 nm.

3. MICROLAYERED PET/PVDF FILMS: MECHANO-OPTICAL BEHAVIOR IN UNIAXIAL EXTENSION

This study combines real time mechano-optical measurements during uniaxial stretching of 32L microlayer PET and PVDF films (50:50 vol% ratio) with offline characterization techniques of DSC, FTIR, WAXS, AFM, and SAXS to obtain a complete picture of changing morphology during orientation. Since ideal processing temperatures for PET and PVDF do not match, an initial processing study was conducted over a wide range of stretching temperatures. From this, optimum processing temperatures were selected, and mechano-optical behavior during deformation was obtained. To elucidate morphology changes during deformation, a series of samples of systematically varying deformation were produced and structurally characterized. These studies confirmed PVDF crystal form transformation from α to β when films were stretched at 95°C, and presence of γ -PVDF due to annealing effect when stretched at 185°C where it is in molten state, sandwiched between solid PET layers. Dielectric properties showed that films stretched at 150°C exhibit low dielectric constant when PVDF phase consists of spherulites and smaller, broken up fibrils, but dielectric constant is higher when PVDF is arranged in long, highly ordered fibrils. Lower dielectric loss was observed after stretching to any amount, but at very high draw ratios (3.5X1) it was significantly decreased further, likely due to smaller, broken up PVDF crystallites which can more easily respond to changes in electric field, thereby lowering dielectric losses. PET morphology does not have a strong correlation with dielectric constant, but higher PET crystallinity and orientation likely helps to lower dielectric losses.

3.1 Introduction

Polymers are a unique class of materials because they are lightweight, generally more affordable, and consume less energy to process than other materials (i.e. metals or ceramics). Additionally, they are highly versatile, with the ability to be tailored to very specific property requirements and applications. Furthermore, when one polymer's properties will not suffice, they can be combined together via, for example, copolymerization, blending, or microlayering and/or with non-polymeric materials such as fillers or coatings to form nanocomposites. These techniques allow for synergistic combination of material properties for specific, engineering applications and each have inherent pros and cons. Blending of polymers with nanofillers can be expensive and has many process parameters to tune, as well as complicated multi-step lamination processes. Copolymerization can be used to combine polymers or add specific chemical groups to polymer chains, but often requires complex synthesis, trial and error, and can result in low yields. Microlayer coextrusion is another option to combine two or more polymers into one film in order to take advantage of each materials' properties, which has many benefits such as flexibility of process parameters and ability to combine two or more polymers into very thin, distinct layers.

Microlayer coextrusion, or Layering Feedblock Technique, was first developed in the 1960s by Harder at Dow Chemical Co. as a way to force hundreds or thousands of polymer layers into a single thin film using their patented interfacial surface generator method [55]. This technique combines polymer melt streams in a traditional feedblock then into one or more layer multiplication dies which cut, spread, and stack the melt stream, thereby multiplying the number of layers [56]. Advantages of this technique include modular design which simplifies process modification, the ability to add a third tie layer for improved interfacial adhesion or a sacrificial skin to protect the film during processing and post-processing, and flexibility to create both vertical and horizontal layers, with either a single or variable thickness "gradient" structure [56]. Furthermore, it is a single, continuous process and has been used to create films with

more than 8000 layers, with individual thicknesses on the nano-size scale. The unique structure of micro- or nanolayer films has found applications in food packaging, optics, and dielectrics (to name a few) [56].

Of specific importance to this work is the combination of polymer materials to improve properties for dielectric films in next generation capacitors. Polymers were first used as dielectric materials in the 1950s to replace insulating materials such as mica and paper [61]. With the clear advantage of very high dielectric breakdown strength and low dielectric loss, biaxially oriented polypropylene (BOPP) has been the state-of-the-art polymer dielectric material for over 20 years [61]. By itself, polypropylene does not make an excellent dielectric material, but the semi-crystalline nature of this polymer allows for further electrical property enhancement due to tailored morphology by biaxial orientation, giving it an energy density of around 1.2 J/cm^3 (and energy density at breakdown of 5 J/cm^3) with maximum usage temperature of 85°C [60]. New, high-tech applications such as hybrid vehicles and photovoltaics require thinner, longer lasting, and more thermally stable electronic capacitors, and the dielectric material is often the limiting factor to achieving these goals. BOPP dielectrics alone cannot meet growing technological capacitor needs, and therefore it is desired to replace this material with one containing high dielectric constant and breakdown field strength, low dielectric loss, and high temperature usage capabilities. In many cases, improving one of these properties debilitates the other(s); thus it has been accepted that any economically feasible improvement in current dielectric material properties would be considered a success [61].

For this study, microlayering process was chosen as a way to combine two semi-crystalline polymer materials - one with high breakdown strength, Poly(ethylene terephthalate) (PET), and one with high dielectric constant, Poly(vinylidene fluoride) (PVDF) - in hopes to take synergistic advantage of both materials' properties, with a focus on processing conditions to understand how mechanical and dielectric properties are affected by morphology. PVDF has the strongest piezoelectric and

pyroelectric responses, as well as one of the highest dielectric constants of any known polymer material, making it an obvious choice for dielectric applications [23]. However, PVDF cannot be used as the lone dielectric material due to extremely high hysteresis, low breakdown strength, and high losses [24]. PVDF is unique in that it is polymorphic and exhibits (at least) four different crystal structures, specifically α , β , γ , and δ -forms. Form II, or α -PVDF, occurs quiescently from the melt and results in anti-parallel chains with zero net dipole moment [23]. Form I, or β form, has all-trans chains in a helix-like structure with dipoles pointing in the same direction, making it the most polar and electrically active crystal form of PVDF and the one of interest to piezoelectrics [23]. γ and δ -forms are less common, but can be made by annealing or high electrical stresses [24]. Since PVDF has a very high crystalline fraction (about 50% on average), understanding the effect of crystal forms on final dielectric and mechanical properties is crucial. PET, on the other hand, contributes high breakdown strength, as well as relatively low electrical losses to the film system. PET is very different from PVDF because it is a slow crystallizing polymer (due to its stiff backbone and bulky aromatic groups) with relatively high T_g (glass transition temperature) in comparison to PVDF. Slow crystallizing polymers are processed in the rubbery region - between T_g and T_{ll} (liquid-liquid transition temperature) - and away from T_{cc} (cold crystallization temperature). This maximizes strain hardening and minimizes thermally induced crystallization, promoting thickness uniformity in the film [72], [218]. PP is also a slow crystallizing, semi-crystalline polymer, and one of the reasons it is an excellent dielectric material is that biaxial orientation process produces a uniform, semi-crystalline morphology which has been proven to increase electrical breakdown strength [219], [218]. PVDF, on the other hand, is a fast crystallizing polymer due to its non-bulky, flexible chains and should be oriented in the partially molten state to ensure affine-like deformation [72]. Therefore, processing strategy for these two polymers is very different and the main focus of this study was to determine which processing conditions produce usable films with morphology favorable to enhancement of dielectric properties. A systematic focus on processing conditions in uniaxial

extension was conducted in this study to determine the effects of on morphology of these complex microlayer films, with select samples tested for dielectric properties. Later works (see Chapter 4) will focus on larger and/or biaxially stretched and heat set samples with the intent to further link processing-morphology-dielectric property relationships.

The microlayer coextrusion process has been studied previously as a method to improve polymer properties. Specifically for dielectrics, researchers have combined high dielectric constant polymer in one layer and high breakdown strength in the other. Furthermore, PVDF is a popular solution for this method because it is relatively easy to process and, again, has the highest known dielectric constant among polymers. Recently, Mackey, et al. showed that microlayered films of polycarbonate (PC) and poly(vinylidene fluoride) (PVDF) homopolymer showed higher breakdown strengths, as well as different breakdown mechanisms (treeing versus single hole) in comparison to control films [200]. Furthermore, dielectric properties were enhanced by taking advantage of the barrier effect, where microlayer film interfaces act as a barrier to charge propagation, which would ordinarily lead to dielectric breakdown in the film [201]. Researchers also tested polyvinylidene fluoride-co-hexafluoropropylene (P(VDF)-HFP) / PC in microlayer coextrusion for dielectric property enhancement [201], [202], [203]. P(VDF-HFP) has better processability and lower melting temperature than PVDF but also has lower usage temperature and lower dielectric constant. These studies found that decreasing layer thickness improved energy density of nanolayer films and that the dielectric strength value fit a series model for individual layers, giving the composite film a relatively high breakdown strength overall [201], [202], [203]. Zhou, et al. also studied use of a tie layer to promote interfacial adhesion between PC/P(VDF-HFP) layers in dielectric films [204]. This work found that, when a tie layer was used that strongly interacted with both materials, a 25% increase in breakdown strength was observed, as well as lower dielectric losses [204].

Post-processing of micro- or nanolayer films, including uniaxial and biaxial orientation and/or heat setting is another strategy which has been explored for further dielectric property improvement. The tenter frame biaxial orientation process is currently used to produce BOPP for dielectric films. Researchers have attempted to mimic this process for microlayer films to determine how it affects polymer morphology, and further how this morphology affects final film properties. Notably, by varying number of layers and volume ratio of PET and P(VDF)-HFP copolymer and measuring structural changes during deformation via in-situ wide angle X-ray scattering, Jordan et. al showed that confined crystallization of PVDF copolymer gives in-plane, single crystal-like structure, leading to higher overall percent crystallinity and modulus of the films after biaxial orientation and melt recrystallization [207]. Several other studies exploring effects of biaxial orientation on dielectric properties exist [177], [208], [2] but will not be discussed in depth here, since the current work does not involve biaxial orientation or heat setting. The main takeaway, however, is that biaxial orientation of microlayer films reduces film thickness which increases capacitance and overall energy density, and can lead to unique morphology development via confined crystallization. Heat setting allows films to be used at high temperature without shrinking by improving thermal stability and can be used to further tailor morphology development.

Though studies involving the orientation of similar microlayered polymer systems containing PET or other high breakdown strength polymer, and PVDF or its co-polymers exist, ours is unique in the ability to measure changes in true stress, true strain, and birefringence in real-time, providing a more complete picture of how molecular mechanisms (such as orientation, crystallization, and relaxation) change during the stretching process. This study also attempts to obtain a more detailed understanding of complex morphological developments of microlayer films in uniaxial orientation, which is lacking in the literature. In the present study, we investigate how uniaxial orientation of microlayered film consisting of alternating layers of PET and PVDF

can be used to enhance electrical properties by creating tailored morphologies during film deformation.

3.2 Materials and experimental procedures

The polymer materials used in this study were Laser+ C 9921 (F65A) poly(ethylene terephthalate) (PET) from DAK Americas (IV 0.80 dL/mg as specified by the supplier), and Solef 6008 homopolymer poly(vinylidene fluoride) (PVDF) from Solvay. All materials, as well as microlayer cast film consisting of 32 alternating layers of these two materials in a 50:50 vol% PET:PVDF ratio, were provided to us by PolymerPlus. Films were produced at a coextrusion temperature of 260°C and cast onto a chill roll kept at 85°C. The films had an initial thickness of approximately 125 μm and were laminated with polyethylene (PE) skin layer to protect during extrusion and prevent damage to the film during storage and handling. This PE layer was removed before subjecting the film to additional processing or testing.

Our instrumented, custom-built uniaxial stretcher was used to measure mechano-optical properties of polymer samples in real time during stretching experiments. Measurements of optical retardation and sample width at the exact center of the film allow for calculation of film thickness and therefore true stress, true strain and birefringence values (at 546 nm wavelength) in real time during stretching. These calculations assume the following:

1) simple extension

$$D_t/D_o = W_t/W_o \quad (3.1)$$

2) incompressibility

$$L_o W_o D_o = L_t W_t D_t \quad (3.2)$$

Using these assumptions, the following parameters are calculated as follows:

Thickness:

$$D_t = (W_t/W_o)D_o \quad (3.3)$$

Birefringence:

$$\Delta n = R/D_t \quad (3.4)$$

True strain:

$$L_t/L_o - 1 = (W_o/W_t)^2 - 1 \quad (3.5)$$

True stress:

$$F_t/(W_t D_t) = F_t/[(W_t^2/W_o)D_o] \quad (3.6)$$

Where R is retardation, Δn is birefringence, D_o , W_o , L_o are initial thickness, width, and length respectively, and D_t , W_t , L_t , F_t , are time variations of thickness, width, length, and force.

Further details of this machine are listed elsewhere [77], [209], [220].

Films were cut into a dogbone shape (67 x 81 mm overall dimensions) using a die cutter to ensure size uniformity. A fluorescent yellow dye was painted on samples in a four-dot pattern for tracking via CCD camera, allowing for measurement of local true strains in both the machine and transverse sample directions. Films were stretched to 5.5X at 10 mm/min, then held taut and quenched by blowing cold air until they reached room temperature (30 minutes). Stretching was first conducted over a range of temperatures to get an idea of behavior based on different morphological starting states of each polymer. Afterwards, the films were stretched at three select temperatures (95, 150, and 185°C) and constant rate (10 mm/min) to a series of stretch ratios, then quenched to produce films for offline structural characterization.

For continuous calculation of birefringence, real time thickness has to be evaluated. To do so, real-time film thicknesses predicted by both the camera (using a four-

point image method) and laser measurements (via mid-plane width monitoring) were compared to that measured offline with a digital micrometer. It was found that, using the machine's basic assumptions, calculated thickness values were incorrect. This was corrected by only assuming incompressibility and performing a volume balance using length and width values obtained from camera measurements at each data point. Comparison of corrected and predicted thicknesses versus actual measured values can be seen in Appendix A Figure A.1.

After stretching, select films were delaminated into separate layers so that PVDF layers could be studied individually. This was done by applying tape and mechanical force to the films to force immiscible layers apart. FTIR-ATR data was run on single layers to verify successful delamination, as shown in Appendix A Figure A.2.

Thermal properties were measured on film control and samples after stretching using TA Instrument Model Q2000 differential scanning calorimeter using a heating rate of 10°C/min, in dry nitrogen environment. Percent crystallinity of each material was calculated using enthalpies of heat of fusion for 100% crystalline polymer, ΔH_o of 105 J/g for PVDF and ΔH_o of 140 J/g for PET [221], [144].

Wide angle X-ray diffraction patterns were obtained using Bruker D8 Quest diffractometer with kappa geometry, an I- μ -S microsource X-ray tube, laterally graded multilayer (Goebel) mirror single crystal for monochromatization, and Photon2 CMOS area detector. The generator was operated at 50 kV at current of 1 mA, beam was monochromatized at Cu K-alpha radiation ($\lambda = 1.54178 \text{ \AA}$) and samples were irradiated for 1 minute. Small angle X-ray scattering patterns were obtained using an Anton Paar SAXSpoint 2.0 machine containing microfocus Cu K-alpha radiation, $\lambda = 1.54178 \text{ \AA}$, source and two dimensional, Eiger R hybrid photon-counting detector. Generator was operated at 50 kV at current of 1 mA, and samples were irradiated for 15-30 minutes, depending on their thickness. Single layer PVDF SAXS samples were irradiated for 6 hours. SAXS and WAXS images were taken in both film normal (through film thickness) and transverse directions.

FTIR measurements were taken on Thermo Nicolet Nexus FTIR, with diamond ATR, a KBr beam splitter, and an MCT detector with 0.125 cm^{-1} spectral resolution.

Atomic force microscopy images (AFM) were taken on Veeco Dimension 3100 AFM and images were processed in Gwyddion software. This machine has X,Y scan range of 90 m square, with lateral accuracy between 1-2%. The Z-range is $5\text{ }\mu\text{m}$ and resolution is 16-bit. Measurements were performed in tapping mode using variable drive voltage to optimize tapping conditions for each individual sample.

3.3 Results and discussion

3.3.1 Selection of processing temperature

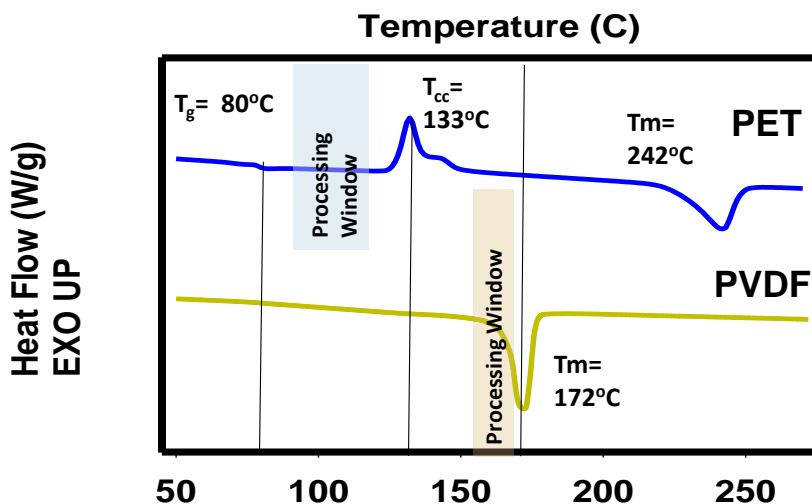


Fig. 3.1.: DSC for individual PET and PVDF materials, with highlighted regions for ideal processing temperatures of each.

Figure 3.1 shows individual DSC curves for PET and PVDF materials, with thermal transitions identified. PET is a slow crystallizing polymer, which is typically quenched to glassy state during casting, and should ideally be processed between

glass transition temperature (T_g) and onset of cold crystallization peak (T_{cc}), where it is in the rubbery state. PVDF is a fast crystallizing polymer, always obtained in semi-crystalline state, and should be processed in partially molten state. Highlighted ideal processing windows for each material are identified, and do not match, making identification of processing conditions for the microlayer film difficult.

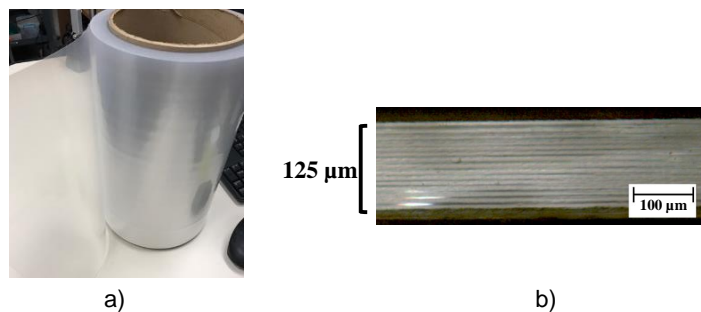


Fig. 3.2.: 32-layer film (a) roll as received and (b) optical microscope cross-section image.

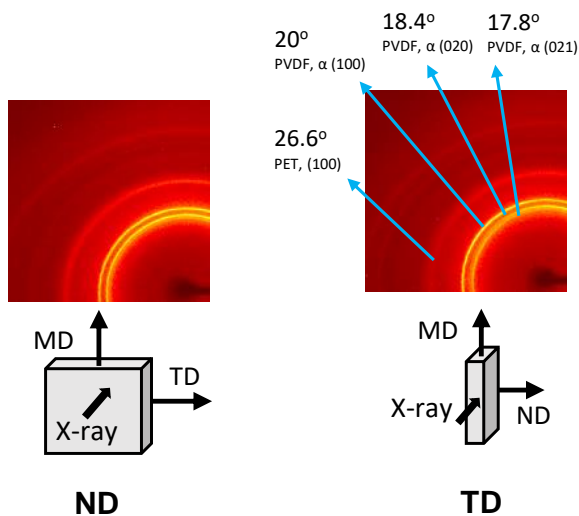


Fig. 3.3.: Characterization of 32-layer film as received via WAXS.

To ensure layer integrity was maintained in the microlayered film in its as cast state, optical microscopy was conducted on the film's cross-section, as shown in Figure 3.2 b. Characterization of starting morphology was investigated via wide angle X-ray scattering (WAXS), with peaks corresponding to crystal planes of interest shown in Figure 3.3. Thermal characterization of the film as received is shown in the DSC curve in Figure 3.4, highlighting the different morphological states of each material in specific temperature ranges; an important item to note when selecting stretching temperatures. Since PET and PVDF are immiscible, the DSC curve in Figure 3.4 shows distinct thermal transitions for each polymer separately and morphology in each of these temperature ranges will be described in more detail in the following sections.

Between PVDF and PET's T_g

PVDF has a glass transition temperature (T_g) near -35°C and, since it is a highly crystalline polymer, this temperature is not relevant to processing of this material; therefore, it is not shown on DSC curve in Figure 3.4. Below T_g of PET, it is glassy and exhibits necking, whereas PVDF remains semi-crystalline, which is not ideal for either material. This morphological region is shown in Figure 3.4a, and is not relevant for processing of either PET or PVDF.

Between T_g and T_{cc} of PET

Since it is a slow crystallizing polymer, PET can be quenched into amorphous state, and therefore, processing should be done in the rubbery state between T_g of 81°C and before onset of cold crystallization temperature (T_{cc}), near 120°C . The temperature region for processing PET in its rubbery (ideal) state is shown in Figure 3.4b. In this temperature region, PVDF is in solid state with a high degree of crystallinity

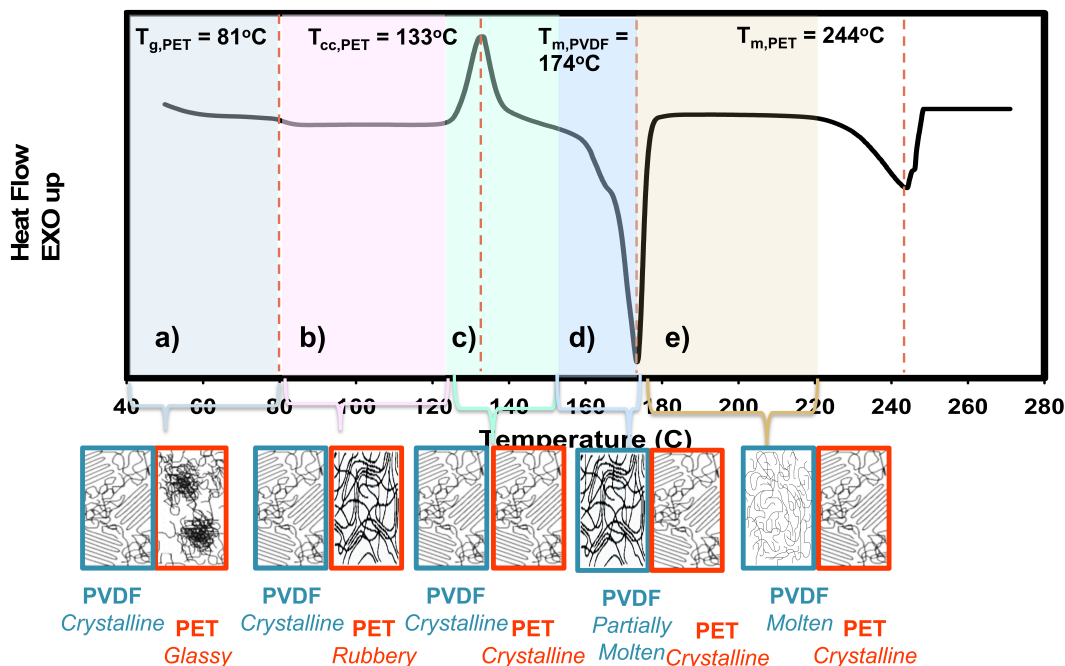


Fig. 3.4.: Cartoon representation of different morphological states of each polymer in different regions of the DSC curve. In (a) PVDF is semi-crystalline, PET is amorphous and glassy, (b) PVDF is semi-crystalline, PET is amorphous and rubbery, (c) PVDF and PET are semi-crystalline, (d) PVDF partially molten, PET semi-crystalline and (e) PVDF fully molten, PET semi-crystalline.

(around 50-70% typically), and may exhibit yielding and thickness non-uniformities during stretching.

Between T_{cc} and onset of PVDF's T_m

In Figure 3.4c, after onset of T_{cc} , thermal crystallization of PET changes morphology of this material from rubbery amorphous to semi-crystalline, while PVDF remains in semi-crystalline state up until onset of melting, around 150°C . Although PVDF can be processed in this temperature window, high stresses of solid state deformation make it non-ideal for orientation.

Passing through PVDF peak T_m

Fast crystallizing nature of PVDF means it cannot be quenched into amorphous state and therefore ideal processing window is between onset of melting ($T=150^{\circ}\text{C}$) to peak melting point (T_m peak = 174°C). Typically, the ideal processing temperature for fast crystallizing polymers is 1/3 of the way between these two values- for this grade of PVDF the ideal processing temperature is 158°C , as shown in Figure 3.4d. In this temperature range, PET remains semi-crystalline (not ideal for processing).

From T_m PVDF to before onset of PET's T_m

Passing through the end of melting of PVDF, the material will be fully molten. Typically, processing of this material could not be done in this range. However, it will be shown later in this work that the PET layers, which remain in solid state, retain enough strength to facilitate stretching of this material at temperatures above PVDF's equilibrium melting point. Onset of melting for PET does not occur until around 220°C , so the temperature range in which PVDF is fully molten and PET is still semi-crystalline is broad, as shown in Figure 3.4e, though processing of neither material is ideal.

3.3.2 Uniaxial Stretching

As described in the previous section, each stretching temperature range is associated with unique morphology for each material. To study the effect of starting state on final morphology of PET and PVDF after stretching, films were first stretched uniaxially at 10 mm/min to 5.5X their initial length at several temperatures ranging from 95°C (where PET is rubbery and PVDF is in solid state) to 200°C (where PET is semi-crystalline and PVDF is fully molten). True stress versus true strain curves are shown

in Figure 3.5, with dashed vertical lines representing onset of strain hardening point. Strain hardening point was determined by taking the derivative of true stress, true strain curve and locating an inflection point after yielding.

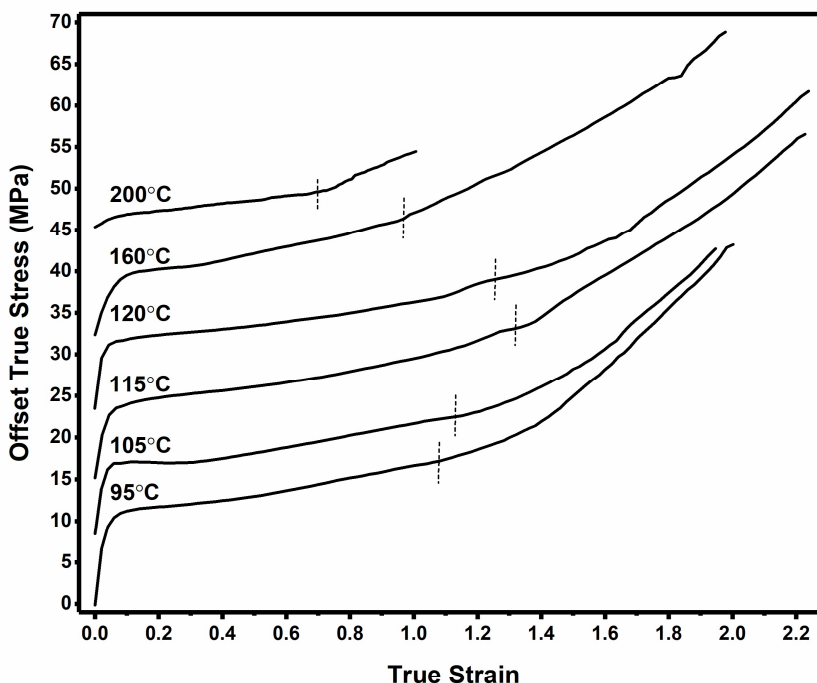


Fig. 3.5.: True stress, true strain curve for 32 layer sample stretched uniaxially at several different temperatures. Dashed vertical lines represent onset of strain hardening. All curves are offset by 8 MPa, except for 200°C sample, which is offset by 13 MPa.

As stretch temperature decreases, the strain value at onset of strain hardening increases as stress increases until the 105°C curve, where the trend reverses. The peak melting temperature of PVDF is around 174°C and onset of melting occurs at about 150°C according to DSC data of the film as cast. Therefore, when stretching in this temperature range, PVDF will have a range of partially molten fraction, which increases with increasing temperature. Initial percent crystallinity of PVDF in the film as cast is about 45%, which is very high compared to the PET layers that are

amorphous in as cast state. Stretching in the partially molten state causes crystalline regions to stretch, break up, and reorient, ultimately leading to highly oriented, highly crystalline PVDF layers. In this temperature range, PET is still semi-crystalline and as temperature decreases, effects of thermally induced crystallization decrease.

The four lowest stretching temperatures (between 95 and 120°C) all fall in the region between T_g and T_{cc} of PET. Slow crystallizing polymers are ideally processed in this region such that the material is still in the rubbery amorphous state, but avoids thermally induced crystallization below T_{cc} because the halftime of crystallization at these temperatures are very long, in the range of hours to days. It is well known that thermal recrystallization causes sample necking, thereby resulting in thickness non-uniformity [72]. Thus, at the high end of this processing temperature range, we expect competition between thermal crystallization (tending to decrease strain at which strain hardening occurs) and ease of orientation of the rigid PET chains. In fact, this is observed when the trend of increasing onset of strain hardening point with decreasing stretch temperature reverses between 115°C and 105°C as shown in Figure 3.5. PVDF is semi-crystalline in this temperature range, being far from both its T_g (around -35°C) and T_m , and possesses high configurational entropy due to its small, flexible structure, making it likely to strongly resist deformation. As entropy increases with stretching temperature, OSH shifts to later true strain values.

From this information, we chose to focus on three main stretching temperatures (95, 150, and 185°C) to further investigate the effects of initial morphology of PET and PVDF on structure development during stretching. 95°C is ideal for processing PET, though PVDF is highly resistant to deformation. 150°C is a unique processing temperature because both PVDF and PET (already past T_{cc}) are solid-state, with PVDF on the verge of being partially molten. At 185°C PVDF is fully molten, and its morphology is not shaped by deformation of previous semi-crystalline regions, whereas PET is semi-crystalline and should behave similarly to the 150°C condition, with the

added effects of decreased stress and increase in rate of thermally induced crystallization.

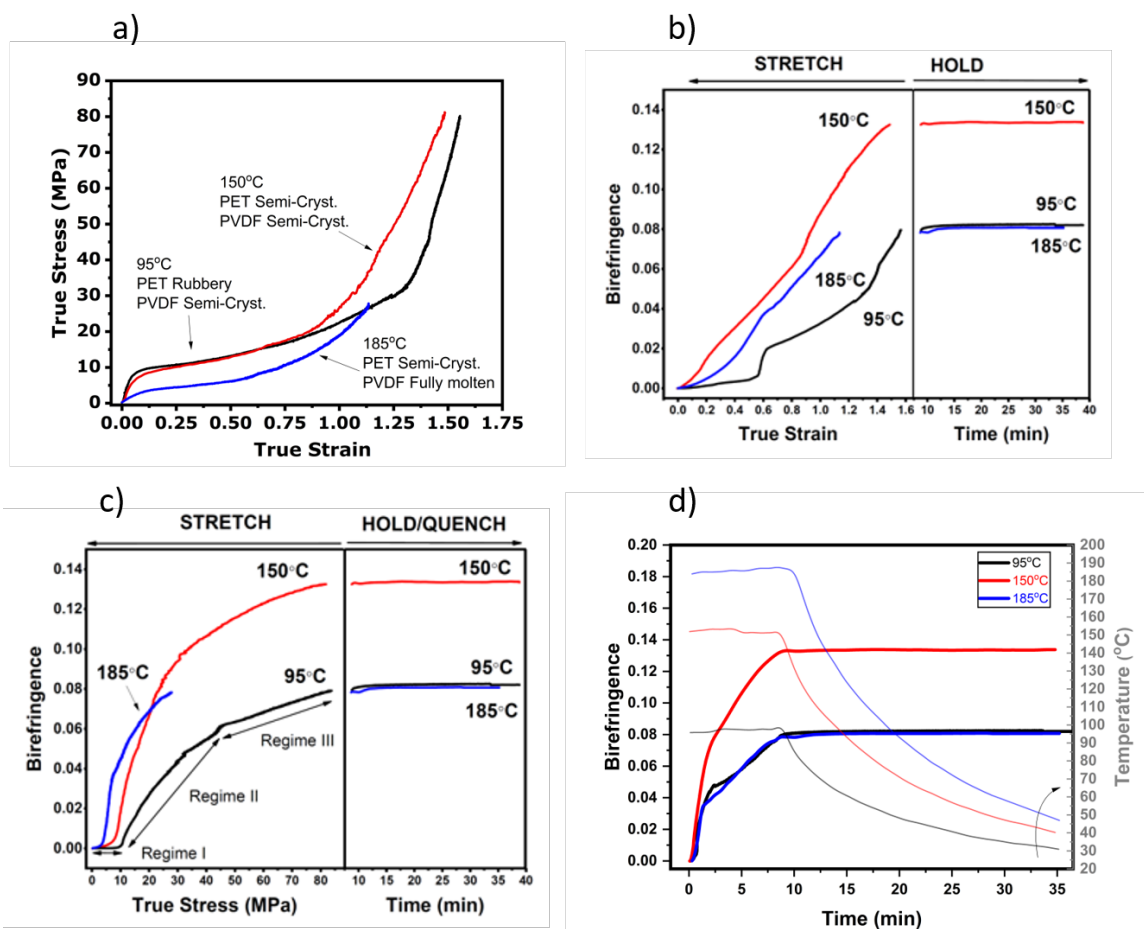


Fig. 3.6.: a) Stress strain, b) strain optical, c) stress optical and d) birefringence, time data for films stretched 5.5X uniaxially at 10 mm/min and 95, 150, and 185°C then quenched with cold air for 30 min.

Figure 3.6a shows true stress, true strain behavior for films stretched at 95, 150, and 185°C. At 185°C, the film exhibits affine deformation, and onset of strain hardening occurs very early, leading to low overall stretchability. At 95°C, significant necking was observed, delaying onset of strain hardening point. Stretching beyond onset of strain hardening leads to decreased surface roughness and thickness uniformity after stretching, thus it is an important mechanism for assuring film quality [14], [72], [218].

Therefore, if onset of strain hardening occurs too late in the stress strain curve, films may have uneven thickness profiles and rough surface after stretching. Interestingly, stress strain behavior when film is stretched at 150°C shows a dramatic change in slope following the onset of strain hardening. This usually indicates some significant change in morphology. One way to confirm this is by plotting birefringence versus true stress and true strain curves, as shown in in Figures 3.6b and c, in which the 150°C curve reaches higher overall value of birefringence by far compared to the other two conditions. Birefringence is a quantitative way to measure optical anisotropy of materials, specifically changes in crystallinity and orientation; therefore it is evident that significant structural changes occur during stretching at 150°C. As mentioned previously, the starting morphology of PET is semi-crystalline and PVDF is barely partially molten.

Stress optical and strain optical behavior of polymer films is important because it gives an indication of how anisotropy in polymer morphology occurs at different values of true stress and true strain. There is a known relationship between application of mechanical force and polymer birefringence. For polymer melts and solutions, and amorphous polymers at low or moderate application of stress, the stress optical rule applies: [222], [223]

$$\Delta n = C\sigma \quad (3.7)$$

or,

$$(n_1 n_2) = C(\sigma_1 - \sigma_2) \quad (3.8)$$

Where Δn is birefringence, C is stress-optical coefficient, σ is applied stress and subscripts 1, 2 refer to principal directions of the aforementioned variables.

At moderate levels of applied stress, most polymers show deviation from linear stress-optical behavior. For example, deviations have been observed to occur due to strain-

induced crystallization, deformation near T_g , and due to non-Gaussian chain conformations when chains near their point of maximum extensibility [222].

Stress-optical curves for each of the three stretching temperatures are shown in Figure 3.6c. For all stretching temperatures, three separate molecular orientation regimes were observed. Regime I is an area of low deformation where molecular stresses are reversible [224]. In this case, the stress-optical coefficient is largely unaffected by stretching temperature, as expected since it is a material constant [224]. It was also observed that the end of Regime I shifts to higher values of stress as stretching temperature decreases. In Regime II, birefringence quickly increases with only small increase in true stress as polymer chains continue to align and undergo stress induced crystallization and the effects are more pronounced as stretching temperature increases. In this region, molecular chains deform plastically up until the point where strain hardening occurs. Molecular orientation in this regime is most pronounced in the 150°C curve and this is likely where high development of birefringence originates. In Regime III, stress begins increasing more rapidly than birefringence since polymer chains are highly oriented and resist further deformation as they reach their finite extensibilities [13], [8]. Table 3.1 lists relevant material properties for PET and PVDF, including intrinsic optical properties. Each PVDF crystal form has different inherent properties. The intrinsic birefringence of PET is much higher than the PVDF and hence these stress optical and strain optical behavior is proportionately dominated by the PET layers.

Finally, Figure 3.6d shows birefringence versus time for stretch and hold (quench) steps. After the stretching process ends and the film is quenched quickly to room temperature, relatively little change in birefringence is observed. This is unexpected because some polymer chain movement or relaxation to a more favorable conformation should occur while the film is constrained and quickly undergoes a large temperature change. This could be due to confining effects of the microlayered film structure, in which layer thicknesses are too small to allow polymer domains to move and rearrange

significantly while the film is being quenched under high stress conditions (i.e. due to constraining in clamps).

Table 3.1.: Relevant intrinsic properties of PET and PVDF [36], [144], [225], [70], [24]

Property	PET	PVDF
Refractive index, n_{\parallel}	1.58	1.54
Refractive index, n_{\perp}	1.57	1.52
Δn° (amorphous)	0.27	0.092
Δn° (crystalline)	0.22	$\alpha=0.095, \beta=0.113, \gamma=0.074$
Density (g/cm^3) (amorphous)	1.37	1.68
Density (g/cm^3) (crystalline)	1.46	$\alpha=1.98, \beta=1.80$

3.3.3 Characterization

A temporal evolution study was conducted by selecting points of interest along the stress, strain curves and stretching individual samples up to that point, then quenching and characterizing each sample's morphology. Combining real-time measured properties with offline characterization techniques at specific values along the true stress, true strain curve allows us to obtain a better idea of how polymer morphology develops in real time during stretching.

Thermal characterization (DSC)

Differential scanning calorimetry results for samples prepared in this manner are shown in Figure 3.7, followed by percent crystallinity in Figure 3.8. In Figure 3.7, the disappearance of PET's cold crystallization peak indicates films have reached maximum stretchability. Further, Figure 3.7a compares endotherms of the film as cast to the final 5.5X stretched samples. Melting peak of PVDF is most sharp after stretching at 150°C, indicating more isotropic and/or perfect crystals in comparison to other stretching temperatures. A secondary, higher melting peak is observed for

samples stretched to low strain at 185°C, which is identified as γ -PVDF which is known to have a higher melting point than other crystal forms [140].

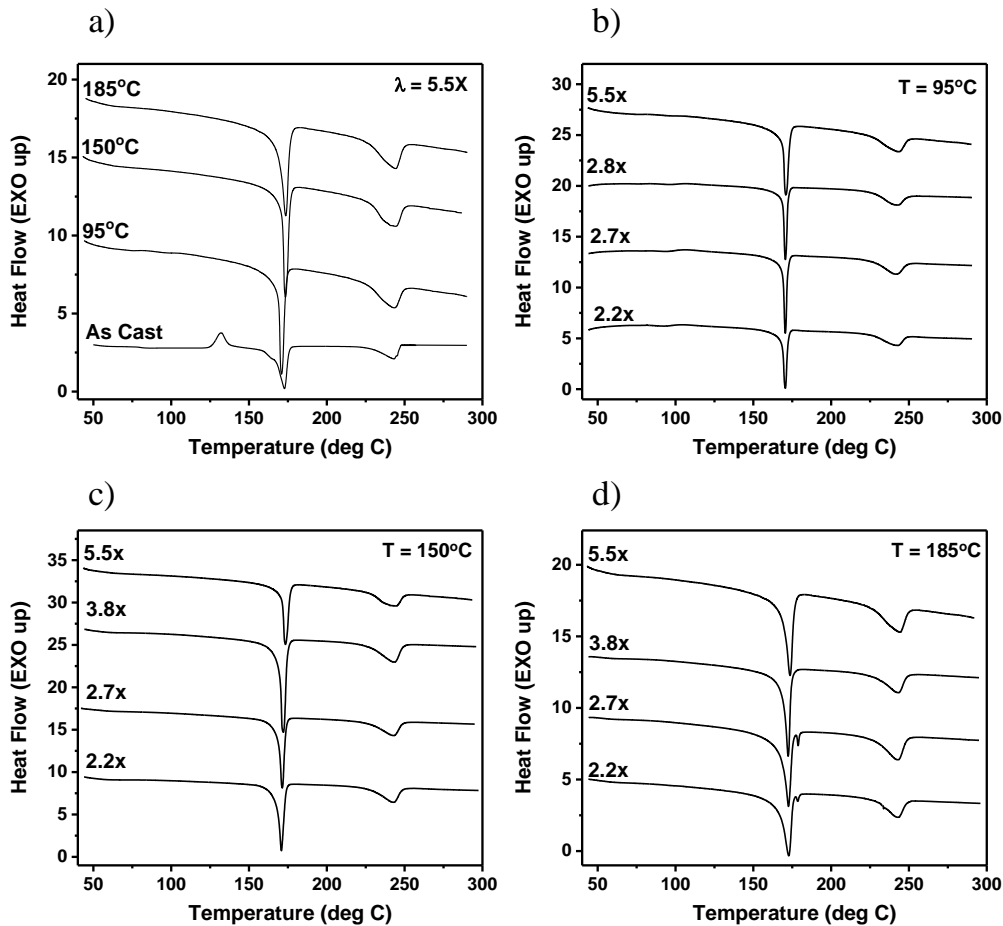


Fig. 3.7.: DSC (1st heat) curves for uniaxial stretching temperature study at 10 mm/min. Figure a) shows final (5.5x extension) for each temperature as well as cast film, b) time slice at 95°C, c) time slice at 150°C, and d) time slice at 185°C.

In Figure 3.8, we see that, in general, percent crystallinity of PET increases with stretching. Stretching at 95°C results in a low overall percent crystallinity value that is due primarily to strain induced crystallization, as polymer chains have low mobility to perfect the crystalline regions by relaxing/diffusing at this temperature. Higher

percent crystallinity values observed for samples stretched at 150°C and 185°C are attributed to strain induced crystallization, which is further increased due to thermal recrystallization, that is kinetically favorable at these temperatures. Overall, percent crystallinity of PET increases from around 3% in the as cast film to a value between 20 and 26%, depending on the stretching temperature. DSC percent crystallinity calculations should be accurate for PET but for the polymorphic PVDF, each crystal form has a different density (see Table 3.1) and quantitative amounts of each present in the sample are unknown (only a total crystalline fraction from DSC); the percent crystallinity values do not take the changes in crystal phase density into account. However, since the theoretical density of each crystal polymorph is known, percent crystallinity calculations still give an idea of relative crystallinity of the samples, and could indicate transformation of crystal phases. At 95°C, calculated percent crystallinity is 40.5% in film as cast, but appears to decrease with stretching, then increase again. PVDF percent crystallinity should in theory increase with increasing draw ratio; therefore, decreasing percent crystallinity values after stretching, shown in Figure 3.8, may indicate a transformation of crystal form - namely when calculated percent crystallinity appears to decrease, it is most likely due to a shift to less dense crystalline form (i.e. from α and γ to β -PVDF) rather than an actual decrease in overall percent crystallinity. X-ray diffraction and FTIR analysis will give a more thorough understanding of morphological changes occurring in PVDF during stretching, as demonstrated in the following sections. The 150°C stretched samples show a large increase in percent crystallinity of PVDF, followed by a leveling off at very high true strains. Increase in percent crystallinity can be attributed to favorable stretching in partially molten state for PVDF. At 185°C, PVDF has high molten fraction so crystals are partially melting and recrystallizing throughout the stretching experiment (i.e. annealing). Large increase in percent crystallinity at low strain is attributed to stress induced crystallization, but percent crystallinity levels off and decreases slightly as stretching experiments become longer (i.e. at higher draw ratios) as more PVDF melts and subsequently recrystallizes.

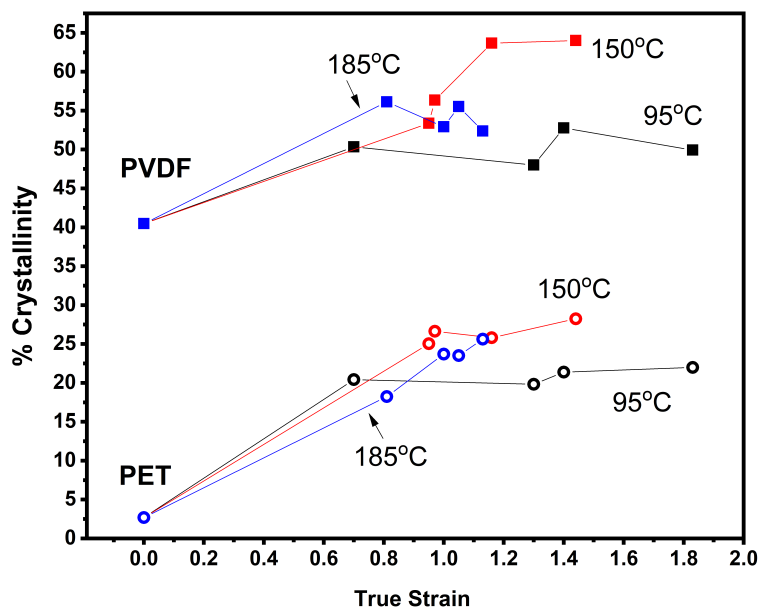


Fig. 3.8.: Calculated percent crystallinity of each polymer material in films stretched at 10 mm/min and 95, 150, and 185°C.

Small angle X-ray scattering

SAXS data are shown in Figure 3.9 at draw ratios corresponding to their neighboring true stress, true strain curves for 32 layer film at the three primary drawing temperatures. Initial in-plane isotropy is observed in the ND SAXS pattern of the film as cast, but there is some anisotropy present in transverse direction patterns, likely due to a layering confinement effect. These films are formed of alternating layers of mainly amorphous PET and semi-crystalline PVDF. What we observe in as cast film is attributed to PVDF only as PET is in structure-less amorphous state that would only give diffuse SAXS scattering, and not a discrete ring. When stretched at 95°C, PET is in the rubbery state and it does not show discrete SAXS ring [226], [227], [228]. In fact, the rest of the SAXS patterns in 95°C column of Figure 3.9 can safely be attributed to the PVDF alone. As the data indicate, the randomly distributed

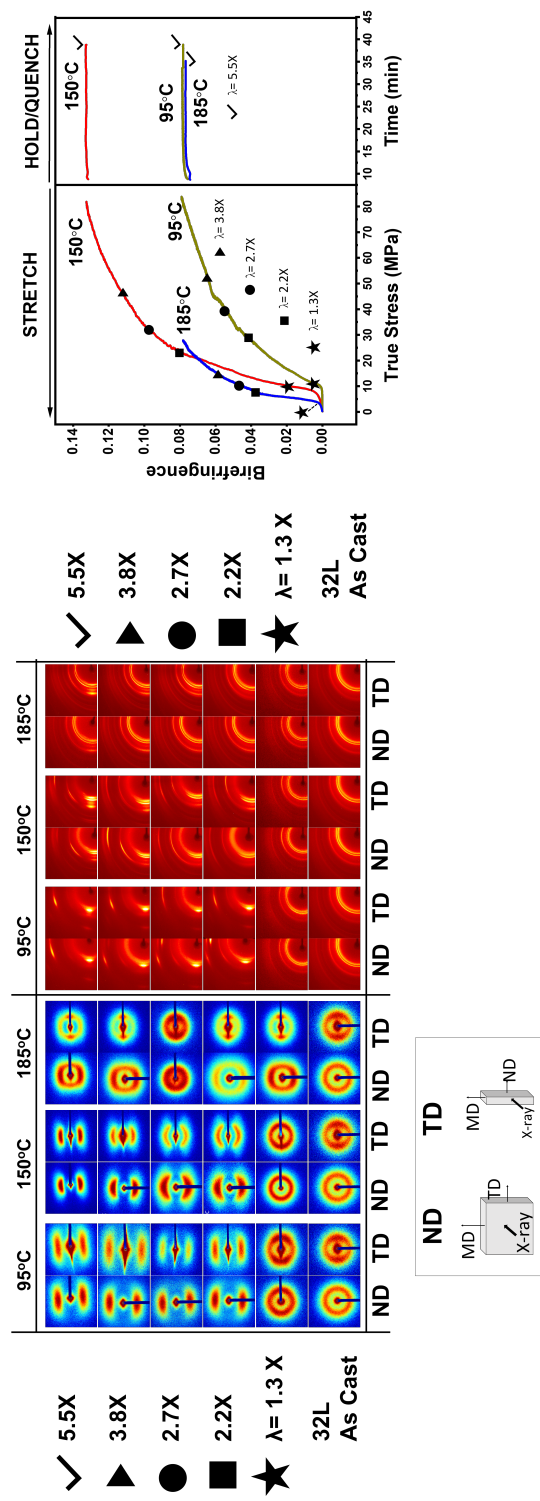


Fig. 3.9.: Stress optical data for 32L film stretched 5.5X, uniaxially at 10 mm/min and 185 and 150 and [Right] SAXS patterns for time-slice study at corresponding stretch ratios along stress optical curves.

lamellar structure gradually becomes preferentially oriented in the machine direction as evidenced by two point pattern formation that is indicative of alternating crystalline lamellae separated by amorphous regions in PVDF. PET crystallizes at other stretching temperatures, 150°C and 185°C, and interpretation of the SAXS patterns become more complex as both PVDF and PET contribute to the scattering pattern formation. At 150°C, SAXS patterns for delaminated PVDF are shown in conjunction with AFM images in following sections to further study morphology. This temperature was chosen as it provided uniformly thick samples suitable for dielectric property testing. Quantitative thickness uniformity study is described in more detail in in Chapter 4.

FTIR

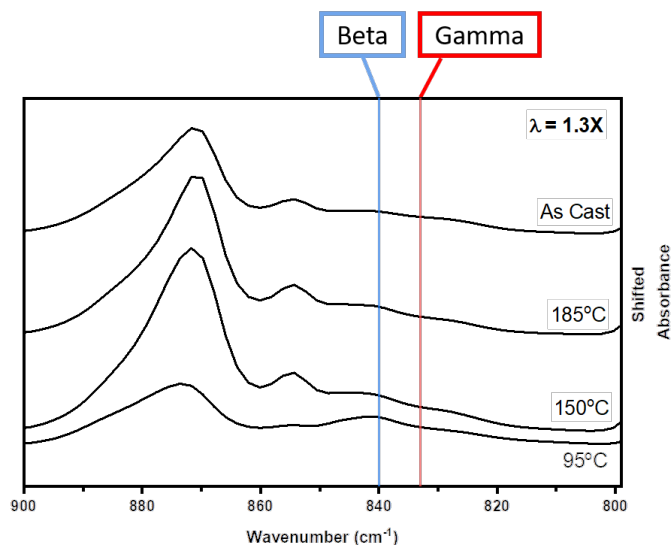


Fig. 3.10.: FTIR spectra for PVDF layer delaminated from 32L film samples stretched to 1.3X at 95, 150, and 185°C in uniaxial extension at 10 mm/min.

FTIR is a useful technique to characterize PVDF crystal forms, as studied in the literature [229], [230], [25], [140], [93]. Absorption peaks unique to PVDF crystal forms are observed at specific wavelenghts. For the purpose of this study, we used

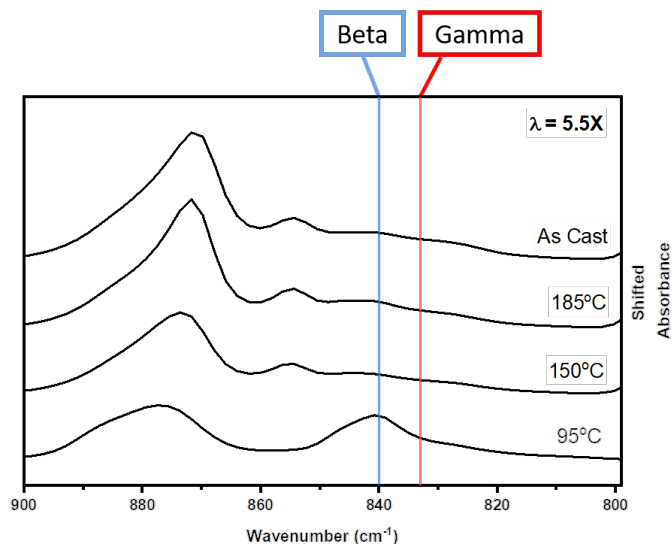


Fig. 3.11.: FTIR spectra for PVDF layer delaminated from 32L film samples stretched to 5.5X at 95, 150, and 185°C in uniaxial extension at 10 mm/min.

833 and 840 cm^{-1} to identify γ -PVDF and distinguish γ from β -PVDF. Example curves are shown in Figure 3.10 for PVDF layer delaminated from films stretched uniaxially to 1.3X draw ratio. Of the samples shown, only 95°C shows clear β -PVDF peak. β -form is known to occur under high stress stretching, such as when PVDF is deformed in solid state (i.e. at 95°C). FTIR curves for PVDF layer delaminated from films stretched to 5.5X initial length are shown in Figure 3.11, where we see a much larger β peak in the 95°C stretched sample, indicating a significant transformation from α to β PVDF occurs with stretching from draw ratio 1.3X to draw ratio 5.5X. None of the samples show distinct γ form in the range of FTIR shown here, which would be indicated by a double peak at 840 and 833 cm^{-1} rather than a broad peak at 840 cm^{-1} , shown for the β form. A summary of PVDF crystal forms identified via FTIR can be found in Figure 3.15. Asterisks in the table refers to possible detection of very small β PVDF peak via FTIR. It should be noted that although there are many distinguishing FTIR peaks for γ -PVDF, none of these peaks were identified exclusively for these samples.

Wide angle X-ray scattering and orientation factors

WAXS data are shown in Figure 3.9 at draw ratios corresponding to their neighboring true stress, true strain curves for 32 layer films at the three primary drawing temperatures. Larger, 2D WAXS images taken in film normal (ND) and transverse (TD) directions are pictured in Appendix A Figure A.3. The films stretched at 95°C show a distinct diffraction peak at 41°, (100) crystalline PET plane, which increases in sharpness during stretching as PET orients in drawing direction. Peak intensity also increases, indicating higher percent crystallinity is developed upon stretching. The later statement is confirmed by calculated percent crystallinity data in Figure 3.8. In contrast, it appears as though this PET peak shifts to around 43.2° ($\bar{1}05$) for the 150°C and 185°C films. This is likely due to the fact that recrystallization is kinetically favorable for PET at these higher temperatures, meaning that crystals are constantly reforming, resulting in a less ordered PET crystalline phase. The effect is magnified at 185°C, where PET is at its optimum thermal recrystallization temperature and this is evidenced by a broader peak in 2θ direction in comparison to the samples stretched at 150°C.

PVDF crystalline diffraction peaks are more complicated, as there are many diffraction peaks for each polymorph. However, WAXS can give some idea of which PVDF crystal form is present. Figures 3.12, 3.13, and 3.14 show 1D WAXS diffraction data for films stretched at 95°C, 150°C, and 185°C, respectively, with vertical lines indicating crystal planes relevant for identifying PVDF polymorphs. Diffraction peaks useful in determining crystal forms for these microlayer films are the (200) β plane at $2\theta = 20.6^\circ$ and γ at $2\theta = 22.8^\circ$, (111) plane. α and γ are hard to distinguish via WAXS as their crystal structures are very similar, and most films likely contain some γ in addition to α . Three characteristic peaks at $2\theta = 20, 18.45, \text{ and } 17.85^\circ$, indicative of α PVDF crystal planes (100), (020), and (021), are present in all diffraction patterns presented here. 95°C stretched films show broadening of these α peaks with stretching, along with sharpening at 20.6° as transformation to β form takes place.

Again, this transformation is known to occur at high stresses, for example, when PVDF is stretched in the solid-state [23], [225], [231], [36]. Furthermore, as observed via DSC, lower calculated percent crystallinity in 95° stretching is likely a shift from α to β form PVDF as confirmed by WAXS peak identification in Figure 3.12. For 150°C stretched samples, α PVDF peaks sharpen as draw ratio increases, suggesting increase in number and perfection of α crystals. At 185°C, α (110), (020), and (100) planes are very sharp, meaning crystals are uniform in size and have a relatively high percent crystallinity. This is likely due to annealing effect inherent to stretching so close to PVDF's equilibrium melting point. Furthermore, a unique peak appears at 22.8°, γ (022) plane, for 185°C stretched samples. It is known that transformation from α to γ -PVDF occurs when annealing PVDF at high temperature (above about 160°C), therefore our results indicate that primarily α -PVDF crystals are formed quiescently or via stress induced crystallization, and transform to γ -PVDF crystals when PVDF is stretched near equilibrium melting temperature and sandwiched between solid PET layers [225], [231]. Unique γ -PVDF peaks were not identified for other stretching temperatures via WAXS analysis. Additionally, β -PVDF was only identified via WAXS in samples stretched at 95°C, as seen in Figure 3.12. A summary of PVDF crystal forms identified via WAXS can be found in Figure 3.15.

In conclusion, WAXS analysis shows that PET crystalline regions appear to orient more readily when films were stretched at 95°C, as evidenced by sharpening of WAXS peaks. Furthermore, stretching PVDF in its semi-crystalline state at 95°C causes transformation of α to β crystals, as evidenced by the shift from three sharp peaks at 2θ values of 20, 18.45, and 17.85° in the as cast samples to the broader peak at 20.6°, which is indicative of (200) β crystal plane. At 185°C, WAXS evidence suggests a transformation from α to γ crystal form, due to annealing effect, where γ (111) plane located at $2\theta = 22.8^\circ$ was identified only in films stretched at 185°C.

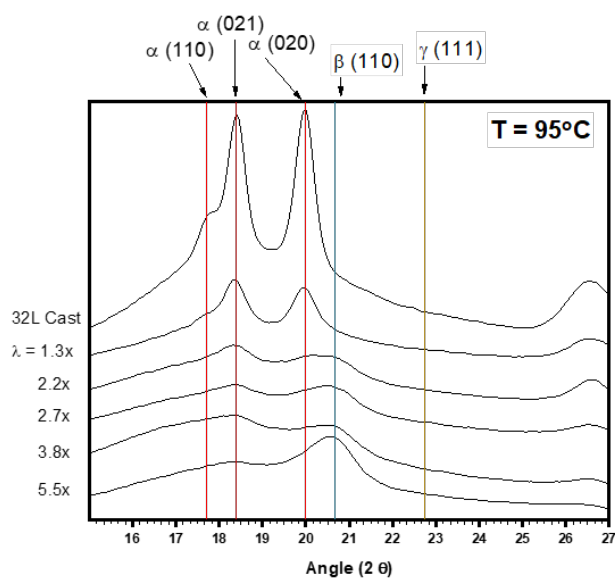


Fig. 3.12.: Select 1D WAXS curves for 32L film stretched at 95°C in uniaxial extension at 10 mm/min.

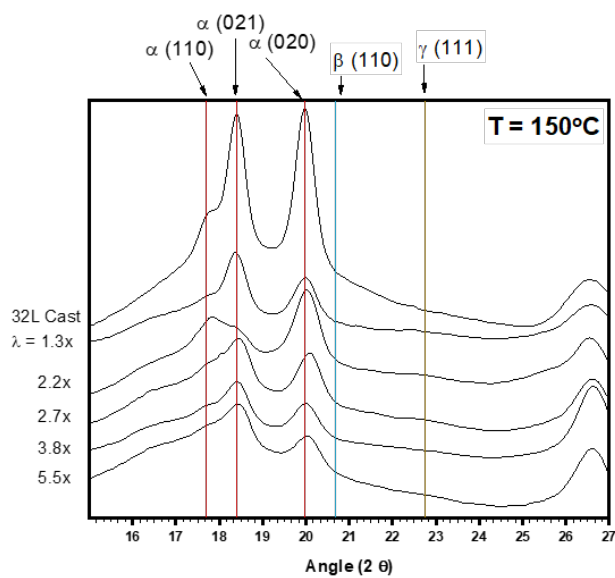


Fig. 3.13.: Select 1D WAXS curves for 32L film stretched at 150°C in uniaxial extension at 10 mm/min.

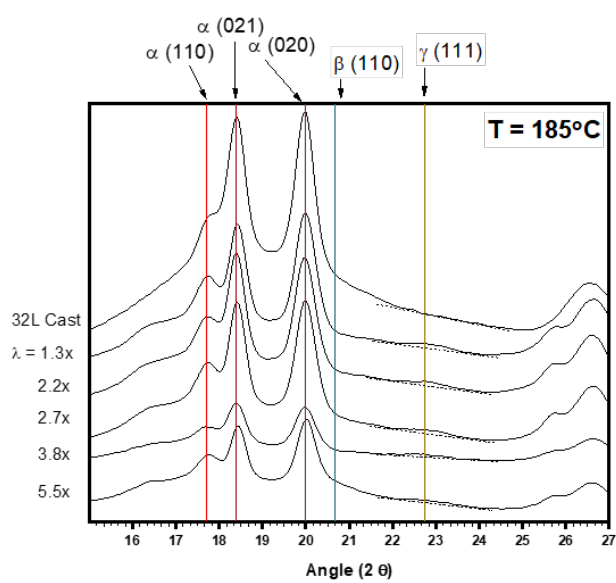


Fig. 3.14.: Select 1D WAXS curves for 32L film stretched at 185°C in uniaxial extension at 10 mm/min.

Fig. 3.15.: Summary of PVDF crystal forms as detected by DSC, FTIR, and WAXS characterization methods.

Sample	β - PVDF		γ - PVDF		
	FTIR	WAXS	FTIR	WAXS	DSC
32L, As Cast	N*	N	N	N	N
1.3X , 95°C	Y	N	N	N	N
2.2X , 95°C	Y	Y	N	N	N
5.5X , 95°C	Y	Y	N	N	N
1.3X , 150°C	N*	N	N	N	N
2.2X , 150°C	N	N	N	N	N
5.5X , 150°C	N	N	N	N	N
1.3X , 185°C	N	N	N	Y	Y
2.2X , 185°C	N	N	N	Y	Y
5.5X , 185°C	N	N	N	Y	N

Orientation Factors

From experimental WAXS data, crystalline orientation factors were calculated by taking an azimuthal scan of 2θ peak corresponding to the crystalline diffraction peak of interest and corrected for background scattering by subtraction of azimuthal intensity of a peak significantly far away from any scattering.

Mean-square cosine values were calculated from plane normals from corrected intensity distribution from WAXS data. The formula is as follows:

$$\langle \cos^2 \phi \rangle_{hkl} = \frac{\int_0^{\frac{\pi}{2}} I(\phi)_{hkl} \sin \phi \cos^2 \phi d\phi}{\int_0^{\frac{\pi}{2}} I(\phi)_{hkl} \sin \phi d\phi} \quad (3.9)$$

and crystalline orientation factor, f , is calculated by:

$$f_{(hkl)} = \frac{1}{2}(3 \langle \cos^2 \phi \rangle_{hkl} - 1) \quad (3.10)$$

where $\langle \cos^2 \phi \rangle_{hkl}$ is the mean-square cosine average over all crystallites of the angle between crystal and reference axis [214]. For any crystallographic axis, $\langle \cos^2 \phi \rangle = 1$ for perfect Z alignment, $\frac{1}{3}$ for random alignment, and 0 for perpendicularity. The value f_{hkl} therefore shows values of 1, 0, and $-\frac{1}{2}$, respectively.

PET has a triclinic unit cell, but Yoshihara and coworkers developed an approximated pseudo-orthorhombic unit cell to analyze crystalline orientation for PET [226], [232], [6]. Wilchinsky method for analyzing orthorhombic unit cell was used to calculate orientation factors from WAXS data of (100), polymer chain axis direction, and (010), perpendicular to aromatic benzyl ring [233], [234]. Unfortunately, due to the complex structural nature and polymorphism of PVDF, these peaks were not uniquely able to be distinguished (in composite film WAXS pattern) in order to perform this calculation.

PVDF α form has a monoclinic crystalline unit cell, therefore the (200) and (020) crystal planes can be used directly to calculate crystalline orientation factor. Crystal planes (200) and (110) can also be used with application of Wilchinskys method, as shown in the following equation [231]:

$$\overline{\cos^2\phi_{c,Z}} = 1 - 1.2647\overline{\cos^2\phi_{110}} - 0.7353\overline{\cos^2\phi_{200}} \quad (3.11)$$

Orientation factors were calculated for PVDF materials after stretching temporal evolution study at 10 mm/min and 150°C. The reason only these values are reported is that this condition produced samples of fair enough quality to be used in dielectric testing experiments, and therefore orientation factors can be directly linked to these properties.

Crystalline c-axis orientation factor for α -PVDF crystals is reported in Figure 3.16. At 150°C stretching temperature, PVDF has very small molten fraction and therefore, already formed crystals deform upon application of strain to the system. Orientation factor for α -PVDF begins around 0.12 in the film as cast, suggesting not much c-axis alignment initially. With small amounts of strain (stretch ratio=2X), orientation factor increases gradually by a small amount, to around 0.2. However, after stretching to 2.5X at 150°C, orientation factor for PVDF increases significantly to a value near 0.6, which indicates well aligned c-axis orientation. This suggests that relatively high amounts of deformation are required for c-axis, α -PVDF crystals to obtain significant alignment with film drawing direction. And finally, increasing draw ratio above 2.5X, PVDFs orientation factor increases slowly to a final value around 0.7.

3.3.4 Dielectric properties

Dielectric constant and dielectric loss values measured at room temperature, in combination with calculated orientation factors for each material, are shown in Figures

3.16, 3.17 and Figures 3.18, 3.19, respectively. Though dielectric breakdown strength is of considerable interest to this study, it could not be tested as final film thicknesses were too high. Dielectric constant for films stretched at 150°C is shown in Figure 3.16 compared to PVDF orientation factor. No data for 95° and 185°C samples is shown, as large thickness non-uniformity prevented legitimate results (for quantitative thickness uniformity analysis, see Chapter 4). For samples stretched at 150°C, dielectric constant decreases until stretching ratio 2X, then increases at 2.5X, before decreasing steadily again. Calculated α -PVDF orientation factor in comparison to these results suggests that, while PVDF remains relatively unoriented up to around 2X deformation, dielectric constant decreases. However, upon stretching to 2.5X, where orientation factor increases by around 3-fold, we see a significant increase in dielectric constant, meaning orientation is likely beneficial overall to dielectric constant. At very large strains, however, dielectric constant begins to decrease again with not much change in orientation factor. In the absence of crystalline orientation factor for PET, percent crystallinity and birefringence (after stretch and hold) were plotted against dielectric constant in Figure 3.17. In the 1.5X sample, percent crystallinity increases significantly from the film as cast, due to thermal recrystallization inherent to stretching at high temperature. Further stretching to 2X increases PET's crystallinity only slightly due to stress induced crystallization, in combination with thermal recrystallization. Birefringence, on the other hand increases only slightly at 1.5X but very significantly after stretching to 2X. Since birefringence increases with amorphous or crystalline orientation and amount of crystallinity, this result suggests significant PET amorphous and/or crystalline alignment with stretching direction after only 2X deformation. With further stretching, percent crystallinity of PET increases and birefringence follows a similar trend. All the while, dielectric constant decreases up to 2X stretching, increases, then decreases again. In this case, orientation

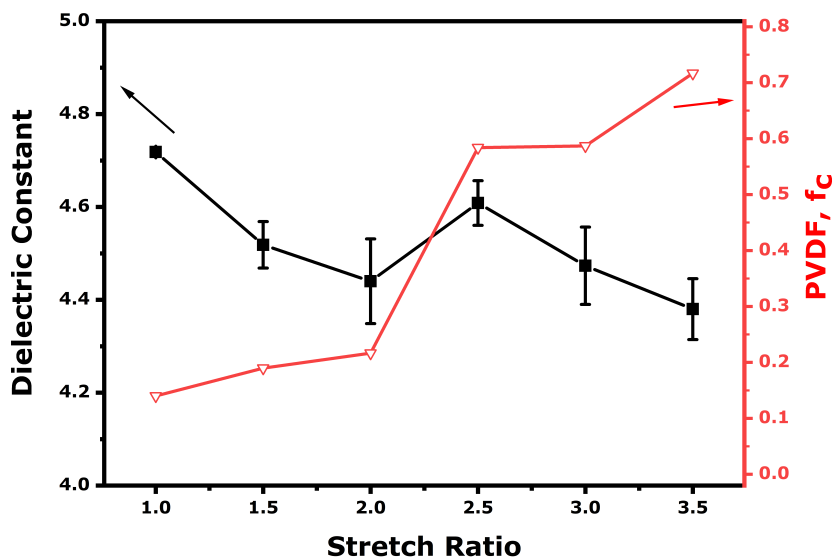


Fig. 3.16.: Dielectric constant (room temperature and $f=1$ kHz) for a series of 32L films stretched in uniaxial extension at 95 and 150°C overlaid with PVDF orientation factors.

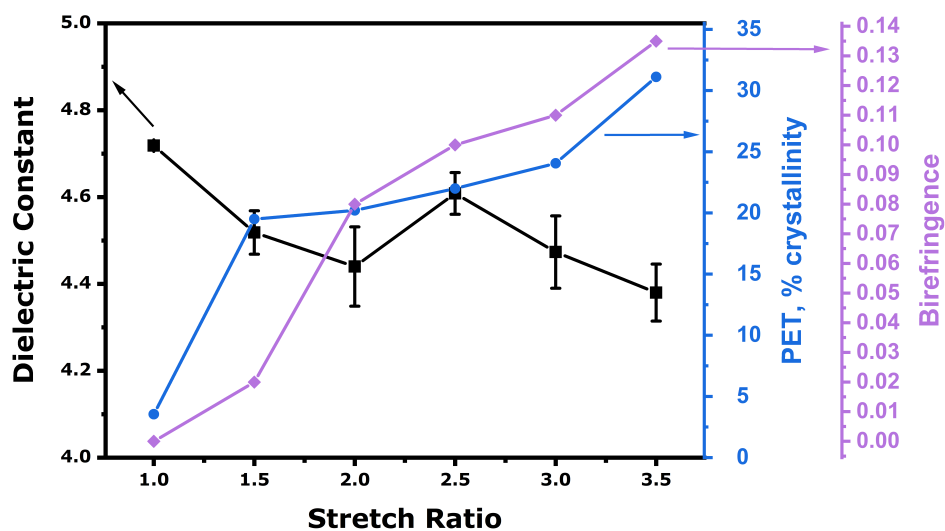


Fig. 3.17.: Dielectric constant (room temperature and $f=1$ kHz) for a series of 32L films stretched in uniaxial extension at 95 and 150°C overlaid with birefringence and PET percent crystallinity.

and increasing percent crystallinity of PET could be detrimental to dielectric constant of this multilayer film. PET is non-polar with relatively low dielectric constant, so likely PVDF morphology has stronger influence on determining this property. Therefore, PVDF layers were delaminated from the composite system and studied further using AFM and SAXS analysis, as shown in Figure 3.20 and discussed in Section 3.3.5.

Dielectric loss for films stretched at 150°C, (Figures 3.18, 3.19) is significantly decreased with increasing stretch ratio. This is likely due to decreasing layer thickness, which immobilizes ions at layer interface, thereby lowering loss [200]. At very high strains (draw ratio 3.5X), loss factor decreases significantly more. In the context of orientation factor, we see a small rise in PVDF's c-axis alignment with drawing direction, but not a very significant one. More likely, PVDF morphology is contributing to this favorable improvement in loss, as will be described in Section 3.3.5. Figure 3.19 shows PET percent crystallinity and birefringence in comparison to dielectric loss. Stretching to 1.5X showed very high PET percent crystallinity development and an increase in birefringence as well, therefore decrease in the film's loss property could be attributed to more oriented, higher crystalline PET layers as well. Amorphous orientation for PET is also likely with high degree of orientation which would contribute to lower system loss due to the dielectric absorption phenomenon [61]. Further stretching to 3X draw ratio shows no significant change in dielectric loss, as birefringence and PET crystallinity continue to increase. However, from 3X to 3.5X, we see significant decrease in dielectric loss, along with an increase in both crystallinity and birefringence for PET, with higher slope than the previous trend. This significant improvement in PET's orientation and crystallinity could also contribute to the rapid decrease in dielectric loss at 3.5X draw ratio.

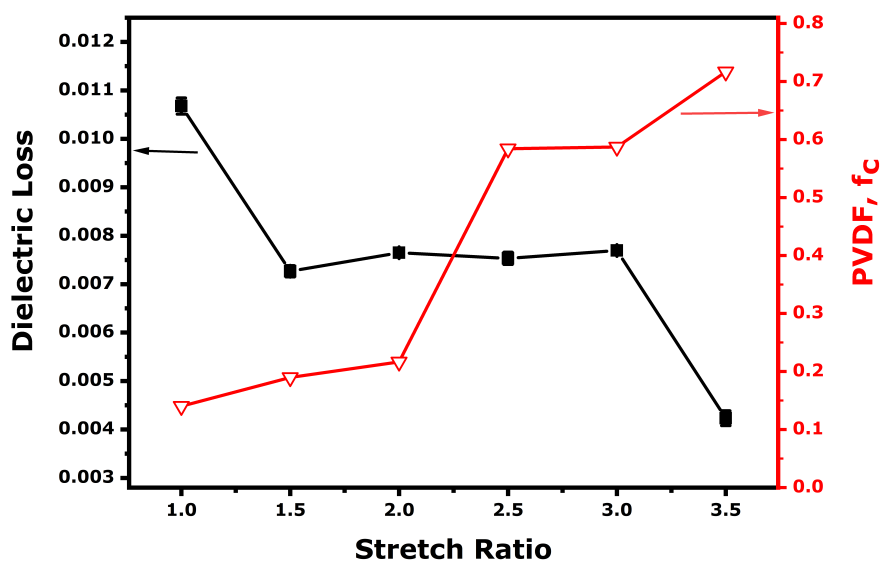


Fig. 3.18.: Dielectric Loss (room temperature and $f=1$ kHz) for a series of 32L films stretched in uniaxial extension at 95 and 150°C overlaid with PVDF orientation factors.

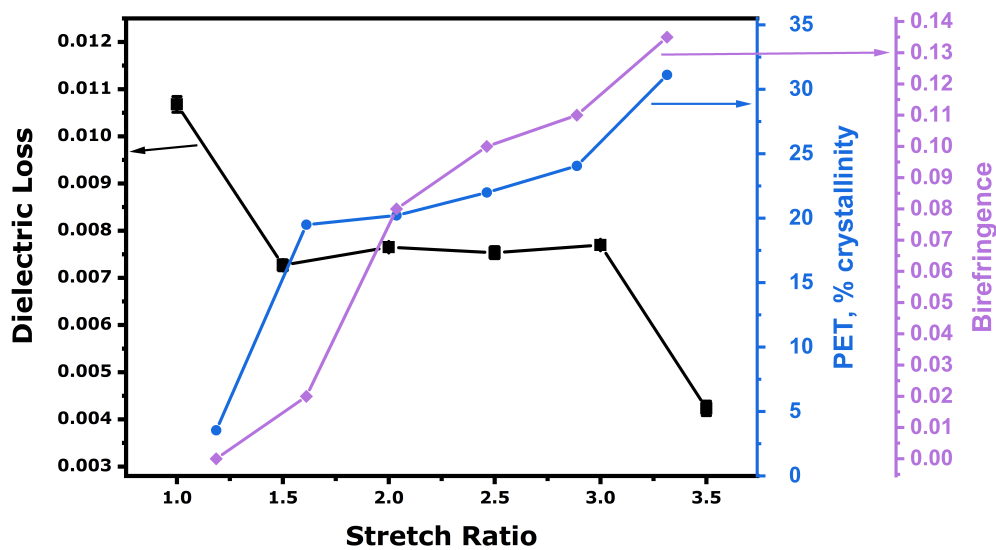


Fig. 3.19.: Dielectric constant (room temperature and $f=1$ kHz) for a series of 32L films stretched in uniaxial extension at 95 and 150°C overlaid with birefringence and PET percent crystallinity.

3.3.5 AFM and Structural Model

A representative structural model based on AFM and SAXS data is proposed in Figure 3.20 for PVDF layers delaminated from 32L films both as cast and after stretching at 150°C. In its as cast state, AFM imaging of single PVDF layer (Figure 3.20a) shows random spherulites, with dark amorphous regions surrounding them. The SAXS pattern confirms this, with the only feature being a broad, isotropic ring indicative of low density contrast (i.e. relatively less crystallinity than, for example, after stretching) and random orientation in the plane of the film. After stretching to 1.5X draw ratio (Figure 3.20b), the SAXS pattern is still isotropic but sharper, indicating more crystallinity (higher electron scattering density). The AFM image for this sample shows Y shaped arms protruding from the spherulite center, with still random orientation. Stretching further appears to lead to formation of microfibrils, as shown in Figure 3.20c. SAXS pattern now shows oriented arcs, suggesting lamellae stacked in stretching direction, and equatorial diffuse scattering streak which can arise from either microvoids or microfibrils [214]. The AFM image for this sample confirms the presence of microfibrils, which are circled in red, and appear as long rod shapes pointing in the machine direction. The structural drawing below shows orientation within these microfibrils which consist of regions of orientated lamellar crystals separated by relatively oriented amorphous regions due to high levels of stress. The final stretching ratio portrayed is 3.5X, in Figure 3.20d. Orientation factor calculated for this system does not change from =2.5X to =3.5X (see Figure 3.16), and this is confirmed by both AFM images and SAXS scattering patterns in Figure 3.20c, d. However, SAXS pattern for the 3.5X (Figure 3.20d) sample has relatively broader arcs compared to 2.5X (Figure 3.20c), which indicates a wider range of lamellar sizes. This is likely due to very high stresses in the system causing breakup of lamellae. The circled region in AFM in Figure 3.20d clearly shows more, smaller microfibril regions compared to the long, continuous cylindrical shapes in image for 2.5X draw ratio shown in Figure 3.20c.

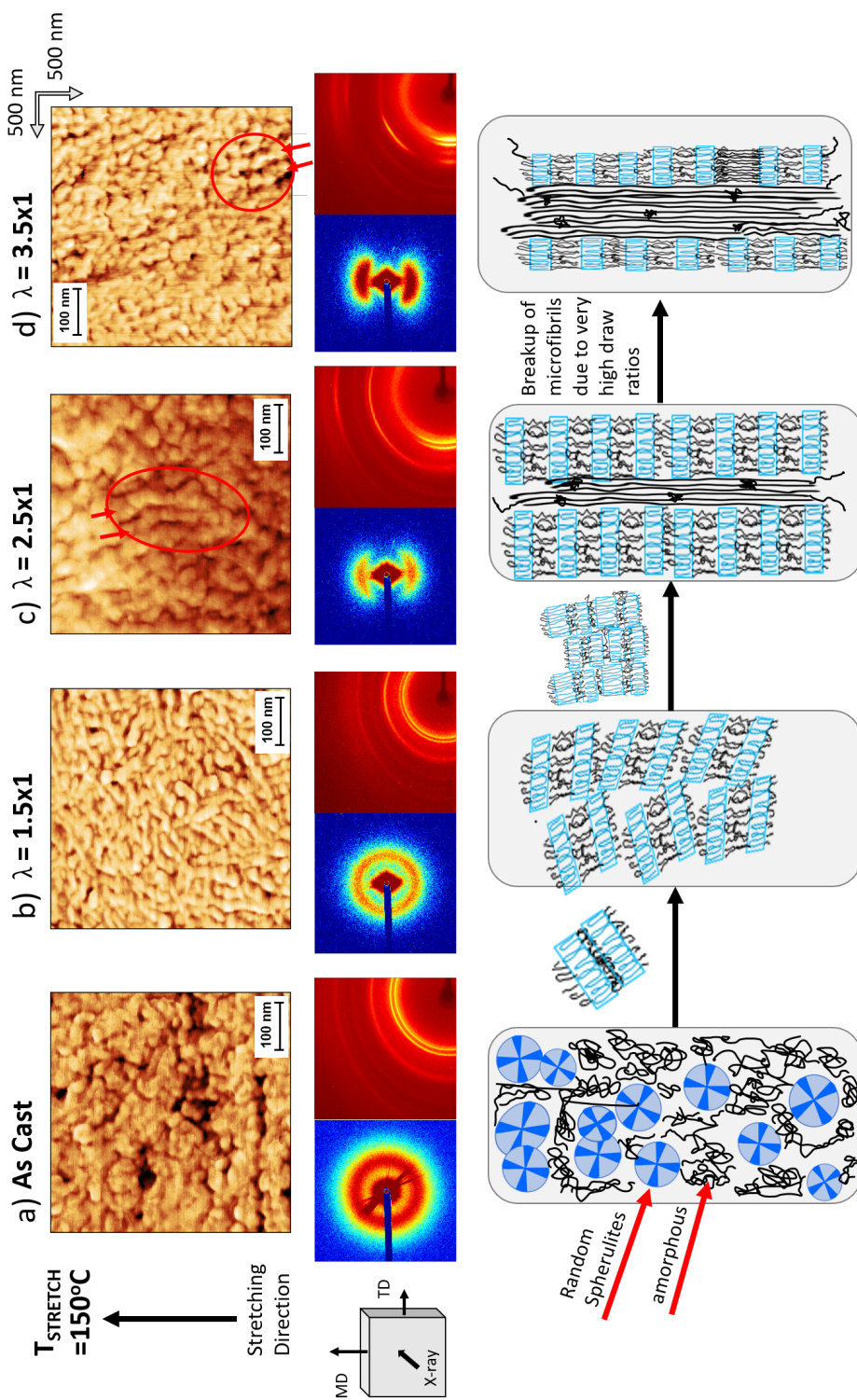


Fig. 3.20.: AFM phase images, and 2D SAXS patterns for PVDF layer only (delaminated from 32L PET/PVDF system). Films portrayed are as cast, as well as uniaxially oriented at 10 mm/min and varying draw ratios.

Morphological link to Dielectric Properties

Dielectric constant (recall Figure 3.16) decreased with stretching until draw ratio of 2X. From AFM and SAXS analysis presented above, this suggests that spherulitic PVDF structure negatively impacts dielectric constant. At 2.5X, the dielectric constant increases again, before decreasing when stretched above 2.5X. The proposed structural model (Figure 3.20c) for 2.5X draw ratio based on AFM and SAXS shows appearance of highly ordered PVDF microfibrils, which aligns dipoles of PVDF, contributing to higher dielectric constant. Upon further stretching, AFM image for 3.5X (Figure 3.20d) draw ratio shows breakup of microfibrils, and a subsequent decrease in dielectric constant ensues as this orientation of dipoles is disrupted.

For dielectric loss measurements, (recall Figure 3.18), we observed significant decrease in loss with stretching from stretch ratio 1X (as cast) to 3X, but not much change in between. In terms of PVDF morphology, this suggests that spherulites (1X, 1.5X) versus aligned microfibrils (2.5X) do not lead to significantly different loss values. However, when drawing ratio is very high, at 3.5X, the loss value drops again by nearly 50%. Structurally, the difference of PVDF in 2.5X sample is large aligned microfibrils versus in 3.5X smaller, broken up microfibrils. This structure therefore may result in lower dielectric losses, likely due to the improved ability for planar switching to occur in the presence of AC electric field that is known to decrease loss [61].

3.4 Conclusions

In conclusion, stretching temperature during uniaxial orientation of microlayer polymer films greatly affects development of polymer morphology, and this was proven by choosing three strategic stretching temperatures and characterizing films stretched stretched in temporal evolution study.

When both PET and PVDF were stretched in primarily semi-crystalline state, namely at 150°C, a very high development of birefringence was observed using our real-time uniaxial stretching system, which indicates either a high development of crystallinity and/or orientation during stretching.

Percent crystallinity calculations show increase of PET percent crystallinity during stretching, especially at the high draw temperatures (150, 185°C) where thermal crystallization occurs.

Percent crystallinity calculations for PVDF are more complicated due to its polymorphic nature. During stretching, when total percent crystallinity of PVDF seems to increase then decrease again, however this is most likely due instead to a shift from a more dense (namely, α) to less dense (β or γ) crystalline phase.

SAXS pattern taken in film ND shows initial in-plane isotropy in as cast film, but some anisotropy is present when viewed in TD, likely due to confinement effect. When stretched at 95 and 150°C, lamellar regions (as viewed in composite film, TD SAXS image) rotate from film normal direction to machine direction orientation after only small strains. This reorganization is not observed when films are stretched at 185°C, likely because PVDF is nearly fully molten during stretching.

Characterization via FTIR confirmed β -PVDF development in films stretched at 95°C, however this method was not useful in determining presence of γ -PVDF.

WAXS experiments show strong, oriented PET peaks when stretched at 95°C as expected since this is near the ideal stretching temperature for PET, and the PVDF at this temperature partially transforms from α to β -form crystals due to high stresses. When stretched at 150 and 185°C however, PET peak shifts to higher 2θ value and only α and γ -PVDF forms are present during stretching at these temperatures.

For PVDF, α c-axis orientation is low in as cast state, and generally orients parallel to stretching direction as stretch ratio increases. There is a significant increase in orientation factor above a critical strain, shown at 2.5X draw ratio.

Dielectric constant measured for films stretched at 150°C first decreases with stretching, increases at draw ratio of 2.5X before decreasing again. This suggests that spherulitic PVDF present in as cast film and low stretching ratios negatively impacts dielectric constant. At 2.5X draw ratio, highly ordered PVDF microfibrils contribute to higher dielectric constant by aligning dipoles. Upon further stretching, we see breakup of microfibrils, which causes lower dielectric constant. For PET, percent crystallinity and orientation (shown from birefringence measurements) increase significantly with stretching as well. This could mean that higher orientation and/or crystallinity of PET negatively impacts dielectric constant in this film. More likely, however, is the fact that PET is non-polar with a relatively low dielectric constant and thus PVDF morphology more strongly dictates the dielectric constant of the composite film.

Dielectric loss for films stretched at 150°C is much lower than the film as cast, but does not change significantly with draw ratio until very high deformation (3.5X). PVDF spherulites observed at 1X, 1.5X and the aligned microfibrils observed at 2.5X therefore lead to samples with similar dielectric loss values. At draw ratio 3.5X, the loss value drops again nearly by 50%, as smaller, broken up microfibrils appear. These smaller crystalline regions of PVDF likely have lower dielectric loss (compared to large microfibrils) due to the improved ability for planar switching in presence of electric field. PET percent crystallinity and orientation may also help decrease dielectric losses in the film, as we observed that birefringence and orientation increase steadily with stretching, and dielectric loss decreases. This is especially evident at very high stretch ratios, where there is a significantly large positive change in slope in both PETs birefringence and percent crystallinity, and also a significantly large negative slope change in the dielectric loss.

3.5 Acknowledgements

The authors would like to thank PolymerPlus for kindly providing the microlayered films for this project. The authors acknowledge and greatly appreciate support, funding, and dielectric property testing from the Office of Naval Research Grant N000141712048. Characterization of this material is supported by the National Science Foundation through the Major Research Instrumentation Program under Grant No. CHE 1625543 (Funding for the single crystal X-ray diffractometer).

4. MICROLAYERED PET/PVDF FILMS: EFFECT OF ORIENTATION AND ANNEALING ON DIELECTRIC PROPERTIES

Kinetics of structural reorganization in uniaxially stretched, microlayer films consisting of 50:50 ratio of PET/PVDF in 32 alternating layers during annealing was carried out using an instrumented, custom built heat setting chamber that tracks in and out of plane birefringence in real time. For this film, we established ideal stretching temperature to be a very narrow range between 145-155°C. Annealing over a range of temperatures around PVDF melting peak caused transformation of PVDF polymorphs from primarily α to mixtures of α and γ and/or γ' . Specifically, when stretched at 150°C and 1.5X1, small amounts of γ and γ' were detected after annealing at 172°C, and only γ' when annealing at higher temperatures. Stretching at 2.5X1 and 3.5X1 at 150°C showed large γ -PVDF amount when annealed at 156°C and 150°C, respectively. Analysis of morphology was studied via DSC, WAXS, SAXS, AFM and FTIR. A structural model was proposed for PVDF layers using mechanical delamination to isolate them from the microlayer film system. Finally, morphology was correlated with dielectric constant and loss values in both constant room temperature and temperature ramping experiments. In temperature ramping dielectric experiments, for the most part, samples containing γ and/or γ' -PVDF showed increasing dielectric constant with increasing temperature, however dielectric loss also greatly increased with increasing temperature. The sample without detectable amounts of γ and/or γ' -PVDF present after annealing had slightly lower dielectric constant but also had much lower loss value at high temperature, making it a potential candidate for high temperature capacitor applications. Furthermore, high percent crystallinity of PET may help improve loss behavior at high temperature testing.

4.1 Introduction

In the 1950s, polymers such as polyethylene, polystyrene, and polytetrafluoroethylene were first used as the dielectric material in capacitor films, replacing materials such as mica and paper [61]. Since that time, biaxially oriented polypropylene (BOPP) capacitors were developed and have dominated the high energy density dielectric material market for over 20 years [61]. Polypropylene is suitable for such devices due to its inherently high volume resistivity, as well as low loss factor and temperature and frequency independent dielectric constant [60]. The semi-crystalline nature of polypropylene allows for further enhancement of electrical properties via tailored morphology by biaxial orientation, giving it an energy density of around 1.2 J/cm^3 with maximum usage temperature of 85°C [60]. To meet consumer and industrial needs for electronic components which are increasingly thinner, longer lasting, and able to perform at higher temperatures, the current dielectric BOPP material needs to be replaced. Optimizing dielectric constant and breakdown field strength, lowering dielectric loss, and increasing intrinsic thermal conductivity is challenging because, in many cases, improving these factors simultaneously is contradictory; thus it has been accepted that improvement in any current dielectric material properties compared to BOPP would be considered a success [61].

One possible solution is to combine polymers in a microlayered structure to take advantage of beneficial thermal and electrical properties inherent to each material, while possibly creating a synergistic combination of the two (i.e. better properties than the sum of individual components). Forced-assembly microlayering is a coextrusion processing technique which was developed in the 1960's by Dow Chemical Company and provides a way to combine between 4 and 1000s of micro- to nanolayer thin polymer layers into a single film. More information on this technology can be found elsewhere [55], [156], [235], [155], [236], [237], [238], [42], [56]. This technique has many advantages, such as continuous processing and the ability to control the number, thickness, and ratio of polymers in layers. For the purpose of this study, two semi-

crystalline polymers, namely poly(ethylene terephthalate) (PET) and poly(vinylidene fluoride) (PVDF), were combined in a multilayer film to take advantage of both the high breakdown strength (570 MV/m) of PET and the extremely high dielectric constant of PVDF ($\epsilon=10$).

Among all known polymers, PVDF has the strongest piezoelectric and pyroelectric responses by far and one of the highest dielectric constants [23]. PVDF is a polymorphic polymer and has (at least) four different crystal structures, specifically α , β , γ , and δ -forms. The most common of which is the α -phase, which occurs quiescently from the melt and results in anti-parallel chains that cancel the net dipole moment [23]. The β form, however consists of all-trans chains in a helix-like structure with dipoles pointing in the same direction, making it the most polar and electrically active crystal form of PVDF [23]. β -PVDF is well known to form due to mechanical deformation or electrical poling. Although γ and δ are less common, they transform from α -PVDF under sufficient stress, heat, or electric field [24]. Since PVDF is a highly crystalline polymer (about 50% on average), understanding how and why these crystalline structures form and their effect on final dielectric and mechanical properties of the film is crucial.

Equally important, the PET layer contributes a very high breakdown strength, as well as low electrical losses, to the microlayer film system. PET is very different from PVDF in that it is a slow crystallizing polymer (due in part to its stiff backbone and bulky aromatic groups) with relatively high T_g (glass transition temperature) in comparison to PVDF. Slow crystallizing polymers are typically processed between T_g and T_{ll} (liquid-liquid transition temperature), and away from T_{cc} (cold crystallization temperature) to maximize effects of strain hardening and minimize thermally induced crystallization - both of which lead to thickness uniformity by preventing necking from non-uniform stress distributions in the film [72], [218]. A uniform, semi-crystalline morphology formed in the slow-crystallizing polymer bulk has been shown to lead to an increase in electrical breakdown strength; the same strategy used in the current

high energy density BOPP material [219], [218]. Conversely, PVDF is a fast crystallizing polymer due to its relatively less bulky, flexible chains. It is advantageous to stretch such materials in the partially molten state to ensure affine-like deformation [72]. It is important to note that the processing strategy for these two polymers is very different, and thus uniaxial orientation processing strategies explored in Chapter 3 were applied to this study, with added quantitative thickness uniformity analysis.

Heat setting of slow-crystallizing polymers is an important processing step in which films, especially following orientation, are heated to just below their melting point, giving chains the thermal energy necessary for rearrangement via relaxation, crystal melting, and re-growth to help improve film properties and increase thermal stability (i.e. reduce shrinkage when re-heated). The purpose of this study is to determine how morphology of oriented microlayer films can be further tailored by use of constrained annealing and its effects on dielectric properties.

The versatility of the microlayer coextrusion process makes a good candidate for improving dielectric properties of polymer films. Our previous work (Chapter 3) provides a more in-depth overview of the method used to produce multilayer films and further orient them uniaxially, and it has been well reviewed elsewhere as well (see [2], [177], [56]). This study focuses on the development of dielectric properties in oriented and further annealed microlayer polymer films. Carr et al. reviewed confined crystallization of nanolayered polymer films, including materials poly(ethylene oxide), poly(ϵ -caprolactone), polypropylene, and poly(vinylidene fluoride) [177]. This study links morphology development to gas barrier properties, and high gas barrier is known to be linked to high dielectric breakdown. Specifically, this review states that whether the confining substrate is amorphous or crystalline changes how confined morphology develops in the system, leading to variable end properties [177]. This work has important implications linking selection of polymer materials, with or without the use of recrystallization, to dielectric and gas barrier property development. However,

the review by Carr in 2011 does not show effects of uniaxial or biaxial orientation on barrier or dielectric properties [177].

Recently, however, Carr and co-workers studied effects of biaxial orientation of polyvinylidene fluoride-co-tetrafluoroethylene (PVDF-TFE) copolymer and polyethylene terephthalate (PET) microlayer films on dielectric properties, and found that morphological structure in both layers had an effect on dielectric properties [146]. Specifically, they found that on-edge PVDF-TFE crystals improve dielectric constant and breakdown strength [146]. The same polymer system, PET and PVDF-TFE nanolayer films, was studied further by A. Jordan et al., who used in-situ wide angle X-ray scattering during orientation to show that confined crystallization of PET and PVDF-TFE during biaxial orientation and melt recrystallization caused in-plane, single crystal-like structure [207]. This unique morphology led to higher percent crystallinity and higher modulus of the nanolayer films [207]. Also, Yin and co-workers used polymethylmethacrylate polymer (PMMA) as a tie layer to further modify the interface between PET/PVDF-HFP nanolayer films [208]. By varying the amount of tie layer, researchers determined an optimum PMMA content to be 8 vol%, and that interdiffusion between PVDF-HFP and PMMA layers during biaxial stretching led to an increase in β -PVDF crystal formation, resulting in a decrease in dielectric loss [208]. Yin also found that breakdown strength was improved by around 33%, and energy density at breakdown was increased by 150% compared to PET/PVDF-HFP films as extruded and without the use of PMMA tie layer [208].

Recently, Baer and Zhu reviewed dielectric properties of multilayered films [2]. Along with the literature listed above, this work is an excellent review of limitations of dielectric polymers, and how microlayering process can be used to overcome these downfalls. Specifically, they note that orientational polarization is a potential approach to increasing polymer dielectric constant while maintaining low losses [2]. PVDF and its co-polymers are discussed because they can reach dielectric constant of 50-70, but have high losses; however it is postulated in this review that losses can

be overcome by layering PVDF with high breakdown and low loss polymers such as PC (polycarbonate) and PSF (polysulfone) [2]. Finally, it is noted that complex polymer solutions to dielectric property improvement should be affordable and able to be scaled up to an industrially relevant process in order to be considered as a feasible solution to replacing dielectric BOPP film [2].

Since PVDF is a highly crystalline polymer, we expect crystal form to play a significant role in its properties. Only a few studies exist in the literature which evaluate the effect of PVDF crystal form on dielectric properties. In 1999, Gregorio and Ueno studied the permittivity and conductivity of α and β -PVDF, reporting that crystal form strongly affects dielectric constant and that orientation increases dielectric constant for both of these crystal forms [26]. Gregorio and Ueno did not, however, consider other PVDF crystal forms. Li, et al. studied PVDF films with primarily α , β , and γ forms and found γ -PVDF films to have the highest breakdown strength (around 400 MV/m) [239]. More recently, Zhao, et al. ran a similar experiment and found γ -PVDF to have highest relative permittivity, slimmer hysteresis loop and a lower leakage current than films containing primarily α or β crystal forms, and that all three had similar loss behavior [28]. These studies seem to suggest high γ -PVDF films will have better dielectric properties, but many factors influence these results such as film fabrication method, orientation, crystallite size, etc. therefore this topic requires further, in-depth study.

Though research involving the orientation of similar microlayered polymer systems containing PET or other high breakdown strength polymer, and PVDF or its copolymers exist, ours is unique in the potential to track true stress, true strain, and birefringence in real-time during orientation and heat setting, providing a more complete picture of how molecular mechanisms (such as orientation, crystallization, and relaxation) change during these processes. The current study builds on information gained previously during small scale uniaxial orientation of microlayered PET/PVDF

32L films (see Chapter 3), by exploring annealing strategies and their effects on crystalline morphology and texture development.

4.2 Materials and experimental procedures

Materials used in this work are Laser+ C 9921 (F65A) poly(ethylene terephthalate) (PET) from DAK Americas (IV 0.80 dL/mg as specified by the supplier), and Solef 6008 homopolymer poly(vinylidene fluoride) (PVDF) from Solvay. The materials and microlayer cast film consisting of 32 alternating layers of 50:50 v/v PET:PVDF were provided by PolymerPlus, Inc. Films were produced at a coextrusion temperature of 260°C and cast onto a chill roll kept at 85°C. The films had an initial thickness of approximately 125-140 microns and were laminated with polyethylene (PE) skin to protect layers during extrusion and prevent damage to the film during storage and handling. This PE layer was removed before subjecting the film to additional processing or testing.

Films were cut into 14 cm x 14 cm squares then stretched to various stretch ratios in UCW mode at 20 mm/min and 150°C. Before stretching, films were allowed thermal equilibration time of 15 minutes in the preheated chamber. After stretching, films were held taut and quenched by blowing cold air until they reached room temperature (about 30 minutes) to lock in morphology. Selection of processing temperature will be explained later, in Section 4.3.1. Films were stretched using an instrumented uniaxial/biaxial stretching machine, referenced in Section 2.5.2, and reviewed in more detail elsewhere [211].

Spectral birefringence technique was adapted to an annealing chamber which simulates the heat setting process of a constrained polymer film and can measure retardation of a white light source passing through the sample in real time [77], [212]. Experimental setup is shown in Figure 4.1.

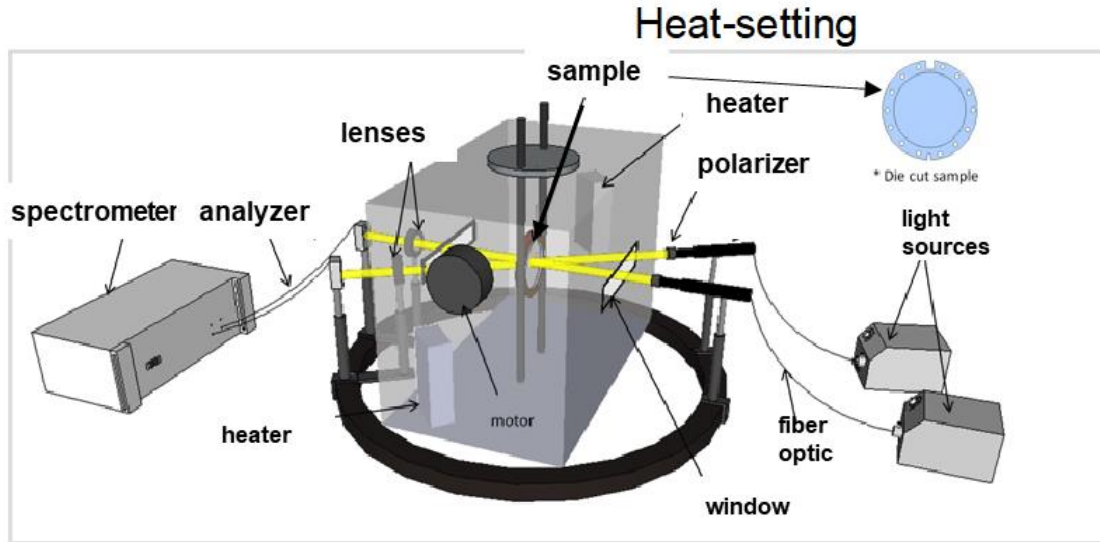


Fig. 4.1.: Annealing chamber illustration and experimental setup.

The spectral birefringence sensor assembly consists of an optical train including a white light source and polarizer, followed by the sample and analyzer. One light source is placed on the same axis location as the sample, 0° , and the other at a 45° crossed position, allowing for the detection of both parallel and perpendicular light intensity signals [211]. Intensity versus wavelength curves are produced, and retardation due to sample interference is calculated by mathematically determining peak points of these spectral curves [211]. Resulting retardation versus wavelength data are fit to a line curve using the Cauchy equation [211].

From retardation values, in- and out - of plane birefringence can be calculated as follows:

$$\Delta n_{12} = \frac{R_o}{d} , \Delta n_{23} = -\frac{1}{d_o} \left[\frac{R_o - R_\phi \left(1 - \frac{\sin^2 \phi}{n^2}\right)^{1/2}}{\frac{\sin^2 \phi}{n^2}} \right] \quad (4.1)$$

Where d_o is film thickness, R_o retardation of film in normal direction, R_ϕ is retardation tilted to $\phi = 45^\circ$ and \bar{n} is average refractive index of the film. Both light sources are polarized using a Glan-Taylor prism and focused via collimating lenses to the geometric center of the sample [211]. The spot size of the light, position, and intensity can all be adjusted to ensure accurate acquisition of retardation data [211]. Light passing through the sample is then sent to fiber optic detectors connected to a four channel spectrometer which measures retardation of light intensity [211]. The machine also gives a reading of percent transmission parallel and perpendicular to the film during the experiment.

The film sample is constrained inside a metal sandwich frame to prevent shrinkage during annealing, then rapidly inserted into a pre-heated chamber so that nearly instantaneous readings of birefringence are detected [77]. When the experiment is complete, the sample drops through a slit at the bottom of the chamber into a cold water bath to quench and freeze in morphology, which can be further studied via off-line techniques such as DSC, X-ray scattering, electron microscopy, etc [77].

After stretching, select films were delaminated into separate layers so that PVDF crystal form could be studied more closely and without effects of the composite structure. This was done by applying tape and mechanical force to the films to force immiscible layers apart. Appendix A Figure B.1 shows confirmation via FTIR that a single PVDF layer was obtained via this method.

Thermal properties were measured on film control and samples after stretching using Netzsch DSC 214 Polyma differential scanning calorimeter, using a heating rate of $10^\circ\text{C}/\text{min}$ in dry nitrogen atmosphere. Percent crystallinity of each material was calculated using enthalpies of heat of fusion for 100% crystalline polymer, ΔH_o of 105 J/g for PVDF and ΔH_o of 140 J/g for PET [221], [144].

Wide angle X-ray measurements were run on Bruker D8 Quest diffractometer with kappa geometry, an I- μ -S microsource X-ray tube, laterally graded multilayer (Goebel) mirror single crystal for monochromatization, and Photon2 CMOS area detector.

Generator was operated at 50 kV at current of 1 mA, beam was monochromatized at Cu K-alpha radiation ($\lambda = 1.54178\text{\AA}$) and samples were irradiated for 1 minute. Small angle X-ray scattering characterization was done on an Anton Paar SAXSpoint 2.0 machine containing microfocus Cu K-alpha radiation, $\lambda = 1.54178\text{\AA}$, source and two dimensional, Eiger R hybrid photon-counting detector. Generator was operated at 50 kV at current of 1 mA, and samples were irradiated for 15-30 minutes, depending on their thickness. Single layer PVDF SAXS samples were irradiated for 6 hours. SAXS and WAXS images were taken in both film normal (through film thickness) and transverse directions.

FTIR measurements were taken on Thermo Nicolet Nexus FTIR, with diamond ATR, a KBr beam splitter, and an MCT detector and 0.125 cm^{-1} spectral resolution.

Atomic force microscopy images (AFM) were taken on Veeco Dimension 3100 AFM and images were processed in Gwyddion software. This machine has X,Y scan range of $90\text{ }\mu\text{m}$ square, with lateral accuracy between 1-2%. The Z-range is $5\text{ }\mu\text{m}$ and resolution is 16-bit. Measurements were performed in tapping mode using variable drive voltage to optimize tapping conditions for each individual sample.

4.3 Results and discussion

PET and PVDF's ideal processing windows do not overlap and therefore selection of processing temperature is crucial to produce usable samples. The following sections discuss relevant considerations in determining ideal processing temperatures for 32L PET/PVDF microlayer film, including initial morphology at desired stretching temperature and its validation using isothermal crystallization in DSC, as well as quantitative measure of thickness uniformity.

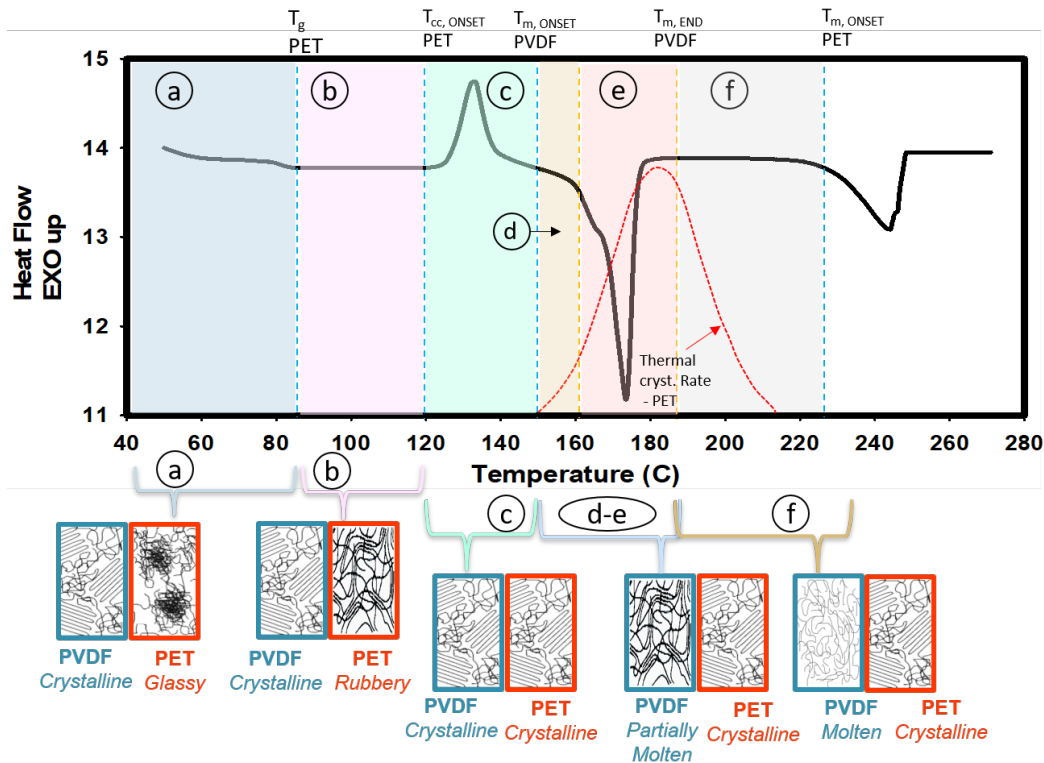


Fig. 4.2.: Cartoon representation of morphological states of each polymer in different regions of the DSC curve. In (a) PVDF is semi-crystalline, PET is amorphous and glassy, (b) PVDF is semi-crystalline, PET is amorphous and rubbery, (c) PVDF and PET are semi-crystalline, (d) PVDF partially molten, PET semi-crystalline, (e) PVDF partially molten, PET semi-crystalline, (f) PVDF fully molten, PET semi-crystalline, and (f) PVDF fully molten, PET partially molten.

4.3.1 Selection of processing temperature

Thermal characterization of the film as received is shown in the DSC curve in Figure 4.2, highlighting the different morphological states of each material during specific temperature ranges; an important item to note when selecting stretching temperatures. Since PET and PVDF are immiscible, the DSC curve in Figure 4.2 shows distinct thermal transitions for each polymer separately. Figure 4.2 (a) highlights the temperature range in which PVDF is semi-crystalline and PET is amorphous and glassy. Neither PVDF nor PET deform ideally in this temperature range. In region (b), PVDF is semi-crystalline and PET is amorphous and rubbery. Due to slow crys-

tallizing behavior of PET, it can be quenched into amorphous state and when reheated between T_g and T_{cc} it behaves rubbery. This is ideal stretching state for PET as the thermal crystallization rates are too low for nucleation and growth of crystallites. PVDF, on the other hand, has high percent crystallinity even as cast, after quenching, since it is a fast crystallizing polymer. PVDF is in solid, semi-crystalline state in the temperature range highlighted as (b). Stretching in region (b) is not favorable for PVDF layers, and caused substantial necking in samples stretched both in UCW and attempted biaxial modes. In (c), both PVDF and PET are semi-crystalline, as this region encompasses the cold crystallization peak of PET. Again, stretching in solid state region is not favorable for either material, so we do not expect ideal deformation behavior in (c). Region (d) was found to be the only viable stretching window for this microlayer film. In (d), PVDF is on the verge of being partially molten, and PET undergoes thermal crystallization at a rate determined by the red dashed line in Figure 4.2. Region (d) occurs between 145-155°C, where PET has relatively slow thermal crystallization rate. In the very small processing window (d), the microlayer film deforms the most uniformly in thickness and without appreciable necking, as will be demonstrated in the following sections. At 155°C, shown in region (e), appreciable onset of melting for PVDF occurs and, as the temperature increases, molten fraction increases until it reaches the equilibrium melting temperature around 185°C. All the while, from the end of T_{cc} for PET in the beginning of region (d), until the end of region (e), PET undergoes thermal crystallization at an increasing rate. After region (e), PET is still semi-crystalline but kinetics dictates that the rate of thermal crystallization now decreases with increasing temperature through region (f). PVDF is nearly fully molten in region (f) and although PET can carry the system to stretch a small amount, appreciable stretching could not be accomplished in this temperature range. As temperature increases to region (g) PET becomes partially molten while PVDF is fully molten and the film loses stretching integrity. This fact, along with the temperature limits of the machine, means stretching in region (g) is not practical. In summary, 32L PET/PVDF microlayer film has a very small processing window as

dictated by starting morphology of each polymer layer at desired stretching temperatures. Specifically, this film stretches most ideally at 150°C, after cold crystallization peak of PET but before rate of thermal crystallization for PET is too high and before appreciable onset of melting for PVDF, but high enough temperature to deform PVDF crystals which are already in the film. In actual experiments, attempts to stretch the 32L film sample at any temperature outside of range (d) shown in Figure 4.2 led to either necking or premature sample breakage.

4.3.2 Isothermal crystallization simulation at 150°C

Samples considered for annealing were stretched in uniaxial constant width (UCW) mode at 150°C because they had the best quality and thickness uniformity, as will be

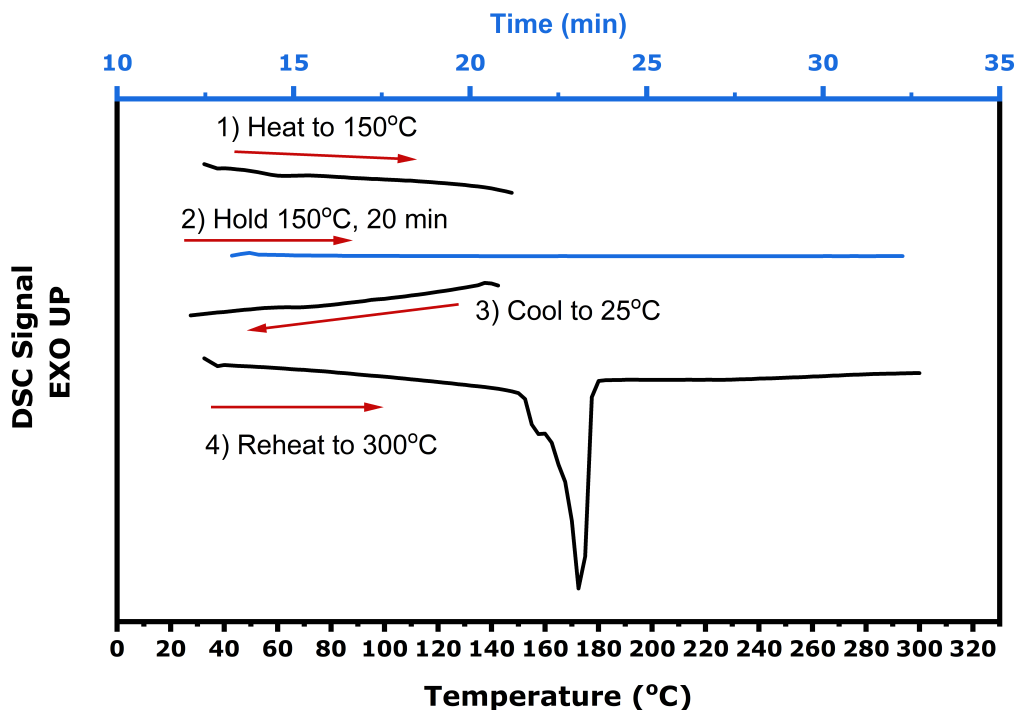


Fig. 4.3.: Isothermal heating experiment for PVDF layer delaminated from 32L film as cast, conducted in DSC to simulate morphology development during thermal equilibration step prior to stretching. Program: heat from 25°C to desired 150°C at 20 K/min, hold 15 min, cool to 25°C at 20 K/min, reheat to 300°C at 10 K/min.

detailed in the next section. To understand this phenomenon better, an isothermal heating simulation was conducted in the DSC for a single PVDF layer, as shown in Figure 4.3. The procedure was: heat from 25°C to desired temperature of 150°C at 20 °C/min, hold isothermal for 15 min then cool to 25°C at 20 °C/min and finally, reheat to 300°C at 10 °C/min. The isothermal heating experiment in Figure 4.3 simulates morphology development during the 15 minute thermal equilibration step prior to stretching, where we see that PVDF has a very small partially molten fraction at this temperature. In step 1, we do not see obvious PVDF melting, however in the reheating step 4, an additional shoulder appears around 153°C on the main PVDF melting peak of 176°C (compare to only one shoulder in film as cast curve, Figure 4.2) which is due to melting of small PVDF crystals when held isothermally at 150°C.

4.3.3 Quantitative thickness uniformity evaluation

Quantitative evaluation of thickness uniformity was conducted by drawing a 1cm x 1cm square grid on film samples and measuring thickness at each grid intersection before stretching, as shown in Figure 4.4. Thickness values were recorded, along with their position in the sample, and measured again (in the same positions) after stretching. By comparing thicknesses at a specific spot in the sample after stretching to the thickness in the film as prepared, we can get an idea as to how uniform the sample deformation is during stretching.

The standard deviation of thickness uniformity in this case is defined as:

$$\theta = \sqrt{\frac{\sum(x - \bar{x})^2}{n}} \quad (4.2)$$

Where θ is standard deviation of thickness uniformity, x is ratio of final to original thickness, and n is the number of spots measured in the grid drawn on the film.

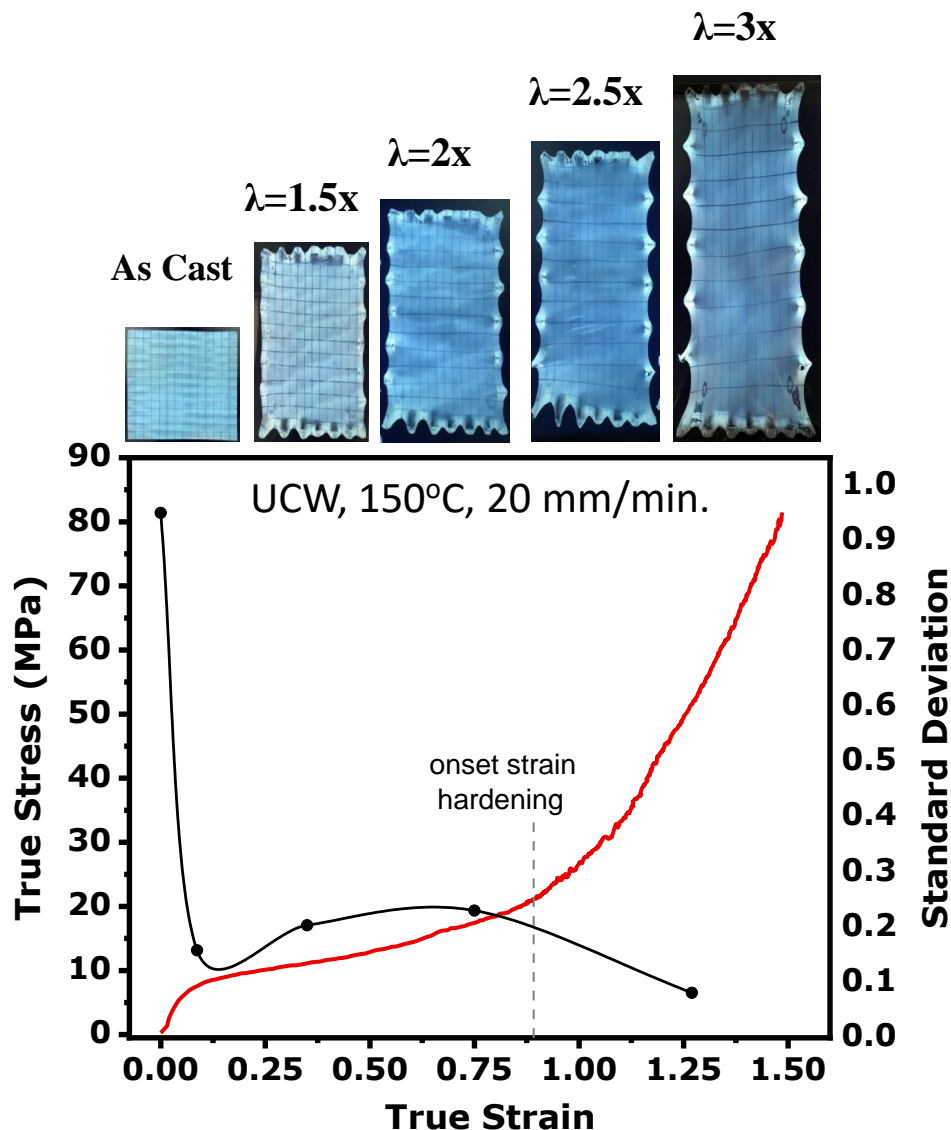


Fig. 4.4.: Quantitative evaluation of thickness uniformity for 32L film stretched in UCW mode at 150°C at 20 mm/min.

Figure 4.4 shows a comparison of standard deviation of final to original thickness measurements to true stress, true strain behavior of film sample stretched in UCW at 150°C. It is well known that to achieve homogeneous properties throughout a polymer film, thickness uniformity is crucial, as studied by Iwakura, who found that the mechanism of strain hardening decreases thickness deviation and surface roughness

in PET films [14]. Up until the point of strain hardening, due to re-orientation of the phenyl rings in PET chains, however, thickness uniformity first becomes worse and then improves (after strain hardening) [14]. This phenomenon was observed for microlayer PET/PVDF films also, as depicted in Figure 4.4.

4.3.4 Annealing Experiments

The above analysis of thickness uniformity and sample quality is crucial because measurement of optical properties in annealing experiments will not be accurate if thickness of the sample is not uniform. For this reason, optical data are only shown for samples stretched in UCW mode to 3.5X1, otherwise thickness non-uniformity prevents capturing of accurate data (i.e. because sample thickness is needed to determine birefringence).

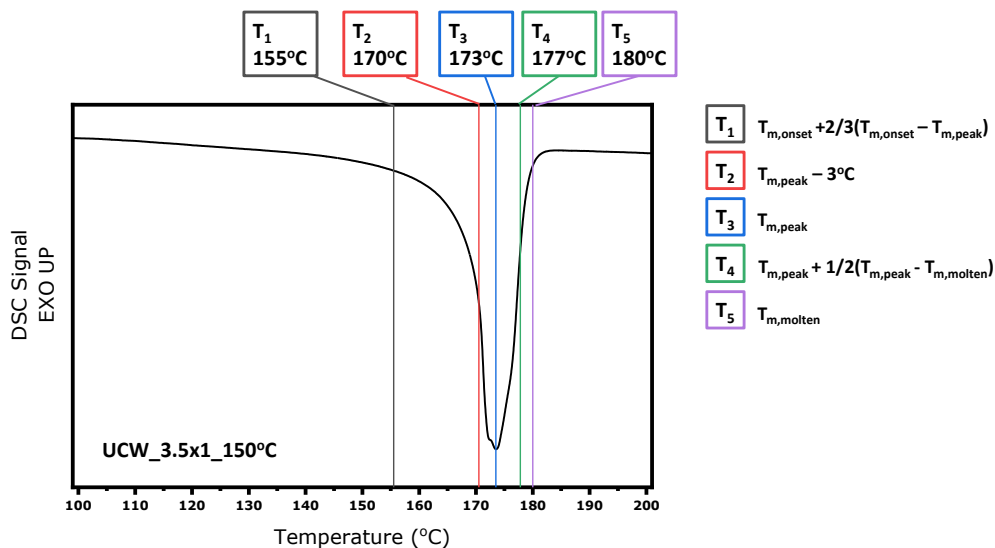


Fig. 4.5.: Close-up of PVDF melting peak DSC curve to prove explanation of selection of annealing temperatures for microlayer sample stretched in UCW mode to 3.5X1, at 150°C and 20 mm/min.

Annealing temperatures were chosen as described in Figure 4.5, which shows PVDF melt peak (from DSC) for sample stretched in UCW mode to 3.5X1 at 150°C and 20 mm/min. Temperature T_1 is $\frac{2}{3}$ of the way between $T_{m,onset}$ and $T_{m,peak}$ of PVDF, T_2 is 3°C less than $T_{m,peak}$, T_3 is peak melting temperature of PVDF, T_4 is $\frac{1}{2}$ way between $T_{m,peak}$ and $T_{m,end}$ for PVDF, and at T_5 , PVDF is near fully molten state. Selection of annealing temperatures for UCW samples stretched to ratios other than 3.5X1 were standardized in this manner as well, since PVDF melting peaks differ for films stretched to different draw ratios.

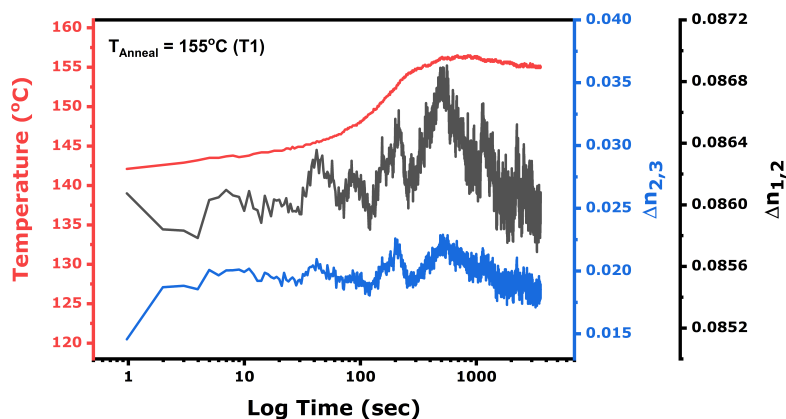


Fig. 4.6.: Birefringence during 1 hour annealing at T_1 , 155°C for 32L film stretched in UCW mode to 3.5X1 at 20 mm/min and 150°C.

Birefringence versus 1 hour annealing data are shown in Figures 4.6 to 4.10, at the five annealing temperatures described above, with real-time temperature measurements, along with in-plane (Δn_{12}) and out-of-plane (Δn_{23}) birefringence. We report actual measured temperature because, although the system is closed and birefringence can be measured nearly instantaneously, some heat escapes when the sample is inserted into chamber, thus the process is not isothermal at the beginning of the experiment. For the sample annealed at $T_1 = 155^\circ\text{C}$, shown in Figure 4.6, both Δn_{12} and Δn_{23} are fairly constant during annealing experiment because neither PET nor PVDF have high molten fractions at this temperature and relaxation time and recrystallization

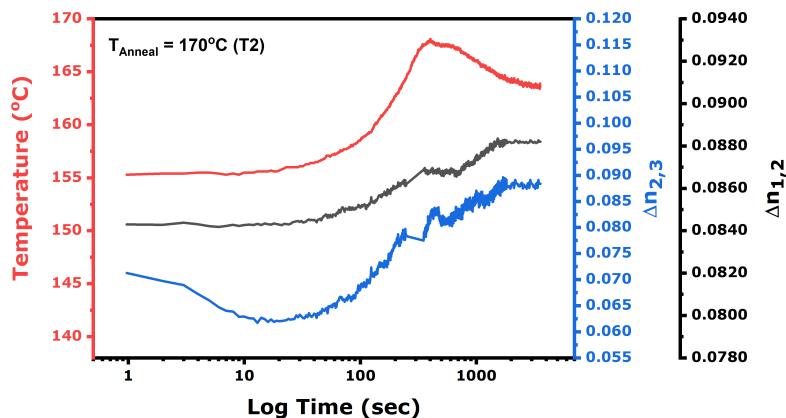


Fig. 4.7.: Birefringence during 1 hour annealing at T2, 170°C for 32L film stretched in UCW mode to 3.5X1 at 20 mm/min and 150°C.

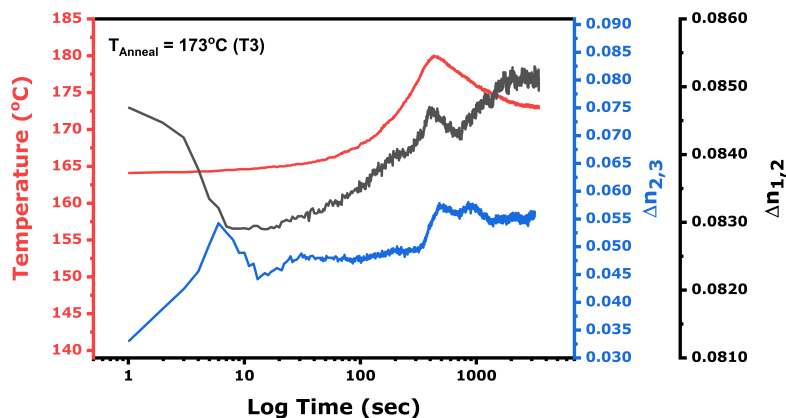


Fig. 4.8.: Birefringence during 1 hour annealing at T1, 173°C for 32L film stretched in UCW mode to 3.5X1 at 20 mm/min and 150°C.

of PET are relatively slow. Therefore, the morphology of the sample is not drastically changed while annealing at T1. When the sample is annealed at T2 = 170°C (as shown in Figure 4.7), Δn_{12} starts constant and then increases after about one minute annealing. The overall change in birefringence is not much, about 0.004, and is likely due to increase in percent crystallinity of PET from thermal crystallization. For T=170°C, Δn_{23} drops initially then begins increasing after about one minute annealing. Again, this is likely when PET thermal recrystallization begins at the given annealing temperature, causing an increase in birefringence, and the one minute time

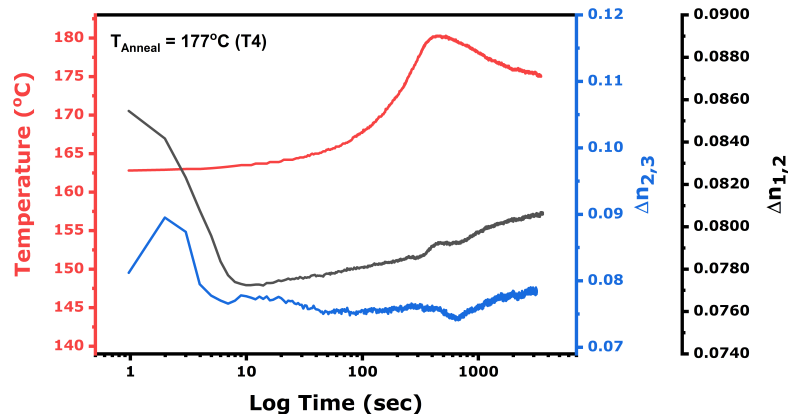


Fig. 4.9.: Birefringence during 1 hour annealing at T1, 177°C for 32L film stretched in UCW mode to 3.5X1 at 20 mm/min and 150°C.

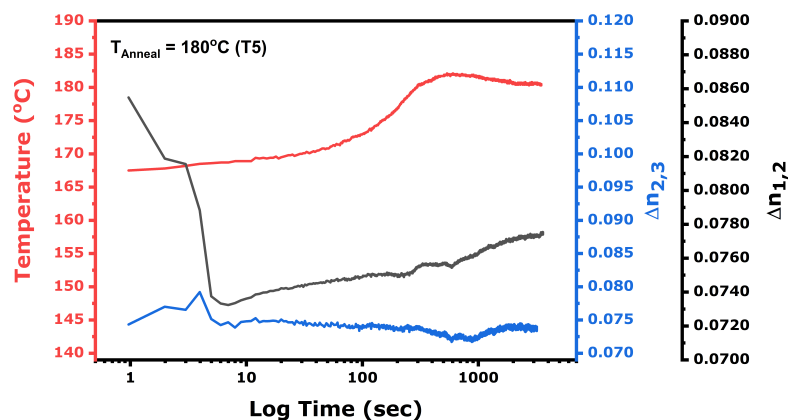


Fig. 4.10.: Birefringence during 1 hour annealing at T1, 177°C for 32L film stretched in UCW mode to 3.5X1 at 20 mm/min and 150°C.

frame also matches with the time at which heater system ramps up to match temperature set point. Δn_{12} for samples annealed at $T=173^\circ\text{C}$, $T=177^\circ\text{C}$, and $T=180^\circ\text{C}$ (Figures 4.8, 4.9, and 4.10, respectively) follows the same trend in which birefringence initially decreases then increases slowly over annealing time, beginning at the point when temperature begins to ramp up again to reach final set point. The heater tends to overshoot the desired final annealing temperature, leading to what appears to be changes birefringence, but are in fact a response to actual measured temperature in the system. This occurs at about 500 seconds in the experiments shown in

Figures 4.6 to 4.10. As annealing temperature increases (from $T=173^{\circ}\text{C}$ to 177°C then 180°C), the drop in birefringence at the beginning of annealing is higher, and the sample reaches a lower final value of birefringence. Initial drop in birefringence corresponds to melting of some amount of PVDF, therefore higher annealing temperature means higher molten fraction and therefore higher initial drop in birefringence. Larger increase in birefringence (after the initial drop) at higher annealing temperatures is caused by faster thermal recrystallization of PET and higher diffusion rates at higher temperatures, which leads to larger crystal size. Out-of-plane birefringence, Δn_{23} , for samples annealed at high temperatures $T=173^{\circ}\text{C}$, 177°C and 180°C first increases as PVDF partially melts then decrease slightly, before increasing again. The slight decrease in Δn_{23} could be caused by relaxation in PET chains before thermal crystallization occurs and birefringence begins to increase again.

The top graph in Figure 4.11 shows in-plane birefringence (Δn_{12}) and the bottom graph shows out of-plane birefringence (Δn_{23}) versus log of annealing time for all five annealing temperatures combined. Birefringence is a measure of crystallinity and molecular orientation so, since all samples were stretched at the same conditions (UCW, 3.5X1, 150°C), initial, in-plane and out-of-plane birefringence values should be approximately equal, which is mostly true for these samples. Exceptions in out-of-plane birefringence values which are not equal initially likely has to do with local thickness non-uniformities in the samples. After annealing, films were quenched quickly in cold water and characterized offline with DSC, X-ray scattering, FTIR, and AFM.

Temporal evolution study was carried out for the sample stretched at 150°C to 3.5X1 then annealed at 180°C because birefringence continued to increase after very long annealing time periods (16 hours). Figure 4.12 shows in-plane birefringence versus time, as well as measured annealing chamber temperature and SAXS and WAXS images for several annealing intervals. SAXS images for films after stretching show discrete arcs in meridional direction, indicating lamellae are stacked in stretching

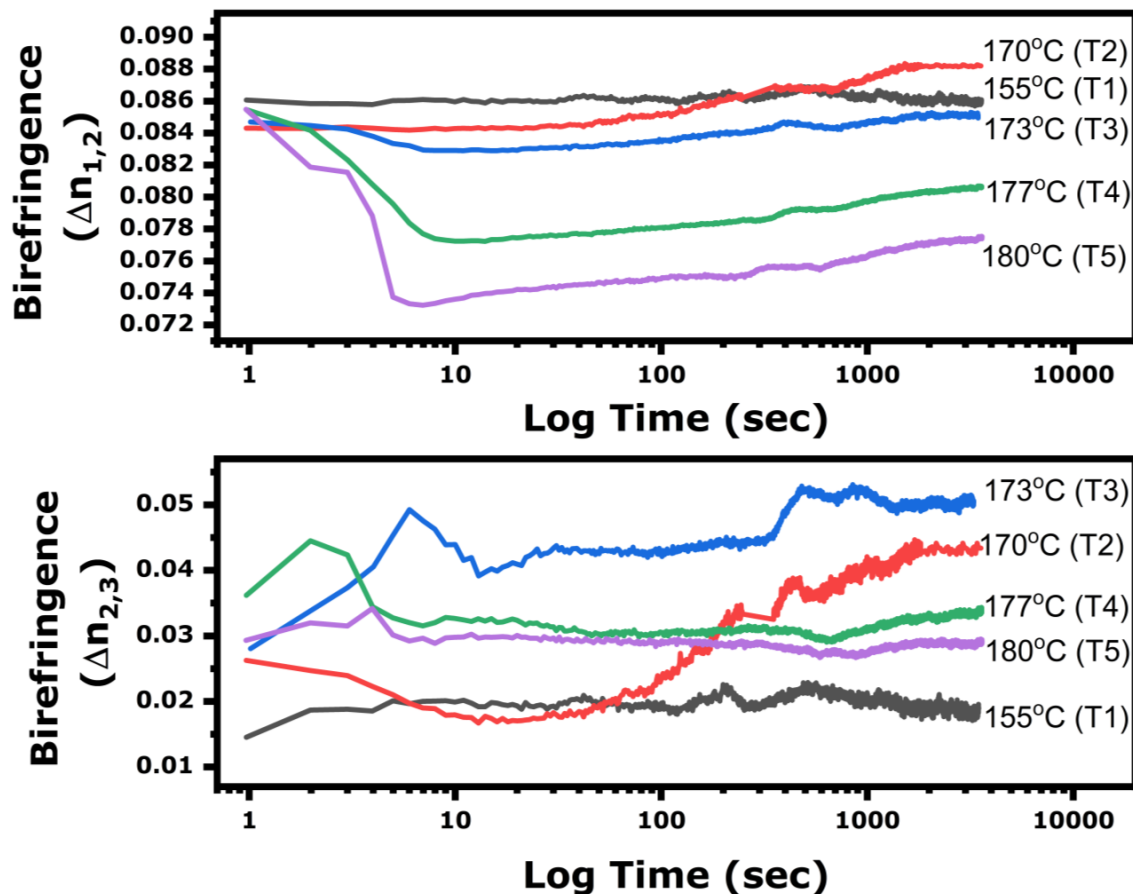


Fig. 4.11.: Evolution of birefringence during 1 hour annealing at specific temperatures for 32L film stretched in UCW mode to 3.5X1 at 20 mm/min and 150°C.

direction as indicated by relatively narrow arcs (compared to after annealing). After annealing even for 3 seconds, the diffuse isotropic ring reappears, indicating loss of some degree of order in lamellar stacking. However, there is still clear anisotropy in meridional direction, indicating lamellae overall are organized in MD. Increasing annealing time causes isotropic arc to be very slightly sharper, indicating increasing crystallinity and the size of the arc in y-direction becomes slightly smaller as annealing time increases, indicating increasing degree of crystal perfection as well.

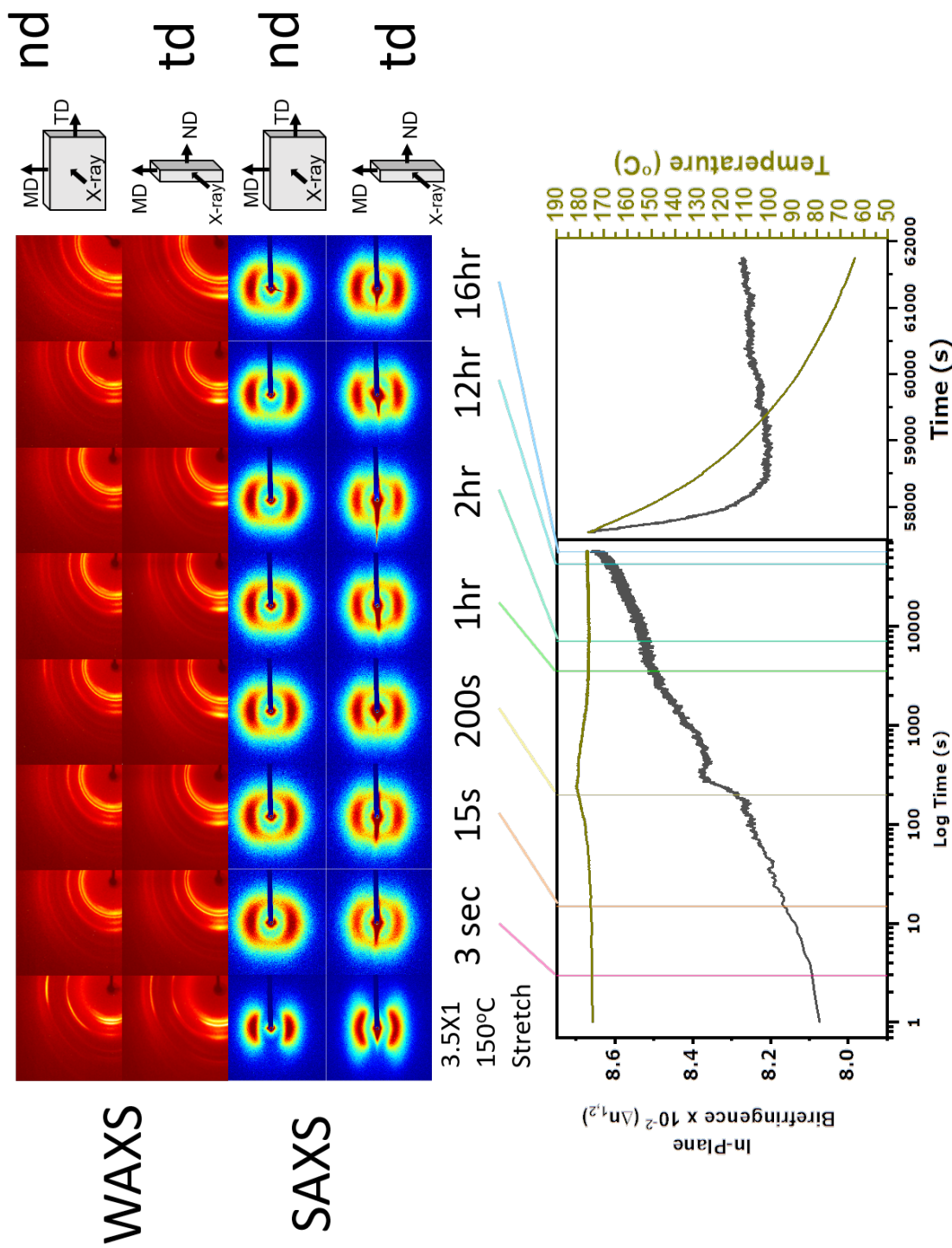
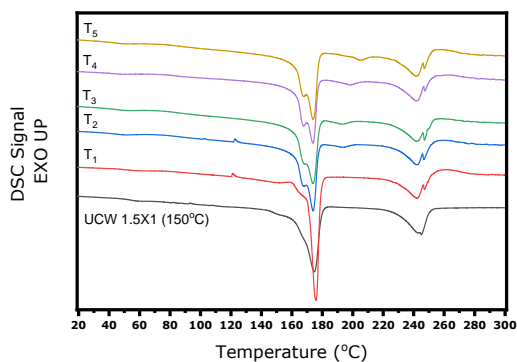


Fig. 4.12.: SAXS data for temporal evolution study for sample stretched at 3.5X1, 150°C, then annealed at 180°C, in which films were stretched to specific time intervals then quenched and studied offline for morphology development. (SAXS images for composite 32L film).

4.3.5 Characterization

Samples stretched in UCW mode to 3.5X1 at 150°C were annealed then characterized offline for morphology and tested for dielectric properties. The following sections discuss analysis of morphology for these samples by use of DSC, X-ray scattering (WAXS and SAXS), AFM, and FTIR methods.

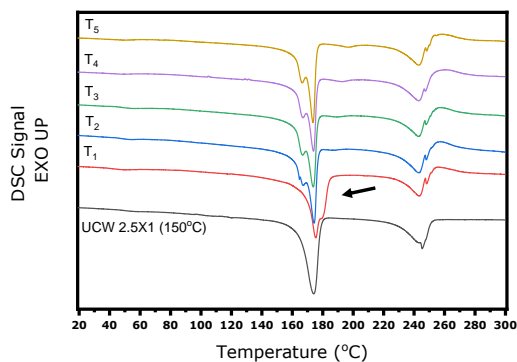
DSC Results



SAMPLE	UCW 1.5X1 , 20 mm/min, T = 150°C					
	As Stretched	156°C T1	172°C T2	175°C T3	179°C T4	184°C T5
α, β - PVDF $T_m = 167-175^\circ \text{C}$	63.5	50.8	52.5	56.0	52.8	58.4
γ - PVDF $T_m = 180^\circ \text{C}$	0	0	0.10	0	0	0
γ' - PVDF $T_m = 190-200^\circ \text{C}$	0	0	1.1	1.7	2.3	1.5
PET	25.5	26.3	19.7	19.7	19.4	18.6

Fig. 4.13.: Calculated percent crystallinity for PVDF crystal forms α , β , γ and γ' , and PET, corresponding to DSC thermograms shown for UCW samples stretched to 1.5X1 at 150°C and 20 mm/min and annealed for one hour at T_1 - T_5 .

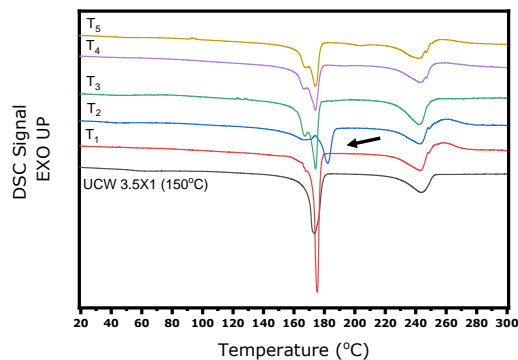
Figure 4.15 shows differential scanning calorimetry results for samples stretched in UCW mode at 150°C and 20 mm/min to 3.5X1. DSC is a useful method in distinguishing γ and γ' -PVDF from other polymorphs because they have a significantly higher melting point than either α or β -PVDF [25]. To clarify, γ form results from melt crystallization and γ' from solid-state transformation from α -PVDF. As ex-



SAMPLE	UCW 2.5X1 , 20 mm/min, T = 150°C					
	As Stretched	156°C T1	171°C T2	174°C T3	178°C T1	183°C T1
α, β - PVDF $T_m = 167-175^\circ \text{C}$	64.9	49.0	52.1	54.3	51.5	51.8
γ - PVDF $T_m = 180^\circ \text{C}$	0	18.1	0.18	0.51	1.3	1.6
γ' - PVDF $T_m = 190-200^\circ \text{C}$	0	0	0.18	0.51	1.3	1.6
PET	27.2	19.7	26.8	21.8	24.2	18.9

Fig. 4.14.: Calculated percent crystallinity for PVDF crystal forms α , β , γ and γ' , and PET, corresponding to DSC thermograms shown for UCW samples stretched to 2.5X1 at 150°C and 20 mm/min and annealed for one hour at T_1 - T_5 .

plained by Martins, γ and γ' are distinguished due to their significantly different melting temperatures [25]. Specifically, α and β -PVDF melt around 167-175°C, γ at about 180°C, and γ' from 190-200°C. After stretching to 3.5X1, PVDF has high percent crystallinity of 64% and PET about 24%. Annealing at low temperature (155°C) increases percent crystallinity of both PVDF and PET by a small amount (shown in Figure 4.15). Annealing at temperatures at or above PVDF's peak melting point (173°, 177°, and 180°C) appears to decrease the total percent crystallinity of PVDF, however changes in peak melting point suggest this is caused instead by formation of a small amount of γ and/or γ' -PVDF. Solid state phase transformation from primarily α to γ -PVDF are known to occur by annealing at high temperatures above about 160°C [115], [24]. Annealing at T_2 (170°C) led to high development of γ -PVDF (see arrow in Figure 4.15); the ratio of which is 50:50 by area to the main



SAMPLE	UCW 3.5X1 , 20 mm/min, T = 150°C					
	As Stretched	155°C T1	170°C T2	173°C T3	177°C T4	180°C T5
α, β - PVDF $T_m = 167-175^\circ \text{C}$	63.6	67.9	25.6	62.2	56.0	55.9
γ - PVDF $T_m = 180^\circ \text{C}$	0	0	24.3	0.20	0	0
γ' - PVDF $T_m = 190-200^\circ \text{C}$	0	0	0	0	0.39	0.10
PET	23.7	24.5	25.2	31.7	30.0	33.7

Fig. 4.15.: Calculated percent crystallinity for PVDF crystal forms α , β , γ and γ' , and PET, corresponding to DSC thermograms shown for UCW samples stretched to 3.5X1 at 150°C and 20 mm/min and annealed for one hour at T_1 - T_5 .

α -PVDF melting peak. This could significantly affect the film's dielectric properties, as mentioned in literature review [239], [28]. For qualitative comparison, DSC was also used to quantify crystal form for films stretched to 1.5X1 and 2.5X1 in UCW mode at 150°C and 20 mm/min, as shown in Figures 4.13 and 4.14, respectively. At the lowest stretch ratio, 1.5X1, a high amount of γ -PVDF was not observed after annealing at any of the temperatures studied. Stretching 2.5X1 led to relatively high percent γ when annealed at low temperature (156°C) with a ratio of about 25:75 γ to the main α -PVDF peak. This leads to three conclusions- First, that development of high amount of γ -PVDF requires a minimum amount of orientation in this micro-layer film system, secondly, higher level of deformation produces higher amount of γ -PVDF. Finally, at 3.5X1 stretch ratio (compared to 2.5X1) the annealing temperature must be closer to peak PVDF melting point in order to form this high γ -PVDF

population. This confirms the idea that orientation plays a role in development of PVDF morphology during annealing. In Figure 4.15, PET percent crystallinity is 24% after stretching and generally increases with increasing annealing temperature (after 3.5X1 stretching) due to increasing rate of thermal recrystallization. Higher stretch ratios lead to higher percent PET crystallinity after stretching due to strain induced crystallization and films stretched to a higher degree obtain higher overall percent crystallinity during annealing because of higher chain alignment in the sample as stretched (compare tables in Figures 4.13, 4.14, and 4.15). Finally, it should be noted that, while DSC percent crystallinity calculations should be accurate for PET, the polymorphic PVDF is not so straightforward. Each crystal form has a different density determined by its unit cell and the percent crystallinity values do not take these differences into account. From literature it is known that α phase is the most dense and β is the least, with γ phase being very similar in density to the α phase and has been described as a transitional phase between α and β [36], [225], [23]. Therefore, DSC can not be used as an exact quantitative measure of PVDF crystal form amounts in the films, but rather a relative value. If heat of fusion for 100% crystalline α , β , γ -PVDF values were known, we could use DSC to correctly quantify each crystal form; these values could not be found in the literature. Overview of which samples contained γ -PVDF is shown in Table 4.1 (β -PVDF is not expected to be present in any film samples produced for the present study).

X-ray Scattering and AFM

SAXS and WAXS data (for composite layered structure) are shown in Figure 4.16 for films stretched in UCW mode to 3.5X1, at 150°C and 20 mm/min and annealed for 1 hour at the five temperatures shown. SAXS is useful because it gives average lamellar morphology data in the sample on a macrostructural scale. In this case, after stretching we see a two point pattern with relatively broad arcs in the meridional position. This indicates lamellar regions are oriented in machine (drawing) direction on

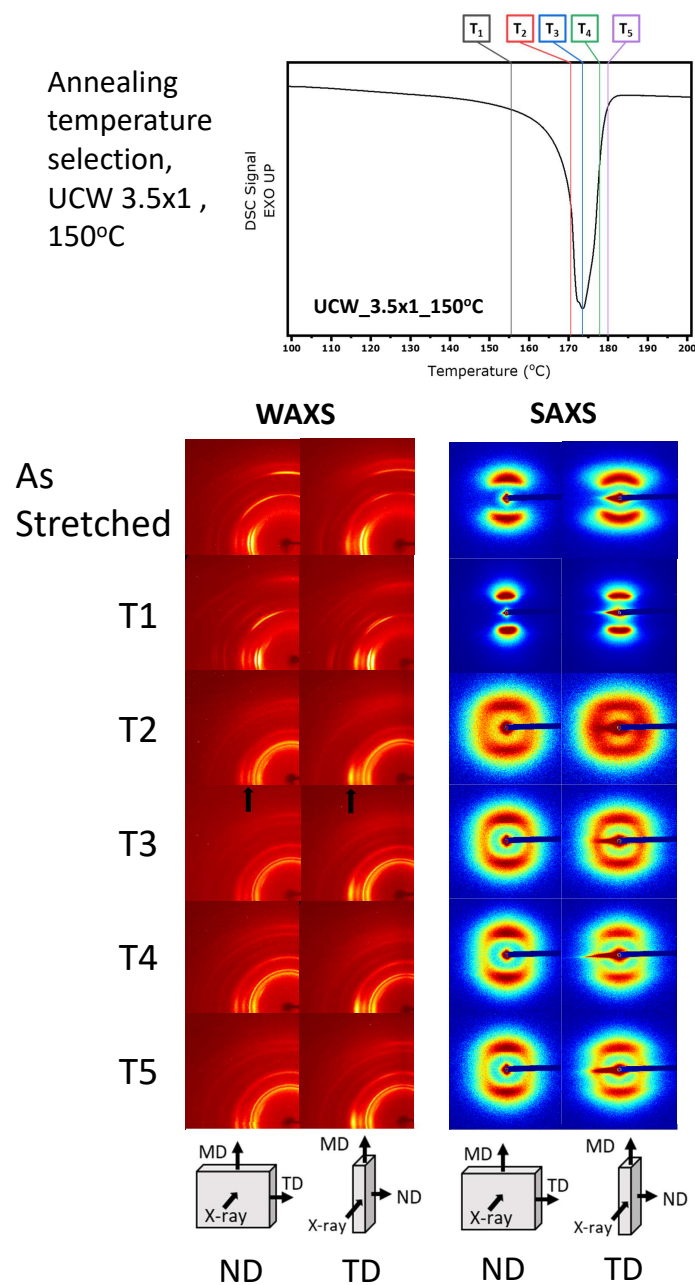


Fig. 4.16.: SAXS and WAXS images for 32L films stretched in UCW to 3.5X1 at 150° and 20 mm/min then annealed to select temperatures for 1 hour. (Both SAXS and WAXS pictured here are for composite structure. SAXS patterns for delaminated films shown next to AFM images).

average, and the azimuthal spread arc pattern (as opposed to a single point) indicates lamellae orientation in MD is not high. The relatively large breadth of these arcs indicates in scattering angle direction indicates a range of d-spacings in these samples. It must also be noted that SAXS patterns shown here are a combination of both PET and PVDF crystalline regions' scattering, since both materials are semi-crystalline and hence the interpretation of data is complex. Despite this, some general interpretations can be made from these data. Annealing at low temperature ($T=155^{\circ}\text{C}$), meridional arcs become smaller. Overall average organization of lamellar stacks remains in the machine direction after annealing at all temperatures. Annealing at higher temperatures, $T=170, 173, 177$ and 180°C , creates reduces scattering ring anisotropy in SAXS pattern taken in both ND and TD directions, presumably due to melting and relaxation of PVDF. Since annealing temperatures are above onset of PVDF melting peak, some degree of crystal melting occurs causing a loss in orientation in PVDF layers. SAXS patterns for lower draw ratios are shown in Appendix Figure B.2 with the only major difference being less MD lamellar organization, as indicated by broader arcs. SAXS data for delaminated PVDF layers is discussed in conjunction with AFM images.

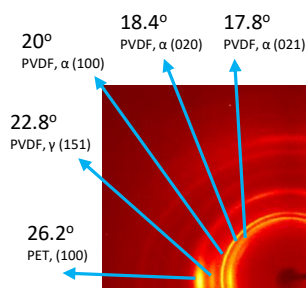


Fig. 4.17.: WAXS image with scattering peaks and corresponding crystal planes identified.

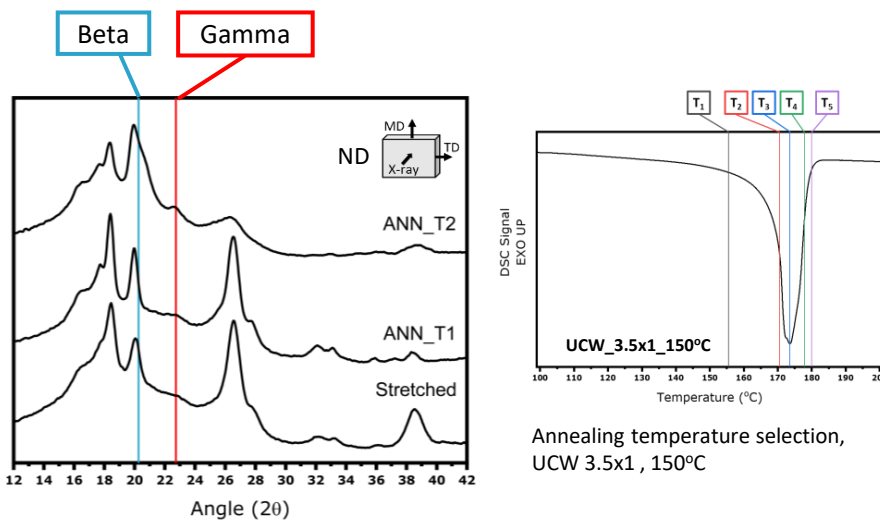


Fig. 4.18.: 1D WAXS data for 32L film at select annealing temperatures for 1 hour, 32L film stretched in UCW to 3.5X1 at 20 mm/min (composite film structure).

WAXS patterns are also shown in Figure 4.16, and peak identification is shown in Figure 4.17. Since WAXS results from individual crystalline planes, it can be used to detect different crystal forms of PVDF. However, since γ -PVDF is difficult to produce on its own and the crystal cells of α and γ -PVDF are similar, it is difficult to distinguish the two via this method; but β -PVDF is easily distinguishable [25]. Anisotropic arcs in all WAXS patterns pictured in Figure 4.16 indicate crystalline orientation primarily in the sample's machine direction. Compared to the as stretched image, $T=155^{\circ}\text{C}$ annealed sample shows sharper arcs at $2\theta = 26.6^{\circ}$, α (021) plane and $2\theta = 38.7^{\circ}$, δ (131) plane, especially evident in equatorial direction, which indicates higher amount of crystalline regions and/or higher crystalline perfection after annealing, which is to be expected. However, annealing above 155°C , orientation decreases as indicated by the peaks mentioned becoming more isotropic. Another interesting observation is that equatorial reflections from around $2\theta = 16\text{-}27^{\circ}$ are brighter in thickness direction scattering patterns compared to normal direction (example shown by black arrows on sample 170°C in Figure 4.16). This indicates higher orientation in TD and is likely due to confinement effect of thin layers. This was observed in

all scattering patterns, including the as-stretched sample and regardless of annealing temperature.

Figure 4.18 shows example 1D WAXS scattering data for the purpose of identifying PVDF crystal polymorphs. There are many diffraction peaks for each crystal form of PVDF and several for PET as well. The vertical lines in Figure 4.18 identify unique β ((200) plane at $2\theta = 20.6^\circ$) and γ ((151) plane at $2\theta = 22.8^\circ$) crystal planes. As mentioned above, α and γ are hard to distinguish by this method, and also most films likely contain some γ in addition to α even if DSC did not show high amounts of γ form. However, we can see in Figure 4.18 that the film annealed at $T=170^\circ\text{C}$ shows a much sharper γ peak at 22.8° , and this sample had a high amount of γ -PVDF as confirmed by DSC. None of the films pictured in Figure 4.18 show evidence of β -PVDF at $2\theta = 20.6^\circ$, which would appear as a much broader diffraction peak at that angle. Overview of which samples contained γ -PVDF is shown in Table 4.1.

AFM imaging and small angle X-ray scattering were run on single PVDF layers (delaminated from microlayer system) to obtain a clearer picture of how morphology of this complex material changes during annealing. Upon stretching to 3.5X1 draw ratio at 150°C , PVDF crystals are small and relatively well oriented in drawing direction, as shown in the AFM image in Figure 4.19a. An equatorial diffuse streak was observed in all SAXS images presented here, suggesting the presence of either microvoids or fibrillar structure [240], of which fibrillar structure is more likely since microvoids were not observed in the AFM images displayed in Figure 4.19. This fibrillar structure is the basis of the proposed structural model, depicted underneath each respective set of images with extended chain crystals in between. Annealing at 155°C , (Figure 4.19b) AFM image shows size of crystals becoming larger due to diffusion which causes lamellae thickening. Annealing near peak melting of PVDF allows some smaller crystals and crystal edges to melt and recrystallize upon cooling to form more perfect crystals (compared to as stretched sample). The SAXS pattern in Figure 4.19b shows evidence of more perfect

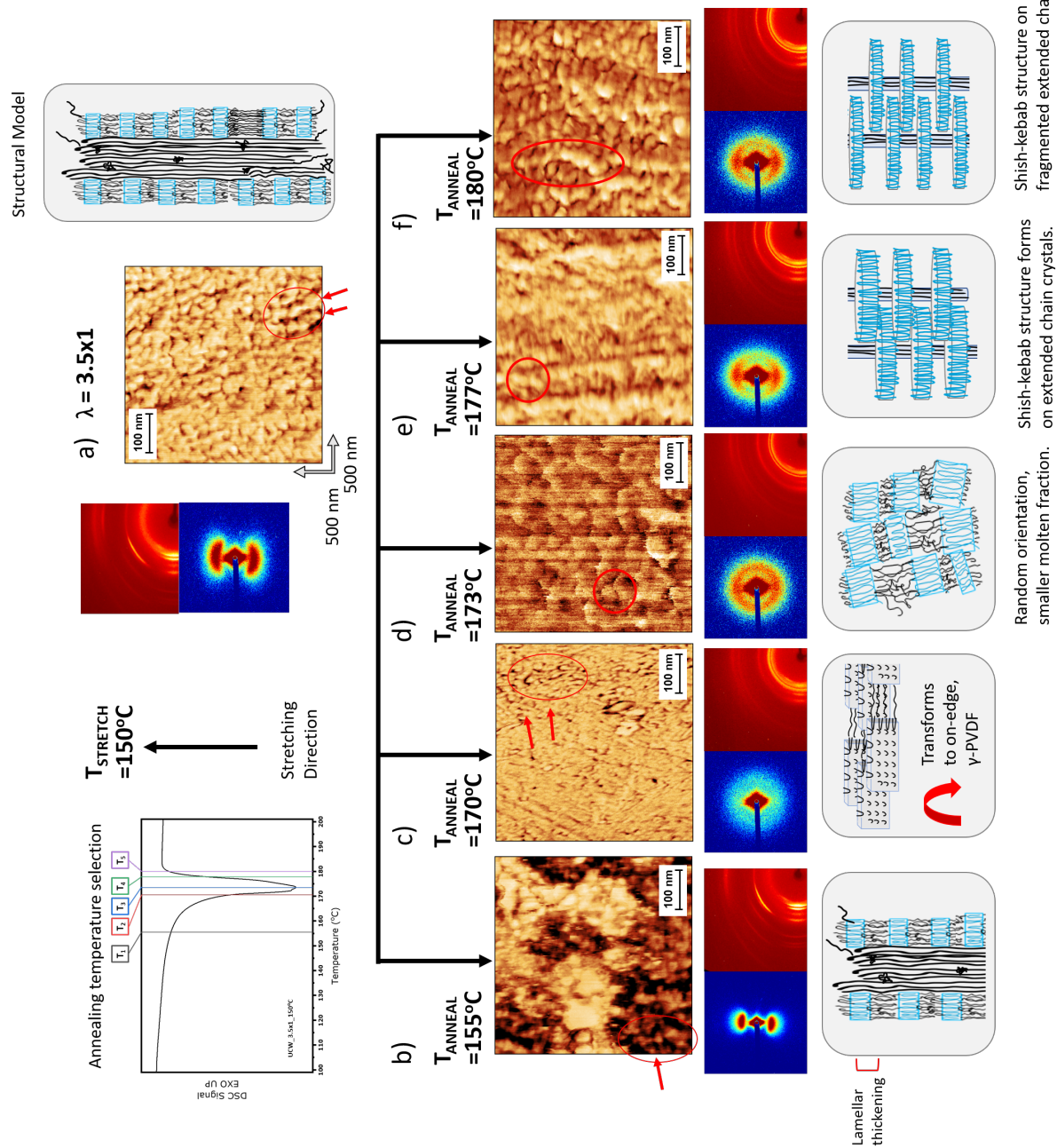


Fig. 4.19.: AFM phase images for a) 3.5X1, 150°C stretched film, annealed at b) 155°C, c) 170°C, d) 173°C, e) 177°C, and f) 180°C. AFM images are presented alongside SAXS patterns for PVDF only (delaminated from layered structure) and structural cartoon model is postulated.

crystals as well, due to smaller spot size as compared to as stretched sample in Figure 4.19a. The AFM image for sample annealed one hour at 170°C (Figure 4.19c) appears to be inconsistent with the neighboring series of images. However, recall from DSC evidence presented in Figure 4.15 that annealing at 170°C produces a large amount of γ form PVDF crystals, which likely explains the difference in size and shape of the crystals. Barrau, et al. showed AFM image containing α PVDF along with what they believed to be γ PVDF; the size and shape of which appears consistent with our findings here [241]. The SAXS image for Figure 4.19c shows little to no contrast, except for diffuse equatorial streak. This could be due to the unique arrangement of γ form PVDF in the plane of the film as hypothesized in structural model. The fact that the diffuse equatorial streak remains suggests order on a large scale, similar in size to fibrillar structure. Films in Figures 4.19d, e, and f were annealed at or above peak melting point of PVDF. SAXS image for sample annealed at 173°C (Figure 4.19d) shows mainly isotropic ring with some preferred lamellar organization in MD and this is corroborated in the AFM image. Additional crystal thickening occurs due to diffusion and partial melting of PVDF, as evidenced by larger crystallites shown in the AFM image. As annealing temperature increases to 177°C (Figure 4.19e) and 180°C (Figure 4.19f), SAXS patterns are nearly equivalent, with still isotropic ring present but more preferred lamellar organization compared to the SAXS image in Figure 4.19d. This can be explained by increased rate of diffusion at higher temperatures (compared to 173°C), allowing for improved rearrangement of chains in aligned crystalline regions. The proposed structural model for high temperature annealing is the formation of shish-kebab structure. At 177°C annealing (Figure 4.19e), the remnants of extended chain crystals remain intact, and melted and recrystallized chains form kebab overgrowths on these shish structures. At 180°C annealing temperature (Figure 4.19e), extended chains formed during stretching remain intact, however they are fragmented due to higher annealing temperature increasing molten fraction. Kebabs still grow on these central shish structures from molten and recrystallized chains.

FTIR Results

FTIR was also used to characterize PVDF crystal forms in these samples; a technique which is well documented in the literature for this purpose [229], [230], [25], [140], [93]. Several wavelengths are unique to PVDF crystal forms. For the purpose of this study 776, 833, and 840 cm^{-1} were useful in identifying γ form. A peak at 776 cm^{-1} indicates γ -PVDF is present. Also, β and γ -PVDF both show FTIR signature peaks at 840 cm^{-1} ; however if γ -PVDF is present, a clear double peak appears at both 833 and 840 cm^{-1} . An example curve is shown in Figure 4.20, in which clear γ -PVDF is shown for sample stretched at 3.5X1 in UCW mode, 20 mm/min, and 150°C then annealed at 170°C. This same procedure was applied to all films stretched in UCW then annealed from 155 to 180°C, and an overview of which samples contained γ -PVDF is shown in Table 4.1.

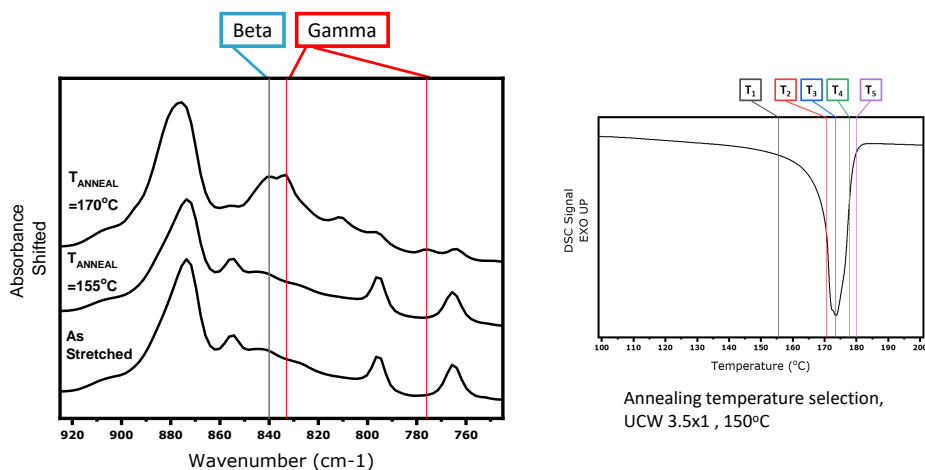


Fig. 4.20.: Select FTIR data for 32L film at select annealing temperatures for 1 hour, 32L film stretched in UCW to 3.5X1 at 20 mm/min (delaminated PVDF layer only).

Table 4.1.: Summary of γ -PVDF detected in samples stretched to 3.5X1 in UCW mode at 150°C and 20 mm/min, with or without annealing.

γ PVDF Characterization			
Annealing Temp.	DSC	FTIR	WAXS
Un-annealed	N	N	Y
155°C	N	N	Y
170°C	Y, High	Y	Y
173°C	Y	N	Y
177°C	Y	N	Y
180°C	Y	N	Y

Orientation Factors

From experimental WAXS data, crystalline orientation factors were calculated by taking an azimuthal scan of 2θ peak corresponding to the crystalline diffraction peak of interest and corrected for background scattering by subtraction of azimuthal intensity of a peak significantly far away from any scattering.

Mean-square cosine values were calculated from plane normals from corrected intensity distribution from WAXS data. The formula is as follows:

$$\langle \cos^2 \phi \rangle_{hkl} = \frac{\int_0^{\frac{\pi}{2}} I(\phi)_{hkl} \sin \phi \cos^2 \phi d\phi}{\int_0^{\frac{\pi}{2}} I(\phi)_{hkl} \sin \phi d\phi} \quad (4.3)$$

and crystalline orientation factor, f , is calculated by:

$$f_{(hkl)} = \frac{1}{2}(3 \langle \cos^2 \phi \rangle_{hkl} - 1) \quad (4.4)$$

where $\langle \cos^2 \phi \rangle_{hkl}$ is the mean-square cosine average over all crystallites of the angle between crystal and reference axis [214]. For any crystallographic axis, $\langle \cos^2 \phi \rangle = 1$ for perfect Z alignment, $\frac{1}{3}$ for random alignment, and 0 for perpendicularity. The value f_{hkl} therefore shows values of 1, 0, and $-\frac{1}{2}$, respectively.

PET has a triclinic unit cell, but Yoshihara and coworkers developed an approximated pseudo-orthorhombic unit cell to analyze crystalline orientation for PET [226], [232], [6]. Wilchinsky method for analyzing orthorhombic unit cell was used to calculate orientation factors from WAXS data of (100), polymer chain axis direction, and (010), perpendicular to aromatic benzyl ring. Unfortunately, due to the complex nature of PVDFs polymorphism, these peaks were not uniquely able to be distinguished (in composite film WAXS pattern) in order to perform this calculation.

PVDF α form has a monoclinic crystalline unit cell, therefore the (200) and (020) crystal planes can be used directly to calculate crystalline orientation factor. Crystal planes (200) and (110) can also be used with application of Wilchinskys method, as shown in the following equation [231]:

$$\overline{\cos^2\phi_{c,Z}} = 1 - 1.2647 \overline{\cos^2\phi_{110}} - 0.7353 \overline{\cos^2\phi_{200}} \quad (4.5)$$

For PVDF, orientation factors for α c-axis alignment are shown in Figure 16. α -PVDF crystals are not well oriented in as cast films, $f_c=0.2$, but become highly oriented, with f_c nearly 0.75 after stretching to 3.5X1. At T=155°C annealing, orientation factor for α -PVDF crystals is almost the same as the unannealed, stretched sample, due to the fact that no complex phase transitions or lamellae rearrangements can occur when little thermal energy is put into the system. This is seen in AFM image and portrayed in proposed structural drawing in Figure 4.19. As annealing temperature increases to 170 and 173°C, orientation factor again begins to decrease as α -PVDFs chain axis becomes less aligned with film stretching direction, due to partial (or full) melting at high annealing temperatures. Some orientation is retained, however, as indicated by the value of f_c still being higher than it was in the as cast film. Annealing at 177°C and 180°C, we see the orientation factor again begin to increase. This is due to lamellar thickening at high annealing temperatures which leads to crystal perfection and therefore higher degrees of orientation.

4.3.6 Dielectric properties

Dielectric constant and dielectric loss values are reported herein for UCW stretched and annealed samples at both constant (room) temperature and select samples in temperature ramping experiments. Though dielectric breakdown strength is of considerable interest to this study and the film of polymer capacitors, it could not be tested due to high film thicknesses.

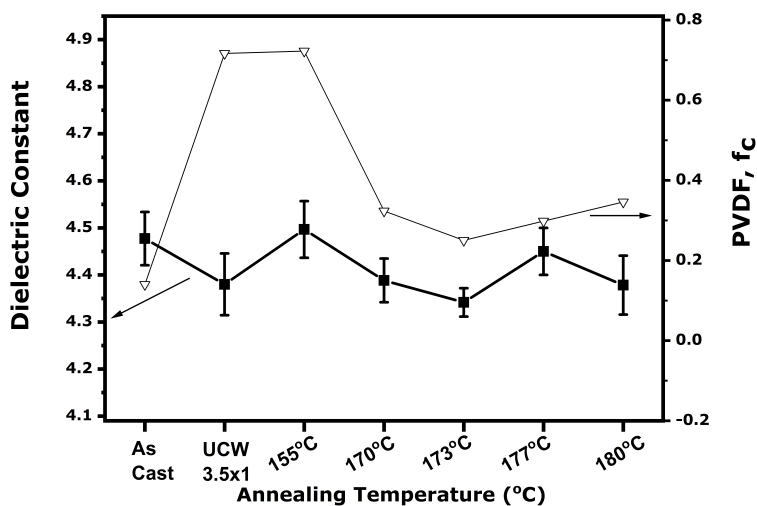


Fig. 4.21.: Dielectric constant measured at room temperature (left y-axis) versus calculated orientation factors for PVDF (right y-axis) for films stretched in UCW mode to 3.5X1, at 150°C and annealed at temperatures displayed on x-axis.

Dielectric properties measured at room temperature and 1kHz for samples stretched in UCW mode, 3.5X1, at 20 mm/min and 150°C, then annealed are shown in Figure 4.21, next to orientation factors calculated for PVDF. For this set of samples, overall dielectric constant value is similar in magnitude to the film as stretched, regardless of annealing temperature. Dielectric constant for sample annealed at 155°C is relatively high, then decreases steadily through annealing temperature 173°C, suggesting low temperature annealing, which retains α -PVDF c-axis alignment, may be beneficial to maintaining higher dielectric constant, as compared to the film as stretched.

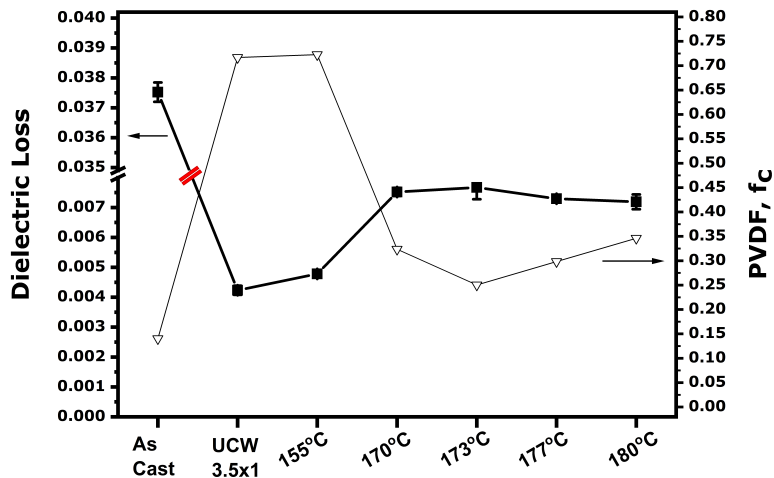


Fig. 4.22.: Dielectric loss measured at room temperature (left y-axis) versus calculated orientation factors for PVDF (right y-axis) for films stretched in UCW mode to 3.5X1, at 150°C and annealed at temperatures displayed on x-axis.

Furthermore, recall that these samples all had γ or γ' -PVDF except for the one annealed at 155°C, which has the highest dielectric constant, meaning γ or γ' -PVDF crystal forms may negatively impact dielectric constant value. Despite the high development of γ -PVDF in sample annealed at 170°C (as shown in Figure 4.15), dielectric constant for this sample does not show significant difference, either good or bad, from the normal trend in dielectric constant compared to other annealed samples. Since orientation factors for PET could not be calculated (due to overlapping WAXD peaks for these two materials), instead sample birefringence at end of annealing and percent crystallinity of PET are shown in Figure 4.23. Because PET is very birefringent in both amorphous and crystalline state, the measurement of birefringence tracks more strongly to PET, giving a sense of orientation and crystallinity during stretching and annealing. (A table of the materials intrinsic birefringence values can be seen in Chapter 3). For the case of dielectric constant, there is no strong correlation between orientation and crystallinity of PET and this property. One interesting point, however, is at annealing $T=155^\circ\text{C}$, where birefringence is lower than the film as cast, and percent crystallinity higher, whereas dielectric constant is also higher than sur-

rounding data points. This could mean that high percent crystallinity of PET with relatively lower orientation (lower in plane birefringence) is beneficial to improving dielectric constant of these films.

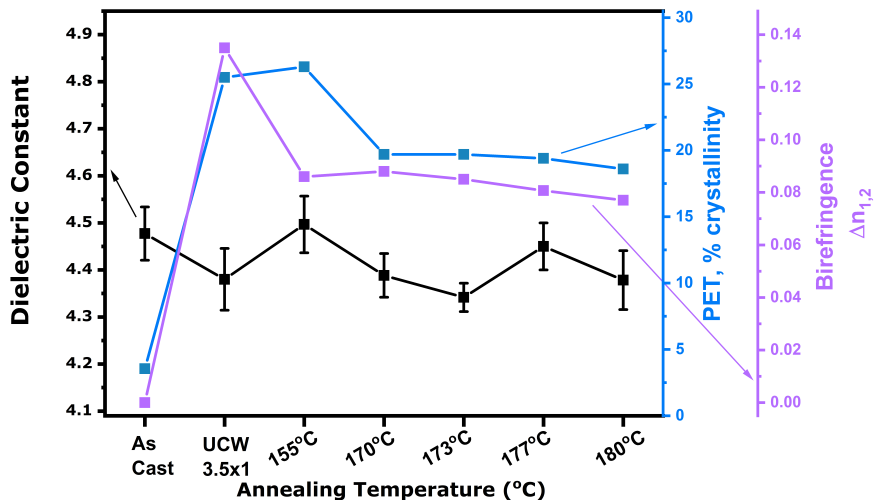


Fig. 4.23.: Dielectric constant measured at room temperature (left y-axis) versus birefringence and calculated percent crystallinity for PET (right y-axis) for films stretched in UCW mode to 3.5X1, at 150°C and annealed at temperatures displayed on x-axis.

In Figure 4.22, dielectric loss is approximately equal for samples annealed at high temperatures, 170°C, 173°C, 177°C, and 180°C. However, while annealing at these four temperatures results in films with similar loss values, annealing at 155°C gives much lower loss. This may be due to retained α -PVDF orientation when sample is annealed at low temperature. Again, this was the only sample not containing γ or γ' -PVDF, which could mean these crystal forms negatively affect dielectric loss. Loss behavior is also plotted against birefringence and percent crystallinity of PET in Figure 4.24. Here we see that samples with low levels of crystallinity and orientation had very high loss (as cast sample). After stretching, high levels of crystallinity and birefringence are observed, as well as the lowest measured loss value at room temperature (UCW 3.5X1 sample). For the sample annealed at 155°C, we see higher percent PET crystallinity with relatively lower birefringence and loss

also increases slightly from the as stretched sample. This suggests that the drop in birefringence (i.e. orientation) may negatively impact loss. For samples annealed at higher temperatures, the percent crystallinity and birefringence are similar, and so are the values for dielectric loss.

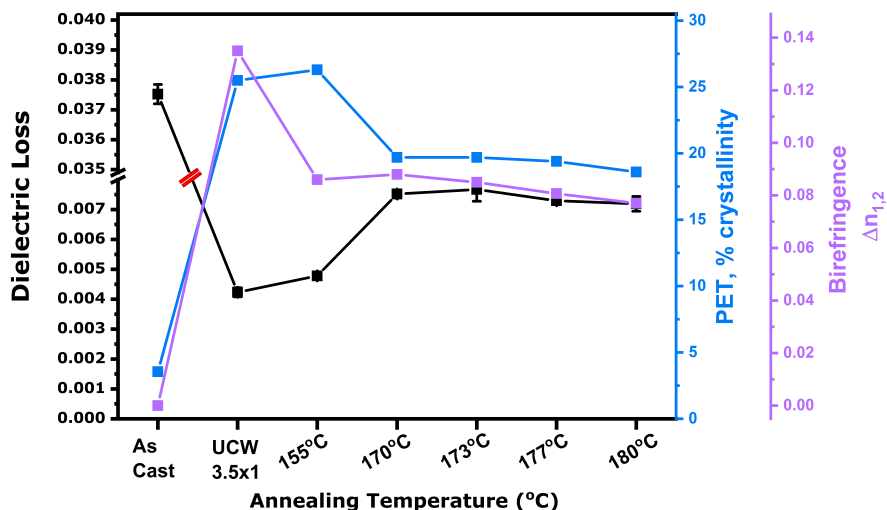


Fig. 4.24.: Dielectric loss measured at room temperature (left y-axis) versus birefringence and calculated percent crystallinity for PET (right y-axis) for films stretched in UCW mode to 3.5X1, at 150°C and annealed at temperatures displayed on x-axis.

Films stretched in UCW mode to 3.5X1 at 20 mm/min and 150°C and annealed were also tested for dielectric constant and loss under temperature ramp experiments, as shown in Figure 4.25. Figure 4.25a shows how dielectric constant changes with testing temperature at constant frequency (1 kHz). The unannealed sample showed significant geometry change (shrinkage, wrinkling and delamination from electrode) as temperature increased past the material's T_g , so dielectric constant is not accurate past around 50°C. This emphasizes the importance of annealing for high temperature capacitor applications. Samples annealed at 170°C, 173°C, 177°C, and 180°C show the same trend in changing dielectric constant with increasing temperature; specifically, dielectric constant increases as testing temperature increases. Furthermore, as

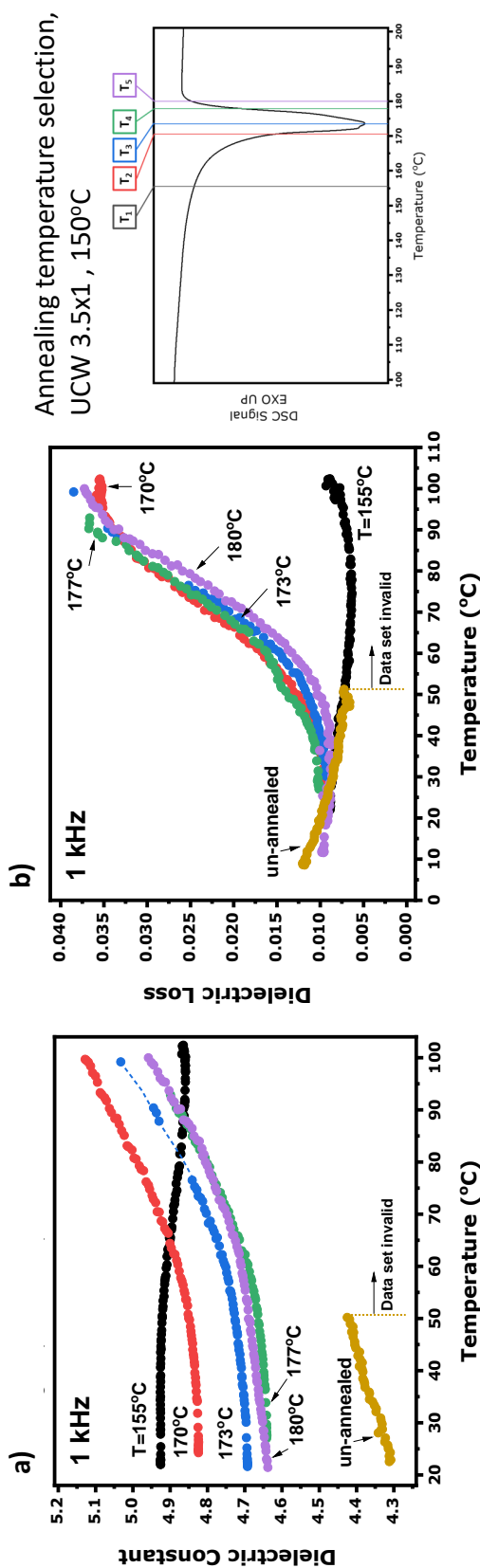


Fig. 4.25.: Dielectric property measurements (temperature ramp, increasing temperature at $f=1\text{kHz}$) for a series of 32L films stretched in UCW mode, 3.5X1, at 20 mm/min at 150°C annealed for 1 hour at select temperatures a) dielectric constant and b) dielectric loss.

annealing temperature increases from 170°C to 180°C, overall dielectric constant is lower, and above peak melting point of PVDF (177°C, and 180°C), the value is approximately equal. Therefore, oriented PVDF regions which remain intact due to low molten fraction at low annealing temperatures are beneficial to maintaining higher dielectric constant at high testing temperatures. In T=155°C, however, the trend in dielectric constant versus testing temperature is opposite. Besides crystalline morphological differences regarding crystal size and perfection due to annealing, the sample annealed at 155°C is the only one of the series that did not have detectable amounts of γ or γ' -PVDF present, according to DSC (see table in Figure 4.15). This suggests that, in absence of other factors, having γ or γ' -PVDF is beneficial to improving high temperature dielectric constant. For PET properties, the film annealed at 155°C had higher percent PET crystallinity, compared to other samples, meaning high PET crystallinity could lead to decreased dielectric constant at high temperatures. However, the relative values of dielectric constant for PET ($\epsilon =$ about 3.3) is significantly lower than PVDF (around 10), therefore PVDF morphology likely is the main contributor to the dielectric constant measured on the composite film.

Temperature ramp dielectric loss curves for the same samples are shown Figure 4.25b, where again 170°C, 173°C, 177°C, and 180°C annealed samples show the same trend in loss value with increasing testing temperature, and the overall value of dielectric loss is very similar for each. Interestingly, the sample annealed at 155°C again shows a different trend in dielectric loss; specifically, dielectric loss decreases with increasing testing temperature. As mentioned, 155°C is the only of these annealed samples that did not have detectable amounts of γ or γ' -PVDF present, thus γ or γ' -PVDF are likely detrimental to dielectric loss at high testing temperatures. Furthermore, 155°C annealed sample has higher c-axis PVDF alignment with drawing direction and relatively small crystals for PET layers compared to higher annealing temperatures, which likely plays a role in the improved loss behavior as well. These findings are significant as they are not expected based on past literature, which states that γ or γ' -PVDF has similar loss values to other crystal forms (see [239] and [28]) - in fact

we see here that it has significantly higher dielectric loss at high testing temperatures, as shown in samples annealed at 170°C, 173°C, 177°C, and 180°C which contain γ or γ' -PVDF, compared to sample annealed at 155°C which does not. As far as PET, the difference in sample annealed at 155°C, again, had higher crystallinity but relatively lower birefringence compared to film as stretched, and therefore it is possible that higher percent crystallinity of PET leads to improved loss behavior at high temperature testing.

4.4 Conclusions

In conclusion, this study found ideal processing temperature for 32L PET/PVDF microlayer film to be around 150°C. Processing at other temperatures was not feasible due primarily to necking in uniaxial mode.

Crystal forms of PVDF can be changed via stretching and/or constrained annealing. Specifically, γ and γ' - PVDF are formed when the film is stretched 1.5X1 in UCW mode at 150°C and 20 mm/min then annealed at 172°C and γ' PVDF only when annealed at 175°C or above. Stretching at 2.5X1, high amount of γ is formed when annealed at 155°C and both γ and γ' - PVDF are obtained when annealing at 171°C or above. Stretching at 3.5X1, high amounts of γ are obtained when annealed at 170°C, small amount when annealed at 173°C, and only γ' when annealed at 177°C and 180°C.

For PVDF, α -form c-axis orientation is nearly random in the as cast film. After stretching in UCW mode to 3.5X1, orientation factor increases significantly. This is observed clearly in AFM microscopy image shown in Figure 4.19. At low annealing temperature (T=155°C), PVDF α crystals remain highly oriented with drawing direction. However, as annealing temperature increases, PVDF becomes less oriented with respect to the drawing direction.

AFM and SAXS data conducted on delaminated PVDF layers were combined to determine a proposed structural model, shown in Figure 4.19. A very different morphology was seen for sample annealed at 170°C, which had high amounts of γ -PVDF. The SAXS image for this sample showed little to no scattering contrast, which may be due to the proposed structural arrangement, as depicted in Figure 4.19c, where microfibrillar arrangement is still proposed to be present, as evidenced by diffuse equatorial streak in SAXS pattern. Annealing at or above the peak melting point of PVDF ($T=173^{\circ}\text{C}$) produces similar structure based on AFM imaging and SAXS patterns, with sharper spots in SAXS patterns, indicating higher lamellar organization in MD. AFM images showed formation of shish-kebab structures at higher annealing temperatures as well.

Dielectric property measurements at room temperature showed that samples containing γ and/or γ' -PVDF had lower dielectric constant and also higher dielectric loss. In order to test dielectric properties of oriented samples at high temperatures, annealing is necessary to prevent significant changes to electrode geometry, which invalidate the test results. Temperature ramp dielectric constant measurements at constant frequency for UCW stretched samples showed a different trend when samples contained γ or γ' -PVDF, with dielectric constant increasing over the full range of testing temperatures. PET morphology is less likely to have an effect on this property, due to the significant difference in dielectric constant for the neat materials. Temperature ramp dielectric loss testing at constant frequency also showed different trend for samples containing γ or γ' -PVDF; specifically, loss value increased significantly over the full temperature testing range, as opposed to the sample not containing γ or γ' -PVDF which decreased consistently. This suggests that the absence of γ or γ' -PVDF is actually beneficial to high temperature dielectric properties, as it allows for relatively high dielectric constant but also much lower dielectric loss. PET may also contribute to lower loss in temperature ramping experiments with significantly higher percent crystallinity at 155°C annealing versus other annealing temperatures.

4.5 Acknowledgements

The authors would like to thank PolymerPlus for kindly providing the microlayered films and materials for this project. The authors acknowledge and greatly appreciate support, funding and dielectric testing from the Office of Naval Research Grant N000141712048. WAXS characterization of this material was made possible by the National Science Foundation through the Major Research Instrumentation Program under Grant No. CHE 1625543 (Funding for the single crystal X-ray diffractometer).

5. MECHANO-OPTICAL BEHAVIOR OF UNIAXIALLY ORIENTED FLUOROPOLYMER FILMS: ETHYLENE TETRAFLUOROETHYLENE COPOLYMER (ETFE) AND TETRAFLUOROETHYLENE- HEXAFLUORO- PROPYLENE- VINYLIDENE FLUORIDE TERPOLYMER (THV)

Changes in morphology during uniaxial orientation were studied for two fluorinated polymers, ETFE and THV. Thin, melt cast, monolayer films (around 40-50 μm) were stretched at a series of temperatures using a custom built machine that detects true stress, true strain, and birefringence in real-time during stretching. Use of offline characterization techniques (DSC, WAXS, SAXS, AFM) at different points in the true stress, true strain curve supplement the above measurements to study structural hierarchy evolution of these polymers during stretching. Specifically, when stretched in partially molten state, THV behaves elastomeric, and shows nearly affine deformation. SAXS and WAXS data show increase in lamellar d-spacing, decrease in overall percent crystallinity, and increasing preferred orientation during stretching of THV. ETFE stretched in solid-state also shows nearly affine deformation. Characterization of ETFE during stretching revealed two different four-point SAXS patterns, indicating tilted lamellae which re-orient at high strains to form a two-point patterning in machine direction. AFM images were used in conjunction with SAXS patterns to construct structural hierarchy models for these materials during uniaxial orientation. Applications for these materials include low k high temperature materials for dielectrics in applications such as HEV and aerospace.

5.1 Introduction

Fluoropolymers are a relatively new class of materials with unique properties compared to other polymers because of their highly polar nature. Due to their generally low dielectric constants (compared to metals) and high chemical inertness, they are used mainly as insulators in energy and electronic industries [79]. Of particular interest to this study is the use of fluoropolymer films as a component in polymer dielectric films for capacitor applications. Current capacitor films are typically made of polymer materials, mainly polypropylene (PP), polycarbonate (PC), and polyethylene terephthalate (PET). Biaxially oriented polypropylene (BOPP) has been the state-of-the-art capacitor dielectric material for over 20 years because it has the highest known energy density at breakdown (5 J/cm^3) of any commercial capacitor film [61]. With very high breakdown strength (around $800 \text{ V}/\mu\text{m}$) and extremely low electrical losses of 0.02 percent (at 1 kHz) up to usage temperature of 85°C , BOPP is an excellent choice in many capacitor applications [60]. However, recent push to develop new technology requires capacitors which have very high energy density and low losses and can be used at high temperatures and/or in pulsed power applications. This challenge motivates research in the area of new polymer materials to replace current materials used as dielectric components in capacitors, which is crucial for validation of emerging technologies including HEV, aerospace, hybrid batteries, solar cells, and so on [29], [60], [3], [2], [61].

With the highest known dielectric constant ($k=10$) of any polymer material, polyvinylidene fluoride (PVDF) and its copolymers seem an obvious choice for high energy density capacitors. However, these materials have low thermal stability with melting peak around 174°C , and they cannot be used as the sole dielectric component in capacitor pulsed power applications due to their low charge-discharge efficiency, which is about 15% lower than BOPP [29]. One way to tailor fluoropolymer properties is by copolymerization which allows several monomers with unique and favorable properties that may otherwise phase separate (i.e. thermodynamically immiscible) to

be combined into a single material. Polytetrafluoroethylene (PTFE) has very high thermal stability (melting point greater than 325°C) and low dielectric loss (about 0.01%) but cannot be processed via melt extrusion and has a relatively low dielectric constant [29]. Copolymerization of monomers ethylene and tetrafluoroethylene (TFE) creates ethylene tetrafluoroethylene copolymer (ETFE), which takes advantage of the dielectric properties of both PTFE and melt processability of hydrocarbon component, ethylene. THV is a terpolymer which combines tetrafluoroethylene, hexafluoropropylene, and vinylidene fluoride or TFE-HFP-VDF monomers. In addition to advantages mentioned above, the HFP (hexafluoropropylene) component helps to lower cost by reducing melting temperature without lowering thermal stability of the material [29].

Two melt-processable, semi-crystalline fluoropolymer materials were chosen for this study: ethylene tetrafluoroethylene copolymer (ETFE) and tetrafluoroethylene hexafluoro-propylene-vinylidene fluoride terpolymer (THV). Developed in 1973, ETFE copolymer was one of the first polymers to combine fluorocarbon and hydrocarbon monomers and thus has properties somewhere in between these two extremes [79]. The hydrocarbon sub-unit gives better flexibility and mechanical properties compared to, for example, polyvinylidene fluoride (PVDF) homopolymer, and its primary applications are wire and cable insulation [79]. ETFE has a dielectric constant of 2.6 (at 106 Hz) and breakdown strength of approximately 14.6 kV/mm, with very low electric loss of 0.010 (at 1 kHz) [21], [36]. Only developed in the mid-1990s, THV is considered the newest fluoropolymer but has already found wide use as a barrier film and again in wire and cable insulation applications due to its excellent adhesion properties and low dielectric constant [21]. Having three monomers allows for favorable combination of the properties of each individual component, making THV a highly flexible and transparent material which can be processed at relatively low temperatures [21]. THV has a dielectric constant of 4-5 (106 Hz), breakdown strength 48-62 kV/mm, and electrical loss around 0.09-0.14 (at 1 kHz) [36], [21].

A few previous studies have looked at the morphology of ETFE and THV and how it changes during orientation. In a series of three papers published in 1986, Tanigami, et al. studied the crystal structure, crystal phase transition, and deformation mechanism of ETFE [30], [32], [31]. These papers confirmed the orthorhombic crystal structure of ETFE, however they found lattice parameters of $a = 8.57 \text{ \AA}$, $b = 11.20 \text{ \AA}$, and $c = 5.04 \text{ \AA}$ which vary from previous values (reported in 1973 by Wilson and Starkweather [143]) due to newly discovered paracrystalline disorder [30]. Tanigami also discovered, by use of X-ray diffraction, the existence of a reversible, thermally induced first-order transition from ordered orthorhombic crystal phase to a disordered hexagonal mesophase of ETFE [32]. And finally, Tanigami studied morphology of ETFE under uniaxial deformation and found that below the processing temperature for mesophase transition ($T=100^\circ\text{C}$), ETFE films deform plastically by breaking up lamellar regions, leading to micro-void formation in amorphous regions, however, when ETFE films are stretched above the $T=100^\circ\text{C}$ transition temperature, they exhibit rubber-like deformation [31]. These results are important for choosing appropriate processing parameters for ETFE, such as rate, temperature, etc. Further studies by Funaki, et al. sought to re-examine the crystal structure of ETFE via fitting different crystal structure models using X-ray diffraction and found the structure to be monoclinic at very low temperatures (down to around -150°C) which transforms to pseudo-hexagonal form around 60°C (exact temperature dependent on E/TFE ratio) [33], [34], [35].

Deformation structure-property relationships for THV have not been studied as thoroughly as ETFE. Freimuth, et al. studied the structure of uniaxially oriented THV terpolymer with composition: 52 mol% VDF, 36 mol% TFE, 12 mol% HFP [37]. WAXS patterns showed two amorphous halos at $q = 12 \text{ nm}^{-1}$ and 27.5 nm^{-1} , and one crystalline peak appearing around $q = 12.89 \text{ nm}^{-1}$. From this data, Freimuth also estimated percent crystallinity in the as-molded sample to be about 10%. After stretching at 100°C to 4.5X draw ratio, WAXS patterns show reflections instead at

around $q = 24.7 \text{ nm}^{-1}$ and $q = 49.3 \text{ nm}^{-1}$ [37]. Since there are few diffraction peaks, a crystalline unit cell could not exclusively be determined for THV, but evidence suggests the crystal structure is similar to the hexagonal crystal unit cells seen in PTFE and PVDF [37]. Furthermore, SAXS patterns show a lamellar long period $L = 12.0 \text{ nm}$ for the undeformed material and, after stretching to 4.5X draw ratio in temperature range 50-100°C, Freimuth and co-workers discovered a four-point SAXS pattern which transforms to a two-point one as stretching temperature increases [37]. In 2008, Emmons and co-workers studied changes in morphology of THV terpolymer under very high pressures and determined by XRD that THV has an interatomic spacing of 0.49 nm at the most intense diffraction peak [44]. This value is close to crystal structure form IV of PTFE and, since the material had high -TFE monomer content, it can be assumed that the TFE portion is that which is crystallizing and thus the PTFE form IV crystalline unit cell can be reasonably approximated as the unit cell for THV [44]. Specifically, PTFE form IV has a hexagonal unit cell structure with parameters $a = 0.566 \text{ nm}$, $b = 0.566 \text{ nm}$, and $c = 1.950 \text{ nm}$ [144]. Rheological [38], [39], dielectric [29], [40], optical [42], spectroscopic [43], [44] and thermodynamic [45] properties, as well as characterization via NMR [41] of THV have all been studied in the literature, but very few studies describe morphology related to orientation.

What makes the current study unique is the ability to measure mechano-optical properties using machines custom built in our lab that provide real-time true stress, true strain and birefringence measurements during stretching. These measurements provide a link between mechanical and optical properties and changing morphology during stretching. Coupling with offline characterization techniques allows for a more thorough and in-depth understanding of how and why morphological changes occur during uniaxial film orientation.

5.2 Materials and experimental procedures

The polymers used in this study are Dyneon THV 815 G (composition TFE/ HFP /VDF: 76/13/11 percent by mass) and DuPont Tefzel 280 ETFE in the form of individual, monolayer, 40-50 μm thick cast films provided by PolyK Technologies. Films were made on a 1.25 inch diameter single screw extruder with 18 inch die. Extrusion temperatures were 330°C for ETFE film and 300°C for the THV film. Both films have some degree of orientation in machine direction due to the casting process.

The chemical structures for ETFE and THV are:

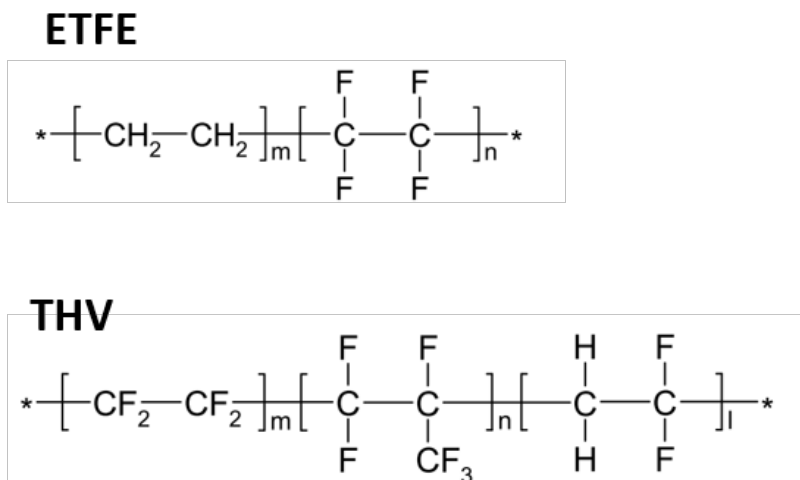


Fig. 5.1.: Chemical structures for [top] ETFE and [bottom] THV.

Our instrumented, custom built uniaxial stretcher was used to measure mechano-optical properties of polymer samples in real time during stretching experiments. Measurements of optical retardation and sample width at the exact center of the film allow for calculation of film thickness and therefore true stress, true strain and birefringence values (at 546 nm wavelength) in real-time during stretching.

These calculations assume the following:

1) simple extension

$$D_t/D_o = W_t/W_o \quad (5.1)$$

2) incompressibility

$$L_o W_o D_o = L_t W_t D_t \quad (5.2)$$

Using these assumptions, the following parameters are calculated:

Thickness:

$$D_t = (W_t/W_o)D_o \quad (5.3)$$

Birefringence:

$$\Delta n = R/D_t \quad (5.4)$$

True strain:

$$L_t/L_o - 1 = (W_o/W_t)^2 - 1 \quad (5.5)$$

True stress:

$$F_t/(W_t D_t) = F_t/[(W_t^2/W_o)D_o] \quad (5.6)$$

Where R is retardation, Δn is birefringence, D_o , W_o , L_o are initial thickness, width, and length respectively, and D_t , W_t , L_t , F_t , are time variations of thickness, width, length, and force. Further details of this machine are listed elsewhere [77], [209], [220].

To validate software calculations for real-time film thickness values, both the camera (tracking fluorescent dots) and laser (which tracks changes in width in sample's center) measurements were compared to that measured offline with a digital micrometer. Comparison of predicted thicknesses versus thicknesses measured after stretching can

be seen in Appendix C, Figures C.1, C.2, C.3 and C.4. This real time thickness is used to calculate birefringence, using Equation 5.4.

For uniaxial stretching, films were prepared with a die cutter (67 x 81 mm overall dimensions) into dogbone shape and painted with fluorescent yellow dye in a four dot pattern. This pattern is traced by CCD camera and allows for calculation of local true stains in sample MD and TD directions. Films were stretched to 3X initial length, then held taut and quenched by blowing cold air until they reached room temperature (about 20 minutes).

Thermal properties were measured on THV film as cast and after stretching using Netzsch DSC 214 Polyma differential scanning calorimeter with a heating rate of 10°C/min in nitrogen atmosphere. Thermal properties were measured on ETFE film as cast and after stretching using TA Instruments Q2000 DSC differential scanning calorimeter with a heating rate of 10°C/min. Percent crystallinity of ETFE was calculated using enthalpy of heat of fusion for 100% crystalline polymer, ΔH_o of 113.4 J/g [242]. This value could not be found in the literature for THV.

Wide angle X-ray measurements were run on Bruker D8 Quest diffractometer with kappa geometry, an I- μ -S microsource X-ray tube, laterally graded multilayer (Goebel) mirror single crystal for monochromatization, and Photon2 CMOS area detector. Generator was operated at 50 kV at current of 1 mA, beam was monochromatized at Cu K-alpha radiation ($\lambda = 1.54178\text{\AA}$) and samples were irradiated for 1 minute. Small angle X-ray scattering characterization was done on an Anton Paar SAXSpoint 2.0 machine containing microfocus Cu K-alpha radiation, $\lambda = 1.54178\text{\AA}$, source and two dimensional, Eiger R hybrid photon-counting detector. Generator was operated at 50 kV at current of 1 mA, and samples were irradiated for 15-30 minutes, depending on their thickness. SAXS and WAXS images were taken in both film normal (through film thickness) and transverse directions.

Atomic force microscopy images (AFM) were taken on Veeco Dimension 3100 AFM and images were processed in Gwyddion software. This machine has X,Y scan range

of 90 μm square, with lateral accuracy between 1-2%. The Z-range is 5 μm and resolution is 16-bit. Measurements were performed in tapping mode using variable drive voltage to optimize tapping conditions for each individual sample.

5.3 Results and discussion

5.3.1 Uniaxial Stretching

Effect of stretching temperature on material deformation was first investigated at a series of processing temperatures, shown as vertical dashed lines in Figure 5.2, where DSC curve for samples are presented with vertical solid lines indicating onset of melting for each material. When stretching was attempted at higher temperatures (i.e. above 160°C), the draw ratio at maximum extension was significantly reduced due to sample breakage. Figures 5.3 and 5.4 show mechano-optical data for ETFE and THV at a range of stretching temperatures with stretching rate 10 mm/min and thermal equilibration time of 10 min prior to stretching. All films were stretched to draw ratio of 3X their initial length, with the exception of ETFE at 160°C which consistently broke before reaching 3X draw ratio.

All samples deformed nearly affinely, with no necking observed, and the shape of stress-strain curves for each material is similar, regardless of stretching temperature. As expected, lower stress develops at increasing stretching temperature. Summaries of mechano-optical properties are shown for ETFE in Table 5.1 and THV in Table 5.2. Stress-optical and strain-optical behavior of polymer films is important because it provides a direct connection between applied strain and stress to molecular behavior as measured birefringence, and can be roughly considered as molecular measure of local chain deformation. For polymer melts and solutions, and amorphous polymers at low or moderate application of stress, the stress-optical rule applies: [222], [223]

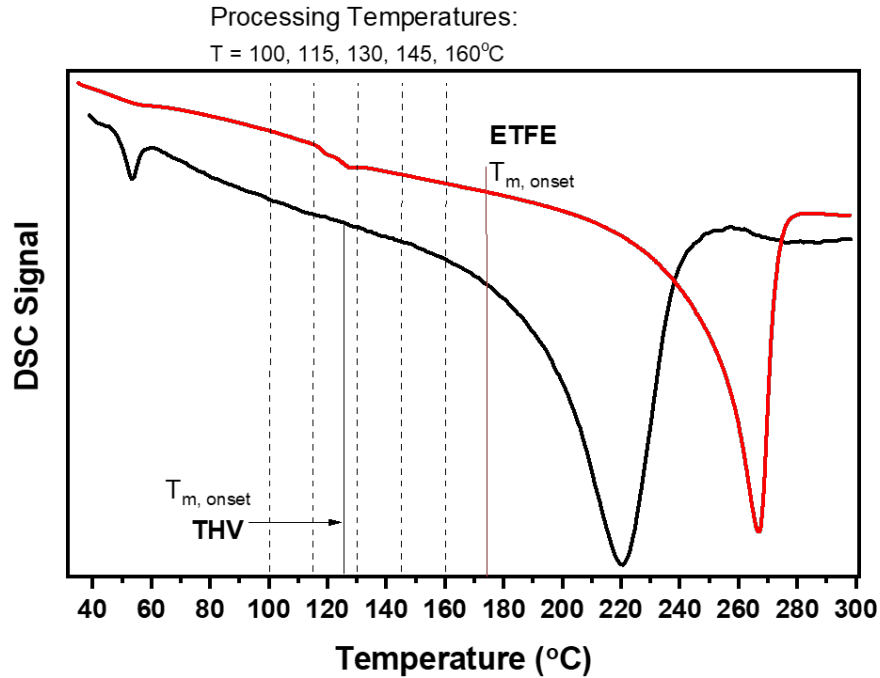


Fig. 5.2.: DSC curves of as cast THV and ETFE films.

$$\Delta n = C\sigma \quad (5.7)$$

or,

$$(n_1 n_2) = C(\sigma_1 - \sigma_2) \quad (5.8)$$

Where Δn is birefringence, C is stress-optical coefficient, σ is applied stress and subscripts 1, 2 refer to principal directions of the aforementioned variables.

At moderate levels of applied stress, most polymers show deviation from linear stress-optical behavior. For example, deviations have been observed to occur due to strain-induced crystallization, deformation near T_g , and due to non-Gaussian chain conformations when chains near their point of maximum extensibility [222].

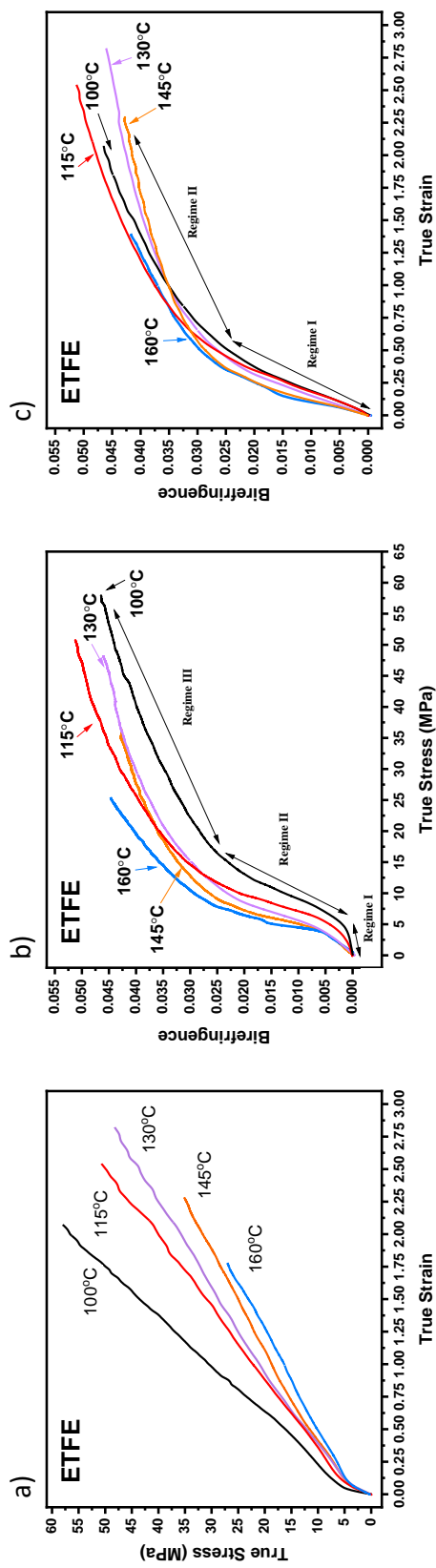


Fig. 5.3.: (a) True stress, true strain, (b) true stress-birefringence, and (c) true strain-birefringence curves for ETFE uniaxially oriented at varying stretch temperatures and a rate of 10 mm/min.

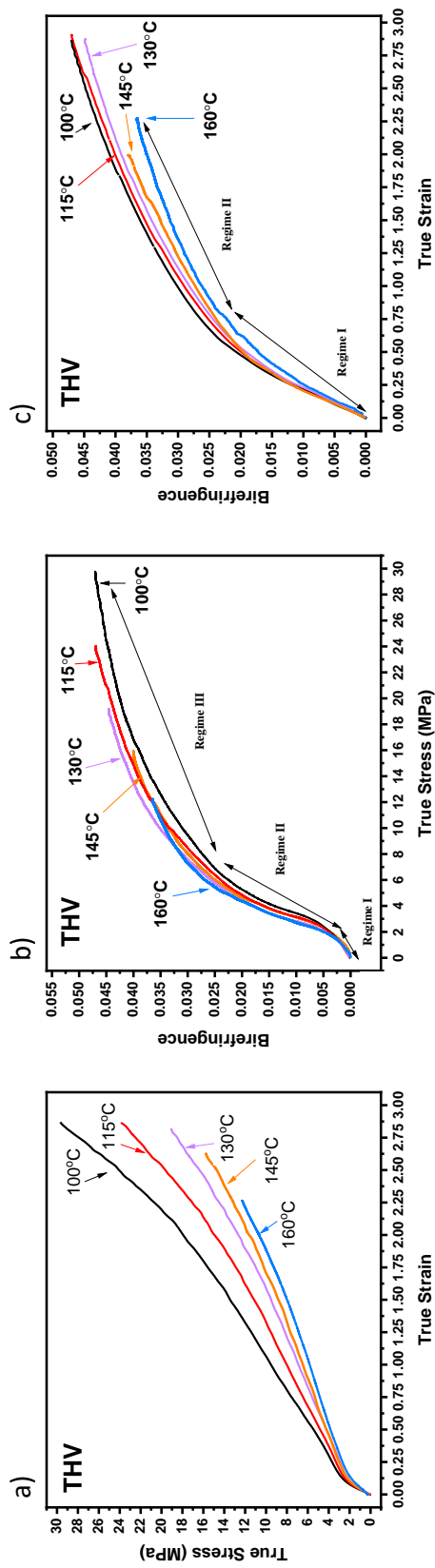


Fig. 5.4.: (a) True stress, true strain, (b) true stress-birefringence, and (c) true strain-birefringence curves for THV uniaxially oriented at varying stretch temperatures and a rate of 10 mm/min.

Table 5.1.: Mechano-optical properties for uniaxially stretched ETFE

Stretch Temperature	Youngs Modulus (Mpa ⁻¹)	Onset Strain Hardening (mm/mm)	Photoelastic Constant (Gpa ⁻¹)	Strain-Optic Constant
100°C	120.6 ±5.0	1.01 ±0.30	0.74 ±0.20	0.059 ±2x10 ⁻³
115°C	62.2 ±1.0	1.23 ±0.20	0.81 ±0.30	0.065 ±4x10 ⁻³
130°C	50.3 ±0.5	1.30 ±0.30	1.37 ±0.20	0.066 ±3x10 ⁻³
145°C	47.9 ±0.8	1.32 ±0.20	1.57 ±0.15	0.083 ±1x10 ⁻³
160°C	51.8 ±1.0	0.62 ±0.20	1.57 ±0.40	0.088 ±3x10 ⁻³

Table 5.2.: Mechano-optical properties for uniaxially stretched THV

Stretch Temperature	Youngs Modulus (Mpa ⁻¹)	Photoelastic Constant (Gpa ⁻¹)	Strain-Optic Constant
100°C	24.4 ±0.3	1.46 ±0.30	0.047 ±2x10 ⁻³
115°C	22.5 ±0.4	1.46 ±0.20	0.041 ±2x10 ⁻³
130°C	20.5 ±0.2	1.67 ±0.30	0.043 ±2x10 ⁻³
145°C	13.4 ±0.1	1.80 ±0.15	0.047 ±1x10 ⁻³
160°C	13.9 ±0.5	2.02 ±0.20	0.038 ±6x10 ⁻³

Both materials are in partially molten state at the temperatures and hence the stress optical behavior developed for melts and polymer rubbers may not apply to them. The strain optical and stress optical behavior of partially molten semicrystalline materials has not been explored in the past due to primarily to difficulties in carrying out experiments in partially molten state where structure is temporally changing as melting and recrystallization occurs at these temperatures. Hence we kept strict protocol on heating temperature and equilibration times for the experiments carried out.

As shown in Table 5.1, the Young's modulus for ETFE decreases with increasing stretch temperature, and remains nearly constant at and above 115°C. As mentioned previously, there is a mesophase transition near 100°C where stretching leads to plastic deformation and lamellar breakup [32] and above which the material deforms elastomer-like. Strain hardening occurs relatively early at low temperature stretching temperatures for ETFE but is delayed as temperature increases. The photoelastic constant, measured from slope Regime I in the stress-birefringence curve, is important because it relates global stress development of the material to its changing structure

through birefringence measurements. In the case of ETFE, Table 5.1 shows stress-optic constant increases with increasing stretching temperature. Strain-optic values for ETFE are nearly constant at low values of true strain, and then increase with increasing stretching temperature.

In Table 5.2, Young's modulus for THV decreases with increasing stretching temperature and is significantly lower after the onset of melting (which occurs around 125°C). Photoelastic constant for THV is equal at low stretch temperatures then increases with increasing temperature above the onset of melting point. Strain-optic constant, however, remains nearly constant (within experimental error) in this temperature range where significant melting has not taken place.

Stretching of ETFE and THV follows a three regime behavior, as shown in Figure 5.3b and c, and Figure 5.4b and c, respectively. Regime I is linear in both stress- and strain-optic properties, where the material behaves like a typical elastic solid, with linear region corresponding to elastic deformation. At higher levels of stress, Regime II, these curves show positive deviation from linearity, as the plastic deformation ensues where significant morphological rearrangements take place that include breakup of crystalline lamellae and their reorientation and formation of extended chain crystals associated with stress-induced crystallization. In Regime III, birefringence development levels off as the polymers begin to reach their finite extensibilities, while stress and strain continue to increase.

5.3.2 Characterization

The 145°C stretching temperature was chosen for both materials to study further by means of a temporal evolution study, where individual films were stretched to points of interest on the stress-strain curve, quenched to “lock-in” morphological state developed up until that point, then characterized offline to link mechanical deformation with polymer structure.

Thermal Characterization (DSC)

Differential scanning calorimetry results for temporal evolution samples are shown for ETFE film in Figure 5.5 and for THV film in Figure 5.6, with true strain and calculated percent crystallinity (heat of fusion for THV) values as listed on each curve. For ETFE (Figure 5.5), the endotherms show a melting peak around 266°C for the film in its as cast state, with a starting percent crystallinity of 44.2%. With increasing draw ratio, melting point shifts slightly higher and the melting peak becomes broader. Furthermore, the percent crystallinity increases overall but decreases slightly at true strain values of 0.68 and 2.0 mm/mm likely due to reorganization of lamellar regions as evidenced by SAXS data, which will be discussed later. For THV (Figure 5.6), the main melting peak occurs at 220°C, and T_g is around 53.4°C.

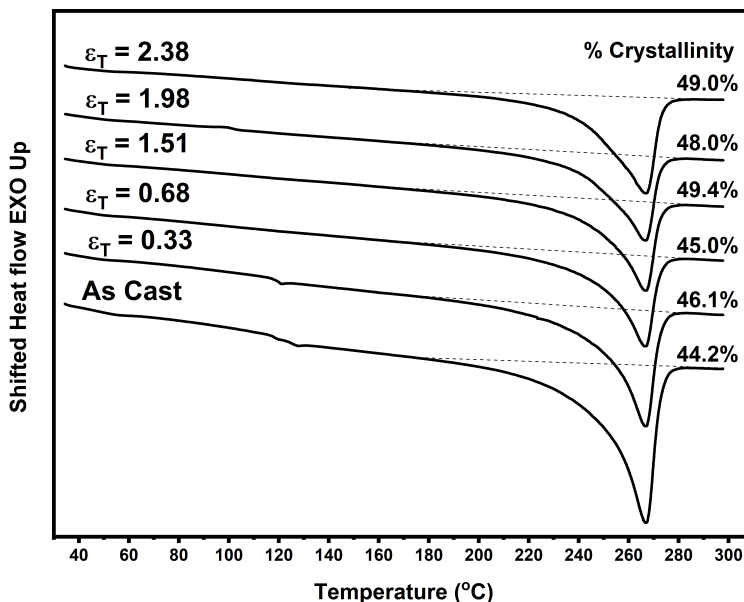


Fig. 5.5.: DSC curves for ETFE samples as cast and after uniaxial orientation.

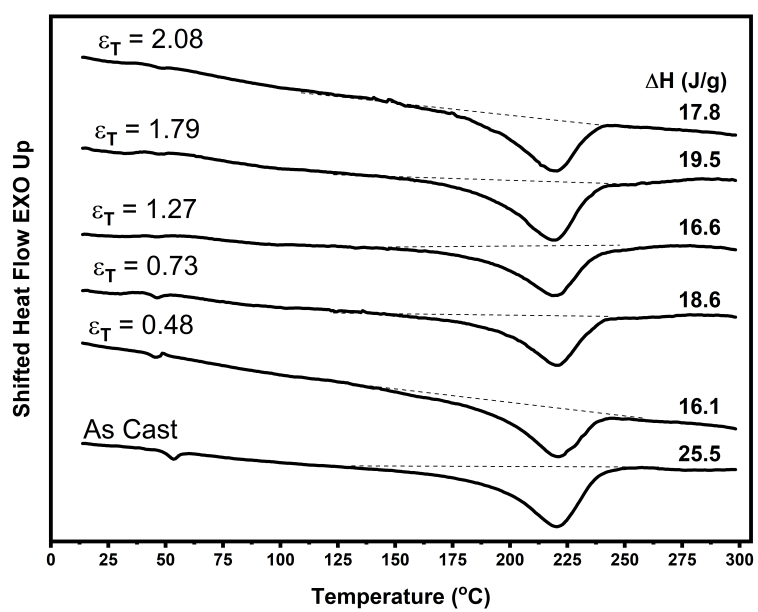


Fig. 5.6.: DSC curves for THV samples as cast and after uniaxial orientation.

After orientation, melting peak decreases very slightly (less than 1°C in total). Since heat of fusion for theoretically 100% crystalline THV could not be found in the literature, instead we report the heat of fusion associated with the main melting peak near 220°C to represent relative changes in crystallinity.

WAXS Results

Wide angle X-ray scattering patterns for both ETFE and THV are shown in comparison to stress and strain optical data in Figure 5.8 and Figure 5.7, respectively. Larger 2D WAXS patterns are also shown in the Appendices (Figure C.8 (ETFE) and Figure C.7 (THV)). WAXS images for THV show some initial orientation and then, as draw ratio increases, a sharpening of the crystalline ring at $2\theta = 18^{\circ}$ as well as sharpening of the amorphous halo at around $2\theta = 39^{\circ}$. There is a second amorphous ring at around $2\theta = 16.5^{\circ}$ which overlaps with the crystalline peak (appearing as a shoulder in 1D data) and does not orient as the film is stretched. The crystalline reflection at 18° corresponds to the (100) plane in the hexagonal crystal structure of crystalline TFE, a reasonable approximation for THV as its exact crystal structure is unknown [37], [44]. ETFE WAXS patterns are isotropic in the as-cast state, and show increasing orientation with increasing strain, as indicated by the sharpening of arcs in each successive 2D WAXS pattern. Crystalline reflections occur around $2\theta = 19^{\circ}$, corresponding to the (120) crystal plane, 22° for the (200) crystal plane, and an amorphous halo is observed near 39° . Assuming orthorhombic crystal structure, these peaks are confirmed in the works of Tanigami and co-workers [31]. All three observed reflections become more oriented during stretching, as evidenced by the increasing sharpness of arcs in the 2D scattering patterns.

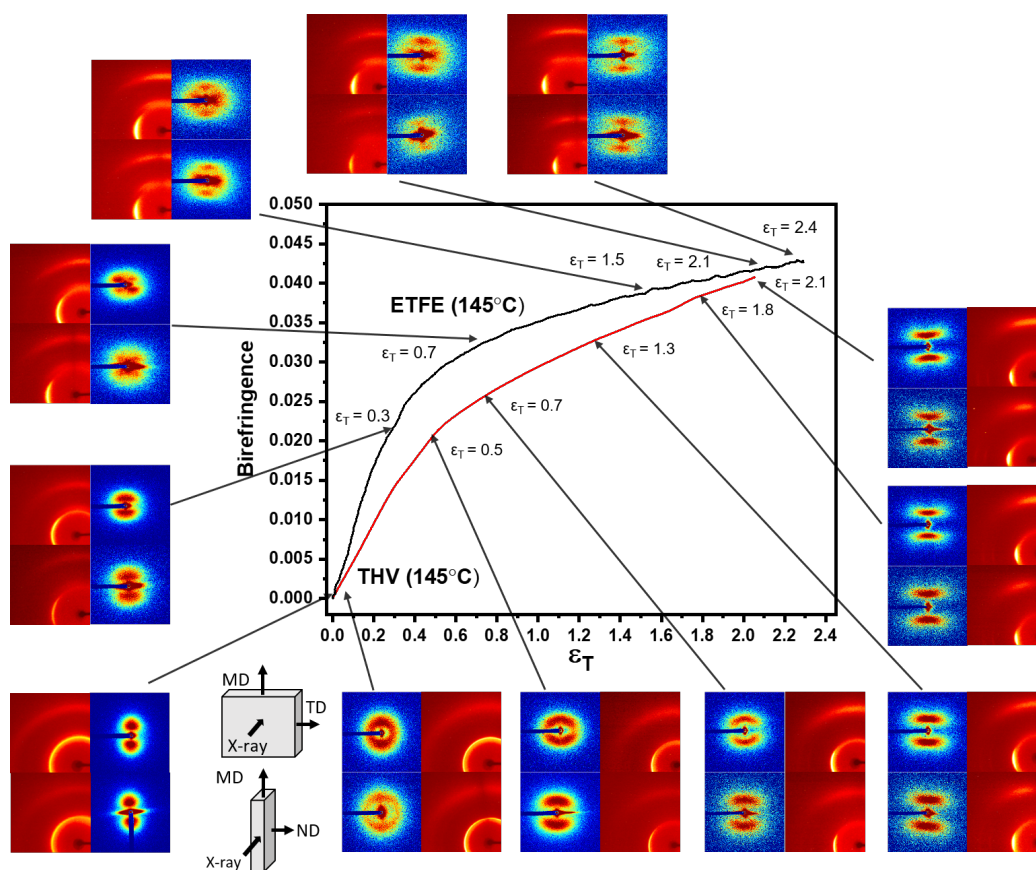


Fig. 5.7.: Strain-optical temporal evolution study and evolution of microstructure via wide and small-angle X-ray scattering images for uniaxially oriented THV and ETFE films at 145°C.

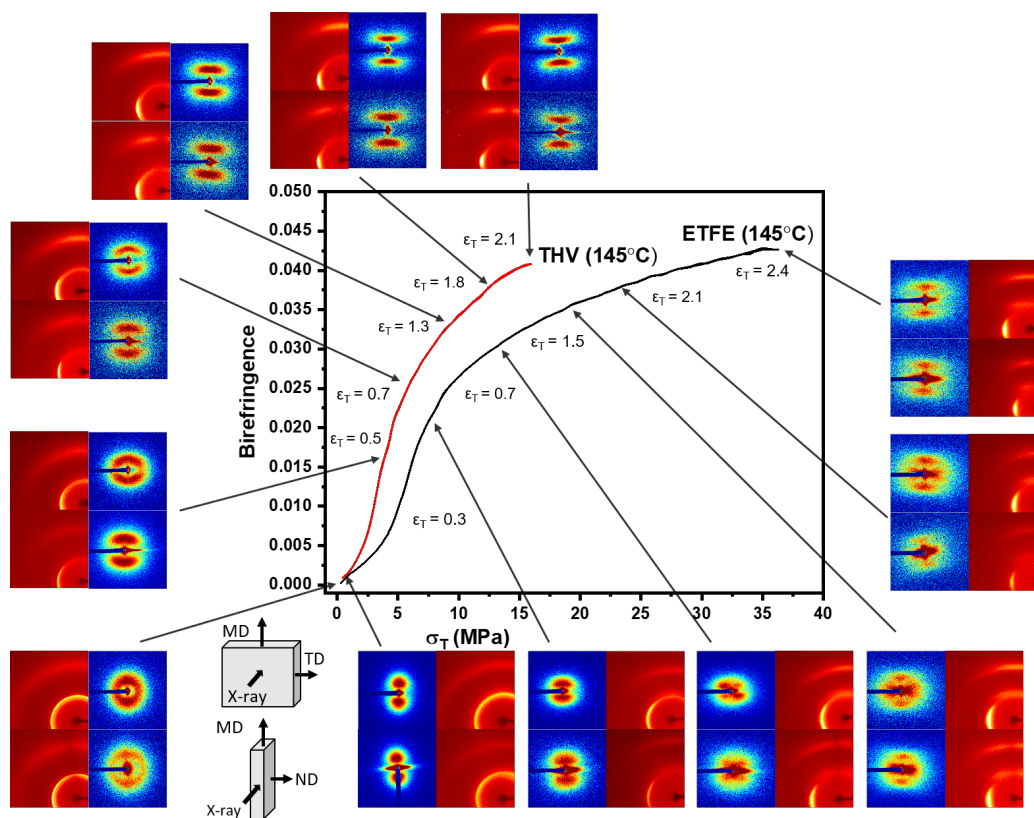


Fig. 5.8.: Stress-optical temporal evolution study and evolution of microstructure via wide and small-angle X-ray scattering images for uniaxially oriented THV and ETFE films at 145°C.

Orientation Factors

From experimental WAXS data, crystalline orientation factors were calculated by taking an azimuthal scan of 2θ peak corresponding to the crystalline diffraction peak of interest, then corrected for background scattering by subtraction of azimuthal intensity of a peak significantly far away from any scattering.

Mean-square cosine values were calculated from plane normals from corrected intensity distribution from WAXS data. The formula is as follows:

$$\langle \cos^2 \phi \rangle_{hkl} = \frac{\int_0^{\frac{\pi}{2}} I(\phi)_{hk0} \sin \phi \cos^2 \phi d\phi}{\int_0^{\frac{\pi}{2}} I(\phi)_{hkl} \sin \phi d\phi} \quad (5.9)$$

and crystalline orientation factor, f , is calculated by

$$f_{(hkl)} = \frac{1}{2}(3 \langle \cos^2 \phi \rangle_{hkl} - 1) \quad (5.10)$$

where $\langle \cos^2 \phi \rangle_{hk0}$ is the mean-square cosine average over all crystallites of the angle between crystal and reference axis [214]. For any crystallographic axis, $\langle \cos^2 \phi \rangle = 1$ for perfect Z alignment, $\frac{1}{3}$ for random alignment, and 0 for perpendicularity. The value f_{hkl} therefore shows values of 1, 0, and $-\frac{1}{2}$, respectively.

As mentioned in literature review, THV does not have a properly understood crystal structure; however it has been approximated as hexagonal form IV of PTFE when high amounts of -TFE contents are present, such as in this case [44]. Hexagonal crystal cells need only one ($00l$) plane of diffraction for uniaxial orientation factor characterization and in this case, (001) was used for THV [214].

For the sake of calculation, ETFE unit cell is approximated as pseudo-hexagonal, as validated by Miranda, et al. al, in which (002) plane is used for calculation of orientation factor [243].

Figures 5.9 and 5.10 show calculated crystalline orientation factors for ETFE and THV films (respectively) stretched uniaxially at 145°C and 10 mm/min. Recall that the crystalline orientation factor, f_c , gives a quantitative indication of alignment with an arbitrary reference direction, in this case we have assigned the film stretching direction. For $f_c = 1$, crystals are perfectly parallel with film stretching direction. For $f_c = -1/2$ they are perpendicularly aligned, and $f_c = 0$ indicates random orientation. For ETFE samples, orientation factor is about 0.2 for as cast film ($\epsilon_T = 0$), indicating only a small amount of crystalline alignment parallel to the stretching direction (MD), and increases rapidly until $\epsilon_T = 0.7$, where f_c levels off to around 0.5. Between $\epsilon_T =$

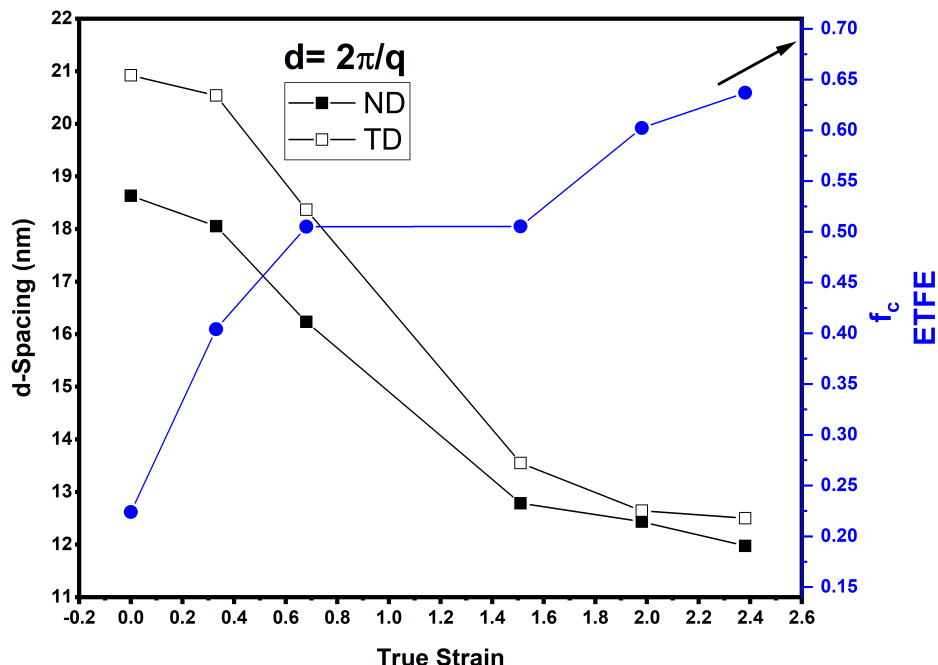


Fig. 5.9.: Calculated d-spacing (left y-axis) and crystalline orientation factors (right y-axis) for ETFE temporal evolution samples stretched at 145°C and 10mm/min.

0.7 and $\epsilon_T = 1.5$, orientation factor remains constant, indicating there is no average change in crystalline alignment while stretching here. Care should be taken with these measurements however, as they represent only overall changes in average orientation, and do not consider individual lamellae. Therefore, it is entirely possible that complex reorientation is occurring in the film during these values of true strain; in fact, from SAXS data this is likely the case (as will be explained later; see Figure 5.11). From SAXS patterns we saw at $\epsilon_T = 0.7$ the development of a four point pattern, indicating rearrangement of lamellae which is likely why average orientation does not change. For higher stretch ratio, $\epsilon_T = 2.1$, f_c again begins increasing despite continuation of the four-point pattern; however in TD the four point pattern has reverted back to a two point one, indicating part of the complex reordering is complete and this is likely why f_c is higher than the previous plateau value. At $\epsilon_T = 2.4$, f_c continues increasing as the c-axis of newly re-ordered lamellar organization structure continues to become more closely aligned parallel to the stretching direction.

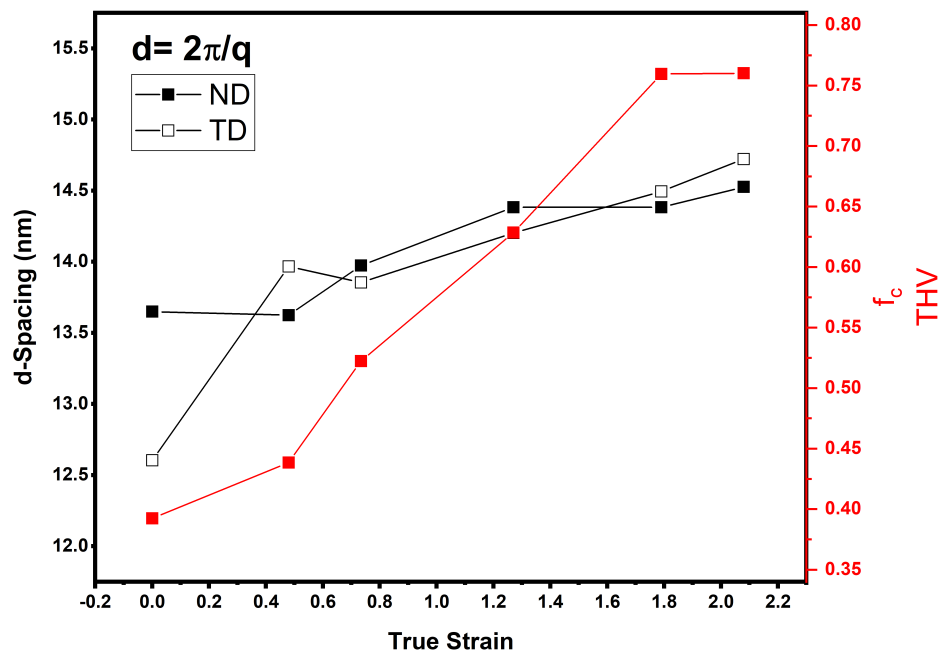


Fig. 5.10.: Calculated d-spacing (left y-axis) and crystalline orientation factors (right y-axis) for THV temporal evolution samples stretched at 145°C and 10mm/min.

Orientation factor for THV, on the other hand, continuously increases as stretch ratio increases (Figure 5.10). Initial orientation in the as cast film is around $f_c = 0.4$, which means crystalline regions are fairly oriented parallel to MD, likely due to MDO in casting process. Since precise crystallinity value could not be calculated for this material due to lack of available literature value for heat of fusion for 100% crystalline THV, we do not know exactly how crystalline the film is, but it can safely be assumed that crystallinity amount is relatively low. Therefore, f_c data suggest the small amount of crystalline regions in THV film as-cast are fairly oriented in MD and orient further during uniaxial stretching, up to a final value of around $f_c = 0.75$.

Small Angle X-ray Scattering

Small angle X-ray scattering patterns are shown in comparison to strain and stress-optical data in Figure 5.8 and Figure 5.7, respectively. X-ray patterns were taken

in both film normal direction (ND) and transverse direction (TD). Larger 2D SAXS patterns are also shown in the Appendix C, Figure C.6 (ETFE) and Figure C.5 (THV).

SAXS patterns for THV depict initially low levels of orientation in machine direction, due to melt casting process. Upon small amount of stretching to true strain = 0.5, which is just past elastic deformation region, lamellar regions begin orienting in stretching direction, as evidenced particularly by TD scattering pattern which shows clear, oriented arcs. However, MD scattering pattern for THV at 0.5 true strain suggests lamellar rearrangement, as scattering arcs become broad and more isotropic compared to as cast pattern. Since this is still in elastic stretching region, this rearrangement is reversible. As stretching continues into plastic deformation region, scattering arcs become smaller and sharper, indicating more regular lamellar regions. The long period between lamellar regions increases (see Figure 5.10) with stretching and it continues to increase as more strain is applied to the system. This long period should continue to increase until the lamellar chains start to unravel or chain breakage occurs. During experimentation, this was observed to occur around true strain of 2.1.

SAXS patterns for ETFE (see Figures 5.8 and 5.7) show initial meridional anisotropy as evidenced in MD and TD scattering images. After stretching to true strain of 0.3, initial oriented spots become elongated arcs as lamellae begin to tilt. This is still in elastic deformation region, so lamellar tilt is reversible. A four point, X-shaped pattern is observed at true strain = 0.7 as lamellae tilt further and strain induced crystallization occurs in plastic deformation region. At true strain of 1.5, an alternate four-point pattern is observed, with two horizontal and two vertical scattering spots (8 total), in deformation Regime III. At very high levels of deformation, lamellae re-orient to be stacked in MD orientation above true strain of 2.1. Observation of this four-point pattern when stretching ETFE in solid state was also confirmed by Tanigami, et al. [31]. AFM imaging (see next section) was used to further study this complex reordering in ETFE during uniaxial orientation. Lamellar long period

decreases consistently with stretching (Figure 5.9) from as cast to true strain of 1.5 as lamellae are broken up and reorient in MD. Increasing true strain from 1.5 to 2.1 to 2.4, d-spacing decreases slightly as complex reordering finishes in plastic deformation Regime III, with final disappearance of 4-point pattern at true strain = 2.4.

5.3.3 Structural Hierarchy Model

AFM images of THV show (Figure 5.12), in more detail, morphology during stretching. In conjunction with SAXS data, a structural model was proposed based on AFM images taken at different stretching ratios. The as cast SAXS pattern with some degree of meridional anisotropy is corroborated by the AFM image, which shows small, sheaf-like lamellae growing in all directions with some MD orientation. Very dark regions in both height and phase images suggest void formation in the film, as air has the highest possible scattering contrast. After stretching to 0.5 true strain, arcs observed in SAXS pattern are broader, indicating a wider range in lamellae size, with isotropic ring still present. AFM phase image does not give much information, but height image shows large bright regions which are aligned in MD (center of image) and twisted (left hand side of image). Combination of the SAXS pattern and AFM images suggests a twisting and breakup of lamellae at this stage. Voids elongate to ovals as stretching ratio increases. Further stretching to 1.3 true strain and above shows discrete arcs in the SAXS 2D patterns, without isotropic ring present anymore, indicating higher degree of MD lamellar organization. Additionally, d-spacing continues to increase as more strain is put on tie chains between lamellae. 1D SAXS data supports this, as d-spacing increases with stretching ratio. AFM images for films stretched to 1.3 true strain, more clearly observed in the height image, show brighter regions with overall alignment in MD, that are separated by relatively small d-spacing. As stretching proceeds, AFM height image for the 2.1 true strain sample shows very bright, flat regions which are clearly aligned in the drawing direction. Freimuth, in absence of having the ability to calculate actual percent crystallinity for

this material since heat of fusion for 100% crystalline polymer is unknown, estimated percent crystallinity to be around 10% for THV as cast based on proposed crystal cell dimensions [37]. This is supported by AFM images shown here which show that bright crystalline regions constitute a relatively small proportion of these images.

AFM phase images for ETFE stretched at 145°C are shown in Figure 5.11, with stretching direction vertical. 1000nm x 1000nm images show large-scale structure, and images to the right show smaller features as image resolution increases. A structural model was also proposed for ETFE during orientation using SAXS and AFM data. As cast AFM images show fibrillar structures, with alternating crystalline and amorphous regions as shown in the cartoon drawing. This is corroborated by two-point SAXS patterns oriented in MD. Upon stretching to true strain of 0.7, a 4-point SAXS pattern appears. Based on AFM images, this is likely caused by bending and onset of breakup of lamellae as they start unraveling locally at high stresses during stretching. This deformation mechanism was proposed by Tanigami when stretching row-crystallized ETFE above T_g [31]. Tanigami also provided SAXS evidence, showing a similar 4-point pattern to the one presented here [31]. An example of lamellar bending is highlighted in the 1000nm x 1000nm resolution image, circled in red. After stretching to 1.5 true strain, previously bent/deformed lamellae break up and twist, forming a complex 8-point SAXS pattern (i.e. two 4-point patterns combined). This mechanism is clearly shown in the AFM images, especially in higher resolution images which show rotating lamellae (500nm x 500nm image) and x-shaped twisting and breaking lamellae (250nm x 250nm image). Finally, upon stretching to 2.4 true strain, AFM image shows broken up lamellar, which are smaller than those observed previously, but still oriented in MD. This is corroborated by SAXS pattern, which now shows broad, 2-point arcs oriented in MD.

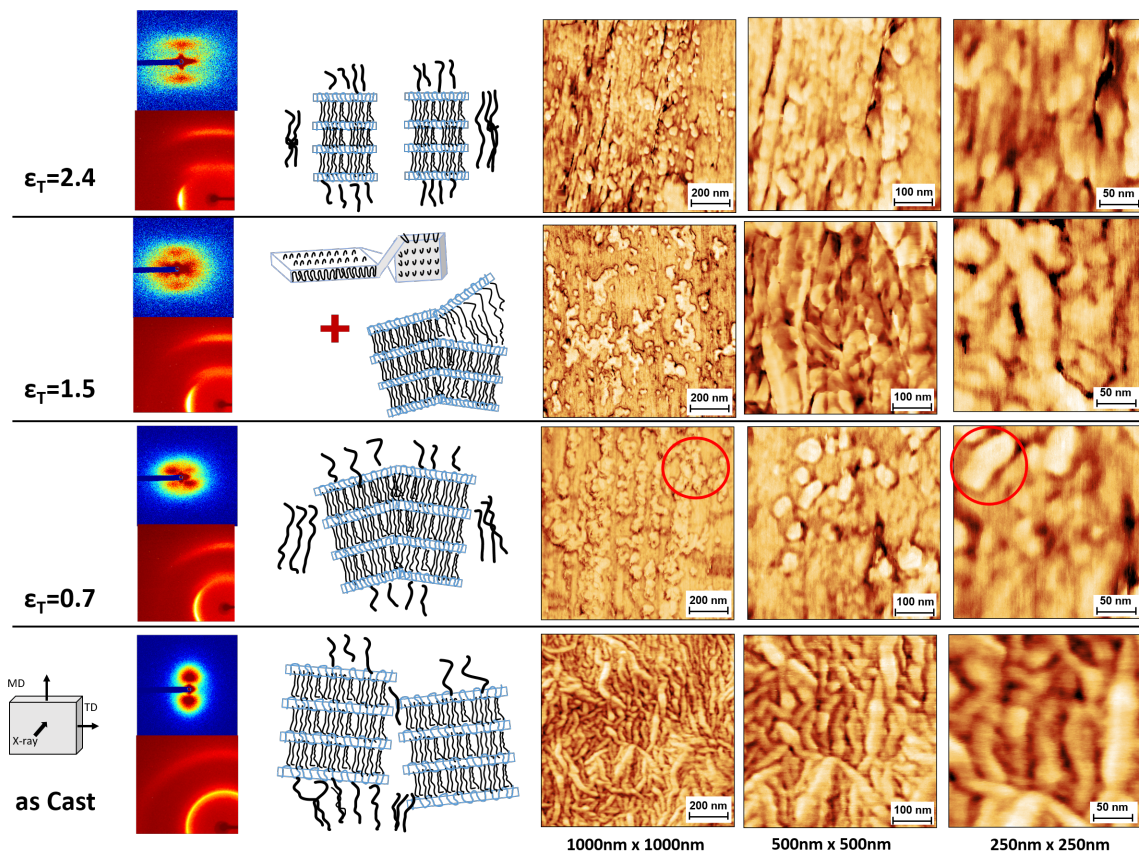


Fig. 5.11.: ETFE structural model cartoon, with SAXS images and AFM for supporting detail. Stretching direction is vertical.

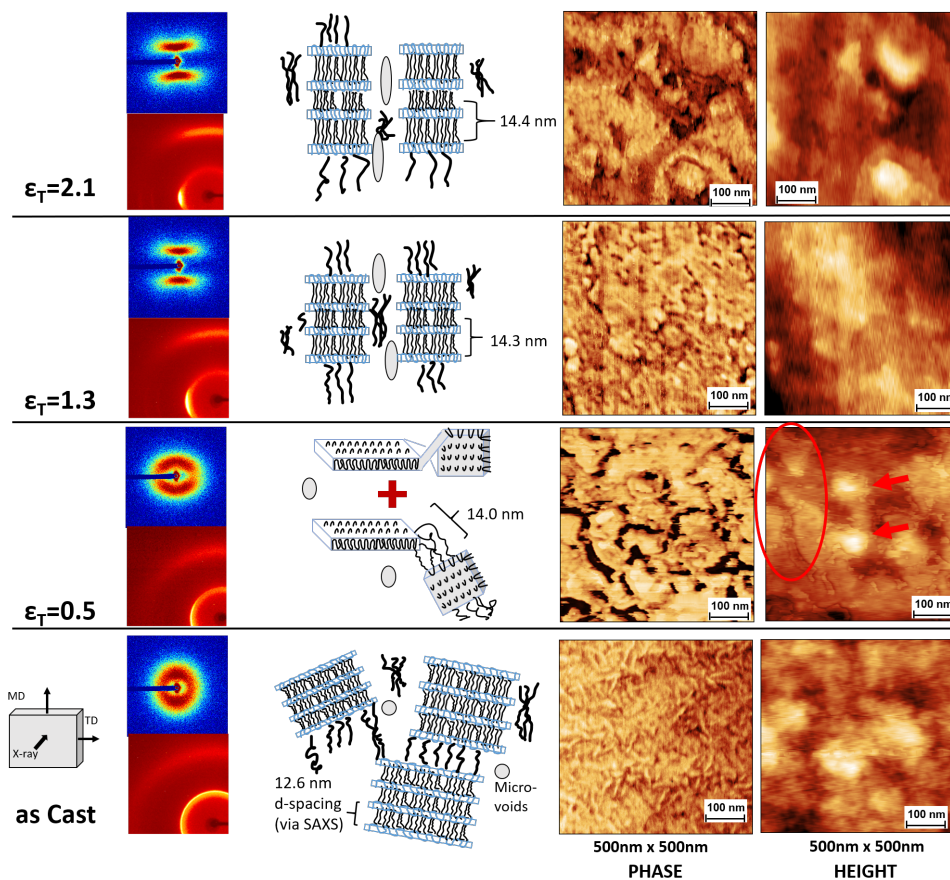


Fig. 5.12.: THV structural model cartoon, with SAXS images and AFM for supporting detail. Stretching direction is vertical.

5.4 Conclusions

The uniaxial deformation behavior of two fluoropolymer films, ETFE and THV, were studied via a custom-built uniaxial stretching machine which measures true stress, true strain, and birefringence in real time. Monolayer films with starting thickness in the range of 40-50 μm were uniaxially stretched at several temperatures. Offline characterization via DSC, WAXS, SAXS, and AFM at targeted values of the true stress, true strain curve were used to supplement the above measurements to obtain a clearer picture of how stretching affects morphology of these materials.

Uniaxial stretching at various temperatures showed that THV deforms nearly affinely, independent of starting morphological state (i.e. solid state or partially molten). The stress-optic constant and strain-optic constant for THV increased with increasing stretch temperature, due to decreasing stress in the system. A temporal evolution study was done at 145°C to characterize films at specific points of deformation. DSC measurements showed a decreasing enthalpy of fusion with increased stretch ratio at 145°C, indicating an overall decrease in percent crystallinity. WAXS patterns show initial in- and out-of plane isotropy, followed by increasing MD orientation after stretching. This is supported by calculated orientation factor which increases with increasing deformation. SAXS 1D information shows long spacing increases with increasing stretch ratio when THV is deformed at 145°C. Combination of AFM and SAXS data were used to construct a structural hierarchy for this material during stretching experiments. As cast, THV has small, sheaf-like lamellae with overall average MD orientation. During stretching to small strains, lamellae twist and break up, then orient in machine direction with increasing d-spacing. The presence of voids was also postulated due to very high contrast regions in AFM images. These voids elongate in stretching direction to oval shape during deformation.

When ETFE was stretched in solid-state, it also showed nearly affine deformation. Stretching ETFE at higher temperatures (i.e. when partially molten) caused premature breakage. DSC results showed an increase in crystallinity during stretching, due to stress-induced crystallization. Total change in percent crystallinity, however, was fairly small at around 5%, due to the relatively high starting percent crystallinity (likely due to initial MDO of these films). WAXS patterns for ETFE show initial in-plane and out-of-plane isotropy, with oriented arcs appearing after small amounts of stretching. Proposed structural hierarchy model based on SAXS and AFM imaging suggests ETFE film in as cast state consists of stacked, relatively unoriented lamellae which, upon stretching, bend and deform, causing the appearance of 4-point scattering pattern (true strain of 0.7). Interestingly, a second complex 4-point scattering pattern appears when ETFE is stretched to true strain of 1.5. AFM patterns show

complex twisting and reorganization of lamellae at this stage which, upon stretching further (i.e. to true strain 2.4), become again oriented with machine direction as shown by reappearance of two discrete scattering arcs arranged in MD.

Since these materials have high melting points, low k values, and good resistance to corrosive chemicals, they may find applications in high temperature dielectrics, photovoltaics and HEV, for example.

5.5 Acknowledgements

The authors would like to thank PolyK Technologies for kindly providing the films for this project. The authors acknowledge and greatly appreciate support and funding from the Office of Naval Research Grant N000141712048. Characterization of this material is supported by the National Science Foundation through the Major Research Instrumentation Program under Grant No. CHE 1625543 (Funding for the single crystal X-ray diffractometer).

6. MECHANO-OPTICAL BEHAVIOR AND MORPHOLOGY OF UNIAXIALLY ORIENTED POLYETHYLENE TEREPHTHALATE (PET) AND ETHYLENE VINYL ALCOHOL COPOLYMER (EVOH) COMPOUNDED BLEND FILMS AND THREE LAYER COEXTRUDED FILMS

Uniaxial orientation of two polymer film systems consisting of PET and EVOH in compatibilized blend films and and coextruded layered structures were studied in uniaxial extension, using custom built, real time spectral birefringence machine. Comparison of morphology-processing-property relations for blend versus layer systems were investigated via real time true stress, true strain, and birefringence values coupled with offline characterization methods DSC, SAXS, and WAXS. Mechano-optical behavior was significantly different for blend versus layered films, with blend films showing higher stress development at high strain values. Time slicing study for layered PET-EVOH-PET films with 30%-40%-30% composition showed overall development of birefringence was the same but blend and layered films took different paths of deformation to get there. Calculation of orientation factors from 1D WAXS data showed that PET orientation was largely unaffected by increasing EVOH content in blend films, but blending was detrimental to orientation of EVOH. In the layered systems, PET's orientation was also largely unaffected by amount of EVOH in the structure. Higher orientation factor for EVOH in all layered films compared to neat EVOH film after stretching suggests that the coextrusion process is beneficial to improved orientation of EVOH.

6.1 Introduction

Barrier properties of polymers are important to many industries, including construction, tires, pharmaceuticals, and food packaging. The specifics governing permeability properties of polymers depends on their polarity, chemical structure, crystallinity, solvent sensitivity, etc. [244], [245]. Non-polar polymers, especially polyolefins like low density polyethylene (LDPE), high density polyethylene (HDPE) and polypropylene (PP), are naturally resistant to water permeability and therefore find heavy use in packaging applications [245]. High crystallinity is valuable because crystalline regions are generally thought of as being impenetrable by small molecule permeants due to a high degree of tight molecular packing; thus diffusing of such molecules occurs only through amorphous regions and crystalline domains create a tortuous path for diffusion through the material [245]. Biaxial orientation of slow crystallizing polymers which can be quenched into amorphous state, such as PP and polyethylene terephthalate (PET), can further improve barrier properties by mechanisms of stress induced crystallization and orientation [245]. Biaxial orientation followed by heat setting (for example, in tenter frame processing) also provides high dimensional stability, defined by high stiffness and low shrinkage in the film plane [245].

Ethylene vinyl alcohol (EVOH) is a random copolymer containing ethylene and vinyl alcohol monomers in varying amounts ranging from 27 to 48% ethylene in the backbone [145]. EVOH is a high oxygen barrier polymer, with higher vinyl alcohol content indicating higher barrier, due to hydrogen bonding which reduces free volume [145]. However, this property must be balanced with processability; as lower vinyl alcohol content (i.e. higher ethylene content) means easier melt processing. Though EVOH has the highest known barrier to oxygen of any polymer, it suffers from low water vapor permeability due again to strong hydrogen bonds [246], [147]. EVOH is also highly crystalline and is a fast crystallizing polymer, making it hard to process and orient and prone to cracking when used on its own [145]. To combat these downfalls, the barrier function of EVOH can be made into useful packing by two general meth-

ods: addition of EVOH as a barrier layer or by compounding it into a base polymer matrix [246]. Both of these techniques will be investigated in the following work.

PET is widely used in rigid and flexible packaging applications, for example water bottles and microwaveable packaging, and has good barrier to aromas and oil. However, in its unoriented state it is highly permeable to oxygen due to its generally low percent crystallinity [145]. In contrast to EVOH, PET is a slow crystallizing polymer which can be quenched into nearly fully amorphous state. Techniques to improve barrier properties of PET include metalization and physical vapor deposition or plasma-enhanced chemical vapor deposition of inorganic SiO_x , for example, all of which add an extra step and cost to producing high barrier PET films [246]. However, Strain induced crystallization during orientation can occur for PET depending on stretching temperature and rate, leading to modest levels of crystallinity up to about 30%. It is well known that the orientation of PET has significant impact on its properties and the extent of which is largely dependent on processing conditions. For example, yield stress, thickness uniformity, surface roughness, permeability, shrinkage and tear strength, optical and dielectric properties, among others, are largely affected by the stretching process. Gas permeability, and especially oxygen permeability has been studied for PET film both before and after orientation. A study on barrier properties in PET by Ozen, et al. found that simultaneous biaxial orientation of PET films to 2X2 and 3X3 reduced oxygen permeability by about 19% and 58%, respectively [11]. Barrier improvement as a result of stretching is explained by stress-induced crystallization, which creates regions impermeable to gas migration [11]. PET adds an amorphous component to EVOH, helping with orientation, and can protect EVOH from degradation due to water in the air. PET also has high barrier itself when oriented because it crystallizes upon orientation form to small crystals [246]. Therefore, preferential the two main factors which largely affect barrier properties of polymer films are preferential orientation and crystallization.

Several patents claim the use of high barrier materials such as EVOH layered with protective materials such as PET [247], [248], [249]. However, EVOH orientation has not been as well studied. One study reports structural development of EVOH and EVOH/clay composites during uniaxial orientation, finding that these materials could be stretched at temperatures above the glass transition (T_g) [51]. Furthermore, when stretched at moderate rates, both EVOH and EVOH/clay films experienced strain-induced crystallization and relaxation and recrystallization of imperfect crystals [51]. Composite structures of PP and EVOH were studied in biaxial orientation by Breil, et al. who found that sequential orientation leads to microfibrillation of EVOH and therefore very poor film quality [47]. However, sequential stretching was possible with films containing EVOH of greater than 44% ethylene content, and simultaneous stretching could be accomplished for any composition [47]. PP/EVOH blend films were studied by Yeo and co-workers who found viscosity ratio of the two components and geometry of dispersed phase morphology to be governing factors in determining barrier properties in films after biaxial orientation [54].

EVOH/PET blend films were studied by Gopalakrishnan, et al. who found that matching rheology of the individual components in the blend was important to obtaining films which can be oriented, leading to good properties afterwards [52]. A compatibilizer was also used in this study and found to be essential to obtaining improved barrier properties; all of the films with compatibilizer showed improved barrier properties to that of neat, oriented PET [52]. Oriented blend films containing EVOH and PET or PEN were also studied more recently by Kit and Schultz [53]. By varying stretching parameters, it was found that morphology of EVOH largely determines the extent to which barrier properties are improved or worsened in oriented blend films [53]. In agreement with Yeo [54], laminar morphology of EVOH with higher aspect ratio were shown to improve barrier properties of the blend films [53]. Kit found that oxygen barrier and mechanical properties were improved with addition of EVOH and orientation as draw ratio increased and drawing temperature decreased [53]. Furthermore, water vapor permeability, which is reasonable in neat

PET and PEN materials and very poor for EVOH, was not largely impacted with addition of up to 15% EVOH [53].

Since PET and EVOH are thermodynamically immiscible, a compatibilizer can be used to help promote better interfacial adhesion. Maleic anhydride-grafted polyolefins are often used a tie layer in multilayer structures or compatibilizer in polymer blends, where the anhydride group bonds to the non-polar polymer and the -OH group bonds to EVOH [145]. PET and EVOH were chosen as common polymers in food packaging which, when combined together, may create synergistic effects on barrier and other film properties. Improvement of properties is not likely in a non-compatible system as proven in previous literature studies [52], [53].

Though several studies exist which investigate effects of combining PET and EVOH in either blend or layer structure, with or without orientation, for the improvement of barrier properties, ours is unique in that custom built equipment in our lab allows for measurement of real-time true stress, true strain and birefringence during stretching. This capability is unique to our group and provides a better understanding of how orientation and crystallization (mapped through birefringence) change at specific values of true stress or true strain during uni- or biaxial orientation of polymer films. The purpose of this work is to determine structure-processing relationship of films consisting of high barrier, FDA approved polymers. Film structures of equivalent materials in a polymer blend versus three layer system were investigated to deduce any benefit of using one type of system over the other in terms of structure, processing and/or properties. This study provides a foundation of material and processing selection with intent to scale up to biaxial stretcher to provide samples large enough for barrier testing (specifically, oxygen and water vapor transmission permeability).

6.2 Materials and experimental procedures

6.2.1 Materials

The materials used in this study are polyethylene terephthalate (PET, 0.80 dL/g IV) grade from Dak Americas, ethylene-vinyl alcohol copolymer (EVOH, 44mol% ethylene) grade from Kuraray and an ethylene-acrylic ester-maleic anhydride terpolymer compatibilizer (Lotader 3210) supplied by Arkema. Typical properties of these materials can be found in Table 6.1. All materials, compounds, and films were kindly produced and provided to us by A. Schulman, Inc.

Table 6.1.: Technical properties for raw polymer materials as specified by supplier.

Component	IV (dL/g)	Melt Index ¹ (g/10min)	T _m (°C)	T _g (°C)	Density (g/mL)
PET	0.80	—	238	83	0.849
EVOH	—	1.7	165	54	1.14
Compatibilizer ²	—	5.0	107	—	0.940

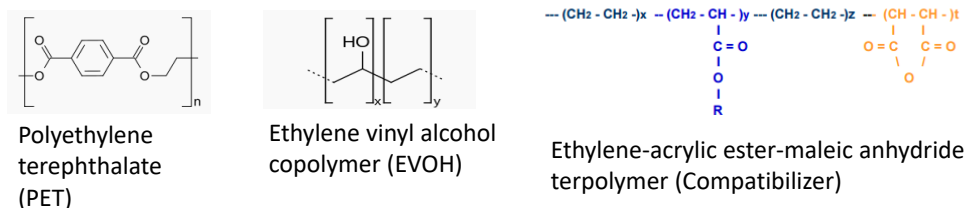


Fig. 6.1.: Chemical structures for materials used in this study.

Chemical structures for polymers used in this study are shown in Figure 6.1.

¹Melt index conditions: 190°C, 2.16 kg.

²Ethylene-acrylic ester-maleic anhydride terpolymer

6.2.2 Processing

Compounds of these materials with varying EVOH amounts were produced on a 25 mm Coperion ZSK-25 twin screw extruder. Processing conditions are shown in Table 6.2. Blends consisted of PET/ EVOH/ Compatibilizer in ratios of 75/20/5, 51/40/9, and 29/60/11 wt%. From these compounds, monolayer films were made on a three-layer Dr. Collin ZK-25, cast film line, with 12 inch die and approximately 0.46 mm die gap. Multilayer films were also made with an ABA structure in amounts which mimic the blend films. The A layer consists of PET/Compatibilizer and the B layer is EVOH/Compatibilizer. A more detailed film structure description can be seen in Table 6.3. Film processing conditions are shown in Table 6.4. During film processing, edge pinning was used and air knife blown on one side of film, while the other contacted a casting chilled roll (held at 65°C) to quench the film into amorphous state.

Table 6.2.: Extruder barrel temperatures for polymer blends.

Zone	1	2	3	4	5	6	7	8	9	10	Die
Temp. (°C)	190	250	250	230	220	220	200	190	190	210	250

Table 6.3.: Overview of film structures tested in this study.

Film Type	Structure ³	Composition		
		EVOH (wt %)	PET (wt %)	Compatibilizer (wt %)
control	monolayer	0	100	0
layered	ABA	20	75	5
layered	ABA	40	51	9
layered	ABA	60	29	11
blend	ABA	20	75	5
blend	ABA	40	51	9
blend	ABA	60	29	11
control	monolayer	100	0	0

³Film Structure ABA refers to PET/EVOH/PET.

Table 6.4.: Film line processing conditions.

Zone	1	2	3	4	5	clamp	Die	chill roll
Temp. (°C)	254	257	260	263	263	263	263	75

For post-processing experiments, our instrumented, custom built uniaxial stretcher was used to measure mechano-optical properties of polymer samples in real time during stretching. Measurements of optical retardation and sample width at the exact center of the film allow for calculation of film thickness and therefore true stress, true strain and birefringence values (at 546 nm wavelength) in real time during stretching. These calculations assume the following:

1) simple extension

$$D_t/D_o = W_t/W_o \quad (6.1)$$

2) incompressibility

$$L_o W_o D_o = L_t W_t D_t \quad (6.2)$$

Using these assumptions, the following parameters are calculated:

Thickness:

$$D_t = (W_t/W_o)D_o \quad (6.3)$$

Birefringence:

$$\Delta n = R/D_t \quad (6.4)$$

True strain:

$$L_t/L_o - 1 = (W_o/W_t)^2 - 1 \quad (6.5)$$

True stress:

$$F_t/(W_t D_t) = F_t/[(W_t^2/W_o)D_o] \quad (6.6)$$

Where R is retardation, Δn is birefringence, D_o , W_o , L_o are initial thickness, width, and length respectively, and D_t , W_t , L_t , F_t , are time variations of thickness, width, length, and force.

Further details of this machine are listed elsewhere [77], [209], [220].

To ensure software calculations were reliable, real-time film thicknesses predicted by laser width measurements were compared to those measured offline with a digital micrometer. Comparison of predicted thicknesses versus actual measured values can be seen in Appendix D, Figure D.1.

For uniaxial stretching, films were cut with a die cutter (44.25 x 76 mm overall dimensions) into dogbone shape and painted with fluorescent yellow dye in a four dot pattern. This pattern is enhanced by UV light and tracked via CCD camera, allowing for calculation of local true stains in the sample's MD and TD directions. Films were allowed to equilibrate for ten minutes before stretching at 30 mm/min, then held taut and quenched by blowing cold air until they reached room temperature (about 20 minutes). Stretching was conducted at 90°C, where PET is in the rubbery state and EVOH is solid state.

Thermal properties were measured on films as cast and after stretching using Netzsch DSC 214 Polyma differential scanning calorimeter with heating rate of 10°C/min. Percent crystallinity of each material was calculated using enthalpy of heat of fusion for 100% crystalline polymer, $\Delta H_o = 175.6$ J/g for EVOH and $\Delta H_o = 140$ J/g for PET [250], [144].

Wide angle X-ray measurements were run on Bruker D8 Quest diffractometer with kappa geometry, an I- μ -S microsource X-ray tube, laterally graded multilayer (Goebel) mirror single crystal for monochromatization, and Photon2 CMOS area detector. The generator was operated at 50 kV at current of 1 mA, beam was monochromatized at Cu K-alpha radiation ($\lambda = 1.54178$ Å) and samples were irradiated for 1 minute, with the exception of neat PET films, which were irradiated for 2 minutes.

Small angle X-ray scattering characterization was done on an Anton Paar SAXSpoint 2.0 machine containing microfocus Cu K- α radiation, $\lambda = 1.54178 \text{ \AA}$, source and two dimensional, Eiger R hybrid photon-counting detector. Generator was operated at 50 kV at current of 1 mA, and samples were irradiated for 30-45 minutes, depending on sample thickness. SAXS and WAXS images were taken in both film normal (through film thickness) and transverse directions.

6.3 Results and discussion

6.3.1 Differential scanning calorimetry (DSC)

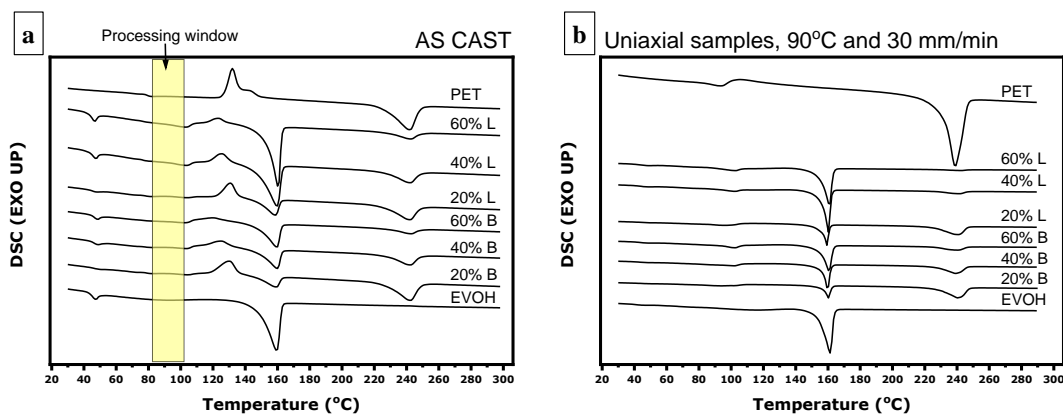


Fig. 6.2.: DSC curves for films a) as cast, with yellow indicating processing window and b) after stretching at 90°C and 30 mm/min to 3.5X initial length.

Thermal characterization for the films as cast is shown in Figure 6.2 (a), where the yellow region highlights chosen processing window for these films, which occurs in the rubbery region above T_g and below T_{cc} of PET. Addition of EVOH material in both blend and layered structures leads to suppression of cold crystallization of PET. Figure 6.2 (b) shows DSC curves for films after stretching at 90°C and 30 mm/min in uniaxial extension. Here we see that cold crystallization peak is almost

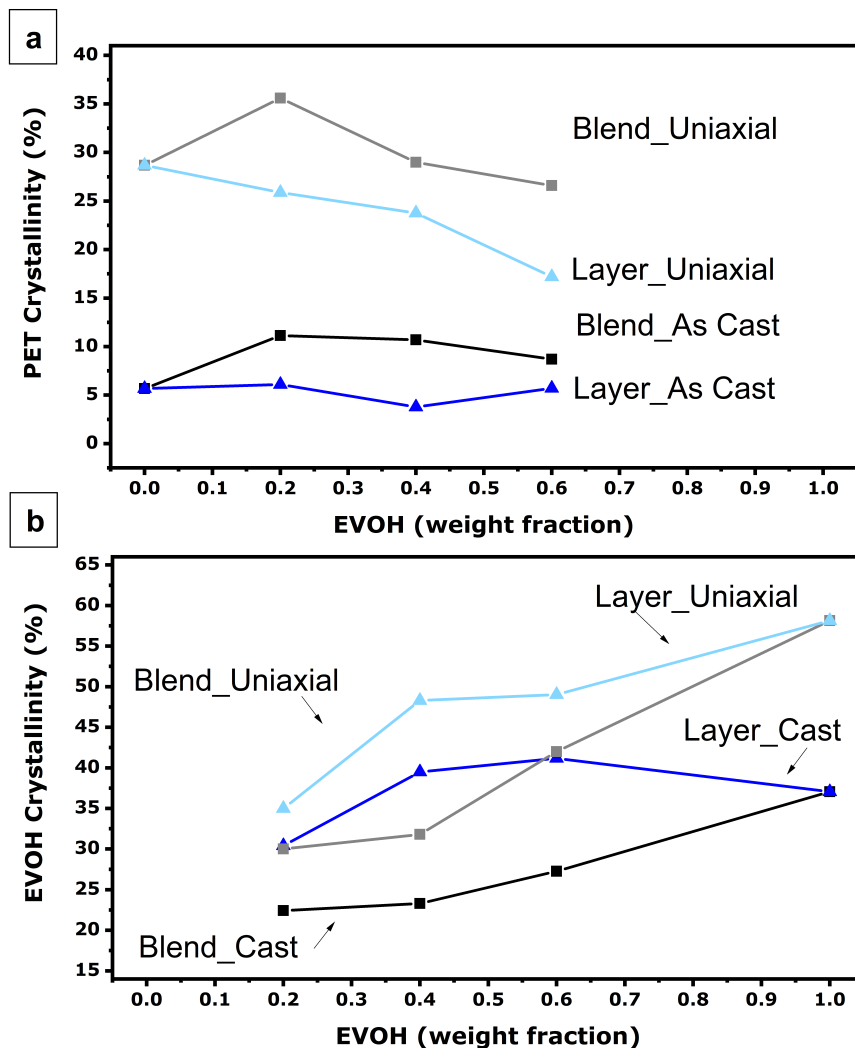


Fig. 6.3.: Calculated percent crystallinity of films both before and after stretching at 90°C and 30 mm/min to 3.5X initial length, normalized for amount of a) PET and b) EVOH in the film.

fully suppressed, indicating that films have nearly reached maximum stretchability. Melting peaks for PET and EVOH are larger when more of each respective material are present as well.

Calculated percent crystallinity values for films as cast and after stretching at 90°C and 30mm/min are shown in Figure 6.3, which have been normalized to the amount of each material in the film sample tested. Figure 6.3a shows percent crystallinity

for PET versus weight fraction of EVOH in each film. As expected, total amount of PET percent crystallinity in films as cast is relatively low, less than about ten percent. Compared to layered films, blend films as cast have slightly higher percent PET crystallinity which is likely due to higher probability of PET chains finding one another since relative volume of nearest neighbors is higher in blend films. The fact that the percent PET crystallinity decreases with increasing EVOH content in blend films supports this statement. In stretched samples, percent crystallinity is much higher than in the films as cast since PET undergoes stress induced crystallization. In general, percent crystallinity of PET in blend and layer films decreases with increasing EVOH content as less PET becomes available to crystallize. Figure 6.3b shows the same information as described for PET but relative to EVOH percent crystallinity. Normalized percent crystallinity of EVOH increases as weight fraction of EVOH increases in both blend and layer system. However, for the as cast layered films, we see leveling off of percent crystallinity in films with 40% and 60% EVOH which is higher than neat EVOH film as cast. This suggests that the layered structure is beneficial to increasing percent crystallinity of EVOH material, and could be due to increased orientation of this material (which will be discussed later; see Figure 6.11) as it is continuous in sandwich structure. After stretching, the amount of EVOH crystallinity in layered films increases greatly as EVOH amount increases from 20% to 40%, then levels off. In the blend films after stretching, EVOH percent crystallinity increases steadily as amount of EVOH increases due to increased probability of like-molecules finding one another.

6.3.2 Mechano-optical properties

Stress-strain results of uniaxial stretching experiments at 90°C and 30 mm/min to 3.5X draw ratio are shown in Figure 6.4. Uniaxial stretching data for blend and layer films with 20% EVOH (labeled as 20% B and 20% L) is compared with stretched

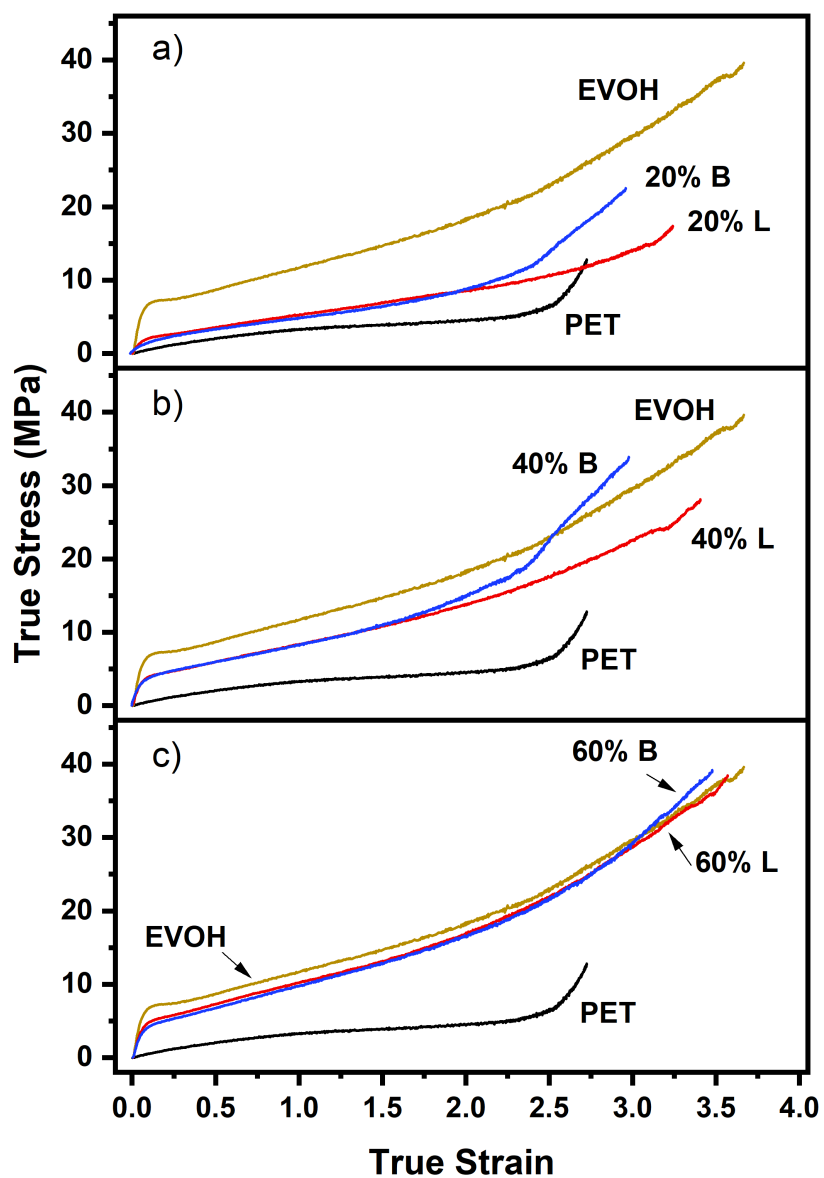


Fig. 6.4.: True stress, true strain curves for film samples stretched at 90°C and 30 mm/min to 3.5X initial length; a) 20% EVOH films, b) 40% EVOH films, and c) 60% EVOH films.

control PET and EVOH films in Figure 6.4a, where the 20% blend and layer film stress strain curves fall in between neat EVOH and neat PET. Furthermore, the 20% blend and layer films show nearly identical true stress, true strain data curves until around a true strain of 2.0, where the slope of the 20% blend film increases more rapidly than the corresponding 20% layer film as higher stresses are developed. The same trend is shown for 40% blend and layer stress strain curves, shown in Figure 6.4b, with the exception that the deviation in similarity of the 40% blend and layer curves occurs at lower true strain, around 1.5, as higher stresses are developed in the 40% blend film. Furthermore, the 40% blend film stress surpasses the EVOH control

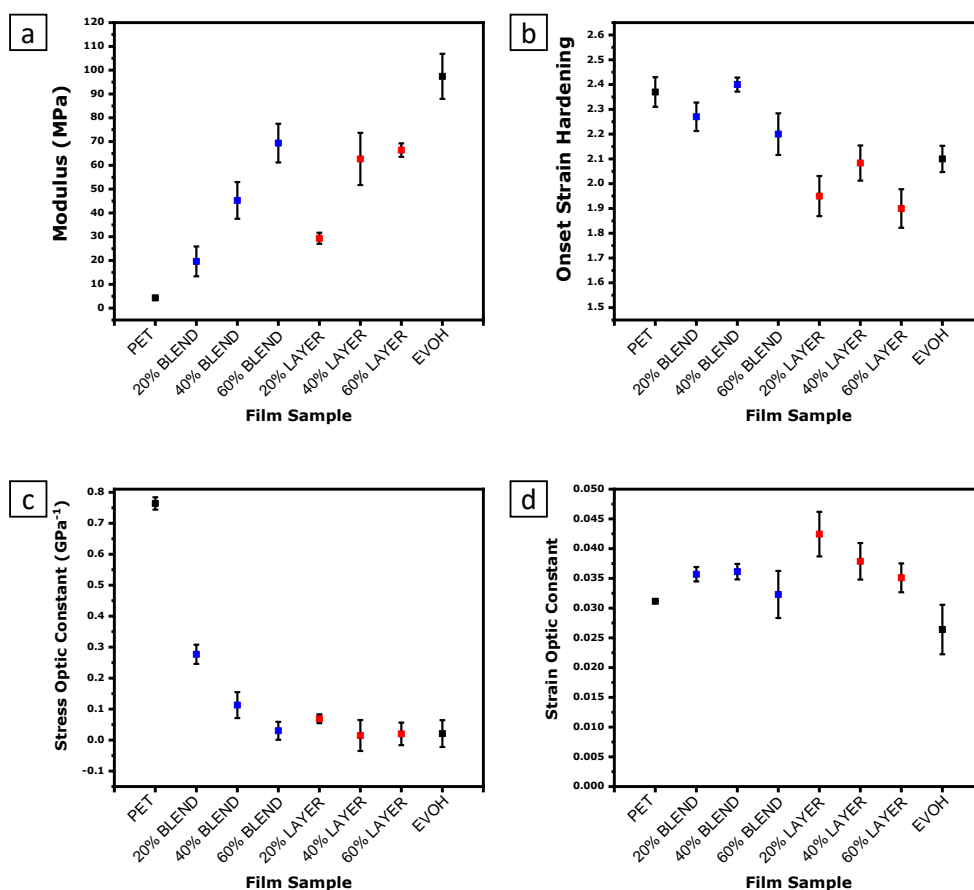


Fig. 6.5.: Mechano-optical properties calculated for PET/EVOH blend and layer films after stretching at 90°C and 30 mm/min to 3.5X initial length. a) Modulus, b) onset strain hardening, c) stress optic constant, and d) strain optic constant.

film, which is unexpected since the maximum value of stress the material experiences during stretching should be dictated by the components in the blend, the highest of which is EVOH. And finally, Figure 6.4c shows that films with 60% EVOH behave essentially the same as neat EVOH control film, with only slightly lower yield stress. Again, it is observed that the 60% blend film's stress at end of stretching increases more rapidly than that of the 60% layer film and also EVOH control; however, in this case the magnitude of difference is not as large compared to the 20% and 40% EVOH cases.

Mechano-optical properties for the uniaxial orientation study presented above are summarized in Figure 6.5. Calculated Young's modulus values, presented in Figure 6.5a, show that all compositions of blend and layered films fall within the two extremes measured from neat PET and EVOH, as expected. The blend film series moduli increase linearly with addition of EVOH, however moduli for the layer films increase from 20% EVOH to 40% EVOH but then the value levels off. This suggests that in a layered film structure, there is a maximum amount of EVOH which increases modulus value. Figure 6.5b shows calculated onset of strain hardening point. Theoretically, we expect OSH values to fall between the two neat materials, with some trend as amount of EVOH is increased in the films, but this is not the case. The 40% EVOH blend and layer films both are higher than expected when compared to the 20 and 60% film systems. As will be discussed further later on, the 40% EVOH curves are outliers in both mechanical and mechano-optical curve behavior, which is the reason they were chosen for further study in a temporal evolution experiment. In general, the layered films' OSH values fall below that of neat EVOH, which is unexpected and, therefore, there could be some synergistic property development which causes OSH to occur sooner in the stretching process or this could be due to some unexpected defect during stretching (for example, film delamination).

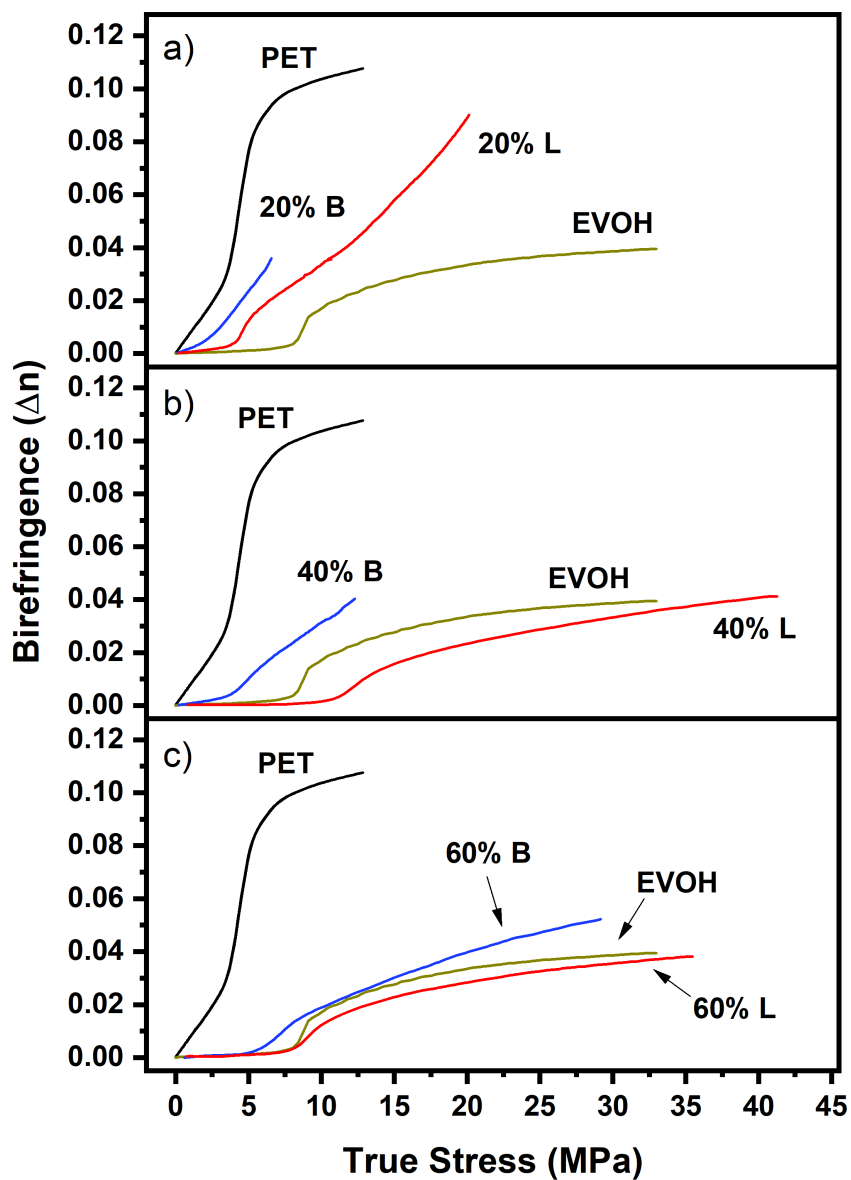


Fig. 6.6.: Stress optical curves for film samples stretched at 90°C and 30 mm/min to 3.5X initial length; a) 20% EVOH films, b) 40% EVOH films, and c) 60% EVOH films.

Birefringence versus true stress results of uniaxial stretching experiments at 90°C and 30 mm/min are shown in Figure 6.6. Films containing 20% EVOH are shown in Figure 6.6a, where again we see that both the 20% blend and layer film curves fall between neat EVOH and neat PET curves. Birefringence development is higher initially in the blend film, and the curve truncates prematurely due to loss of optical signal caused by high film opacity. The 20% blend film has a higher stress-optic constant than the 20% layer film, and this trend is observed throughout the series of EVOH concentrations, though the gap in the difference in these two curves decreases as amount of EVOH increases (in other words, as EVOH amount increases, the blend and layer film stress optical curves more closely resemble one another). Furthermore, films (either blend or layer compositions) with high amounts of EVOH closely resemble the neat EVOH curve, but films with low amounts of EVOH do not closely resemble PET curves. This means that adding even a relatively low amount of EVOH (20%) greatly affects morphological development of the films. The effect is more prevalent in the layered films, as observed by lower stress-optic constant (stress optical behavior less closely mirrors that of neat PET). Finally, we see a very large gap in stress optical property development in the 40% layered film compared to its blended analogue and compared to trends observed at other compositions. Stress optical behavior for 40% EVOH layered film is significantly outside the range of neat materials' curves (i.e. lower than EVOH's behavior). This is unexpected and may indicate some synergistic effect or, on the other hand, could be indication of a defect in stretching, for example delamination. Although 60% layer film's stress optical behavior falls slightly out of line with neat EVOH behavior, it is much closer to the EVOH curve compared to 40% layer film, and could be the same within experimental error. It is worth investigating why the 40% layer curve is so drastically different, and, again, this is why a temporal evolution study was chosen to be performed for this material.

Birefringence versus true strain results of uniaxial stretching experiments at 90°C and 30 mm/min are shown in Figure 6.7. Again we see that samples with 20% EVOH fall on or in between the strain optical curves of the neat materials, while higher

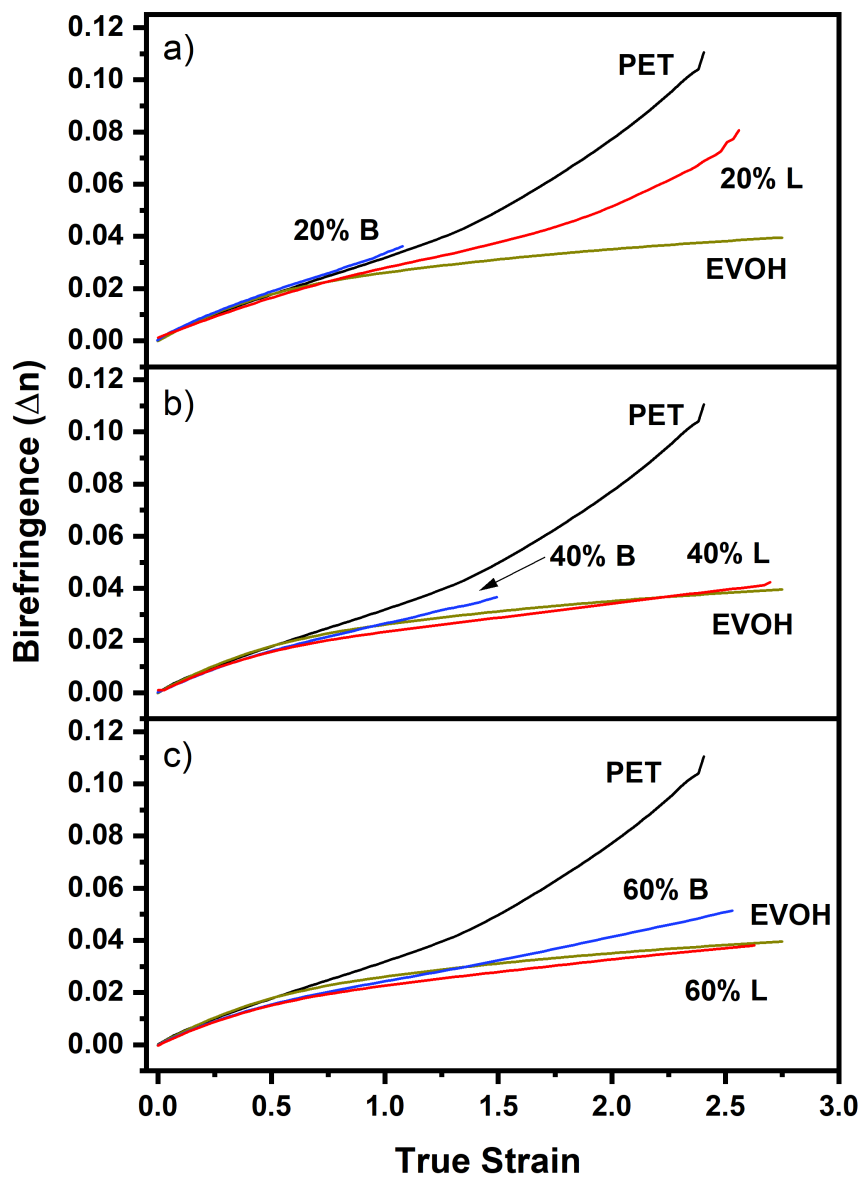


Fig. 6.7.: Strain optical curves for film samples stretched at 90°C and 30 mm/min to 3.5X initial length; a) 20% EVOH films, b) 40% EVOH films, and c) 60% EVOH films.

compositions do not. 20% EVOH blend films follow more closely PET behavior and the layered films for all compositions more closely resemble EVOH. Similar to stress optical behavior, 40% EVOH and 60% EVOH layer films fall below neat EVOH trend, meaning some complex deformation mechanism occurs in the layered structure which does not follow expected trends of neat materials.

A summary of calculated mechano-optical properties for films stretched as detailed above is shown in Figure 6.5, where part (c) shows stress optic constant. All blend and layer films show stress-optic constant falling in between neat PET and EVOH values, but much closer to EVOH, even at small additions of this material to the system. In fact, PET shows a very high stress-optic constant, which has been corroborated in the literature [13]. stress-optic constant for the blend films is higher than their layered counterparts, and decreases steadily with addition of EVOH, likely due to the stress distribution being more anisotropic in the blend film, which have heterophasic composition, versus the layered ones which are more homogeneous in each layer and can therefore more evenly distribute stress among like-polymer chains. The layered films have relatively constant stress-optic constant despite changing EVOH content, suggesting that individual layers play an equal role in determining this behavior.

Figure 6.5c gives overall strain optic values for neat materials, blend, and layered films stretched according to above descriptions. Strain optic values are the initial linear portion of birefringence versus true strain curves and indicate how materials deform on a micromolecular scale. Here we see that strain optic values do not fall between neat PET and EVOH values and the layered films trend higher than their blend counterpart, overall. This means that PET/EVOH layered films experience orientation/chain alignment more quickly than the blend films (i.e. birefringence rises more rapidly than true strain leading to higher slope in the linear region). This is likely due to less interactions between dissimilar polymers in layer structure versus compounded blend, where PET, EVOH and compatibilizer material must move past one another to “find” their own chains. Furthermore, strain optic values decrease with

increasing EVOH composition. Neat EVOH material has lower strain optic constant than PET so that addition of more EVOH into the system brings the average value down and secondly, EVOH can be thought of as more “contamination” in the blend system. This is also why the layered films show more dramatic decrease in strain optic constant with increasing EVOH content, whereas the blend film shows no real change until 60% EVOH composition.

6.3.3 X-ray scattering

SAXS images for films as cast (Appendix D.4), show mainly amorphous scattering, but there is some organization in the machine (stretching) direction (MD) for 60% EVOH blend and layer films. ND and TD patterns are very similar, as expected since layers are not thin enough to cause confined crystallization effects. After stretching at 90°C and 30 mm/min, SAXS images in Appendix D.5 show anisotropic arcs in stretching (MD) direction. In blend and layer films with 40% and 60% EVOH, we see two scattering arcs which must be due to higher amounts of compatibilizer in these films, as there is no second arc (and no compatibilizer) observed in neat EVOH patterns.

WAXS images as cast (Appendix D.2) show amorphous rings for neat PET, as expected since percent crystallinity is low. After stretching, as seen in Appendix D.3, neat PET shows crystalline peaks at 17.25° and 26.24° corresponding to the (010) and (100) planes, respectively, which are oriented in MD. Neat EVOH shows scattering peak and arc at 20.3°, (101) plane but this peak changes to 19.2° after stretching due to mesomorphic rearrangement during deformation [251]. In all blends and layered structures, there is a crystalline scattering ring around 20.3° consistent with neat EVOH material’s (101) plane. Scattering patterns for blend and layered films after stretching show high amounts of orientation in MD and it appears as though

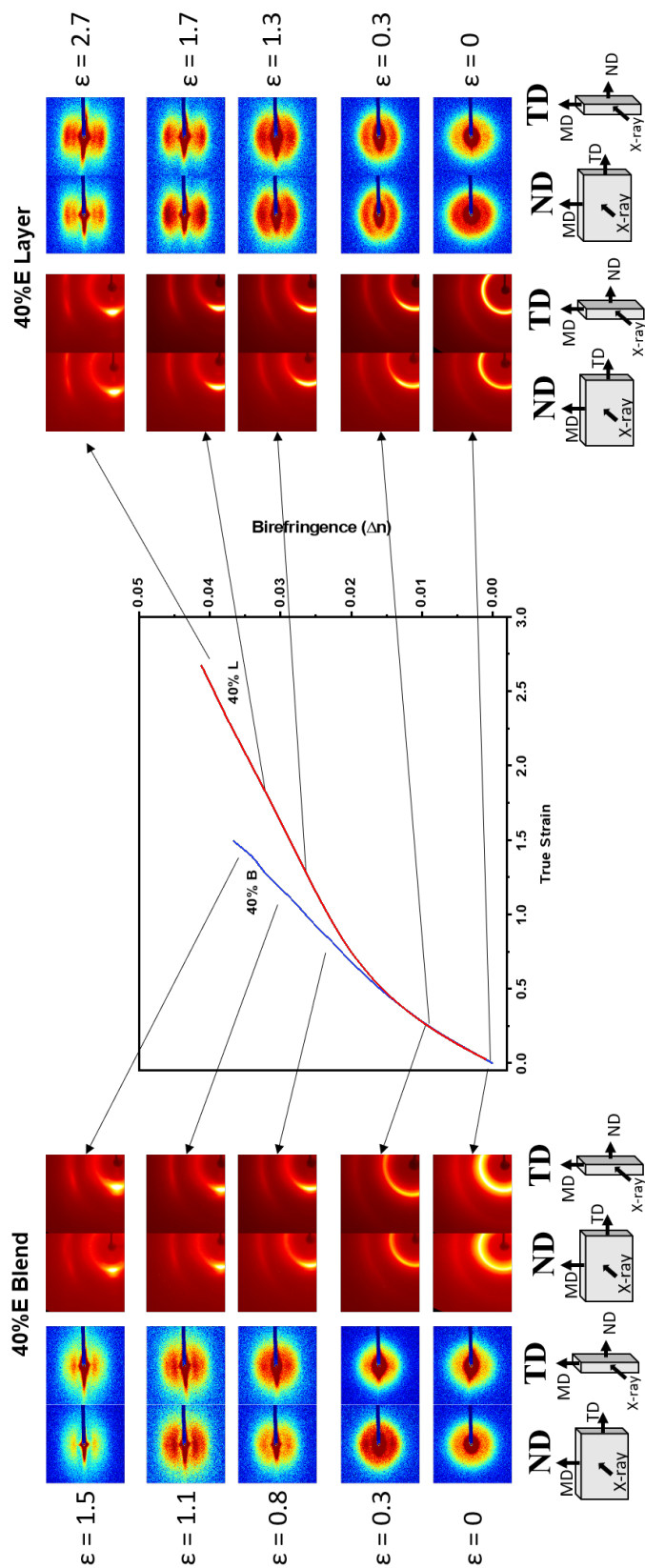


Fig. 6.8.: SAXS and WAXS images at temporal evolution intervals, strain optical data for 40% EVOH blend and layered films stretched at 90°C and 30 mm/min to 3.5X initial length.

both PET and EVOH materials are highly oriented in MD. This will be discussed in the next section, where layered films were layered films were separated in order to distinguish scattering peaks from another and calculate orientation factors for each material individually. Again, in both as cast and oriented WAXS images, there is not much difference in ND and TD WAXS scattering patterns, as expected for these relatively thick film layers.

X-ray scattering images overlaying strain optical data for 40% EVOH blend and layer films stretched at 90°C and 30 mm/min in a temporal evolution study are shown in Figure 6.8. 40% blend films as cast show amorphous scattering, indicated by diffuse halos in SAXS images and isotropic amorphous halos in WAXS images. As strain increases to 0.3 mm/mm, WAXS images show sharpening of the ring at 19.2°, indicating higher crystallinity and/or orientation in the material just after the point of elastic deformation. Further stretching transforms these rings into highly oriented arcs. Strain optical behavior for the blend film is nearly linear and deviation from linearity is accompanied by clear orientation at true strain near 0.8 mm/mm, as observed by WAXS scattering patterns. SAXS images show similar transformation from amorphous rings to oriented arcs as stretching proceeds. The 40% EVOH layered film shows much stronger deviation from linearity, occurring around true strain value of 0.5 mm/mm. This is likely due to the different deformation behavior of each material in its respective layer. Compared with blend morphology, in the layered system we already see orientation in the films stretched to true strain of 0.3 mm/mm, which is right after the elastic deformation region, as indicated by anisotropic arcs in both WAXS and SAXS images.

Figure 6.9 shows temporal evolution study for the same materials as above, with X-ray patterns overlaying stress optical data. Again, we note that the 40% blend material shows a more linear stress optical behavior than the layered film of the same composition, which deviates highly from linearity. Deviation from linearity

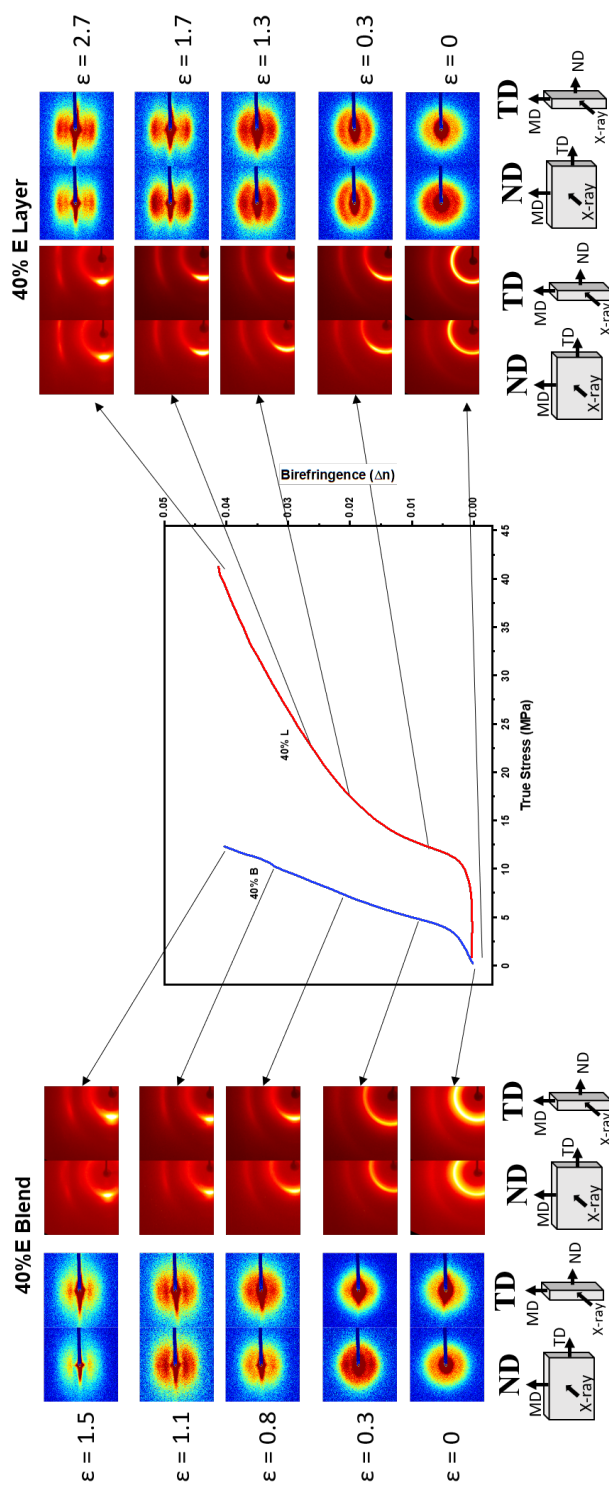


Fig. 6.9.: SAXS and WAXS images at temporal evolution intervals, stress optical data for 40% EVOH blend and layered films stretched at 90°C and 30 mm/min to 3.5X initial length.

corresponds to higher stresses developed in the layered film, accompanied by stress induced crystallization of PET. Overall final values of birefringence are nearly equal, but the deformation path the material takes to reach final birefringence is very different for melt blended versus coextruded layered films.

6.3.4 Orientation factors

From experimental WAXS data, crystalline orientation factors were calculated by taking an azimuthal scan of 2θ peak corresponding to the crystalline diffraction peak of interest was corrected for background scattering by subtraction of azimuthal intensity of a peak significantly far away from any scattering ($2\theta = 50^\circ$).

Mean-square cosine values were calculated from plane normals from corrected intensity distribution from WAXS data. The formula is as follows:

$$\langle \cos^2 \phi \rangle_{hkl} = \frac{\int_0^{\frac{\pi}{2}} I(\phi)_{hkl} \sin \phi \cos^2 \phi d\phi}{\int_0^{\frac{\pi}{2}} I(\phi)_{hkl} \sin \phi d\phi} \quad (6.7)$$

and crystalline orientation factor, f , is calculated by:

$$f_{(hkl)} = \frac{1}{2}(3 \langle \cos^2 \phi \rangle_{hkl} - 1) \quad (6.8)$$

where $\langle \cos^2 \phi \rangle_{hkl}$ is the mean-square cosine average over all crystallites of the angle between crystal and reference axis [214]. For any crystallographic axis, $\langle \cos^2 \phi \rangle = 1$ for perfect Z alignment, $\frac{1}{3}$ for random alignment, and 0 for perpendicularity. The value f_{hkl} therefore shows values of 1, 0, and $-\frac{1}{2}$, respectively.

PET has a triclinic unit cell, but Yoshihara and coworkers developed an approximated pseudo-orthorhombic unit cell to analyze crystalline orientation for PET [226], [232], [6]. Wilchinsky method for analyzing orthorhombic unit cell was used to calculate

orientation factors from WAXS data of (100), polymer chain axis direction, and (010), perpendicular to aromatic benzyl ring, as follows: [233], [234],

$$\overline{\cos^2\phi_{c,Z}} = 1.00581\overline{\cos^2\phi_{010,Z}} - 0.99413\overline{\cos^2\phi_{100,Z}} \quad (6.9)$$

and

$$\overline{\cos^2\phi_{\alpha,Z}} = 1.0778\overline{\cos^2\phi_{100,Z}} - 0.0779\overline{\cos^2\phi_{010,Z}} \quad (6.10)$$

for c-axis and poles of planes (α) containing phenyl group, respectively, and Z refers to stretching direction or transverse direction.

EVOH with high vinyl alcohol content has a crystalline unit cell modeled as hexagonal, with prominent reflections of the type ($hk0$) at (100) and (200) used for calculations [46].

where simplifying assumption for perpendicular $hk0$ reflections was applied [214]:

$$\langle \cos^2\phi \rangle_c = 1 - 2 \langle \cos^2\phi_{hk0} \rangle \quad (6.11)$$

Appendix D.6 shows example 1D WAXS scattering curves where overlapping crystalline peaks for PET and EVOH materials and explains why delamination study for layered films was necessary in order to obtain accurate orientation factor values. For blend films which cannot be delaminated for obvious reasons, orientation factors were calculated using a deconvolution procedure in which the azimuthal curves were fitted to an nth degree Legendre expansion [252].

$$I(s, \phi) = \sigma a_{2n} P_{2n}(\cos\phi) \quad (6.12)$$

where P_n is Legendre polynomial of order n , s is scattering vector ($s=2\sin(\theta)/\lambda$), and a_{2n} are Legendre coefficients.

This allows for peak separation of PET and EVOH materials for more accurate determination of orientation factor in blend films.

Appendix D.7 shows an example WAXS peak deconvolution which was applied to blend films.

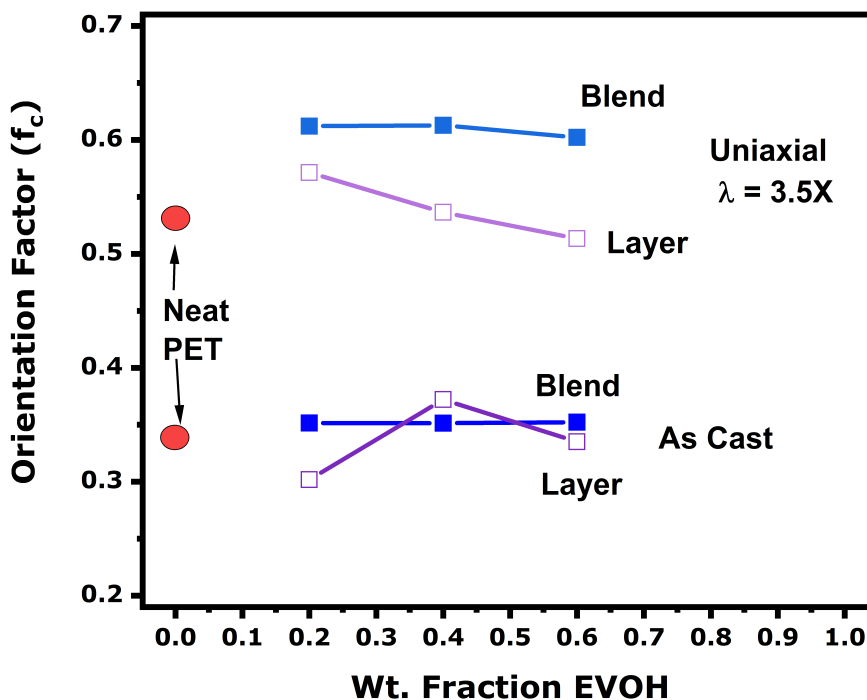


Fig. 6.10.: Calculated orientation factors for blend films (peak deconvolution applied) and delaminated PET from 20, 40, and 60% layered films stretched at 90°C and 30 mm/min to 3.5X initial length.

Calculated orientation factors for the delaminated layers and deconvoluted blend films stretched at 90°C and 30 mm/min to 3.5X are shown in Figures 6.10 and 6.11 for PET and EVOH, respectively. Both are plotted against weight fraction of EVOH for ease of comparison. In Figure 6.10, the 0% EVOH data point shows orientation factor for neat PET film. This control film shows how the material orients in the absence of EVOH layer. In the as cast films, we see that orientation factor of PET is largely

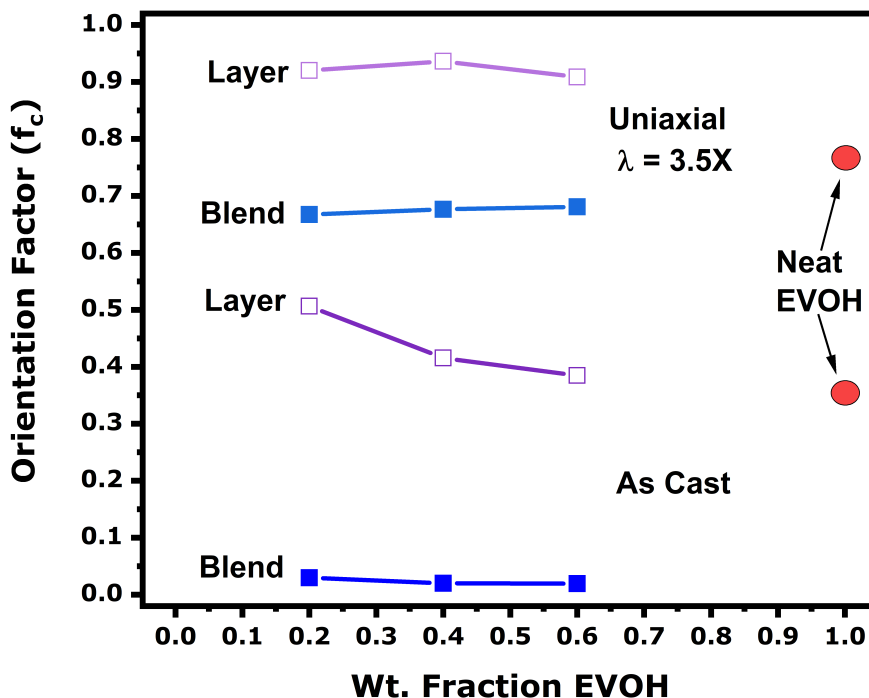


Fig. 6.11.: Calculated c-axis crystalline orientation factors for blend and delaminated EVOH from 20, 40, and 60% layered films stretched at 90°C and 30 mm/min to 3.5X initial length.

unaffected by the amount of EVOH in the structure. After orientation at 90°C to $\lambda = 3.5X$, as amount of EVOH in coextruded structure increases, the orientation factor for PET layer decreases linearly. For blend films, however there is not much change. This is consistent with stress strain data (Figure 6.4) where onset strain hardening point is delayed in blend films, leading to higher overall orientation, whereas layered film deform more elastomerically. In Figure 6.11, weight fraction EVOH equal to 1 is neat EVOH film. Orientation factor for control EVOH film is lower than the layered films but higher than the blend films, suggesting that coextruded layer structure is beneficial to increasing EVOHs orientation but blend film is detrimental. This is because EVOH is the dispersed phase in PET matrix and deforms in solid state. Since each dispersed phase of EVOH contains relatively small amount of EVOH (compared to bulk PET phase) and it is deforming in solid state, these findings make sense.

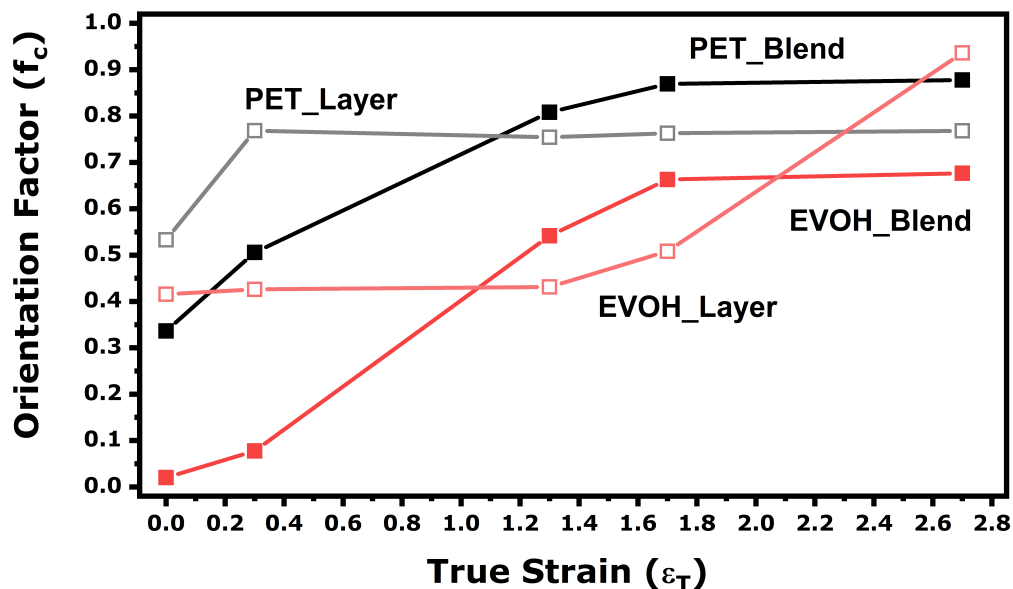


Fig. 6.12.: Calculated c-axis crystalline orientation factors for 40% layered films stretched at 90°C and 30 mm/min to a sequence of true strain values, then delaminated into individual PET and EVOH layers, compared to blend films.

After stretching, the amount of EVOH in the structure does not have much effect on final orientation of EVOH since it is deforming in solid state, and can only orient a finite amount without chain breakage.

Orientation factor for temporal evolution study of delaminated 40% EVOH layer and deconvoluted blend films stretched to varying values of true strain at 90°C and 30 mm/min, quenched are shown in Figure 6.12. The PET layer in as cast film has an orientation factor of around $f_c = 0.35$ and after stretching this value increases immediately to around 0.55. Stretching further does not affect the orientation of PET. This suggests that the amount of PET in the layered structure has larger effect on orientation than does the stretch ratio. For EVOH layers, orientation is relatively low for the first several stretching intervals, then increases rapidly past 1.5 mm/mm

true strain. From Figure 6.9, this corresponds with a change in slope in stress optical behavior as the material becomes more oriented. For blend films, both PET and EVOH steadily increase in orientation with increasing stretch ratio.

6.4 Conclusions

Mechano-optical behavior for blend and layered films were significantly different. In 20% and 40% EVOH films, mechano-optical deformation is similar at low values of strain, but deviate as stress increases rapidly in blend films at higher levels of strain. In stress-optical behavior, adding even small amounts of EVOH to blend and layered films greatly affects morphological development, as observed by the fact that 20% EVOH films' stress-optical behavior significantly deviating from neat PET behavior. Mechano-optical behavior for 40% EVOH films is different then expected based on neat film and 20 and 60% EVOH film behavior. This composition was chosen for further temporal evolution study. Investigating 40% EVOH films at strategic true strain values showed that overall birefringence developed in the films was the same, but deformation mechanism was significantly different for blend and layer films.

Calculation of orientation factors for blend versus layered films showed that layer structure is beneficial to increasing percent crystallinity of EVOH, even when compared to stretching neat EVOH. Orientation factor of PET in layered films decreased with increasing EVOH content, but was constant in blend system. This finding was consistent with delay of onset strain hardening (OSH) in blend versus layered films. In layered film structure, PET reached higher overall orientation, due to delayed onset of strain hardening whereas orientation of PET in blend films was largely unaffected by EVOH content. Blending EVOH with PET (compared to layering) is detrimental to orientation development of the dispersed (EVOH) phase. Orientation factor results showed that the amount of PET in layered structures had larger effect on orientation than the stretching ratio for temporal evolution samples. Finally, orientation factors

for delaminated EVOH layers is higher than that of neat EVOH films after stretching, suggesting that coextruded structure is beneficial to increasing orientation of EVOH.

6.5 Acknowledgements

The authors would like to thank A. Schulman, Inc. for kindly providing the films for this project. The authors acknowledge and greatly appreciate support and funding from the Office of Naval Research Grant N000141712048. Characterization of this material is supported by the National Science Foundation through the Major Research Instrumentation Program under Grant No. CHE 1625543 (Funding for the single crystal X-ray diffractometer).

7. SUMMARY AND RECOMMENDATIONS

7.0.1 Chapter 3 Summary

In conclusion, Chapter 3 examined uniaxial stretching behavior of microlayer PET and PVDF (50:50 ratio) films with 32 total layers and film thickness around 125 micron. It was found that stretching temperature had a significant effect on polymer morphology, and three select stretching temperatures were chosen to examine this further. Stretching at 150°C, where both PET and PVDF are primarily in semi-crystalline state, led to very high development of birefringence, indicating either very high crystallinity and/or orientation development during stretching.

DSC thermal characterization showed increase of PET percent crystallinity during stretching, especially at high temperatures (150, 185°C) where thermal recrystallization occurs. For PVDF, percent crystallinity calculations are more complicated because it is polymorphic in nature, and instances where percent crystallinity of PVDF increases during stretching then decrease again is likely a change to less dense crystal form rather than a true decrease in overall percent crystallinity. SAXS patterns showed initial in-plane isotropy in as cast film, but out-of-plane anisotropy was observed, likely due to confinement effect. When stretched at 95 and 150°C, rotation of lamellar stacks were observed to flip from normal direction to machine direction orientation at only small strains. This was not observed when films are stretched in fully molten PVDF region (i.e. at 185°C). FTIR shows α to β -PVDF transformation for films stretched at 95°C. WAXS technique was used to deduce orientation of PET and PVDF crystalline regions. 2D diffraction patterns showed oriented PET peaks after 95°C stretched and transformation of PVDF α to β -form crystals due to high stresses (as shown in 1D diffraction data). Stretching 150 and 185°C shows primarily

α (150°C) and α and mixture of γ -PVDF (185°C) forms are present during stretching at these temperatures. Formation of γ -PVDF at 185°C stretching can be attributed to the annealing effect during high temperature stretching.

Films stretched at 150°C were the only candidates for dielectric property testing, due to acceptable thickness uniformity measurements. Room temperature dielectric constant for these films showed low overall dielectric constant, and AFM was used to correlate lower dielectric constant to PVDF morphologies of spherulites and smaller, broken up fibrils. Dielectric constant for the film increased when PVDF was arranged in long, highly ordered fibrils. Uniaxial drawing led to greatly lower dielectric loss, which significantly decreased further at very high strains, likely due again to these long, arranged fibrils. PVDF spherulites and long, aligned microfibrils were shown to likely have similar loss values. When this morphology changes to smaller, broken up microfibrils, the loss value drops nearly by 50%. Morphology of PET did not have a strong correlation with dielectric constant (likely since its dielectric constant is very small compared to PVDF's), but higher PET crystallinity and orientation likely helps to lower dielectric losses.

7.0.2 Chapter 4 Summary

Chapter 4 continued the work of Chapter 3, by subjecting the PET/PVDF micro-layered films to heat setting after orientation. Annealing at temperatures around PVDF's peak melting point allowed for crystal form transformation from primarily α to combined α and γ and/or γ' forms. After stretching to 1.5X1 at 150°C, DSC, FTIR and WAXS characterization techniques showed only small amounts of γ and γ' -PVDF were detected after annealing. For the films stretched at 2.5X1 at 150°C, a high amount of γ was observed after annealing at 155°C and both γ and γ' -PVDF were present when annealing at 171°C or above. Stretching at 3.5X1 led to high

amounts of γ -PVDF only when annealed at 170°C, small amount when annealed at 173°C, and only γ when annealed at high temperatures of 177°C and 180°C.

Characterization led to structural model for PVDF layers alone, by de-laminating film layers. Then, morphology was correlated with dielectric properties by testing films at room temperature, and at constant frequency, temperature ramping experiments. Temperature ramping dielectric experiments showed that high percent crystallinity of PET may also help improve loss behavior at high temperature testing. Furthermore, samples containing γ and/or γ' -PVDF had increasing dielectric constant with increasing temperature, however dielectric loss also greatly increased with increasing temperature. Significant conclusion was that the annealed sample without γ and/or γ' -PVDF present had only a slightly lower dielectric constant at high temperature testing, but also had much lower loss, making it a potential candidate for high temperature capacitor applications.

Combined AFM and SAXS data taken on single layer PVDF (de-laminated from the composite structure) were used to propose a morphology structural model. A significantly different morphology was seen for sample containing high amounts of γ -PVDF (annealed at 170°C). Proposed morphology was microfibrillar arrangement as evidenced by diffuse equatorial streak in SAXS pattern, with not much scattering contrast elsewhere. AFM images for films annealed at or above the peak melting point of PVDF ($T=173^\circ\text{C}$) showed similar morphologies via AFM and SAXS patterns. SAXS patterns showed slightly higher orientation as annealing temperature increased in this range.

Dielectric properties were tested for films stretched at 3.5X1, 150°C at both room temperature and at constant frequency in a temperature ramping sequence. Samples with any amount of γ and/or γ' -PVDF had lower dielectric constant and also higher dielectric loss. Annealing is necessary to test these films at high temperatures, in order to prevent significant changes to electrode geometry, which invalidate the test results. Temperature ramp dielectric constant showed a different trend when samples

contained any amount of γ or γ' - PVDF, and dielectric constant increased over the full range of testing temperatures. For PET, with much lower dielectric constant than PVDF, its morphology is not likely a strong influencing factor. Temperature ramp dielectric loss results were also different in trend for samples containing any amount γ or γ' - PVDF. Loss value increased significantly over the full temperature testing range for samples containing γ or γ' - PVDF, and the sample not containing γ or γ' - PVDF showed consistently decreasing loss. This suggests that the absence of γ or γ' - PVDF is beneficial to high temperature dielectric properties, allowing for relatively high dielectric constant and also much lower dielectric loss. The PET material may contribute to lower loss in temperature ramping experiments with significantly higher percent crystallinity at 155°C annealing versus other annealing temperatures.

7.0.3 Chapter 5 Summary

Chapter 5 examined morphology-structure-property relationships during uniaxial orientation of two fluoropolymer films - ETFE and THV. Both films were monolayer, with beginning thickness of 40-50 μm , and both contained some initial, observable machine direction orientation due to the casting process. Both materials deformed affinely during stretching, and mechano-optical properties were studied at several stretching temperatures. A temporal morphology evolution study was done at 145°C to characterize films at specific points of deformation. This was coupled with offline characterization techniques to obtain a clearer picture of morphology development during orientation.

DSC measurements showed percent crystallinity of THV likely decreased with stretching at 145°C. WAXS patterns for THV showed initial in- and out-of plane isotropy, and increasing MD orientation after stretching, and calculated orientation factor shows high c-axis alignment with MD during stretching. 1D SAXS data shows that, when stretched uniaxially at 145°C, lamellar long spacing for THV increases with

increasing stretch ratio. Combined AFM and SAXS data helped construct a proposed structural morphology hierarchy model, which showed THV as cast consists of small, sheaf-like lamellae with overall average MD orientation. As stretching increases, lamellae first twist and break up, then re-orient in MD, as d-spacing increases. Voids, which elongate to oval shape in stretching during during film orientation, were also observed as very high contrast regions in AFM images.

Characterization of ETFE via DSC suggested increasing crystallinity during stretching at 145°C which is due to stress-induced crystallization. Since these films initially had high levels of crystallinity, total change in percent crystallinity during stretching was fairly low, around 5%. 2D WAXS images for ETFE show initial in-plane and out-of-plane isotropy, followed by oriented arcs after small amounts of stretching. This increase in orientation was confirmed via orientation factor calculations. ETFE was also studied via SAXS and AFM to propose a structural hierarchy model. ETFE film in as cast state showed stacked, relatively unoriented lamellae. After stretching, these lamellae bend and deform, thus showing a 4-point scattering pattern in 2D SAXS images (true strain of 0.7). AFM confirms complex twisting and reorganization of lamellae at 1.5X draw ratio, which leads to a pseudo-8 point scattering pattern. Upon stretching further, twisted lamellae again orient with machine direction, confirmed by SAXS, which shows reappearance of two discrete scattering arcs arranged in MD.

7.0.4 Chapter 6 Summary

In Chapter 6, films consisting of blended and three layered PET/EVOH materials were studied for potential high barrier food packaging applications. Films with varying amounts of EVOH were studied in uniaxial deformation, and these two film systems showed significantly different mechano-optical behavior. Films containing 20% and 40% EVOH, in both blend and layer structures, showed similar mechano-optical

properties at low deformation but deviated as stress increased more rapidly in blend films at higher levels of strain. Addition of small amounts of EVOH to both blend and layered films caused significant deviations in stress-optical behavior. Films containing 40% EVOH had unexpected mechano-optical behavior based on neat films, and the trends of 20 and 60% EVOH film behavior. This composition was therefore chosen for study via temporal evolution, which showed that blend and layered film structures of this composition had similar overall birefringence development, but significantly different paths of deformation.

Offline characterization was used to study morphology of these films. Crystalline orientation factors from 1D WAXS data showed that *c*-axis orientation for PET was largely unaffected by increasing EVOH content in blend films. On the other hand, blending did cause a decrease in orientation factor for EVOH. Orientation of PET in layered films was also not drastically changed by adding EVOH to the system. In all layered film structures, regardless of composition, EVOH had higher orientation factor compared to the neat, oriented film. This suggests that coextrusion into a layered film helps increase orientation of EVOH.

7.0.5 Recommendations

The bulk of this research focuses on improvement of dielectric properties of polymer films for high temperature, high energy density capacitor applications. Other techniques were also studied in hopes of creating synergistic property (be it dielectric properties, or barrier) effect of polymers are co-polymerization of fluorine containing monomers (ETFE copolymer and THV terpolymer, Chapter 5) and blending (PET and EVOH, Chapter 6). With all materials studied, the overall goal has been to gain a deeper knowledge of how polymer structure is affected by processing and influences overall properties. Because each polymer material is unique and complicated in their own ways, as of now there is no way to accurately predict these correlations.

Emerging technology requires higher energy density capacitors which can be used at high operating temperatures for pulsed power applications such as the railgun and hyperloop, and “green technologies” such as hybrid car batteries, and photovoltaics. The current market solution, BOPP, is unable to meet technological needs in these areas.

Further research in this area will require collaboration and funding from universities and organizations, such as the Navy who we are grateful to for collaboration. Current research is already looking at PVDF materials (due to their high dielectric constant and current use in capacitors), multilayer films (to gain synergistic properties from polymers), nanocomposites, and copolymerization to improve dielectric properties. Some emerging technologies focus more on computer simulation and modeling to predict dielectric property development, since the standard research method of testing hypothesis is time consuming and these materials can be particularly expensive, and simulations allow for initial screening of materials to be accomplished digitally in order to relieve some costs [61]. As described in the review by Huan, et al. published in 2016, the following areas have already been pre-screened for further in depth study: functionalized organic polymers and organometallic polymers. One important thing is being able to process developed materials into films, which as of yet has not been accomplished and requires use of advanced processing-structure studies, such as the ones carried out for this work. Successful experiments in this space will lead to development of technologies not even imagined today.

REFERENCES

REFERENCES

- [1] Z. Ahmad, “Polymer Dielectric Materials,” in *Dielectric Material*. InTech, oct 2012, pp. 3–26. [Online]. Available: <http://www.intechopen.com/books/dielectric-material/polymer-dielectric-materials>
- [2] E. Baer and L. Zhu, “50th Anniversary Perspective: Dielectric Phenomena in Polymers and Multilayered Dielectric Films,” *Macromolecules*, vol. 50, no. 6, pp. 2239–2256, 2017.
- [3] L. Qi, L. Petersson, and T. Liu, “Review of Recent Activities on Dielectric Films for Capacitor Applications,” *Journal of International Council on Electrical Engineering*, vol. 4, no. 1, pp. 1–6, 2014.
- [4] T. Asano and T. Seto, “Morphological studies of cold drawn PET.pdf,” *Polymer Journal*, vol. 5, no. 1, pp. 72–85, 1973.
- [5] S. Lee, H. Miyaji, and P. H. Geil, “Morphology of amorphous polyethylene terephthalate,” *Journal of Macromolecular Science, Part B*, vol. 22, no. 3, pp. 489–496, 1983. [Online]. Available: <http://www.tandfonline.com/doi/abs/10.1080/00222348308215203>
- [6] R. Daubeny and C. W. Bunn, “The Crystal Structure of Polyethylene Terephthalate,” *Proceedings of the Royal Society A: Mathematical, Physical and Engineering Sciences*, vol. 226, no. 1167, pp. 531–542, 1954. [Online]. Available: <http://rspa.royalsocietypublishing.org/content/226/1167/531>
- [7] T. Asano, F. J. Baltá Calleja, A. Flores, M. Tanigaki, M. F. Mina, C. Sawatari, H. Itagaki, H. Takahashi, and I. Hatta, “Crystallization of oriented amorphous poly(ethylene terephthalate) as revealed by X-ray diffraction and microhardness,” *Polymer*, vol. 40, no. 23, pp. 6475–6484, 1999.
- [8] M. Hassan and M. Cakmak, “Mechano optical behavior of polyethylene terephthalate films during simultaneous biaxial stretching: Real time measurements with an instrumented system,” *Polymer (United Kingdom)*, vol. 54, no. 23, pp. 6463–6470, 2013. [Online]. Available: <http://dx.doi.org/10.1016/j.polymer.2013.09.045>
- [9] S. Rabinowitz, I. M. Wardt, and D. S. C. Parry, “The Effect of Hydrostatic Pressure on the Shear Yield Behaviour of Polymers,” *JOURNAL OF MATERIALS SCIENCE*, vol. 5, pp. 29–39, 1970. [Online]. Available: <https://link.springer.com/content/pdf/10.1007%2F978-94-011-5844-2>
- [10] I. M. Ward, Ed., *Structure and Properties of Oriented Polymers*. Dordrecht: Springer Netherlands, 1997. [Online]. Available: <http://link.springer.com/10.1007/978-94-011-5844-2>

- [11] I. Özen, G. Bozoklu, C. Dalgiçdir, O. Yücel, E. Ünsal, M. Çakmak, and Y. Z. Mencilolu, "Improvement in gas permeability of biaxially stretched PET films blended with high barrier polymers: The role of chemistry and processing conditions," *European Polymer Journal*, vol. 46, no. 2, pp. 226–237, 2010.
- [12] M. K. Hassan, "Novel true stress-true strain-birefringence measurement systems for real time measurement during multi-axial deformation and heat setting of polymer films "application on PET films"," Ph.D. dissertation, The University of Akron, 2004.
- [13] C. I. Martins and M. Cakmak, "Control the strain-induced crystallization of polyethylene terephthalate by temporally varying deformation rates: A mechano-optical study," *Polymer*, vol. 48, no. 7, pp. 2109–2123, mar 2007. [Online]. Available: <http://dx.doi.org/10.1016/j.polymer.2007.02.029>
<http://linkinghub.elsevier.com/retrieve/pii/S0032386107001437>
- [14] K. Iwakura, Y. D. Wang, and M. Cakmak, "Effect of Biaxial Stretching on Thickness Uniformity and Surface Roughness of PET and PPS Films," *International Polymer Processing*, vol. 7, no. 4, pp. 327–333, 1992.
- [15] A. Ajji, J. Guèvremont, K. C. Cole, and M. M. Dumoulin, "Orientation and structure of drawn poly(ethylene terephthalate)," *Polymer*, vol. 37, no. 16, pp. 3707–3714, 1996.
- [16] P. D. Habermel, "Plastic Film Capacitors," *Radio and Electronic Engineer*, vol. 40, no. 5, pp. 259–264, 1970.
- [17] J. L. Nash, "Biaxially Oriented Polypropylene Film in Power Capacitors," *Polymer Engineering & Science*, vol. 28, no. 13, pp. 862–870, 1988.
- [18] J. Blok and D. G. Legrand, "Dielectric Breakdown of Polymer Films," *Journal of Applied Physics*, vol. 40, no. 1, pp. 288–293, 1969.
- [19] T. R. Jow and P. J. Cygan, "Dielectric breakdown of polyvinylidene fluoride and its comparisons with other polymers," *Journal of Applied Physics*, vol. 73, no. 10, pp. 5147–5151, 1993.
- [20] L. Yang, J. Ho, E. Allahyarov, R. Mu, and L. Zhu, "Semicrystalline structure-dielectric property relationship and electrical conduction in a biaxially oriented poly(vinylidene fluoride) film under high electric fields and high temperatures," *ACS Applied Materials and Interfaces*, vol. 7, no. 36, pp. 19 894–19 905, 2015.
- [21] H. Teng, "Overview of the Development of the Fluoropolymer Industry," *Applied Sciences*, vol. 2, no. 4, pp. 496–512, 2012. [Online]. Available: <http://www.mdpi.com/2076-3417/2/2/496/>
- [22] A. E. Tonelli, "Conformational Characteristics of Poly(vinylidene fluoride)," *Macromolecules*, vol. 9, no. 4, pp. 547–551, jul 1976. [Online]. Available: <http://pubs.acs.org/doi/abs/10.1021/ma60052a003>
- [23] A. Lovinger, "Ferroelectric Polymers," *American Association for the Advancement of Science*, vol. 220, no. 4602, pp. 1115–1121, 1983.
- [24] Multiple Authors, *Developments in Crystalline Polymers*, D. C. Bassett, Ed. Applied Science Publishers, 1988. [Online]. Available: <http://link.springer.com/10.1007/978-94-009-1341-7>

- [25] P. Martins, A. C. Lopes, and S. Lanceros-Mendez, "Electroactive phases of poly(vinylidene fluoride): Determination, processing and applications," *Progress in Polymer Science*, vol. 39, no. 4, pp. 683–706, 2014. [Online]. Available: <http://dx.doi.org/10.1016/j.progpolymsci.2013.07.006>
- [26] R. Gregorio Jr., E. M. Ueno, R. Gregorio, E. M. Ueno, R. Gregorio Jr., and E. M. Ueno, "Effect of crystalline phase, orientation and temperature on the dielectric properties of poly (vinylidene fluoride) (PVDF)," *Journal of Materials Science*, vol. 34, no. 18, pp. 4489–4500, 1999. [Online]. Available: <http://dx.doi.org/10.1023/A%3A1004689205706>
- [27] A. B. da Silva, C. Wisniewski, J. V. A. Esteves, and R. Gregorio, "Effect of drawing on the dielectric properties and polarization of pressed solution cast β -PVDF films," *Journal of Materials Science*, vol. 45, no. 15, pp. 4206–4215, aug 2010. [Online]. Available: <http://link.springer.com/10.1007/s10853-010-4515-3>
- [28] Y. Zhao, W. Yang, Y. Zhou, Y. Chen, X. Cao, Y. Yang, J. Xu, and Y. Jiang, "Effect of crystalline phase on the dielectric and energy storage properties of poly(vinylidene fluoride)," *Journal of Materials Science: Materials in Electronics*, vol. 27, no. 7, pp. 7280–7286, 2016.
- [29] S. Zhang, C. Zou, D. I. Kushner, X. Zhou, R. J. O. Jr, N. Zhang, and Q. M. Zhang, "Semicrystalline Polymers with High Dielectric Constant , Melting Temperature , and Charge-Discharge Efficiency," *IEEE Transactions on Dielectrics and Electrical Insulation Vol.*, vol. 19, no. 4, pp. 1158–1166, 2012.
- [30] T. Tanigami, K. Yamaura, S. Matsuzawa, M. Ishikawa, K. Mizoguchi, and K. Miyasaka, "Structural studies on ethylene-tetrafluoroethylene copolymer 1. Crystal structure," *Polymer*, vol. 27, no. 7, pp. 999–1006, jul 1986. [Online]. Available: <http://linkinghub.elsevier.com/retrieve/pii/0032386186900637>
- [31] T. Tanigami, K. Yamaura, S. Matsuzawa, M. Ishikawa, and K. Miyasaka, "Structural studies on ethylene-tetrafluoroethylene copolymer: III. Deformation mechanism of row-crystallized film," *Polymer Engineering and Science*, vol. 26, no. 19, pp. 1323–1331, oct 1986. [Online]. Available: <http://doi.wiley.com/10.1002/pen.760261907>
- [32] T. Tanigami, K. Yamaura, S. Matsuzawa, M. Ishikawa, K. Mizoguchi, and K. Miyasaka, "Structural studies on ethylene-tetrafluoroethylene copolymer: 2. Transition from crystal phase to mesophase," *Polymer*, vol. 27, no. 10, pp. 1521–1528, oct 1986. [Online]. Available: <http://linkinghub.elsevier.com/retrieve/pii/0032386186900984>
- [33] A. Funaki, K. Arai, S. Aida, S. Phongtamrug, and K. Tashiro, "Influence of third monomer on the crystal phase transition behavior of ethylene-tetrafluoroethylene copolymer," *Polymer*, vol. 49, no. 25, pp. 5497–5503, 2008.
- [34] A. Funaki, S. Phongtamrug, and K. Tashiro, "Crystal structure analysis of ethylene-tetrafluoroethylene alternating copolymer," *Macromolecules*, vol. 44, no. 6, pp. 1540–1548, 2011.
- [35] A. Funaki and K. Tashiro, "Influence of the third monomer component on the X-ray-analyzed crystal structure of ethylene-tetrafluoroethylene copolymer," *European Polymer Journal*, vol. 49, no. 6, pp. 1532–1540, 2013. [Online]. Available: <http://dx.doi.org/10.1016/j.eurpolymj.2013.01.020>
- [36] J. G. Drobny, *Fluoroplastics*. Rapra Review Reports, 2006.

- [37] H. Freimuth, C. Sinn, and M. Dettenmaier, "Structure and deformation behaviour of a vinylidene-fluoridetetrafluoroethylene-hexafluoropropylene terpolymer," *Polymer*, vol. 37, no. 5, pp. 831–836, 1996. [Online]. Available: <http://www.pc-ehemaligentreffen.de/hpchrissi/polymer3.pdf>
- [38] S. Siengchin and T. N. Abraham, "Morphology and rheological properties of high density polyethylene/ fluorothermoplastics blends," *Journal of Applied Polymer Science*, vol. 127, no. 2, pp. 919–925, 2013.
- [39] J. Stange, S. Wächter, H. Münstedt, and H. Kaspar, "Linear Rheological Properties of the Semifluorinated Copolymer Tetrafluoroethylene-Hexafluoropropylene-Vinylidene fluoride (THV) with Controlled Amounts of Long-Chain Branching," *Macromolecules*, vol. 40, no. 7, pp. 2409–2416, apr 2007. [Online]. Available: <http://pubs.acs.org/doi/abs/10.1021/ma0626867>
- [40] Y. Thakur, T. Zhang, M. Lin, Q. M. Zhang, and M. H. Lean, "Mitigation of conduction loss in a semi-crystalline polymer with high dielectric constant and high charge-discharge efficiency," *Proceedings of the 2016 IEEE International Conference on Dielectrics, ICD 2016*, vol. 1, pp. 59–63, 2016.
- [41] S. Ok, S. Sadaf, and L. Walder, "Basic characterization and investigation of a fluorinated terpolymer in pure state and in mixtures with kaolinite at solid interphases of thin films prepared by facile solution cast and nonsolvent methods," *High Performance Polymers*, vol. 26, no. 7, pp. 779–789, 2014.
- [42] M. Ponting, T. M. Burt, L. T. Korley, J. Andrews, A. Hiltner, and E. Baer, "Gradient multilayer films by forced assembly coextrusion," *Industrial and Engineering Chemistry Research*, vol. 49, no. 23, pp. 12 111–12 118, 2010.
- [43] E. Emmons, "Vibrational spectroscopy of polymers at high pressure," *UNR KN Microform Coll. MARS*, 2007. [Online]. Available: <http://search.proquest.com/openview/440b66ead5147872515ded1eedc6a7c6/1?pq-origsite=gscholar&cbl=18750&diss=y>
- [44] E. D. Emmons, N. Velisavljevic, J. R. Schoonover, and D. M. Dattelbaum, "High-pressure Raman spectroscopy and X-ray diffraction studies of a terpolymer of tetrafluoroethylene-hexafluoropropylene-vinylidene fluoride: THV 500," *Applied Spectroscopy*, vol. 62, no. 2, pp. 142–148, 2008.
- [45] D. M. Dattelbaum, S. A. Sheffield, D. Stahl, M. Weinberg, C. Neel, and N. Thadhani, "Equation of state and high pressure properties of a fluorinated terpolymer: THV 500," *Journal of Applied Physics*, vol. 104, no. 11, 2008.
- [46] M. Takahashi, K. Tashiro, and S. Amiya, "Crystal structure of ethylene-vinyl alcohol copolymers," *Macromolecules*, vol. 32, no. 18, pp. 5860–5871, 1999.
- [47] J. Breil, R. Lund, and M. Wolf, "Development of new BOPP Barrier Films by Coextrusion and Simultaneous Biaxial Orientation," in *TAPPI*. Brueckner, GmbH, 2008, pp. 1–16.
- [48] J. Feng, Z. Li, A. Olah, and E. Baer, "High oxygen barrier multilayer EVOH/LDPE film/foam," *Journal of Applied Polymer Science*, vol. 135, no. 26, pp. 1–9, 2018.
- [49] H. Su, J. Xue, P. Cai, J. Li, and S. Guo, "Structure and oxygen-barrier properties of (linear low-density polyethylene/ethylene-vinyl alcohol copolymer)/linear

- low-density polyethylene composite films prepared by microlayer coextrusion,” *Journal of Applied Polymer Science*, vol. 132, no. 27, pp. 1–7, 2015.
- [50] E. Franco-Urquiza, O. O. Santana, J. Gámez-Pérez, a. B. Martínez, and M. L. MasPOCH, “Influence of processing on the ethylene-vinyl alcohol (EVOH) properties: Application of the successive self-nucleation and annealing (SSA) technique,” *Express Polymer Letters*, vol. 4, no. 3, pp. 153–160, 2010.
- [51] E. A. Franco-Urquiza, J. Gámez-pérez, J. C. Velázquez-Infante, O. Santana, A. M. Benasat, and M. L. MasPOCH, “Effect of the Strain Rate and Drawing Temperature on the Mechanical Behavior of EVOH and EVOH Composites,” *Advances in Polymer Technology*, vol. 32, no. S1, pp. E287–E296, mar 2013. [Online]. Available: <http://doi.wiley.com/10.1002/adv.21274>
- [52] R. Gopalakrishnan, J. M. Schultz, and R. M. Gohll, “Effect of Blend Rheology on the Transport Property of Oriented Poly (ethylene terephthalate) Blends,” *Journal of Applied Polymer Science*, vol. 56, pp. 1749–1759, 1971.
- [53] K. M. Kit, J. M. Schultz, and R. Gohil, “Morphology and barrier properties of oriented Blends of Poly (Ethylene Terephthalate) and Poly(Ethylene 2,6-Naphthalate) with Poly(Ethylene-co-Vinyl Alcohol),” *Polymer Engineering and Science*, vol. 35, no. 8, pp. 680–692, 1995.
- [54] J. H. Yeo, C. H. Lee, C.-s. Park, K.-j. Lee, J.-D. Nam, and S. W. Kim, “Rheological, morphological, mechanical, and barrier properties of PP/EVOH blends,” *Advances in Polymer Technology*, vol. 20, no. 3, pp. 191–201, 2001. [Online]. Available: <http://doi.wiley.com/10.1002/adv.1015>
- [55] R. E. D. C. Harder, “Interfacial Surface Generator,” 1965.
- [56] D. Langhe, M. Ponting, M. P. Deepak Langhe, N. Applications, M. P. Films, D. Langhe, M. Ponting, D. Langhe, M. Ponting, M. P. Deepak Langhe, P. Reflector, and B. See, “Manufacturing and Novel Applications of Multilayer Polymer Films,” *Manufacturing and Novel Applications of Multilayer Polymer Films*, pp. 221–230, 2016. [Online]. Available: <http://www.sciencedirect.com/science/article/pii/B9780323371254000071>
- [57] C. Mueller, J. Kerns, T. Ebeling, S. Nazarenko, A. Hiltner, and E. Baer, “Micro-layer coextrusion processing and applications,” *Polymer Process Engineering*, vol. 97, pp. 137–157, 1997.
- [58] R. Y. F. Liu, A. P. Ranade, H. P. Wang, T. E. Bernal-Lara, A. Hiltner, and E. Baer, “Forced Assembly of Polymer Nanolayers Thinner Than the Inter-phase,” *Macromolecules*, vol. 38, no. 26, pp. 10 721–10 727, 2005.
- [59] M. Ponting, A. Hiltner, and E. Baer, “Polymer nanostructures by forced assembly: Process, structure, and properties,” *Macromolecular Symposia*, vol. 294, no. 1, pp. 19–32, 2010.
- [60] D. Tan, L. Zhang, Q. Chen, and P. Irwin, “High-Temperature Capacitor Polymer Films,” *Journal of Electronic Materials*, vol. 43, no. 12, pp. 4569–4575, 2014.
- [61] T. Doan Huan, S. Boggs, G. Teyssedre, C. Laurent, M. Cakmak, S. Kumar, and R. Ramprasad, “Advanced polymeric dielectrics for high energy density applications,” *Progress in Materials Science*, vol. 83, pp. 236–269, 2016. [Online]. Available: <http://dx.doi.org/10.1016/j.pmatsci.2016.05.001>

- [62] G. Picci and M. Rabuffi, "Status quo and future prospects for metallized polypropylene energy storage capacitors," *PPPS 2001 - Pulsed Power Plasma Science 2001*, vol. 1, no. 5, pp. 417–420, 2015.
- [63] Z.-M. Dang, W.-T. Yan, and H.-P. Xu, "Novel high-dielectric-permittivity poly(vinylidene fluoride)/polypropylene blend composites: The influence of the poly(vinylidene fluoride) concentration and compatibilizer," *Journal of Applied Polymer Science*, vol. 105, no. 6, pp. 3649–3655, sep 2007. [Online]. Available: <http://doi.wiley.com/10.1002/app.26447>
- [64] R. A. Khare, A. R. Bhattacharyya, A. R. Kulkarni, M. Saroop, and A. Biswas, "Influence of multiwall carbon nanotubes on morphology and electrical conductivity of PP/ABS blends," *Journal of Polymer Science Part B: Polymer Physics*, vol. 46, no. 21, pp. 2286–2295, nov 2008. [Online]. Available: <http://doi.wiley.com/10.1002/pen.20921><http://arxiv.org/abs/cond-mat/0406218><http://dx.doi.org/10.1002/polb>
<http://doi.wiley.com/10.1002/polb.21560>
- [65] A. Mahendrasingam, D. Blundell, C. Martin, W. Fuller, D. MacKerron, J. Harvie, R. Oldman, and C. Riekkel, "Influence of temperature and chain orientation on the crystallization of poly(ethylene terephthalate) during fast drawing," *Polymer*, vol. 41, no. 21, pp. 7803–7814, oct 2000. [Online]. Available: <http://linkinghub.elsevier.com/retrieve/pii/S0032386100001294>
<https://www.sciencedirect.com/science/article/pii/S0032386100001294>
- [66] J. W. Ellis, "Uniaxially and Biaxially Drawn PET," *Engineering*, no. 8, pp. 1619–1627, 2000.
- [67] A. E. Zachariades, W. T. Mead, and R. S. Porter, "Recent developments in ultraorientation of polyethylene by solid-state extrusion," *Chemical Reviews*, vol. 80, no. 4, pp. 351–364, aug 1980. [Online]. Available: <http://pubs.acs.org/doi/abs/10.1021/cr60326a005>
- [68] I. M. Ward, "Optical and Mechanical Anisotropy in Crystalline Polymers," *Proc. Phys. Soc.*, vol. 80, 1962.
- [69] C. Choy, W. Luk, and F. Chen, "Thermal conductivity of highly oriented polyethylene," *Polymer*, vol. 19, no. 2, pp. 155–162, feb 1978. [Online]. Available: <https://www.sciencedirect.com/science/article/pii/0032386178900320>
- [70] P. R. Pinnock and I. M. Ward, "Mechanical and optical anisotropy in polyethylene terephthalate fibres," *British Journal of applied physics*, vol. 15, pp. 1559–1568, 1964.
- [71] S. A. Jabarin, "Strain-Induced Crystallization of Poly(Ethylene Terephthalate)," *Polymer Engineering and Science*, vol. 32, no. 18, pp. 1341–1349, 1992.
- [72] A. Cunha, S. Fakirov, and NATO Science Series, Eds., *Structure development during polymer processing*. Kluwer Academic Publishers, 2000.
- [73] F. P. Alles, "Process for producing improved polymeric terephthalate film," 1959.
- [74] A. W. Christiansen, E. Baer, and S. V. Radcliffe, "The mechanical behaviour of polymers under high pressure," *Philosophical Magazine*, vol. 24, no. 188, pp. 451–467, aug 1971. [Online]. Available:

<https://www.tandfonline.com/doi/pdf/10.1080/14786437108227400?needAccess=true>
<https://www.tandfonline.com/doi/full/10.1080/14786437108227400>

- [75] H. Ito, K. Suzuki, T. Kikutani, and K. Nakayama, "PPS 18th conference proceedings," in *PPS 18th conference proceedings*, Portugal, 2002.
- [76] D. S. Ryu, T. Inoue, and K. Osaki, "A birefringence study of polymer crystallization in the process of elongation of films," *Polymer*, vol. 39, no. 12, pp. 2515–2520, 1998.
- [77] T. F. Serhatkulu and M. Cakmak, "The application of new spectral birefringence technique to characterize the structural changes that take place in heat setting of preoriented PET homopolymer and copolymer films," *Annu. Tech. Conf. - Soc. Plast. Eng.*, vol. 57th, no. Vol. 2, pp. 1645–1649, 1999.
- [78] A. Ajji and X. Zhang, "Biaxial orientation characterization on-line and off-line and structure properties correlations in films," *Macromolecular Symposia*, vol. 185, pp. 3–14, 2002.
- [79] J. Gardiner, "Fluoropolymers: Origin, Production, and Industrial and Commercial Applications," *Australian Journal of Chemistry*, vol. 68, no. 1, pp. 13–22, 2015.
- [80] H. Kawai, "The piezoelectricity of poly(vinylidene fluoride)," *Jpn.-J.-Appl.-Phys.*, vol. 8, pp. 975–976, 1969.
- [81] J. G. Bergman, J. H. McFee, and G. R. Crane, "Pyroelectricity and optical second harmonic generation in polyvinylidene fluoride films," *Applied Physics Letters*, vol. 18, no. 5, pp. 203–205, 1971.
- [82] K. Nakamura and Y. Wada, "Piezoelectricity, pyroelectricity, and the electrostriction constant of poly(vinylidene fluoride)," *Journal of Polymer Science Part A-2: Polymer Physics*, vol. 9, no. 1, pp. 161–173, jan 1971. [Online]. Available: <http://doi.wiley.com/10.1002/pol.1971.160090111>
- [83] C. W. Wilson, "NMR study of molecular chain structure of polyvinylidene fluoride," *Journal of Polymer Science Part A: General Papers*, vol. 1, no. 4, pp. 1305–1310, apr 1963. [Online]. Available: <http://doi.wiley.com/10.1002/pol.1963.100010419>
- [84] C. W. Wilson and E. R. Santee, "Polymer analysis by high-resolution NMR, with applications to poly(vinylidene fluoride) and poly(vinyl fluoride)," *Journal of Polymer Science Part C: Polymer Symposia*, vol. 8, no. 1, pp. 97–112, mar 1965. [Online]. Available: <http://doi.wiley.com/10.1002/polc.5070080110>
- [85] F. A. Bovey, F. C. Schilling, T. K. Kwei, and H. L. Frisch, "Dynamic Carbon-13 NMR Measurements on Poly(vinylidene fluoride) and Poly(methyl methacrylate) and Their Mixed Solutions," *Macromolecules*, vol. 10, no. 3, pp. 559–561, may 1977. [Online]. Available: <http://pubs.acs.org/doi/abs/10.1021/ma60057a012>
- [86] R. C. Ferguson and E. G. Brame, "High resolution nuclear magnetic resonance of fluoro polymers. 2. Fluorine-19 spectra and chain structure of poly(vinylidene fluoride)," *The Journal of Physical Chemistry*, vol. 83, no. 11, pp. 1397–1401, may 1979. [Online]. Available: <http://pubs.acs.org/doi/abs/10.1021/j100474a010>

- [87] M. Kobayashi, K. Tashiro, and H. Tadokoro, "Molecular Vibrations of Three Crystal Forms of Poly(vinylidene fluoride)," *Macromolecules*, vol. 8, no. 2, pp. 158–171, mar 1975. [Online]. Available: <http://pubs.acs.org/doi/abs/10.1021/ma60044a013>
- [88] M. A. Bachmann, W. L. Gordon, J. Koenig, and J. B. Lando, "An infrared study of phase III poly(vinylidene fluoride)," *Journal of Applied Physics*, vol. 50, no. 10, pp. 6106–6112, oct 1979. [Online]. Available: <http://aip.scitation.org/doi/10.1063/1.325780>
- [89] S. L. Hsu, J. P. Sibilio, K. P. O'Brien, and R. G. Snyder, "A Spectroscopic Analysis of the Structure of a Hexafluoroisobutylene-Vinylidene Fluoride Copolymer," *Macromolecules*, vol. 11, no. 5, pp. 990–995, sep 1978. [Online]. Available: <http://pubs.acs.org/doi/abs/10.1021/ma60065a028>
- [90] G. J. Welch and R. L. Miller, "Crystallization of poly(vinylidene fluoride): Equilibrium melting point and heat of fusion of the α -polymorph," *Journal of Polymer Science: Polymer Physics Edition*, vol. 14, no. 9, pp. 1683–1692, sep 1976. [Online]. Available: <http://doi.wiley.com/10.1002/pol.1976.180140913>
- [91] S. Ali and A. K. Raina, "Dilute solution behavior of poly(vinylidene fluoride). Intrinsic viscosity and light scattering studies," *Die Makromolekulare Chemie*, vol. 179, no. 12, 1979.
- [92] K. Nakagawa and Y. Ishida, "Annealing effects in poly(vinylidene fluoride) as revealed by specific volume measurements, differential scanning calorimetry, and electron microscopy," *Journal of Polymer Science Part A-2: Polymer Physics*, vol. 11, no. 11, pp. 2153–2171, nov 1973. [Online]. Available: <http://doi.wiley.com/10.1002/pol.1973.180111107>
- [93] P. Corradini and G. Guerra, "Polymorphism in Polymers," *Advances in Polymer Science*, vol. 100, pp. 183–215, 1992.
- [94] J. B. Lando, H. G. Olf, and A. Peterlin, "Nuclear magnetic resonance and x-ray determination of the structure of poly(vinylidene fluoride)," *Journal of Polymer Science Part A-1: Polymer Chemistry*, vol. 4, no. 4, pp. 941–951, apr 1966. [Online]. Available: <http://doi.wiley.com/10.1002/pol.1966.150040420>
- [95] R. Hasegawa, Y. Takahashi, Y. Chatani, and H. Tadokoro, "Crystal Structures of Three Crystalline Forms of Poly(vinylidene fluoride)," *Polymer Journal*, vol. 3, no. 5, pp. 600–610, sep 1972. [Online]. Available: <http://www.nature.com/doi/10.1295/polymj.3.600>
- [96] B. L. Farmer, A. J. Hopfinger, and J. B. Lando, "Polymorphism of poly(vinylidene fluoride): potential energy calculations of the effects of head-to-head units on the chain conformation and packing of poly(vinylidene fluoride)," *Journal of Applied Physics*, vol. 43, no. 11, pp. 4293–4303, nov 1972. [Online]. Available: <http://aip.scitation.org/doi/10.1063/1.1660919>
- [97] J. B. Lando and W. W. Doll, "The polymorphism of poly(vinylidene fluoride). I. The effect of head-to-head structure," *Journal of Macromolecular Science, Part B*, vol. 2, no. 2, pp. 205–218, jun 1968. [Online]. Available: <https://www.tandfonline.com/doi/full/10.1080/00222346808212449>
- [98] E. Galperin, B. P. Kosmyin, and R. A. Bychkov, "About third form of poly(vinylidene fluoride) crystals (SIC)," *Vysokomolekulyarnye Soedineniya B.*, vol. 12.7, p. 555, 1970.

- [99] S. Weinhold, M. H. Litt, and J. B. Lando, "The crystal structure of the gamma phase of Poly(vinylidene fluoride)," *Macromolecules*, vol. 13, no. 5, p. 117801183, sep 1980. [Online]. Available: <http://pubs.acs.org/doi/abs/10.1021/ma60077a029>
- [100] A. J. Lovinger, "Unit cell of the γ phase of poly(vinylidene fluoride)," *Macromolecules*, vol. 14, no. 2, pp. 322–325, mar 1981. [Online]. Available: <http://pubs.acs.org/doi/abs/10.1021/ma50003a018>
- [101] A. J. Lovinger and H. D. Keith, "Electron Diffraction Investigation of a High-Temperature Form of Poly(vinylidene fluoride)," *Macromolecules*, vol. 12, no. 5, pp. 919–924, sep 1979. [Online]. Available: <http://pubs.acs.org/doi/abs/10.1021/ma60071a026>
- [102] S. K. Tripathy, R. Potenzzone, A. J. Hopfinger, N. C. Banik, and P. L. Taylor, "Predicted Chain Conformation for a Possible Phase III Form of Poly(vinylidene fluoride)," *Macromolecules*, vol. 12, no. 4, pp. 656–658, jul 1979. [Online]. Available: <http://pubs.acs.org/doi/abs/10.1021/ma60070a019>
- [103] N. C. Banik, P. L. Taylor, S. K. Tripathy, and A. J. Hopfinger, "Chain Conformation of Phase III Poly(vinylidene fluoride)," *Macromolecules*, vol. 12, no. 5, pp. 1015–1016, sep 1979. [Online]. Available: <http://pubs.acs.org/doi/abs/10.1021/ma60071a050>
- [104] Y. Takahashi and H. Tadokoro, "Crystal Structure of Form III of Poly(vinylidene fluoride)," *Macromolecules*, vol. 13, no. 5, pp. 1317–1318, sep 1980. [Online]. Available: <http://pubs.acs.org/doi/abs/10.1021/ma60077a057>
- [105] M. Bachmann, W. L. Gordon, S. Weinhold, and J. B. Lando, "The crystal structure of phase IV of poly(vinylidene fluoride)," *Journal of Applied Physics*, vol. 51, no. 10, p. 5095, 1980. [Online]. Available: <http://scitation.aip.org/content/aip/journal/jap/51/10/10.1063/1.327425>
- [106] K. Okuda, T. Yoshida, M. Sugita, and M. Asahina, "Solution-grown crystals of poly(vinylidene fluoride)," *Journal of Polymer Science Part B: Polymer Letters*, vol. 5, no. 6, pp. 465–468, 1967. [Online]. Available: <http://doi.wiley.com/10.1002/pol.1967.110050605>
- [107] K. Sakaoku and A. Peterlin, "Poly(vinylidene fluoride) single crystals," *Journal of Macromolecular Science, Part B*, vol. 1, no. 2, pp. 401–406, aug 1967. [Online]. Available: <https://www.tandfonline.com/doi/full/10.1080/00222346708212784>
- [108] R. L. Miller and J. Raison, "Single crystals of poly(vinylidene fluoride)," *Journal of Polymer Science: Polymer Physics Edition*, vol. 14, no. 12, pp. 2325–2326, dec 1976. [Online]. Available: <http://doi.wiley.com/10.1002/pol.1976.180141216>
- [109] D. T. Grubb and K. W. Choi, "The annealing of solution grown crystals of alpha and gamma poly(vinylidene fluoride)," *Journal of Applied Physics*, vol. 52, no. 10, pp. 5908–5915, oct 1981. [Online]. Available: <http://aip.scitation.org/doi/10.1063/1.329830>
- [110] Y. Toida and R. Chûjô, "High-Resolution NMR Spectra and Conformation of Poly(vinylidene fluoride) and Their Relation with Crystal Modifications," *Polymer Journal*, vol. 6, no. 2, pp. 191–193, mar 1974. [Online]. Available: <http://www.nature.com/doi/10.1295/polymj.6.191>

- [111] T. Miyazaki, Y. Takeda, M. Akasaka, M. Sakai, and A. Hoshiko, "Preparation of isothermally crystallized γ -form poly(vinylidene fluoride) films by adding a KBr powder as a nucleating agent," *Macromolecules*, vol. 41, no. 7, pp. 2749–2753, 2008.
- [112] G. Gianotti, A. Capizzi, and V. Zamboni, "New aspects of polymorphism in polyvinylidenefluoride. Its relation with the morphology and crystallization kinetics," in *Chimica & L'Industria*, vol. 55, no. 6, 1973, pp. 501–506.
- [113] S. Nakamura, T. Sasaki, J. Funamoto, and K. Matsuzaki, "Dynamic cooling and isothermal crystallizations of poly(vinylidene fluoride) from the melt," *Die Makromolekulare Chemie*, vol. 176, no. 11, 1975.
- [114] C. Mancarella and E. Martuscelli, "Crystallization kinetics of poly(vinylidene fluoride)," *Polymer*, vol. 18, no. 12, pp. 1240–1242, dec 1977. [Online]. Available: <http://linkinghub.elsevier.com/retrieve/pii/0032386177902865>
- [115] A. J. Lovinger, "Crystalline transformations in spherulites of poly(vinylidene fluoride)," *Polymer (United Kingdom)*, vol. 21, no. 11, pp. 1317–1322, nov 1980. [Online]. Available: <http://linkinghub.elsevier.com/retrieve/pii/0032386180902001>
- [116] B. S. Morra and R. S. Stein, "The crystalline morphology of poly(vinylidene fluoride)/poly(methylmethacrylate) blends," *Polymer Engineering and Science*, vol. 24, no. 5, pp. 311–318, apr 1984. [Online]. Available: <http://doi.wiley.com/10.1002/pen.760240505>
- [117] H. Pan, B. Na, R. Lv, C. Li, J. Zhu, and Z. Yu, "Polar phase formation in poly(vinylidene fluoride) induced by melt annealing," *Journal of Polymer Science Part B: Polymer Physics*, vol. 50, no. 20, pp. 1433–1437, oct 2012. [Online]. Available: <http://doi.wiley.com/10.1002/polb.23146>
- [118] T. Hattori, M. Kanaoka, and H. Ohigashi, "Improved piezoelectricity in thick lamellar β -form crystals of poly(vinylidene fluoride) crystallized under high pressure," *Journal of Applied Physics*, vol. 79, no. 4, pp. 2016–2022, feb 1996. [Online]. Available: <http://aip.scitation.org/doi/10.1063/1.361055>
- [119] W. W. Doll and J. B. Lando, "The polymorphism of poly(vinylidene fluoride) IV. The structure of high-pressure-crystallized poly(vinylidene fluoride)," *Journal of Macromolecular Science, Part B*, vol. 4, no. 4, pp. 889–896, dec 1970. [Online]. Available: <https://www.tandfonline.com/doi/full/10.1080/00222347008217130>
- [120] C. Ribeiro, V. Sencadas, J. L. G. Ribelles, and S. Lanceros-Méndez, "Influence of Processing Conditions on Polymorphism and Nanofiber Morphology of Electroactive Poly(vinylidene fluoride) Electrospun Membranes," *Soft Materials*, vol. 8, no. 3, pp. 274–287, sep 2010. [Online]. Available: <http://www.tandfonline.com/doi/abs/10.1080/1539445X.2010.495630>
- [121] J. Zheng, A. He, J. Li, and C. C. Han, "Polymorphism Control of Poly(vinylidene fluoride) through Electrospinning," *Macromolecular Rapid Communications*, vol. 28, no. 22, pp. 2159–2162, nov 2007. [Online]. Available: <http://doi.wiley.com/10.1002/marc.200700544>
- [122] A. Lund and B. Hagström, "Melt spinning of β -phase poly(vinylidene fluoride) yarns with and without a conductive core," *Journal of Applied Polymer*

- Science*, vol. 120, no. 2, pp. 1080–1089, apr 2011. [Online]. Available: <http://doi.wiley.com/10.1002/app.33239>
- [123] G. Zhong, L. Zhang, R. Su, K. Wang, H. Fong, and L. Zhu, “Understanding polymorphism formation in electrospun fibers of immiscible Poly(vinylidene fluoride) blends,” *Polymer*, vol. 52, no. 10, pp. 2228–2237, may 2011. [Online]. Available: <http://dx.doi.org/10.1016/j.polymer.2011.03.024> <http://linkinghub.elsevier.com/retrieve/pii/S003238611100214X>
- [124] A. Baji, Y.-W. Mai, X. Du, and S.-C. Wong, “Improved Tensile Strength and Ferroelectric Phase Content of Self-Assembled Polyvinylidene Fluoride Fiber Yarns,” *Macromolecular Materials and Engineering*, vol. 297, no. 3, pp. 209–213, mar 2012. [Online]. Available: <http://doi.wiley.com/10.1002/mame.201100176>
- [125] D. Yang and Y. Chen, “ β -phase formation of poly(vinylidene fluoride) from the melt induced by quenching,” *Journal of Materials Sciences Letters*, vol. 6, no. 5, pp. 599–603, 1987.
- [126] A. Gradys, P. Sajkiewicz, S. Adamovsky, A. Minakov, and C. Schick, “Crystallization of poly(vinylidene fluoride) during ultra-fast cooling,” *Thermochimica Acta*, vol. 461, no. 1-2, pp. 153–157, sep 2007. [Online]. Available: <http://linkinghub.elsevier.com/retrieve/pii/S0040603107002420>
- [127] K. Matsushige and T. Takemura, “Melting and crystallization of poly(vinylidene fluoride) under high pressure,” *Journal of Polymer Science: Polymer Physics Edition*, vol. 16, no. 5, pp. 921–934, may 1978. [Online]. Available: <http://doi.wiley.com/10.1002/pol.1978.180160516>
- [128] K. Matsushige, “Crystallization of macromolecules under high pressure,” *Journal of Crystal Growth*, vol. 48, no. 2, pp. 343–354, feb 1980. [Online]. Available: <http://linkinghub.elsevier.com/retrieve/pii/0022024880902213>
- [129] K. Matsushige, K. Nagata, S. Imada, and T. Takemura, “The II-I crystal transformation of poly(vinylidene fluoride) under tensile and compressional stresses,” *Polymer*, vol. 21, no. 12, pp. 1391–1397, dec 1980. [Online]. Available: <http://linkinghub.elsevier.com/retrieve/pii/003238618090138X>
- [130] A. N. Ozerin, M. KONSTANT., and Y. A. Zubov, “Structural transformations during uniaxial compression of oriented poly (vinylidene fluoride) films,” *VYSOKOMOLEKULYARNYE SOEDINENIYA SERIYA*, vol. 11, 1974.
- [131] T. T. Wang, “Piezoelectricity in β phase poly(vinylidene fluoride) having a “singlecrystal” orientation,” *Journal of Applied Physics*, vol. 50, no. 10, pp. 6091–6094, oct 1979. [Online]. Available: <http://aip.scitation.org/doi/10.1063/1.325777>
- [132] B. Kosmynin, E. Galperin, and D. Tsvankin, “Structure changes at deformation of polyvinylidene fluoride,” *VYSOKOMOLEKULYARNYE SOEDINENIYA SECTION A*, vol. 12, no. 6, p. 1254, 1970.
- [133] J. MCGRATH and I. WARD, “High effective draw as a route to increased stiffness and electrical response in poly(vinylidene fluoride),” *Polymer*, vol. 21, no. 8, pp. 855–857, aug 1980. [Online]. Available: <http://linkinghub.elsevier.com/retrieve/pii/0032386180902372>
- [134] R. Hasegawa, M. Kobayashi, and H. Tadokoro, “Molecular Conformation and Packing of Poly(vinylidene fluoride). Stability of Three

- Crystalline Forms and the Effect of High Pressure,” *Polymer Journal*, vol. 3, no. 5, pp. 591–599, sep 1972. [Online]. Available: <http://www.nature.com/doi/10.1295/polymj.3.591>
- [135] B. Servet, D. Broussoux, F. Micheron, and C. Lacabanne, “CRYSTALLINE TRANSITIONS IN POLY (VINYLIDENE FLUORIDE) FROM UNORIENTED-GAMMA TO ORIENTED-BETA,” *BULLETIN OF THE AMERICAN PHYSICAL SOCIETY*, vol. 26, no. 3, pp. 433–434, 1981.
- [136] S. Weinhold, M. H. Litt, and J. B. Lando, “Oriented phase III poly(vinylidene fluoride),” *Journal of Polymer Science: Polymer Letters Edition*, vol. 17, no. 9, pp. 585–589, sep 1979. [Online]. Available: <http://doi.wiley.com/10.1002/pol.1979.130170907>
- [137] R. Imamura, A. B. Silva, and R. Gregorio, “ $\gamma\beta$ Phase transformation induced in poly(vinylidene fluoride) by stretching,” *Journal of Applied Polymer Science*, vol. 110, no. 5, pp. 3242–3246, dec 2008. [Online]. Available: <http://doi.wiley.com/10.1002/app.28851>
- [138] T. Boccaccio, A. Bottino, G. Capannelli, and P. Piaggio, “Characterization of PVDF membranes by vibrational spectroscopy,” *Journal of Membrane Science*, vol. 210, no. 2, pp. 315–329, dec 2002. [Online]. Available: <http://linkinghub.elsevier.com/retrieve/pii/S0376738802004076>
- [139] R. Gregorio and M. Cestari, “Effect of Crystallization Temperature on the Crystalline Phase Content and Morphology of Poly (vinylidene Fluoride),” *Journal of Polymer Science: Part B: Polymer Physics*, vol. Vol. 32, pp. 859–870, 1994.
- [140] R. Gregorio, “Determination of the α , β , and γ crystalline phases of poly(vinylidene fluoride) films prepared at different conditions,” *Journal of Applied Polymer Science*, vol. 100, no. 4, pp. 3272–3279, may 2006. [Online]. Available: <http://doi.wiley.com/10.1002/app.23137>
- [141] B. S. Morra and R. S. Stein, “Melting studies of poly(vinylidene fluoride) and its blends with poly(methyl methacrylate),” *Journal of Polymer Science: Polymer Physics Edition*, vol. 20, no. 12, pp. 2243–2259, dec 1982. [Online]. Available: <http://doi.wiley.com/10.1002/pol.1982.180201207>
- [142] W. M. Prest and D. J. Luca, “The formation of the γ phase from the α and β polymorphs of polyvinylidene fluoride,” *Journal of Applied Physics*, vol. 49, no. 10, pp. 5042–5047, 1978.
- [143] F. C. Wilson and H. W. Starkweather, “Crystal structure of an alternating copolymer of ethylene and tetrafluoroethylene,” *Journal of Polymer Science Part A-2: Polymer Physics*, vol. 11, no. 5, pp. 919–927, may 1973. [Online]. Available: <http://doi.wiley.com/10.1002/pol.1973.180110509>
- [144] J. E. Mark, Ed., *Polymer Data Handbook*, 2nd ed. Oxford University Press, 1999.
- [145] B. A. Morris, *The Science and Technology of Flexible Packaging*. Elsevier Inc., 2017. [Online]. Available: <http://linkinghub.elsevier.com/retrieve/pii/B9780323242738000101>
- [146] J. M. Carr, M. MacKey, L. Flandin, D. Schuele, L. Zhu, and E. Baer, “Effect of biaxial orientation on dielectric and breakdown properties of

- poly(ethylene terephthalate)/poly(vinylidene fluoride-co-tetrafluoroethylene) multilayer films,” *Journal of Polymer Science, Part B: Polymer Physics*, vol. 51, no. 11, pp. 882–896, 2013.
- [147] K. K. Mokwena and J. Tang, “Ethylene Vinyl Alcohol: A Review of Barrier Properties for Packaging Shelf Stable Foods,” *Critical Reviews in Food Science and Nutrition*, vol. 52, no. 7, pp. 640–650, 2012.
- [148] V. F. Lvovich, *Impedence spectroscopy*. John Wiley & Sons, Inc., 2012.
- [149] L. A. Dissado and J. C. Fothergill, *Electrical degradation and breakdown in polymers*, G. C. Stevens, Ed. Institution of Engineering and Technology, 1992.
- [150] I. Rytöluoto, K. Lahti, M. Karttunen, and M. Koponen, “Large-area dielectric breakdown performance of polymer films - Part i: Measurement method evaluation and statistical considerations on area-dependence,” *IEEE Transactions on Dielectrics and Electrical Insulation*, vol. 22, no. 2, pp. 689–700, 2015.
- [151] C. Xu, J. Ho, and S. Boggs, “Automatic breakdown voltage measurement of polymer films,” *IEEE Electrical Insulation Magazine*, vol. 24, no. 6, 2008.
- [152] X. Yuan, Y. Matsuyama, T. C. M. Chung, Y. Masuyama, T. C. M. Chung, Y. Matsuyama, and T. C. M. Chung, “Synthesis of functionalized isotactic polypropylene dielectrics for electric energy storage applications,” *Macromolecules*, vol. 43, no. 9, pp. 4011–4015, 2010.
- [153] J. A. Langsten, R. H. Colby, F. Shimizu, T. Suzuki, M. Aoki, and T. C. M. Chung, “One-pot synthesis of Long Chain Branch PP (LCBPP) using Ziegler-Natta catalyst and branching reagents,” *Macromolecular Symposia*, vol. 260, pp. 34–41, 2007.
- [154] I. L. Hosier, A. S. Vaughan, and S. G. Swingler, “An investigation of the potential of polypropylene and its blends for use in recyclable high voltage cable insulation systems,” *Journal of Materials Science*, vol. 46, no. 11, pp. 4058–4070, jun 2011. [Online]. Available: <http://link.springer.com/10.1007/s10853-011-5335-9>
- [155] W. J. Schrenk, “Apparatus for multilayer coextrusion of sheet or film,” 1975.
- [156] W. J. Schrenk and T. Alfrey, “Some physical properties of multilayered films,” *Polymer Engineering & Science*, vol. 9, no. 6, pp. 393–399, 1969.
- [157] J. Dooley, K. S. Hyun, and K. Hughes, “An experimental study on the effect of polymer viscoelasticity on layer rearrangement in coextruded structures,” *Polymer Engineering & Science*, vol. 38, no. 7, pp. 1060–1071, 1998. [Online]. Available: <http://doi.wiley.com/10.1002/pen.10274>
- [158] J. Dooley, S. Jenkins, and J. Naumovitz, “Method for preparing multilayer films,” 2004.
- [159] G. Michler and F. J. Baltá Calleja, Eds., *Mechanical properties of polymers based on nanostructure and morphology*. Boca Raton, Fla.: Taylor & Francis, 2005.
- [160] Weber, Stover, Gilbert, Nevitt, Ouderkirk, M. F. Weber, C. A. Stover, L. R. Gilbert, T. J. Nevitt, A. J. Ouderkirk, Weber, Stover, Gilbert, Nevitt, Ouderkirk, M. F. Weber, C. A. Stover, L. R. Gilbert, T. J. Nevitt, and A. J. Ouderkirk, “Giant birefringent optics in multilayer polymer mirrors,”

- Science (New York, N.Y.)*, vol. 287, no. 5462, pp. 2451–6, mar 2000. [Online]. Available: <http://www.sciencemag.org/cgi/doi/10.1126/science.287.5462.2451>
<http://www.ncbi.nlm.nih.gov/pubmed/10741958>
- [161] R. C. Allen, L. W. Carlson, A. J. Ouderkirk, M. F. Weber, A. L. Kotz, T. J. Nevitt, C. A. Stover, and B. Majumdar, “Brightness enhancement film,” 2000.
- [162] J. Dooley, “Viscoelastic flow effects in multilayer polymer coextrusion,” Ph.D. dissertation, Technische Universiteit Eindhoven, 2002.
- [163] D. R. Paul and S. Newman, Eds., *Polymer Blends*, 2nd ed. Elsevier, 1978.
- [164] J. L. White, R. C. Ufford, K. R. Dharod, and R. L. Price, “Experimental and theoretical study of the extrusion of two-phase molten polymer systems,” *Journal of Applied Polymer Science*, vol. 16, no. 6, pp. 1313–1330, jun 1972. [Online]. Available: <http://doi.wiley.com/10.1002/app.1972.070160601>
- [165] R. Y. F. Liu, Y. Jin, A. Hiltner, and E. Baer, “Probing Nanoscale Polymer Interactions by Forced-Assembly,” *Macromolecular Rapid Communications*, vol. 24, no. 16, pp. 943–948, nov 2003. [Online]. Available: <http://doi.wiley.com/10.1002/marc.200300051>
- [166] P. C. Lee, H. E. Park, D. C. Morse, and C. W. Macosko, “Polymer-polymer interfacial slip in multilayered films,” *Journal of Rheology*, vol. 53, no. 4, pp. 893–915, jul 2009. [Online]. Available: <http://sor.scitation.org/doi/10.1122/1.3114370>
- [167] J. Zhang, T. P. Lodge, and C. W. Macosko, “Interfacial slip reduces polymer-polymer adhesion during coextrusion,” *Journal of Rheology*, vol. 50, no. 1, pp. 41–57, jan 2006. [Online]. Available: <http://pubs.acs.org/doi/abs/10.1021/cm049594l>
<http://sor.scitation.org/doi/10.1122/1.2135330>
- [168] P. Dias, Y. Lin, B. Poon, H. Chen, A. Hiltner, and E. Baer, “Adhesion of statistical and blocky ethyleneoctene copolymers to polypropylene,” *Polymer*, vol. 49, no. 12, pp. 2937–2946, jun 2008. [Online]. Available: <http://linkinghub.elsevier.com/retrieve/pii/S0032386108003431>
- [169] P. J. Cole and C. W. Macosko, “POLYMER-POLYMER ADHESION IN MELT-PROCESSED LAYERED STRUCTURES,” *Journal of Plastic Film and Sheeting*, vol. 16, no. 3, pp. 213–222, jul 2000. [Online]. Available: <http://sor.scitation.org/doi/10.1122/1.1427912>
<http://journals.sagepub.com/doi/10.1177/8756087913487542>
<http://journals.sagepub.com/doi/10.1106/6N2B-V63L-32AW-4JYD>
- [170] N. Alipour, U. W. Gedde, M. S. Hedenqvist, S. Yu, S. Roth, K. Brüning, A. Vieyres, and K. Schneider, “Structure and properties of polyethylene-based and EVOH-based multilayered films with layer thicknesses of 150nm and greater,” *European Polymer Journal*, vol. 64, pp. 36–51, mar 2015. [Online]. Available: <https://linkinghub.elsevier.com/retrieve/pii/S0014305714004418>
- [171] L. Ren, J. Zhao, S.-J. Wang, J.-W. Zha, G.-H. Hu, and Z.-M. Dang, “Remarkably variable dielectric and magnetic properties of poly(vinylidene fluoride) nanocomposite films with triple-layer structure,” *Composites Science and Technology*, vol. 107, pp. 107–112, feb 2015. [Online]. Available: <https://linkinghub.elsevier.com/retrieve/pii/S0266353814004254>

- [172] T. Kazmierczak, H. Song, A. Hiltner, and E. Baer, "Polymeric One-Dimensional Photonic Crystals by Continuous Coextrusion," *Macromolecular Rapid Communications*, vol. 28, no. 23, pp. 2210–2216, oct 2007. [Online]. Available: <http://doi.wiley.com/10.1002/marc.200700367>
- [173] T. Alfrey, E. F. Gurnee, and W. J. Schrenk, "Physical optics of iridescent multilayered plastic films," *Polymer Engineering and Science*, vol. 9, no. 6, pp. 400–404, nov 1969. [Online]. Available: <http://doi.wiley.com/10.1002/pen.760090605>
- [174] A. Vasicek, *Optics of thin films*. Amsterdam: North-Holland, 1960.
- [175] M. Francon, *Interscience Tracts*. New York: John Wiley & Sons, Inc., 1963.
- [176] W. Koros, "Barrier polymers and barrier structures," *American Chemical Society: Washington D.C.*, vol. 423, 1990. [Online]. Available: [https://scholar.google.com/scholar_lookup?title=Barrier Polymers and Structures%2C ACS symposium series 423&author=W.J. Koros&publication_year=1990](https://scholar.google.com/scholar_lookup?title=Barrier+Polymers+and+Structures%2C+ACS+symposium+series+423&author=W.J.+Koros&publication_year=1990)
- [177] J. M. Carr, D. S. Langhe, M. T. Ponting, A. Hiltner, and E. Baer, "Confined crystallization in polymer nanolayered films: A review," *Journal of Materials Research*, vol. 27, no. 10, pp. 1326–1350, may 2012. [Online]. Available: http://www.journals.cambridge.org/abstract_S0884291412000179
- [178] D. S. Langhe, A. Hiltner, and E. Baer, "Melt crystallization of syndiotactic polypropylene in nanolayer confinement impacting structure," *Polymer*, vol. 52, no. 25, pp. 5879–5889, nov 2011. [Online]. Available: <https://linkinghub.elsevier.com/retrieve/pii/S003238611100855X>
- [179] P. Wang, K. Meng, H. Cheng, S. Hong, J. Hao, C. C. Han, and H. Haeger, "Reactive compatibilization of polyamide-12/poly(butylene terephthalate) blends with hyperbranched PEI-g-PA12: Morphology and thermal properties," *Polymer*, vol. 50, no. 9, pp. 2154–2160, 2009. [Online]. Available: <http://dx.doi.org/10.1016/j.polymer.2009.02.040>
- [180] H. Wang, J. K. Keum, A. Hiltner, and E. Baer, "Confined crystallization of peo in nanolayered films impacting structure and oxygen permeability," *Macromolecules*, vol. 42, no. 18, pp. 7055–7066, 2009.
- [181] E. L. Cussler, S. E. Hughes, W. J. Ward, and R. Aris, "Barrier membranes," *Journal of Membrane Science*, vol. 38, no. 2, pp. 161–174, 1988.
- [182] H. Wang, J. K. Keum, A. Hiltner, and E. Baer, "Crystallization Kinetics of Poly(ethylene oxide) in Confined Nanolayers," *Macromolecules*, vol. 43, no. 7, pp. 3359–3364, apr 2010. [Online]. Available: <http://pubs.acs.org/doi/abs/10.1021/ma902780p>
- [183] H. Schönherr and C. W. Frank, "Ultrathin Films of Poly(ethylene oxides) on Oxidized Silicon. 1. Spectroscopic Characterization of Film Structure and Crystallization Kinetics," *Macromolecules*, vol. 36, no. 4, pp. 1188–1198, feb 2003. [Online]. Available: <http://pubs.acs.org/doi/abs/10.1021/ma020685i>
- [184] H. Wang, J. K. Keum, A. Hiltner, and E. Baer, "Impact of Nanoscale Confinement on Crystal Orientation of Poly(ethylene oxide)," *Macromolecular Rapid Communications*, vol. 31, no. 4, pp. 356–361, feb 2010. [Online]. Available: <http://doi.wiley.com/10.1002/marc.200900653>

- [185] S. J. Pan, J. Im, M. J. Hill, A. Keller, A. Hiltner, and E. Baer, "Structure of ultrathin polyethylene layers in multilayer films," *Journal of Polymer Science Part B: Polymer Physics*, vol. 28, no. 7, pp. 1105–1119, jun 1990. [Online]. Available: <http://doi.wiley.com/10.1002/polb.1990.090280709>
- [186] G. Zhang, P. C. Lee, S. Jenkins, J. Dooley, and E. Baer, "The effect of confined crystallization on high-density poly(ethylene) lamellar morphology," *Polymer*, vol. 55, no. 2, pp. 663–672, jan 2014. [Online]. Available: <https://linkinghub.elsevier.com/retrieve/pii/S0032386113011270>
- [187] T. Suzuki, T. Tanaka, M. Nakajima, H. Yoshimizu, and Y. Tsujita, "Characterization of the Cavity in Poly(4-methyl-1-pentene) Crystal by Gas Permeation and ^{129}Xe NMR Measurements," *Polymer Journal*, vol. 34, no. 12, pp. 891–896, dec 2002. [Online]. Available: <http://www.nature.com/doi/10.1295/polymj.34.891>
- [188] M. Ponting, Y. Lin, J. K. Keum, A. Hiltner, and E. Baer, "Effect of Substrate on the Isothermal Crystallization Kinetics of Confined Poly(ϵ -caprolactone) Nanolayers," *Macromolecules*, vol. 43, no. 20, pp. 8619–8627, oct 2010. [Online]. Available: <http://pubs.acs.org/doi/abs/10.1021/ma101625h>
- [189] A. M. Chatterjee, F. P. Price, and S. Newman, "Heterogeneous nucleation of crystallization of high polymers from the melt. I. Substrate-induced morphologies," *Journal of Polymer Science: Polymer Physics Edition*, vol. 13, no. 12, pp. 2369–2383, dec 1975. [Online]. Available: <http://doi.wiley.com/10.1002/pol.1975.180131211>
- [190] M. MacKey, L. Flandin, A. Hiltner, and E. Baer, "Confined crystallization of PVDF and a PVDF-TFE copolymer in nanolayered films," *Journal of Polymer Science, Part B: Polymer Physics*, vol. 49, no. 24, pp. 1750–1761, 2011.
- [191] T. Lüpke, S. Dunger, J. Sänze, and H. J. Radusch, "Sequential biaxial drawing of polypropylene films," *Polymer*, vol. 45, no. 20, pp. 6861–6872, 2004.
- [192] M. R. Kamal, H. Garmabi, S. Hozhabr, and L. Arghyris, "The development of laminar morphology during extrusion of polymer blends," *Polymer Engineering & Science*, vol. 35, no. 1, pp. 41–51, 1995.
- [193] C.-L. Chiang and C.-C. Ma, *Polymer Nanocomposites*, Y.-W. Mai and Z.-Z. Yu, Eds. Woodhead Publishing Limited, 2006. [Online]. Available: <http://www.sciencedirect.com/science/article/pii/B9781855739697500180>
- [194] Y. Lin, A. Hiltner, and E. Baer, "A new method for achieving nanoscale reinforcement of biaxially oriented polypropylene film," *Polymer*, vol. 51, no. 18, pp. 4218–4224, 2010. [Online]. Available: <http://dx.doi.org/10.1016/j.polymer.2010.06.059>
- [195] Y. Lin, E. Baer, and A. Hiltner, "Nanolayer enhancement of biaxially oriented polypropylene film for increased gas barrier," *Polymer*, vol. 51, no. 24, pp. 5807–5814, nov 2010. [Online]. Available: <https://linkinghub.elsevier.com/retrieve/pii/S0032386110008542>
- [196] P. Chandran and S. A. Jabarin, "Biaxial orientation of poly(ethylene terephthalate). Part III: Comparative structure and property changes resulting from simultaneous and sequential orientation," *Advances in Polymer Technology*, vol. 12, no. 2, pp. 153–165, 1993. [Online]. Available: <http://doi.wiley.com/10.1002/adv.1993.060120204>

- [197] R. Y. Liu, Y. S. Hu, D. A. Schiraldi, A. Hiltner, and E. Baer, "Crystallinity and oxygen transport properties of PET bottle walls," *Journal of Applied Polymer Science*, vol. 94, no. 2, pp. 671–677, 2004.
- [198] P. Kim, S. C. Jones, P. J. Hotchkiss, J. N. Haddock, B. Kippelen, S. R. Marder, and J. W. Perry, "Phosphonic Acid-Modified Barium Titanate Polymer Nanocomposites with High Permittivity and Dielectric Strength," *Advanced Materials*, vol. 19, no. 7, pp. 1001–1005, apr 2007. [Online]. Available: <http://doi.wiley.com/10.1002/adma.200602422>
- [199] A. Maliakal, H. Katz, P. M. Cotts, S. Subramoney, and P. Mirau, "Inorganic Oxide Core, Polymer Shell Nanocomposite as a High K Gate Dielectric for Flexible Electronics Applications," *Journal of the American Chemical Society*, vol. 127, no. 42, pp. 14 655–14 662, oct 2005. [Online]. Available: <http://pubs.acs.org/doi/abs/10.1021/ja052035a>
- [200] M. Mackey, D. E. Schuele, L. Zhu, L. Flandin, M. A. Wolak, J. S. Shirk, A. Hiltner, and E. Baer, "Reduction of dielectric hysteresis in multilayered films via nanoconfinement," *Macromolecules*, vol. 45, no. 4, pp. 1954–1962, 2012.
- [201] M. Mackey, A. Hiltner, E. Baer, L. Flandin, M. A. Wolak, and J. S. Shirk, "Enhanced breakdown strength of multilayered films fabricated by forced assembly microlayer coextrusion," *Journal of Physics D: Applied Physics*, vol. 42, no. 17, p. 175304, 2009. [Online]. Available: <http://stacks.iop.org/0022-3727/42/i=17/a=175304?key=crossref.d72e8846e92f5221eb7e572918ff1c36>
- [202] M. Mackey, D. E. Schuele, L. Zhu, and E. Baer, "Layer confinement effect on charge migration in polycarbonate/poly(vinylidene fluorid-co-hexafluoropropylene) multilayered films," *Journal of Applied Physics*, vol. 111, no. 11, p. 113702, 2012. [Online]. Available: <http://scitation.aip.org/content/aip/journal/jap/111/11/10.1063/1.4722348>
- [203] M. A. Wolak, M. J. Pan, A. Wan, J. S. Shirk, M. MacKey, A. Hiltner, E. Baer, and L. Flandin, "Dielectric response of structured multilayered polymer films fabricated by forced assembly," *Applied Physics Letters*, vol. 92, no. 11, pp. 8–11, 2008.
- [204] Z. Zhou, J. Carr, M. Mackey, K. Yin, D. Schuele, L. Zhu, and E. Baer, "Interphase/interface modification on the dielectric properties of polycarbonate/poly(vinylidene fluoride-co-hexafluoropropylene) multilayer films for high-energy density capacitors," *Journal of Polymer Science, Part B: Polymer Physics*, vol. 51, no. 12, pp. 978–991, 2013.
- [205] J. K. Tseng, S. Tang, Z. Zhou, M. Mackey, J. M. Carr, R. Mu, L. Flandin, D. E. Schuele, E. Baer, and L. Zhu, "Interfacial polarization and layer thickness effect on electrical insulation in multilayered polysulfone/poly(vinylidene fluoride) films," *Polymer*, vol. 55, no. 1, pp. 8–14, 2014. [Online]. Available: <http://dx.doi.org/10.1016/j.polymer.2013.11.042>
- [206] X. Lin, L. Fan, D. Ren, Z. Jiao, P. Coates, and W. Yang, "Enhanced dielectric properties of immiscible poly (vinylidene fluoride)/low density polyethylene blends by inducing multilayered and orientated structures," *Composites Part B: Engineering*, vol. 114, pp. 58–68, 2017. [Online]. Available: <http://dx.doi.org/10.1016/j.compositesb.2017.01.065>

- [207] A. M. Jordan, W. R. Lenart, J. M. Carr, E. Baer, and L. T. J. Korley, "Structural Evolution during Mechanical Deformation in High-Barrier PVDF-TFE/PET Multilayer Films Using in Situ X-ray Techniques," *Acs Applied Materials & Interfaces*, vol. 6, no. 6, pp. 3987–3994, 2014.
- [208] K. Yin, Z. Zhou, D. E. Schuele, M. Wolak, L. Zhu, and E. Baer, "Effects of Interphase Modification and Biaxial Orientation on Dielectric Properties of Poly(ethylene terephthalate)/Poly(vinylidene fluoride-co-hexafluoropropylene) Multilayer Films," *ACS Applied Materials and Interfaces*, vol. 8, no. 21, pp. 13555–13566, 2016.
- [209] D. Valladares, S. Toki, T. Z. Sen, B. Yalcin, and M. Cakmak, "The effect of natural rubber crosslink density on real time birefringence, true stress and true strain behavior," *Macromolecular Symposia*, vol. 185, pp. 149–166, 2002.
- [210] Y. Koike, T. Z. Sen, and M. Cakmak, "Real time development of orientation in PP during stretching as detected by spectral birefringence technique," *Annu. Tech. Conf. - Soc. Plast. Eng.*, vol. 60th, no. Vol. 2, pp. 1550–1555, 2002.
- [211] M. Cakmak, M. Hassan, E. Unsal, and C. Martins, "A fast real time measurement system to track in and out of plane optical retardation/ birefringence, true stress, and true strain during biaxial stretching of polymer films," *Review of Scientific Instruments*, vol. 83, no. 12, 2012.
- [212] S. Bicaçci and M. Cakmak, "Kinetics of rapid structural changes during heat setting of preoriented PEEK/PEI blend films as followed by spectral birefringence technique," *Polymer*, vol. 43, no. 9, pp. 2737–2746, 2002.
- [213] D. Campbell, R. A. Pethrick, and J. R. White, *Polymer Characterization: Physical Techniques*, 2nd ed. CRC Press, 2000.
- [214] L. E. Alexander, *X-ray diffraction methods in polymer science*. New York: Wiley-Interscience, 1969. [Online]. Available: <http://books.google.co.il/books?id=EgmFAAAAIAAJ>
- [215] P. Hiemenz and T. Lodge, *Polymer Chemistry*. CRC Press, 2007.
- [216] S. N. Magonov and D. H. Reneker, "Characterization of Polymer Surfaces With Atomic Force Microscopy," *Annual Review of Materials Science*, vol. 27, no. 1, pp. 175–222, 1997.
- [217] G. Oncins, J. Díaz-Marcos, and A. Force Microscopy, "Atomic Force Microscopy: probing the Nanoworld Handbook of instrumental techniques from CCiTUB," CCiTUB, Tech. Rep. [Online]. Available: http://diposit.ub.edu/dspace/bitstream/2445/32162/1/MT07 - Atomic Force Microscopy_ed2.pdf
- [218] M. Cakmak and M. Simhambhatla, "Dynamics of uni and biaxial deformation and its effects on the thickness uniformity and surface roughness of poly (ether ether ketone) films," *Polymer Engineering & Science*, vol. 35, no. 19, pp. 1562–1568, 1995.
- [219] S. Kolesov, "The Influence of Morphology on the Electric Strength of Polymer Insulation," *IEEE Transactions on Electrical Insulation*, vol. EI-15, no. 5, pp. 382–388, 1980.

- [220] Y. Koike and M. Cakmak, "Real time development of structure in partially molten state stretching of PP as detected by spectral birefringence technique," *Polymer*, vol. 44, no. 15, pp. 4249–4260, 2003.
- [221] Solvay, "Solef PVDF Design and Processing Guide," Solvay, Tech. Rep., 2015. [Online]. Available: http://www.solvay.com/en/binaries/Solef-PVDF-Design-and-Processing-Guide_EN-229547.pdf
- [222] H. Janeschitz-Kriegl, *Polymer Melt Rheology and Flow Birefringence*. Berlin: Springer-Verlag, 1983.
- [223] R. C. Reiss-Nunes, E. Riande, J. Guzmán, and N. A. Chavez, "Stress optical behavior of partially fluorinated aliphatic polyesters," *Macromolecules*, vol. 33, no. 25, pp. 9464–9467, 2000.
- [224] J. L. White, D. D. Choi, and S. Development, *Polyolefins*. Cincinnati: Hanser, 2005.
- [225] D. M. Esterly, "Manufacturing of Poly (vinylidene fluoride) and Evaluation of its Mechanical Properties," Ph.D. dissertation, Virginia Polytechnic Institute and State University, 2002.
- [226] M. Cakmak, J. E. Spruiell, and J. L. White, "A basic study of orientation in poly(ethylene terephthalate) stretchblow molded bottles," *Polymer Engineering & Science*, vol. 24, no. 18, pp. 1390–1395, 1984.
- [227] L. A. Baldenegro-Perez, D. Navarro-Rodriguez, F. J. Medellin-Rodriguez, B. Hsiao, C. A. Avila-Orta, and I. Sics, "Molecular weight and crystallization temperature effects on poly(ethylene terephthalate) (PET) homopolymers, an isothermal crystallization analysis," *Polymers*, vol. 6, no. 2, pp. 583–600, 2014.
- [228] R. M. Gohil, "Morphology-Property Relationships in Oriented Pet Films: A Role," *Journal of Applied Polymer Science*, vol. 48, pp. 1635–1648, 1993.
- [229] S. Lanceros-Méndez, J. F. Mano, A. M. Costa, and V. H. Schmidt, "Ftir and Dsc Studies of Mechanically Deformed -Pvdf Films," *Journal of Macromolecular Science, Part B*, vol. 40, no. 3-4, pp. 517–527, 2001. [Online]. Available: <http://www.tandfonline.com/doi/abs/10.1081/MB-100106174>
- [230] A. Salimi and A. A. Yousefi, "FTIR studies of β -phase crystal formation in stretched PVDF films," *Polymer Testing*, vol. 22, no. 6, pp. 699–704, 2003.
- [231] Y. Wang, M. Cakmak, and J. L. White, "Structure development in melt spinning poly(vinylidene fluoride) fibers and tapes," *Journal of Applied Polymer Science*, vol. 30, no. 6, pp. 2615–2632, 1985.
- [232] N. Yoshihar, A. Fukushima, Y. Watanabe, A. Nakai, S. Nomura, and H. Kawai, "STUDIES ON THE INTER-RELATION OF STRUCTURE AND BULK PROPERTIES OF POLY (ETHYLENE TEREPHTHALATE). III . CORRELATION BETWEEN MOLECULAR ORIENTATION AND VISCOELASTIC ANISOTROPY," *Sen-I Gakkaishi*, vol. 37, no. 10, pp. 41–68, 1981.
- [233] Z. W. Wilchinsky, "On crystal orientation in polycrystalline materials," *Journal of Applied Physics*, vol. 30, no. 5, p. 792, 1959.
- [234] —, "Measurement of orientation in polypropylene film," *Journal of Applied Physics*, vol. 31, no. 11, pp. 1969–1972, 1960.

- [235] E. Helfand and Y. Tagami, "Theory of the interface between immiscible polymers. II," *The Journal of Chemical Physics*, vol. 56, no. 7, pp. 3592–3601, 1972.
- [236] W. Schrenk, "Multilayer polymer flow in flat die coextrusion," in *SPE*, 1980, p. 291.
- [237] C. D. Han and R. Shetty, "Studies on multilayer film coextrusion I. The rheology of flat film coextrusion," *Polymer Engineering & Science*, vol. 16, no. 10, pp. 697–705, 1976.
- [238] M. MA, K. Vijayan, A. Hiltner, E. Baer, and J. Im, "Thickness effects in microlayer composites of polycarbonate and poly(styrene-acrylonitrile)," *Journal of materials science*, vol. 25, pp. 2039–2046, 1990.
- [239] J. Li, Q. Meng, W. Li, and Z. Zhang, "Influence of crystalline properties on the dielectric and energy storage properties of poly(vinylidene fluoride)," *Journal of Applied Polymer Science*, vol. 122, no. 3, pp. 1659–1668, nov 2011. [Online]. Available: <http://doi.wiley.com/10.1002/app.34020>
<http://www.ncbi.nlm.nih.gov/pubmed/19875328>
- [240] D. R. Salem, *Structure formation in polymeric fibers*. Hanser, 2001.
- [241] S. Barrau, A. Ferri, A. Da Costa, J. Defebvin, S. Leroy, R. Desfeux, and J. M. Lefebvre, "Nanoscale Investigations of α - And γ -Crystal Phases in PVDF-Based Nanocomposites," *ACS Applied Materials and Interfaces*, vol. 10, no. 15, pp. 13 092–13 099, 2018.
- [242] B. Hirschmann, G. Oreski, and G. Pinter, "Thermo-mechanical characterisation of fluoropolymer films for concentrated solar thermal applications," *Solar Energy Materials and Solar Cells*, vol. 130, pp. 615–622, 2014. [Online]. Available: <http://dx.doi.org/10.1016/j.solmat.2014.08.013>
- [243] D. F. Miranda, C. Yin, S. Zhang, and J. Runt, "Fluoropolymer microstructure and dynamics: Influence of molecular orientation induced by uniaxial drawing," *Polymer*, vol. 91, pp. 211–221, 2016. [Online]. Available: <http://dx.doi.org/10.1016/j.polymer.2016.03.057>
- [244] J. M. Lagaron, R. Catalá, and R. Gavara, "Structural characteristics defining high barrier properties in polymeric materials," *Materials Science and Technology*, vol. 20, no. 1, pp. 1–7, 2004.
- [245] D. Feldman, "Polymer Barrier Films," *Journal of Polymers and the Environment*, vol. 9, no. 2, pp. 49–55, 2001. [Online]. Available: <http://dx.doi.org/10.1023/A:1020231821526>
- [246] J. Lange and Y. Wyser, "Recent Innovations in Barrier Technologies for Plastic Packaging - A Review," *Packaging Technology and Science*, vol. 16, no. 4, pp. 149–158, 2003.
- [247] E. Percec, L. Melamud, and G. Coffey, "Multilayered barrier structures for packaging," 1989.
- [248] W. Collette and S. Schmidt, "Oxygen scavenging composition for multilayer preform and container," 1994.
- [249] A. Degrassi, J. Fryer, A. Hitzel, and M. Matas, "Retortable, high oxygen barrier polymeric films."

- [250] J. B. Faisant, a. Aït-Kadi, M. Bousmina, and L. Deschênes, "Morphology, thermomechanical and barrier properties of polypropylene-ethylene vinyl alcohol blends," *Polymer*, vol. 39, no. 3, pp. 533–545, 1998.
- [251] R. Sguaa, K. Djezzara, L. Penel, J.-m. Lefebvrea, and Y. Germainb, "Tensile drawing of ethylene - vinyl-alcohol copolymers :," *Polymer*, vol. 40, pp. 47–52, 1998.
- [252] W. Ruland, "Elimination of the effect of orientation distributions in fiber diagrams," *Colloid and Polymer Science Kolloid-Zeitschrift & Zeitschrift für Polymere*, vol. 255, no. 9, pp. 833–836, 1977.

APPENDICES

A. SUPPORTING FIGURES FOR CHAPTER 3

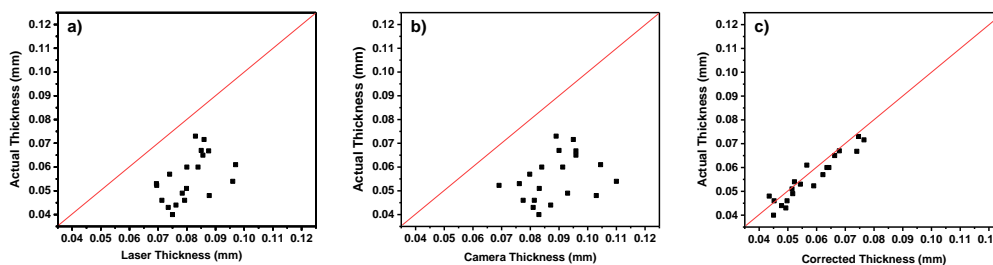


Fig. A.1.: Verification of real time change in sample thickness during stretching calculated using (a) laser and (b) camera data versus actual measured thickness. Plot (c) compares corrected values to actual measured thickness.

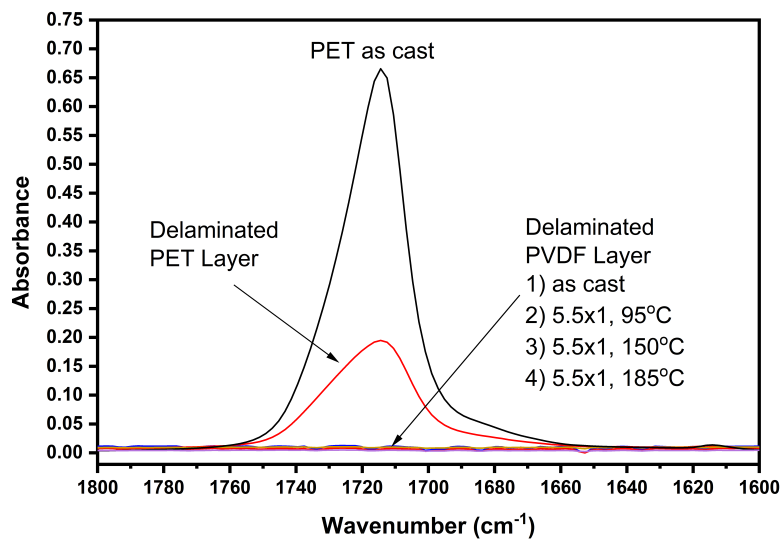


Fig. A.2.: FTIR spectra for select samples to verify delamination was successful in producing a single PVDF layer.

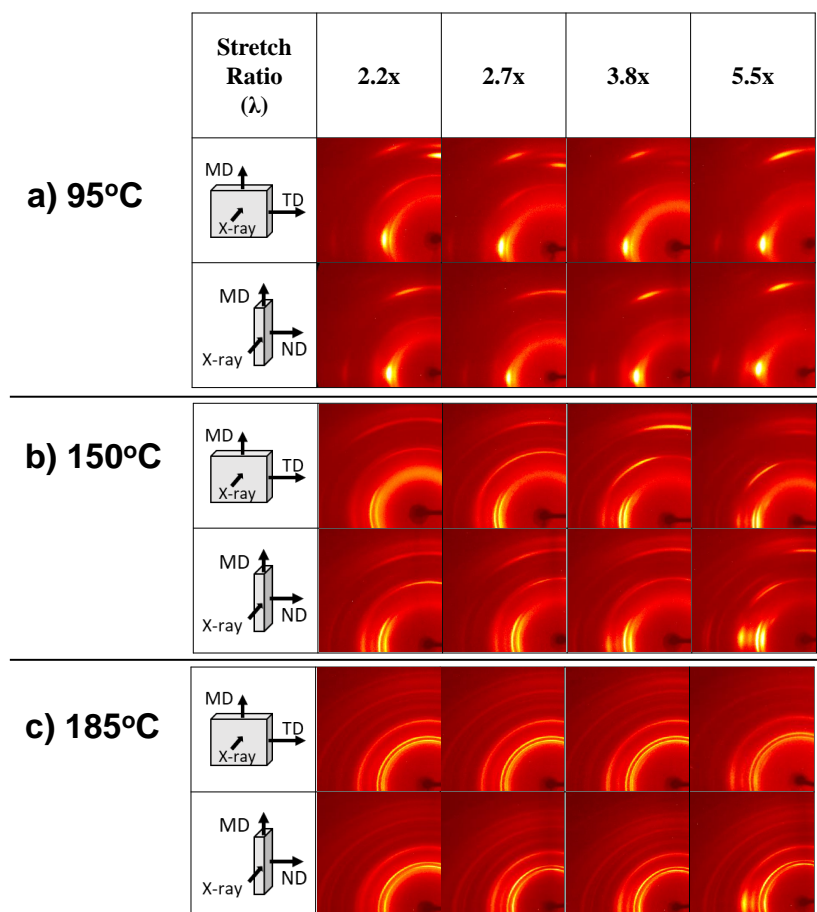


Fig. A.3.: Wide angle X-ray scattering images for time slice temperature study films stretched at a) 95°C, b) 150°C, and c) 185°C at a rate of 10 mm/min.

B. SUPPORTING FIGURES FOR CHAPTER 4

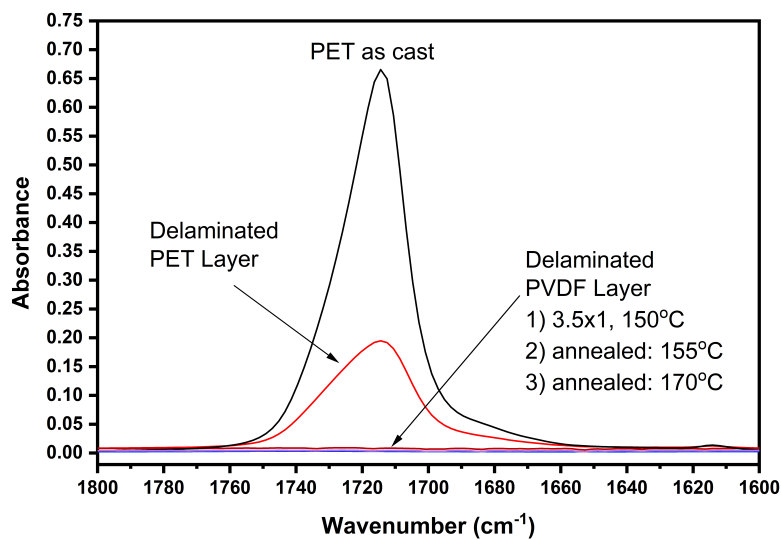


Fig. B.1.: FTIR spectra of PET control film, as cast, compared to PET layer delaminated from 32L microlayer film as cast. Both PET curves show strong absorption peak at 1710 cm^{-1} . PVDF samples shown were also delaminated from 32L microlayer film- 1) as cast, 2) after uniaxial orientation to 3.5X1 at 150°C and finally, stretching same conditions as 2, with 1 hour annealing at 3) 155°C and 4) 170°C .

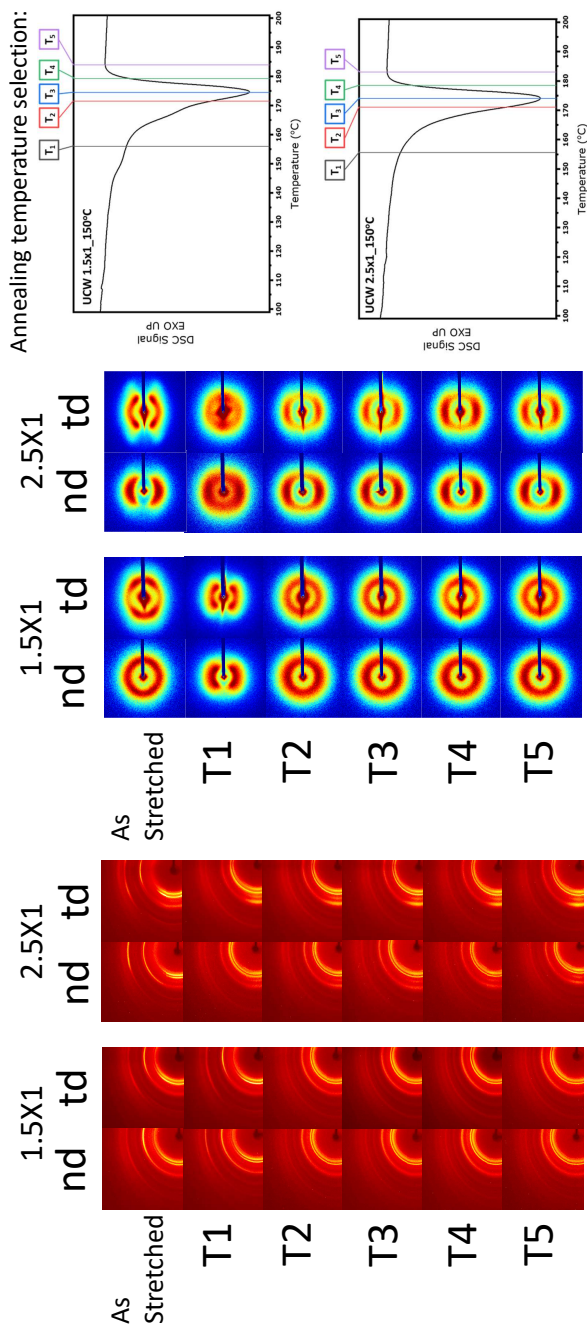


Fig. B.2.: SAXS and WAXS images for annealing chamber at select annealing temperatures for 1 hour annealing, 32L film stretched in UCW to 1.5X1 and 2.5X1 at 150°C and 20 mm/min.

C. SUPPORTING FIGURES FOR CHAPTER 5

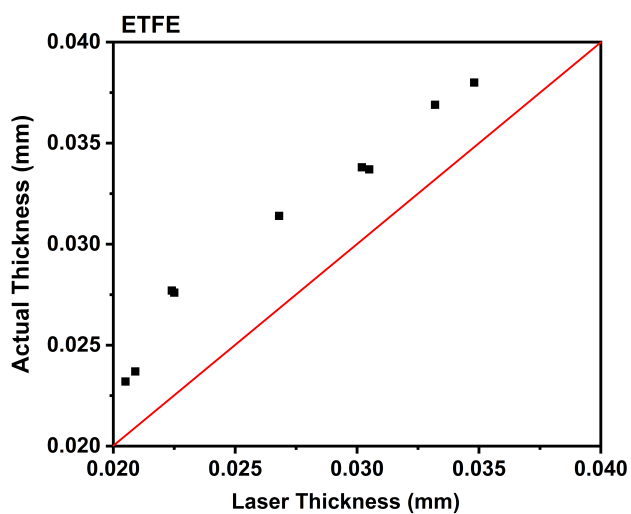


Fig. C.1.: Laser system predicted thickness for ETFE films.

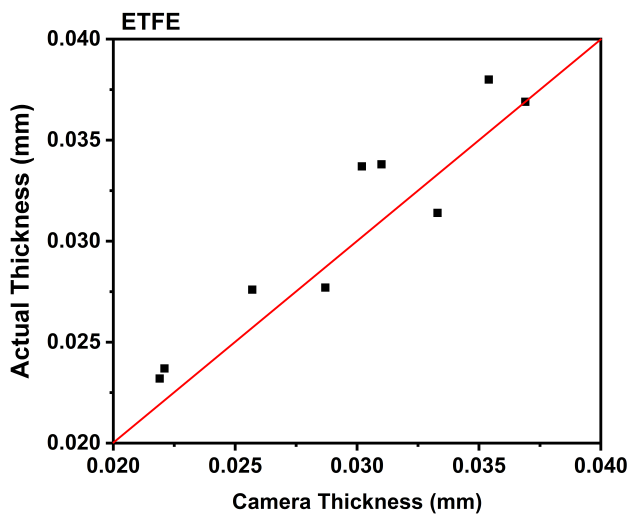


Fig. C.2.: Camera system predicted thickness for ETFE films.

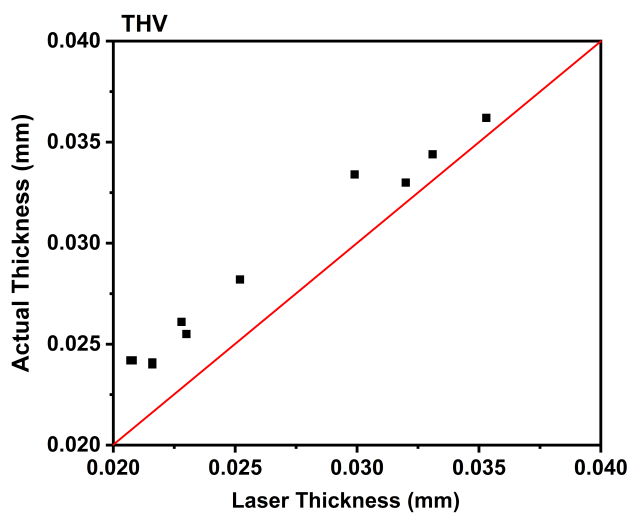


Fig. C.3.: Camera system predicted thickness for THV films.

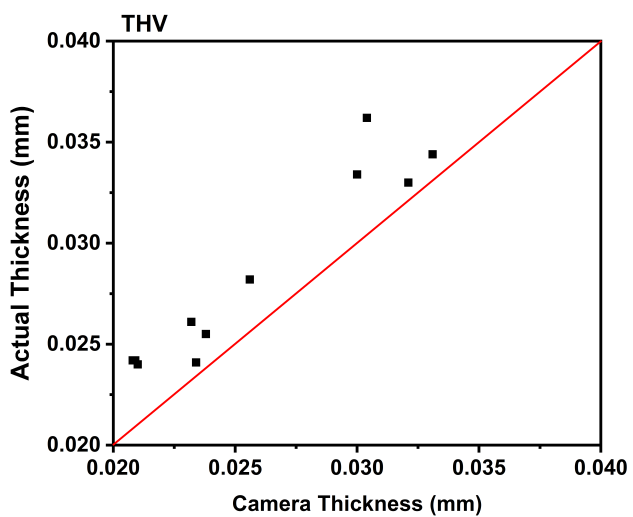


Fig. C.4.: Camera system predicted thickness for THV films.

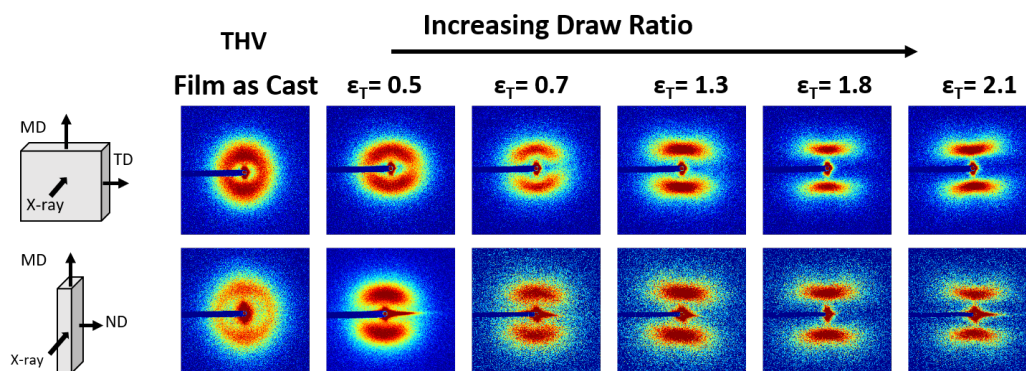


Fig. C.5.: Small angle X-ray scattering patterns for uniaxially oriented THV films, showing structural evolution from as cast state.

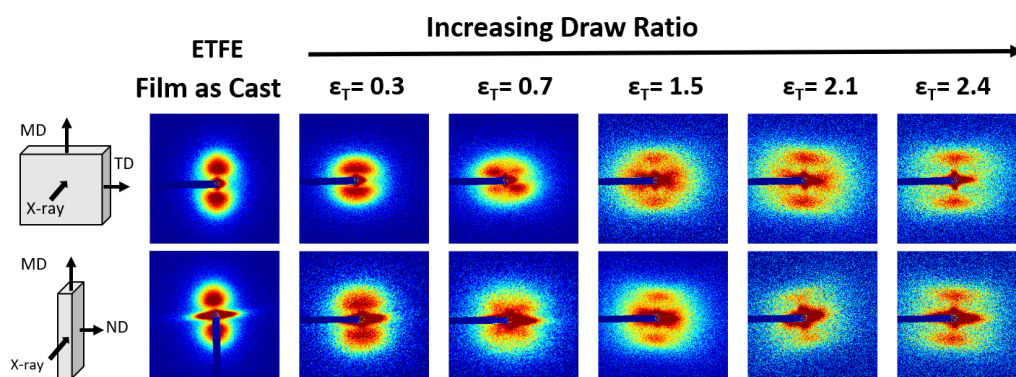


Fig. C.6.: Small angle X-ray scattering patterns for uniaxially oriented ETFE films, showing structural evolution from as cast state.

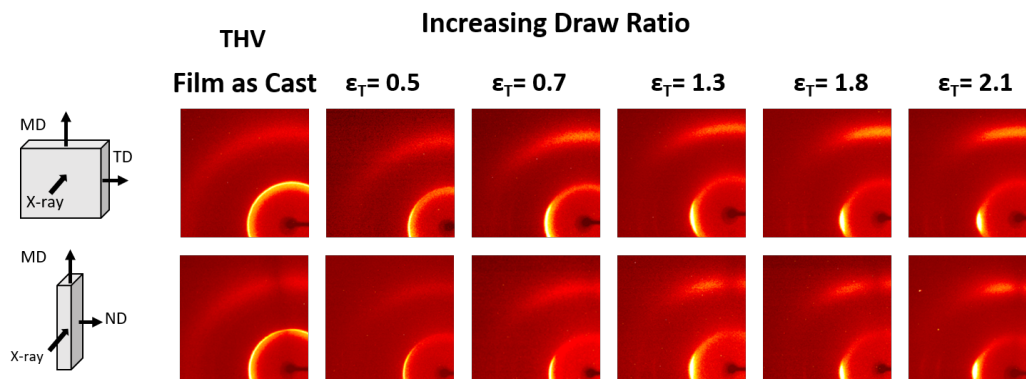


Fig. C.7.: Wide angle X-ray scattering patterns for uniaxially oriented THV films, showing structural evolution from as cast state.

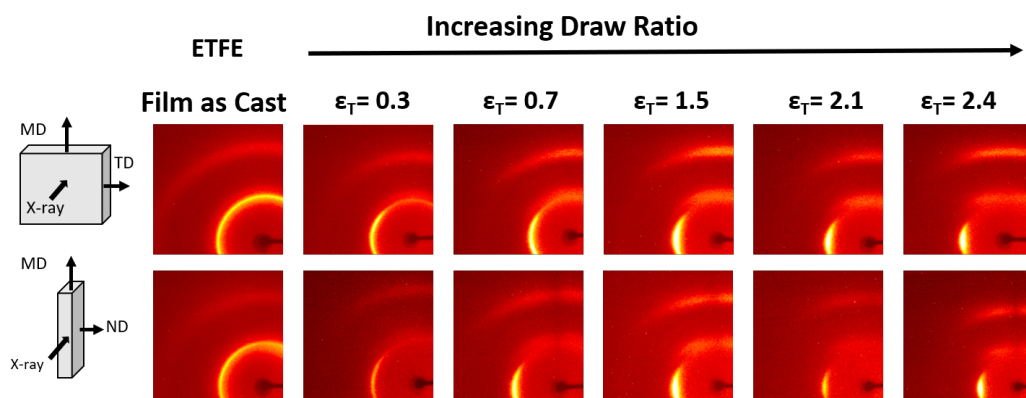


Fig. C.8.: Wide angle X-ray scattering patterns for uniaxially oriented ETFE films, showing structural evolution from as cast state.

D. SUPPORTING FIGURES FOR CHAPTER 6

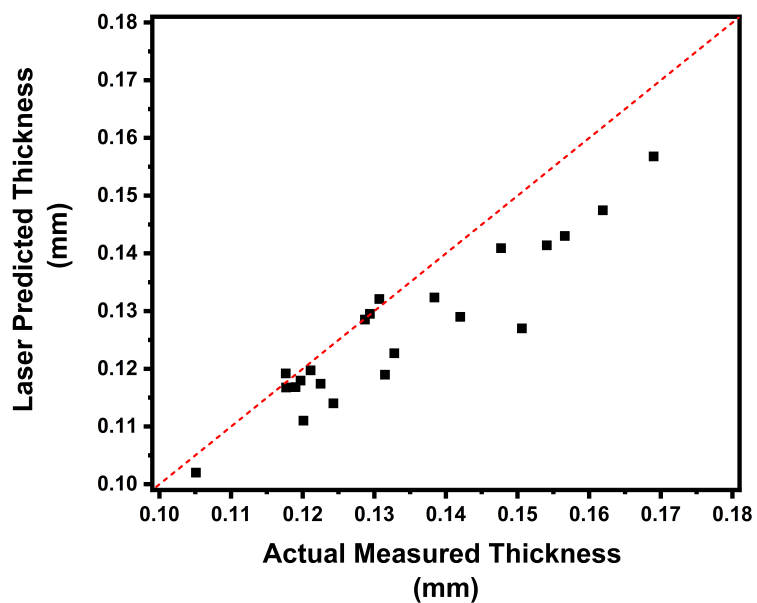


Fig. D.1.: Verification of thickness calculations made by laser device during uniaxial stretching.

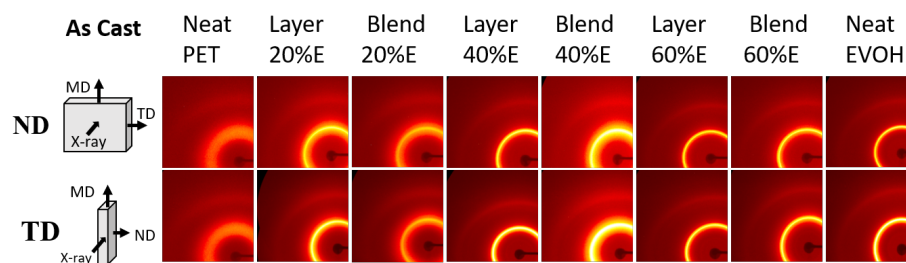


Fig. D.2.: WAXS images for blend and layer films in as cast state.

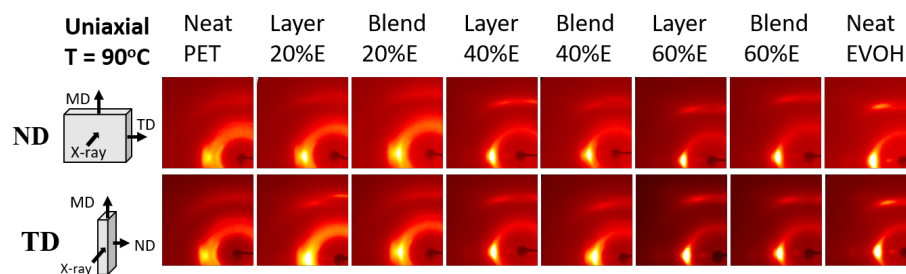


Fig. D.3.: WAXS images for blend and layer films after stretching at 90°C and 30 mm/min to 3.5X initial length.

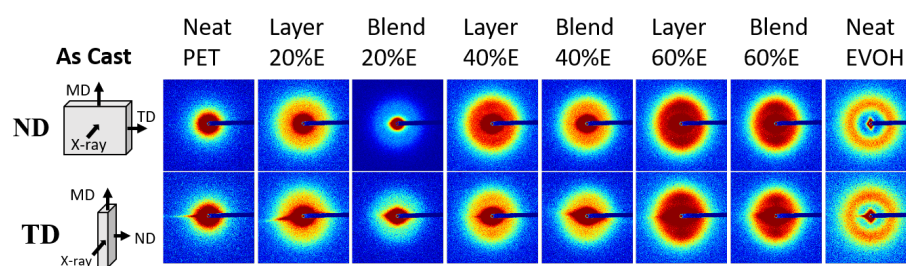


Fig. D.4.: SAXS images for blend and layer films in as cast state.

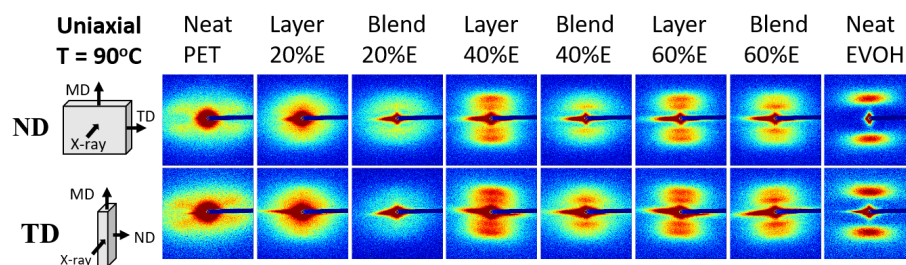


Fig. D.5.: SAXS images for blend and layer films after stretching at 90°C and 30 mm/min to 3.5X initial length.

40-20-40 % PET-EVOH-PET Layer Film
3.5X, 90°C, 30 mm/min

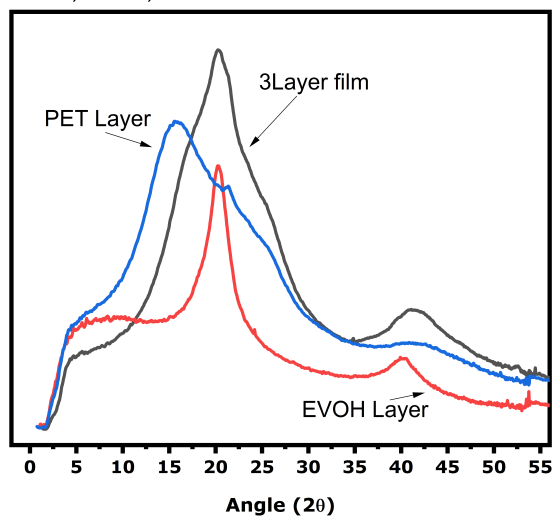


Fig. D.6.: 1D WAXS curves for 20% EVOH layered film after stretching 90°C and 30 mm/min to 3.5X initial length, versus individual separated layers.

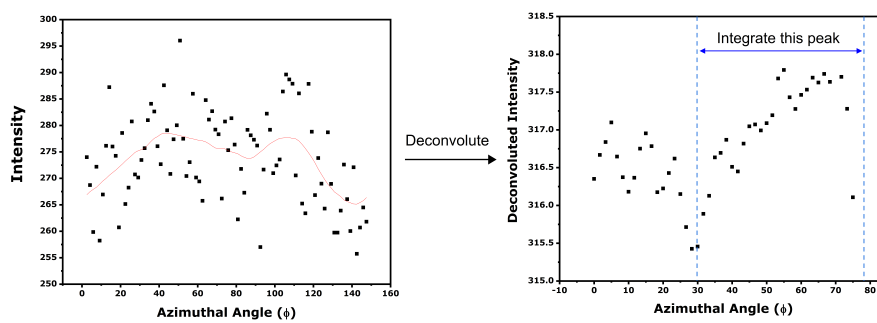


Fig. D.7.: Example deconvolution of $2\theta = 26.24^\circ$ PET peak from WAXS.

VITA

VITA

Megan E. Forshey

EDUCATION**Doctor of Philosophy**

Purdue University, West Lafayette, IN.

Material Science and Engineering, August 2016-July 2019.

Dissertation title: "Orientation of polymer films for improvement of dielectric properties for high-energy density capacitor applications".

Bachelor of Science

Rose-Hulman Institute of Technology, Terre Haute, IN.

Chemical Engineering, May 2012.

ACADEMIC EMPLOYMENT

Graduate Teaching Assistant, Department of *Material Science and Engineering*, Purdue University, January 2018. Responsibilities include: assisting with preparation of course materials, teaching weekly lectures, preparing and overseeing polymer processing laboratory experiments.

Teaching Assistant for Purdue Super Saturdays Outreach Program, January - March, 2017. Responsibilities include: Assistant taught, as a volunteer, an electrical engineering course to gifted middle school children.

INDUSTRIAL WORK EXPERIENCE**Braskem**

2019-present

Research and develop polypropylene grades with optimized properties to meet customer and market needs.

A. Schulman

2013-2016.

Formulate polymer additive compounds to solve customer specific engineering problems. Record project details in Stage-Gate system to manage and track these developments. Analyze and communicate lab data to customers and sales personnel.

Halliburton

2012-2013.

Calculate and simulate parameters for cementing jobs in the oilfield, with a focus on safety. Perform and evaluate laboratory testing on cement slurries. Write proposals describing cement volume, additives, and cost estimates to customers.

PUBLICATIONS

Microlayered PET/PVDF films: Mechano-optical behavior in uniaxial extension (Expected, 2019).

Microlayered PET/PVDF films: Effect of orientation and annealing on dielectric properties (Expected, 2019).

Mechano-optical behavior of uniaxially oriented fluoropolymer films: ethylene tetrafluoroethylene copolymer (ETFE) and tetrafluoroethylene- hexafluoropropylene- vinylidene fluoride terpolymer (THV) (Expected, 2019).

Mechano-optical behavior and morphology of uniaxially oriented polyethylene terephthalate (PET) and ethylene vinyl alcohol copolymer (EVOH) compounded blend films and three layer coextruded films (Expected, 2019).

PRESENTATIONS AT PROFESSIONAL MEETINGS

Polymer Processing Society (PPS) Conference, Boston, MA: Orientation of polymer films to improve dielectric properties for capacitor applications, 2018.

MURI Technical Meeting at Georgia Tech, Atlanta, GA: Processing strategies to tailor polymer morphology of microlayer coextruded films to optimize dielectric properties, 2018.

Soft Materials Summer Symposium at Purdue University: Microlayered PET/PVDF Films: Mechano-Optical Behavior in Uniaxial Extension, 2017.

Research poster presentation at Kent State University: *Investigation of Side Chain Length and Functionality on Surface Freezing Phenomenon of Polymers*, 2010.

ACADEMIC AWARDS

Estus H. and Vashti L. Magoon Graduate Teaching Award, Department of Material Science and Engineering, Purdue University, 2019.

Conference Travel Funds Award, College of Engineering, Purdue University, 2018.

Women in Engineering Program travel grant to attend National Conference for College Women Student Leaders, Purdue University, 2016.

Rose-Hulman Merit Scholar scholarship award, Rose-Hulman Institute of Technology, 2008-2012.

Alpha Lambda Delta Collegiate Honor Society inductee, Rose-Hulman Institute of Technology, 2008-2012.

Access to Education scholarship recipient, Rose-Hulman Institute of Technology, 2011.

ACFEA General John. A. Wickman scholarship recipient, Rose-Hulman Institute of Technology, 2011.

Donald F. Othmer Academic Excellence Award, Rose-Hulman Institute of Technology, 2009.

PROFESSIONAL MEMBERSHIPS

Society of Plastics Engineers Member, 2014-present.